Na$_v$-igating Voltage-Gated Sodium Channels

Structure, Biophysics and Modulation

Von der Fakultät für Mathematik und Naturwissenschaften der RWTH Aachen University zur Erlangung des akademischen Grades eines Doktors der Naturwissenschaften genehmigte Dissertation

vorgelegt von

Sudha Bhagavath Eswaran, Vishal M.Sc.

aus

Trivandrum, Kerela, Indien

Berichter:

Univ.-Prof. Paolo Carloni, Ph.D.

Univ.-Prof. Dr. med. Angelika Lampert

Univ.-Prof. Dr. rer. nat. Geraldine Zimmer-Bensch

Tag der mündlichen Prüfung:

18.11.2025

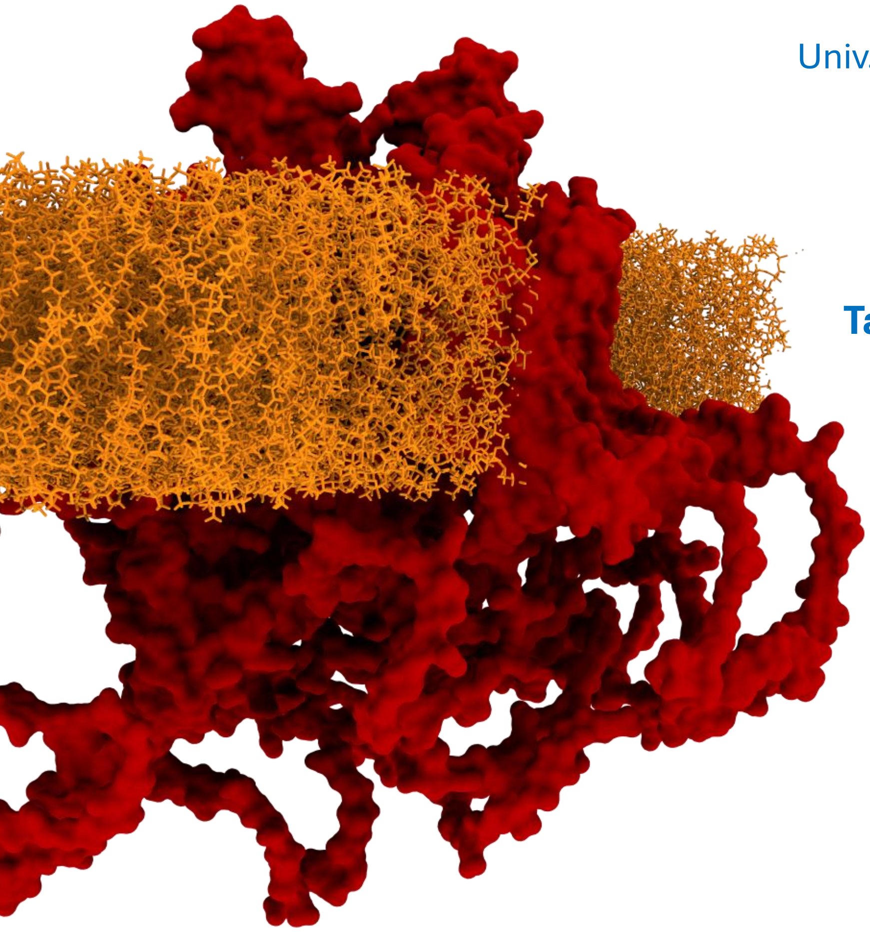

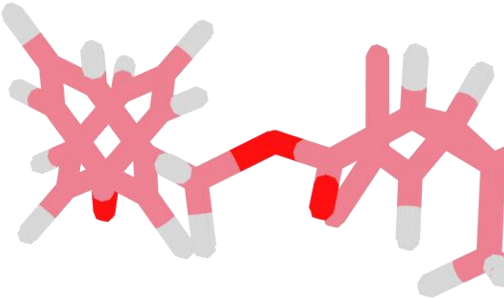

This thesis is dedicated to my dear wife Sunayana for her unconditional support and encouragement to pursue my dreams, without which none of this would be feasible.

Eidesstattliche Erklärung

Declaration of Authorship

I, **Vishal Sudha Bhagavath Eswaran**

declare that this thesis and the work presented in it are my own and has been generated by me as the result of my own original research.

Hiermit erkläre ich an Eides statt / I do solemnely swear that:

1. This work was done wholly or mainly while in candidature for the doctoral degree at this faculty and university;

2. Where any part of this thesis has previously been submitted for a degree or any other qualification at this university or any other institution, this has been clearly stated;

3. Where I have consulted the published work of others or myself, this is always clearly attributed;

4. Where I have quoted from the work of others or myself, the source is always given. This thesis is entirely my own work, with the exception of such quotations;

5. I have acknowledged all major sources of assistance;

6. Where the thesis is based on work done by myself jointly with others, I have made clear exactly what was done by others and what I have contributed myself;

7. Parts of this work have been published before as:

    - *Albani, S.*, **Eswaran, V.S.B.*,** Piergentili, A., De Souza, P.C.T., Lampert, A. and Rossetti, G., 2024. Depletion of membrane cholesterol modifies structure, dynamic and activation of Nav1. 7. International Journal of Biological Macromolecules, 278, p.134219.(* shared first authorship)*
    - *Toklucu, I., **Sudha Bhagavath Eswaran, V**., Bott, R.A., Kesdoğan, A.B., Gaebler, A.J., Stingl, J., Hausmann, R., Körner, J. and Lampert, A., 2025. α-Adrenoreceptor blocker phentolamine inhibits voltage-gated sodium channels via the local anaesthetic binding site. British Journal of Pharmacology.*

Date

signature

Acknowledgements

I would like to first and foremost express my heartfelt gratitude to my supervisor Prof. Dr. Angelika Lampert for her guidance throughout my doctoral studies. She was involved throughout my doctoral program while ensuring I had the freedom to develop strategies for my own projects. Her supervision and professionalism serve as an inspiration for a young scientist such as myself, and I cannot begin to express the monumental role she has played and will continue to do so in helping me kick-start my academic journey.

Great supervisors also bring great teams, and this is what I experienced with members of the Institute for Neurophysiology. The friendly and open work environment also helped in me having a memorable doctoral study program. Petra Hautvast and Marina Wolf-El Houari provided much-needed technical assistance and ensured I had all the plasmids and cells I needed. Jannis Körner and Idil Toklucu also have my hearfelt thanks for the opportunity to work on the phentolamine project. Dr. Markos Xenakis always had time to indulge in my hypotheses and showed a different perspective in which one can understand these enigmatic channels. Aylin Kesdogan gave me the opportunity to collaborate on the gain-of-function project and was also my table-tennis teammate without whom I would not have won the AG Lampert BBQ Table Tennis Tournament (a highly acclaimed tournament I must say). Andelain Erickson helped me with various biochemical techniques with the loss-of-function project. I give my thanks also to Dawi Bajunaid (boys, boys, boys) for wanting to learn from me and be part of my projects, providing much needed help. Fiona Roll made going through endless troubleshooting of the HEKA patch systems less tiresome, and I had a lot of fun being part of the KinderUni promo video (I still have the video of you bumping your head against the pole) and the documentary about Na_vs. Anika Neureiter helped with immunostaining experiments of the HA-tagged constructs. To other members of the lab who supported me in some capacity big or small – you have my heartfelt thanks.

I would like to thank Simone Albani for his constant support with my *in-silico* methodologies and indulging in my “conspiracy” theories on various Na_v-related topics over some ramen.

I also would like to thank the RTG2416 “MultiSenses MultiScales”, especially the coordinators Oke Nommensen and Dr. Jennifer Spehr for their administrative support. The RTG also allowed financial support to attend various conferences, organize talks and engage with the vibrant student cohort in internal retreats.

I would like to thank Prof. Dr. Ralf Hausmann, his bachelor student Amdiya Botchoi and his lab technician Sylvia Destro-Dassen for their invaluable help in generating extracellularly tagged HA cell lines, which helped answer a pivotal question in one of my projects.

I would like to also extend my gratitude to the other members of my thesis committee, Prof. Dr. Giulia Rossetti, Prof. Dr. Paolo Carloni and Prof. Dr. Enrico Leipold for their guidance.

I would like to thank the vibrant members of the Scientific Center for Neuropathic Pain Aachen ($SCN^{AAACHEN}$) committee for providing a platform in which to discuss various Na_v-related projects.

I would finally like to thank my parents, parents-in-law, my brother, my “adopted sister” Devki Mishra and all my friends who ensured I never felt alone in another country and provided much needed emotional support.

Table of Contents

Zusammenfassung

Spannungsgesteuerte Natriumkanäle (Na$_v$s) sind wichtig für die Übertragung elektrischer Reize durch Neuronen und erzeugen den schnellen Aufstrich der Aktionspotenziale. Verschiedene Kanalopathien dieser Membranproteine führen zu einer Vielzahl von klinischen Krankheitsphänotypen, die sich grob in eine Verstärkung oder einen Verlust der Funktion einteilen lassen. Wenn wir verstehen, wie diese Kanäle entweder physiologisch oder extern durch künstlich hergestellte chemische Verbindungen moduliert werden können, wird dies unser Verständnis der Funktionsweise dieser Kanäle verbessern und bessere Strategien zur Behandlung von Krankheiten ermöglichen. In dieser Arbeit untersuche ich die modulatorischen Aspekte von Navs anhand verschiedener Systeme, die als Beispiel für physiologische (Punktmutationen, Membranzusammensetzung) oder künstliche Nav-Modulation dienen:

1. Ich verwende eine Kombination aus grobkörniger Molekulardynamik, Ganzzell-Patch-Clamp- und extrazellulären Protein-Tagging-Techniken, um zu zeigen, dass eine Loss-of-Function-Mutation, die sich in der Membran befinden kann , die Geometrie der äußeren Pore stören und damit die Ionenleitung blockieren kann.

2. Ich verwende ein modifiziertes Protokoll für grobkörnige Molekulardynamik, um zu zeigen, wie wichtig die Geometrie der Kanalstruktur für die Gewährleistung einer ordnungsgemäßen schnellen Inaktivierung ist und wie diese bei Funktionsgewinnmutationen gestört wird.

3. Ich zeige mit *In-vitro*- und *In-silico*-Experimenten, dass der Cholesteringehalt der Zellmembran für das korrekte Na$_v$1.7-Gating entscheidend ist und dass eine pharmakologische Reduzierung des Cholesterins zu einer Funktionssteigerung von Na$_v$1.7 führt.

4. Ich sage voraus, dass die Lokalanästhesiestelle die wahrscheinlichste Bindungsstelle für den α-Adrenorezeptorblocker Phentolamin in Navs ist, indem ich computergestützte Andockstrategien für Arzneimittel anwende.

In meiner Dissertation stelle ich ein neues Paradigma zum Verständnis der Struktur-Funktions-Beziehungen von Na$_v$s vor, indem ich verschiedene *In-silico*-Tools mit *In-vitro*-Techniken kombiniere. Auf molekularer Ebene etabliere ich Methoden zur Visualisierung und Analyse struktureller Veränderungen und verbinde sie mit mechano-funktionellen Signaturen. Außerdem validiere ich diese Signaturen mit *In-vitro*-Tools auf zellulärer Ebene. Dies wiederum ermöglicht die Untersuchung von Struktur-Funktions-Beziehungen aus verschiedenen Blickwinkeln und erweitert unser Verständnis der Wechselwirkungen von Na$_v$s mit der Zellmembran und der Modulation durch externe Medikamente.

Thesis Summary English

Voltage-gated sodium channels (Na_vs) are important for the transmission of electrical stimuli across neurons, creating the upstroke phase of an action potential. Various channelopathies in these membrane proteins lead to a variety of clinical disease phenotypes, broadly categorizable into either gain or loss of function. Thus, understanding how these channels can be modulated either physiologically or externally by artificially generated compounds will improve our understanding of how these channels function, allowing better strategies for treatment of diseases. In this thesis, I explore the modulatory aspects of Na_vs using various systems as an example for either physiological (point mutations, membrane composition) or artificial Na_v modulation:

1. I utilize a combination of coarse-grained molecular dynamics, whole-cell patch clamp and extracellular protein tagging techniques to show that a loss-of-function mutation successfully trafficking to the membrane can disrupt the geometry of the outer pore and thus block ion conduction.

2. I utilize a modified protocol for coarse-grained molecular dynamics to show the importance of geometry in ensuring proper fast inactivation and how this is disrupted in gain-of-function mutations.

3. I show with *in-vitro* and *in-silico* experiments that cholesterol content of the cell membrane is crucial for proper Na_v1.7 gating and pharmacological depletion of cholesterol results in gain-of-function of Na_v1.7.

4. I predict the local anaesthetic site to be the most probable binding site for the α-adrenoreceptor blocker phentolamine in Na_vs by using computational drug docking strategies.

My thesis introduces a novel paradigm on how to understand the structure-function relationships of Na_vs by combining various *in-silico* tools with *in-vitro* techniques. At a molecular level, I establish methods to visualize and analyze structural changes and link them to mechano-functional signatures. I also validate these signatures using in-vitro tools at a cellular level. This in turn allows the investigation of structure-function relationships from multiple angles, augmenting our understanding of Nav interactions with the membrane and modulation by external drugs.

List of Abbreviations

AP – Action potentials
APL – Area per lipid
BrS – Brugada syndrome
CC – Central cavity
CD – Current densities
CGMD – Coarse-grained molecular dynamics simulations
chol – Cholesterol
CIP – Congenital insensitivity to pain
CNS – Central nervous system
DMEM – Dulbecco's modified eagle medium
ECG – Electrocardiogram
ECS – extracellular solution
ENC – extracellular negative cluster
ER – Endoplasmic reticulum
Ex11del – hNa$_v$1.7 c.1602+2delT
FA$_{1.5}$ – hNa$_v$1.5 F1760A
FA$_{D1}$ – hNa$_v$1.7 F344A
FA$_{D3}$ – hNa$_v$1.7 F1378A
FA$_{D4}$ – hNa$_v$1.7 F1670A
FBS/FCS – Fetal bovine or calf serum
GFP – Green fluorescent protein
GoF – Gain of function
HEK – Human embryonic kidney cells
ICS – Intracellular solution
IEM – Inherited erythromelagia
IG – Intracellular gate
Ig - Immunoglobin
INC – Intracellular negative cluster
KL-divergence – Kullback-Leiber divergence
K$_v$ – Voltage-gated potassium channels
LA – Local anaesthetics
LoF – loss of function
LQT3 - Long-QT type 3 syndrome
MA – hNa$_v$1.7 M899A
MAP – Microtubule-associated protein
MC – hNa$_v$1.7 M899C
MF – hNa$_v$1.7 M899F
MI – hNa$_v$1.7 M899I
MI$_{1.5}$ – hNa$_v$1.5 M881I
MI$_{GFP}$ – hNa$_v$1.7 M899I-GFP fusion protein
MI$_{HACterm,TO}$ – hNa$_v$1.7 M899I C-term-HA Tet-on
MI$_{HAext1,TO}$ – hNa$_v$1.7 P149-HA-P150 M899I Tet-on
MI$_{HAext2,TO}$ – hNa$_v$1.7 L280-HA-E281 M899I Tet-on
MI$_{HAext3,TO}$ – hNa$_v$1.7 L293-HA-E294 M899I Tet-on
MI$_{non\text{-}tagged,TO}$ – hNa$_v$1.7 M899I Tet-on without HA tag
ML – hNa$_v$1.7 M899L
MT$_{1.2}$ – hNa$_v$1.2 M925T
MV – hNa$_v$1.7 M899V
MßCD – Methyl-beta-cyclodextrin
NaCl – Sodium chloride
Na$_v$ - Voltage-gated sodium channels
NK$_{1.5}$ – hNa$_v$1.5 N1765K
NGS – Next generation sequencing
PEPD – paroxysmal extreme pain disorder
PKA – protein kinase A
PKC – protein kinase C
PM – Pore module
PNS – Peripheral nervous system
POPC – Phosphatidylcholine
PTM – post-translational modification
QST – Quantitative sensory testing
RMP – Resting membrane potential
RMSD – Root mean square deviations
RMSF – Root mean square fluctuations
R$_{pip}$ – Pipette resistance
R$_{series}$ – Series resistance

TM – Transmembrane
TO – Tet-on
TTX – Tetrodotoxin
V_{error} – Voltage error
VGICs – Voltage-gated ion channels
VSD – Voltage sensor domain
WT – hNa$_v$1.7 wild-type
WT$_{1.2}$ – hNa$_v$1.2 wild-type
WT$_{1.5}$ – hNa$_v$1.5 wild-type
WT$_{GFP}$ - hNa$_v$1.7 WT-GFP fusion protein
WT$_{HACterm,TO}$ – hNa$_v$1.7 WT C-term-HA Tet-on
WT$_{HAext1,TO}$ – hNa$_v$1.7 WT P149-HA-P150 Tet-on
WT$_{HAext2,TO}$ – hNa$_v$1.7 WT L280-HA-E281 Tet-on
WT$_{HAext3,TO}$ – hNa$_v$1.7 WT L293-HA-E294 Tet-on
WT$_{non\text{-}tagged,TO}$ – hNa$_v$1.7 WT Tet-on without HA tag
ß – beta subunits

“If something is in me which can be called religious then it is the unbound admiration for the structure of the world so far as our science can reveal it.”

- **Albert Einstein**

Chapter 0: Aim of the Thesis

Voltage-gated sodium channels (Na$_v$s) are membrane proteins important for a variety of bodily functions – the major one being in the transmission of electric signals along neurons. Thus, understanding these proteins and how they can be modulated can help us answer important questions on the mechanisms of channelopathies and their treatment using externally applied drugs or compounds. The aim(s) of the thesis are to build a structure-function picture of Na$_v$s using a mutli-scale approach. The aims are as follows:

1. Understand how genetic mutations of Na$_v$s can influence structure and subsequently functioning of the channel.
2. Understand the impact of the lipid bilayer on gating of Na$_v$s.
3. Understand the structural mechanism of action of drugs that bind to Na$_v$s.

To this extent, the aims were to be achieved with the following objectives:

1. Utilization of hNa$_v$1.7 mutations in a patient with a partial insensitivity to pain to understand mechanism of loss of function via *in vitro* (cellular scale) and *in silico* (atomic scale) techniques.
2. Utilization of a hNa$_v$1.7 mutation in a patient with paroxysmal extreme pain disorder to understand mechanism of gain of function using molecular dynamics simulations (atomic scale).
3. Describing the effects of depleting cholesterol from the lipid bilayer on Nav gating using whole-cell patch clamp (cellular scale).
4. Determine the binding of the drug phentolamine on hNa$_v$1.5 and its possible structural mechanism of action (atomic scale).

Chapter 1: Introduction to Voltage-gated Sodium Channels

Chapter 1 starts by introducing Na$_v$s and their physiological relevance in the human body **(section 1.1 – 1.2).** I then transition briefly into the structural architecture of eukaryotic Na$_v$s **(section 1.3)**, before connecting structure and physiology to give an insight into what structure-function relationship of Na$_v$s look like **(section 1.4)**. I then discuss the various ways in which this structure-function relationship of Na$_v$s can be modulated, both internally by the body and externally by various compounds **(section 1.5)**. I end the chapter by briefly touching on the most important points of the subsequent chapters – how and why do we need to study these proteins **(section 1.6)**.

1.1 What are Voltage-gated Sodium Channels?

All living organisms are composed of fundamental units called cells. Cells typically have an outer double-layered membrane which is almost impermeable to ions due to their lipophilicity. However, movement of ions in and out of the cell are crucial for life as they control diverse processes such as signal propagation across neurons, transducing sensory signals, hormonal secretion and osmotic regulation (Ashcroft, 1999). This problem is overcome by the presence of specialized proteins embedded in the membrane. These membrane proteins can either be channels, transporters or pumps. Of the three, ion channels are pores whose opening and closing are controlled either intrinsically (like leak channels) or extrinsically (by ligands, voltage changes or mechanical stimuli) (Ashcroft, 1999). This opening or closing of the channel allows for ions to flow in or out of the cell depending on the difference in ionic concentrations. Voltage-gated ion channels (VGICs) are channels whose pores allow passage of select inorganic ions and are extrinsically controlled by sensing changes in the transmembrane voltage (Sands et al., 2005). This voltage gradient is achieved by manipulation of ionic concentrations across the membrane.

Voltage-gated sodium channels are one such ion channel superfamily that allow predominantly sodium ions to flow into the cell when a transmembrane voltage change appears across the bilayer. Mammalians express a total of nine different Na_v subtypes ($Na_v1.1$ – $Na_v1.9$) and are encoded by the SCN1A-11A genes respectively (Nishino and Okamura, 2018) (Table 1). $Na_v1.1$-$Na_v1.3$ and $Na_v1.6$ are primarily expressed in the central nervous system (CNS), $Na_v1.7$-$Na_v1.9$ are mostly expressed in the peripheral nervous system (PNS), $Na_v1.4$ is highly expressed in the skeletal system and $Na_v1.5$ is highly expressed in the cardiac system (Nishino and Okamura, 2018) (Table 1).

Table 1: The various subtypes of mammalian Na_vs, the respective genes encoding them and the region in which they are majorly expressed. Table adapted from (Nishino and Okamura, 2018). CNS: Central nervous system, PNS: Peripheral nervous system

Gene Name	Encoded Channel Subtype	Major Region of Expresssion
SCN1A	$Na_v1.1$	CNS
SCN2A	$Na_v1.2$	CNS
SCN3A	$Na_v1.3$	CNS
SCN4A	$Na_v1.4$	Skeletal muscle
SCN5A	$Na_v1.5$	Heart
SCN8A	$Na_v1.6$	CNS
SCN9A	$Na_v1.7$	PNS
SCN10A	$Na_v1.8$	PNS
SCN11A	$Na_v1.9$	PNS

1.2 Physiological relevance of Na_vs

Propagation of the electrical signals happens along the axon of the neuron, by altering the ionic concentrations of the neuronal membrane. This was the basis for the model proposed by Hodgkin and Huxley, who showed that "action potentials" (AP) are generated along the giant squid axon when various ions like sodium, potassium, calcium and chloride pass in and out of the cell membrane due to changes in the transmembrane potential that are facilitated by VGICs (Hodgkin and Huxley, 1952).

The transmembrane potential is a result of an electrochemical gradient – the chemical gradient drives ions from a high to a low concentration region and the electrical gradient drives ions towards a region with a net opposite charge. The chemical gradient for sodium and potassium ions is set up by the active transport of three sodium ions outside and two potassium ions inside by the Na-K ATPase pump. This results in potassium ions having a concentration gradient from inside to the outside of the cell, and vice versa for the sodium ions. In a non-excited state (i.e. at rest) however, most Na_vs are closed and only the potassium leak channels stay open. This allows for the movement of potassium ions across the semi-permeable bilayer along the chemical gradient setup by the Na-K ATPase pump. The movement results in more cationic potassium ions moving outside the cell while leaving behind the anions inside the cell, causing the potential of the inside of the cell to be more negative relative to the outside. Such an ion flow proceeds until the electrostatic force exerted by the anion on the remaining cations inside the cell is equal and opposite to the chemical gradient along which the cationic potassium ion flows, resulting in no movement of ions. The potential at which this occurs for an ion is the equilibrium potential of that specific ion. For potassium ions, this is around -90mV. This means that when the potential of the inside is 90mV more negative than the outside, there is no flow of potassium ions across the membrane. However, this does not equate to equal number of potassium ions between the inside and outside of the cell. It means instead that the chemical gradient and the electrostatic force are now equal and opposite to each other. In a neuronal membrane, although the permeability to potassium ions is high at rest, the permeability to other ions is not zero. This contribution of the permeabilities of other ions results in the resting membrane potential slightly depolarized, but close to the equilibrium potential of potassium ions, around -70mV.

When an electric stimulus is felt in the neuronal membrane, the membrane potential of the inside relative to the outside of the cell starts to depolarize (i.e. become more positive). At a certain point, the membrane potential depolarizes enough to start the opening of Na_vs. This “threshold” potential results in a feed-forward loop where opening of some Na_vs results in opening of more Na_vs, causing rapid depolarization of the membrane potential, observed as the upstroke of the AP. Although the threshold for voltage-gated potassium channels (K_vs) are similar to Na_vs, their kinetics are much slower. The opening of K_vs thus coincides with the quick closure of Na_vs, resulting in the repolarization of the membrane potential as K_vs start to move from inside to the outside of the cell. As the potential falls below the threshold, both Na_vs and K_vs start to transition into a closed state. The slower kinetics of the K_vs however means that they are slow to close and stay open longer than needed to return the potential to RMP, causing hyperpolarization and bringing the membrane potential to potentials more negative than the RMP. The AP cycle is illustrated in Figure 1.

As is observable in Table 1, $Na_v1.7$ is mostly expressed in peripheral neurons, thus playing an important role in propagation of signals from receptors in the skin to the CNS. Some noxious signals at the level of our skin could pose a threat to our homeostasis. Decisions must be made relatively quickly on how to respond to these stimuli, as this could be the difference between removing the hand from a burning stove and having second degree burns. The processing of these noxious stimuli is termed nociception and often leads to a sensation of pain (Dubin and Patapoutian, 2010). Nociception allows for either a quick reflex response (stimuli transmitted from periphery to spinal cord and back) or more complex motor processing (stimuli transmitted from periphery to higher order brain regions and back) (Dubin and Patapoutian, 2010).

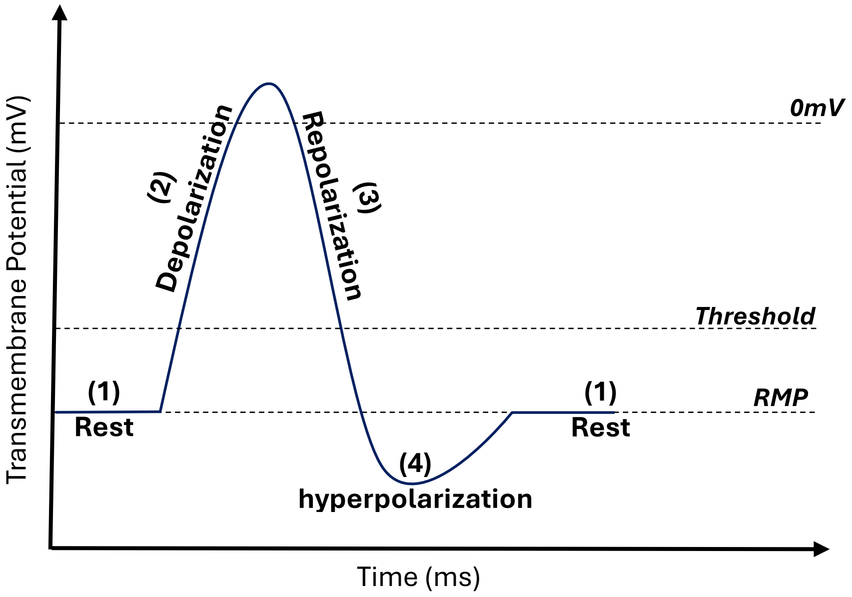

Figure 1 – Simplified Action Potential Action potentials (APs) are generated due to changes in ionic concentrations across neuronal membranes. An AP is made up of four major phases. At rest (1), the membrane potential (resting membrane potential or RMP) is negative. When a stimulus felt by nerve endings in the skin raises the membrane potential above a threshold it results in depolarization of the membrane potential above 0mV due to the opening of Na_Vs. (2). After a few ms, Na_Vs start to close while the slower K_Vs start to open. This causes the flow of sodium ions to stop and potassium ions to move extracellularly, causing repolarization of the membrane potential (3). The slow kinetics of K_Vs result in more outflux of potassium ions even when there is no influx of sodium ions, continuing repolarization even below RMP and causing hyperpolarization before bringing the membrane potential back to the RMP (4).

1.3 Architecture of Na_Vs

Eukaryotic Na_Vs are large proteins folded into four homologous domains (D1, D2, D3 and D4) from a single polypeptide chain made up of around 2000 amino acid residues (Körner and Lampert, 2020). The start and end of the protein are flanked by an N- and C-terminus respectively (Figure 2A). Each domain is composed of three regions – the voltage sensor domain (VSD1, VSD2, VSD3 and VSD4) formed by four transmembrane α-helices (S1, S2, S3 and S4), the pore module (PM1, PM2, PM3 and PM4) formed by two transmembrane helices (S5 and S6) and two re-entrant pore helices (P1 and P2) and the helical S4-S5 linker connecting the VSD and PM (D1 S4-S5, D2 S4-S5, D3 S4-S5 andD4 S4-S5) (Figure 2A, B, C). The domains are connected to each other via long intracellular linkers (D1-D2, D2-D3 and D3-D4), with D3-D4 housing the "IFM" motif. The various structural components play a crucial role in the transition of Na_Vs through the various gating stages. The VSD senses changes in the transmembrane voltage, with the S4 helix moving towards the outside ("up" or activated state) or inside of the cell ("down" or deactivated state) depending on the transmembrane voltage. The PM helps in attracting cations, controls selectivity for sodium ions via the DEKA filter (Figure 2A) and passage of sodium ions across the membrane through a hydrophobic intracellular gate. The S4-S5 linker couples the VSD with the PM (Figure 2A, C). Thus, in an activated state, the PM opens and allows ion flow while in a deactivated state, the PM is closed and blocks ion flow. However, it is not necessary for the VSD to be in a deactivated state for blocking conduction. The IFM motif in the D3-D4 plays an important role in closure of the channel in a few ms to prevent ion flow by binding to a hydrophobic pocket near D3 and D4 – a process termed "fast inactivation" (Figure 1A and D). Thus, we can separate the cycle of

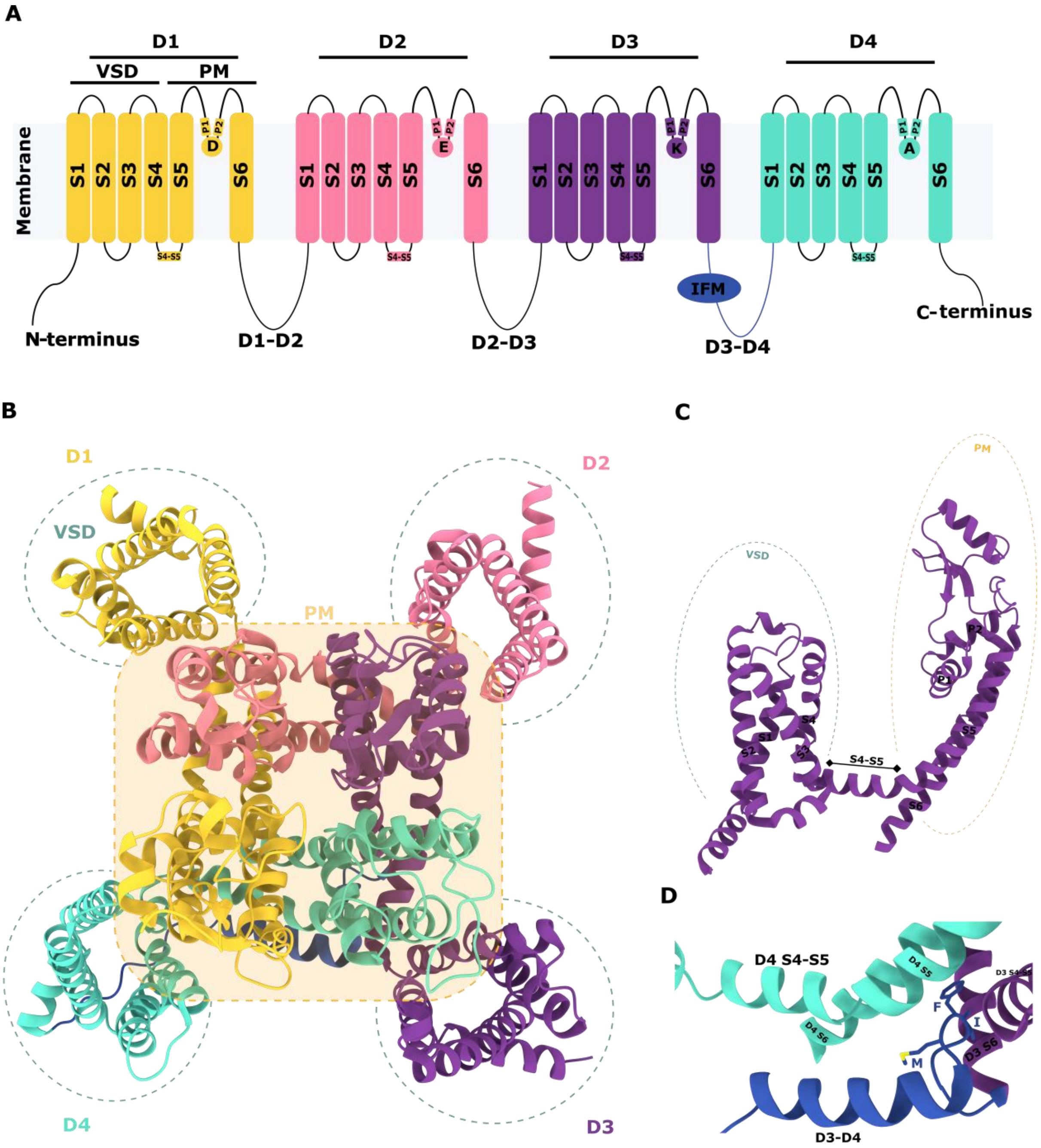

Figure 2 – Topology of Na$_v$s **(A)** 2D schematic of Na$_v$s. Na$_v$s are formed by the folding of a single polypeptide into four homologous domains (D1, D2, D3, D4). Each domain is made of six transmembrane (S1, S2, S3, S4, S5 and S6) and two membrane re-entrant (P1 and P2) helices. In each domain S1, S2, S3 and S4 form the voltage sensor domain (VSD1, VSD2, VSD3 and VSD4) and S5, P1, P2 and S6 form the pore module (PM1, PM2, PM3 and PM4). The PM contains the DEKA motif that allows for Na$_v$s to selectively conduct sodium ions. D1 and D4 are flanked at the start and end by the N- and C-terminus respectively. Domains are connected to each other by long intracellular loops (D1-D2, D2-D3 and D3-D4). The D3-D4 hosts the IFM motif that is important for fast inactivation. The linker between S4 and S5 (S4-S5) acts as a bridge connecting the VSD to the PM. **(B)** An extracellular view of the 3D structure of Na$_v$1.7 (PDB ID: 7W9K, published by (G. Huang et al., 2022a)). The domains are arranged in a domain-swapped manner (i.e. VSD1 interacts with PM2 and so on). The VSDs are shown by dotted circles, while the PMs are shown by a rounded square with dotted lines. The PMs come together to form a channel across the membrane through which ions can flow. (**C**) 3D domain topology of Na$_v$1.7. A look at a specific domain (in this case D3) shows the individual helices. VSD is formed by S1, S2, S3 and S4 helices, PM by S5, P1, P2 and S6 and the S4-S5 connects both these regions. (**D**) The IFM Motif. The IFM motif is a set of 3 hydrophobic residues that bind to a hydrophobic pocket formed by D3 S4-S5, D3 S6, D4 S4-S5, D4 S5 and D4 S6. Binding of this motif quickly closes the Na$_v$ in a few ms in a process termed fast inactivation.

transitions that Na_vs undergo throughout its functional lifetime into 3 major states – resting/deactivated state, activated state and fast-inactivated state.

1.3.1 The voltage sensor

The VSDs sense changes in membrane potential across the membrane. They are composed in each domain by the S1, S2, S3 and S4 helices (Figure 2A, C). The S4 helix hosts a total of four to eight positively charged amino acids – either lysine (K) or arginine (R) – spaced by two hydrophobic amino acids (Figure 2A, B). These positively charged residues move towards the region which is relatively more negative- like the sunflower moving towards sunlight. While most prokaryotic Na_vs have a homo-tetrameric arrangement, mammalian Na_vs have a single polypeptide folded into four domains i.e. the VSDs are similar (homologous) but also different from each other (Gamal El-Din et al., 2018). This is seen in VSDs mainly as varying gating charges on the S4. VSD1, VSD2, VSD3 and VSD4 have four, five, six and eight gating charge residues respectively. While all VSDs contribute to the gating process of Na_vs, VSD1 activation is considered necessary for activation while VSD4 activation is considered necessary for fast inactivation (Capes et al., 2013). VSD3 has been shown to also be involved in the fast-inactivation process with VSD4 (Angsutararux et al., 2021). The S2 helix contains an aromatic amino acid that forms a hydrophobic constriction site, acting as a "gate" through which the gating charges traverse. While many models were conceptualized to explain the mechanism of voltage-sensing, the sliding helix model along with the gating charge transfer model are currently the consensus among many ion channel experts (Catterall, 2023). These models have also been validated by cryo-EM structures of human and bacterial Na_vs, showing an almost 10A° transition of the gating charges going from a resting to an activated state of the VSDs (Clairfeuille *et al.*, 2019; Wisedchaisri *et al.*, 2019, 2021; G. Huang *et al.*, 2022b). The S4 helix is surrounded by the S1, S2 and S3 helices. These helices contain negatively charged residues forming clusters in the extra- and intra-cellular regions of the VSD (extracellular negative cluster and intracellular negative cluster respectively). The Extracellular and intracellular negative clusters help in neutralizing the gating charges, stabilizing their transmembrane position and allowing them to exist within the hydrophobic bilayer (Jiang et al., 2022; Catterall, 2023).

In the sliding helix model, the S4 helix rotates across towards the region of the cell that is relatively more electronegative. We can broadly group the VSDs as being in an activated (or "up") or deactivated (or "down") state. Given that the overall mechanism is the same across all VSDs, we will explain the model with VSD1 as an example. In the resting state, the S4 helix is seen deep in the cytosol, with the first gating charge neutralized by the INC and the rest of the gating charges located in the cytosol (Figure 3A). During activation, the gating charges move ~10A° through the hydrophobic constriction site towards the extracellular surface, exchanging ion pair partners with the intracellular and extracellular negative clusters along the way (Figure 3B). Such exchanges allow for the neutralization of the positively charged gating charge residues, allowing them to exist in the hydrophobic bilayer and move across the hydrophobic constriction site. Recent cyro-EM structures have shown that the entire VSD can also rotate as a whole around the pore axis (G. Huang et al., 2022b; X. Huang et al., 2022).

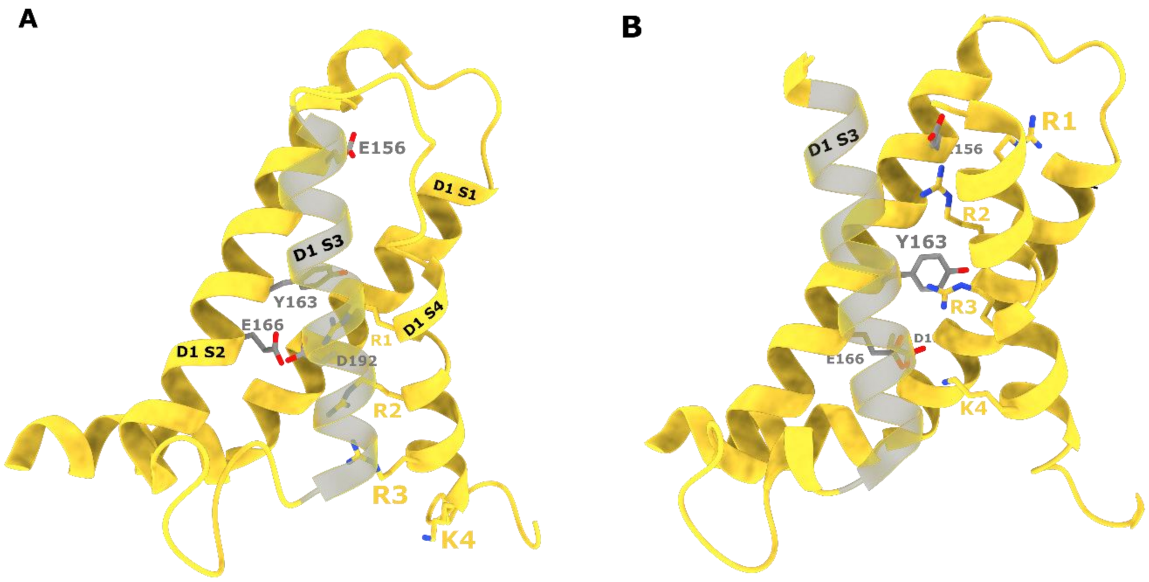

Resting State **Activated State**

Figure 3 – VSD1 of Na_v1.7 VSDs of Na_v1.7 are made up of the S1, S2, S3 and S4 helices, with the S4 hosting between four to eight positively charged residues (gating charges) that sense changes in transmembrane voltage. The gating charges must slide through a hydrophobic constriction site, with the charges neutralized during movement by the negatively charged residues present at the extra- and intra-cellular part of the VSD. In VSD1, four gating charges exist (R1, R2, R3 and K4), with **Y163** forming the hydrophobic constriction site and **E156, E166** and **D192** forming the extracellular and intracellular negative clusters that coordinate the gating charges during sliding of the S4 helix. **(A)** VSD1 of Na_v1.7 in the resting state (PDB ID: 7XVE, (G. Huang et al., 2022b)). Most of the gating charges are deep in the cytosol, below the hydrophobic constriction site residue Y163. R1 is coordinated by the intracellular negative cluster. (**B)** VSD1 of Na_v1.7 in the activated state (PDB ID: 7XVF, (G. Huang et al., 2022b)). The S4 helix rotates and slides through the hydrophobic constriction site residue Y163, with almost three gating charges above the Y163.

1.3.2 The pore module

The PM is formed by 2 transmembrane helices S5 and S6, a re-entrant helix-loop-helix motif formed by P1 and P2, and long extracellular loops between the various helices (Figure 3). The pore module can be dissected into four major regions (Figure 4A). The outer vestibule of the PM forms a funnel-like region, which is rich in negatively charged residues and attracts cations towards the centre of the pore (Figure 4B). This region is defined by a ring of negatively charged residues (EETD for Na_v1.7) which bind neurotoxins like tetrodotoxin (TTX) and are also involved in permeation and gating (Cervenka et al., 2010).

The outer vestibule leads into the narrowest part of the outer pore, the selectivity filter region. This allows Na_vs to only allow dehydrated sodium ions to enter deeper into the pore. The selectivity filter is formed by a ring of four residues (DEKA motif) and backbone atoms of neighboring residues (Figure 4C). The lysine in the ring (K) has been found to be the most important determinant for only allowing sodium ions to pass the selectivity filter (Sun et al., 1997). Unlike prokaryotic and voltage-gated calcium channels, the selectivity filter residues are arranged asymmetrically. Although counterintuitive, Jiang et al., 2020 showed with their Na_v1.5 structure that the glutamate (E) side chain "dunks" (rotates around a torsion angle), allowing K to delocalize its positive charge with nearby backbone carbonyl groups and coordinate sodium ions into the inner pore. Given the large size of the side chain of K, only sodium (or lithium) ions would be able to join in the charge delocalization complex and be small enough to pass the bottleneck formed at the selectivity filter. Further molecular dynamics studies have shown that the protonation of

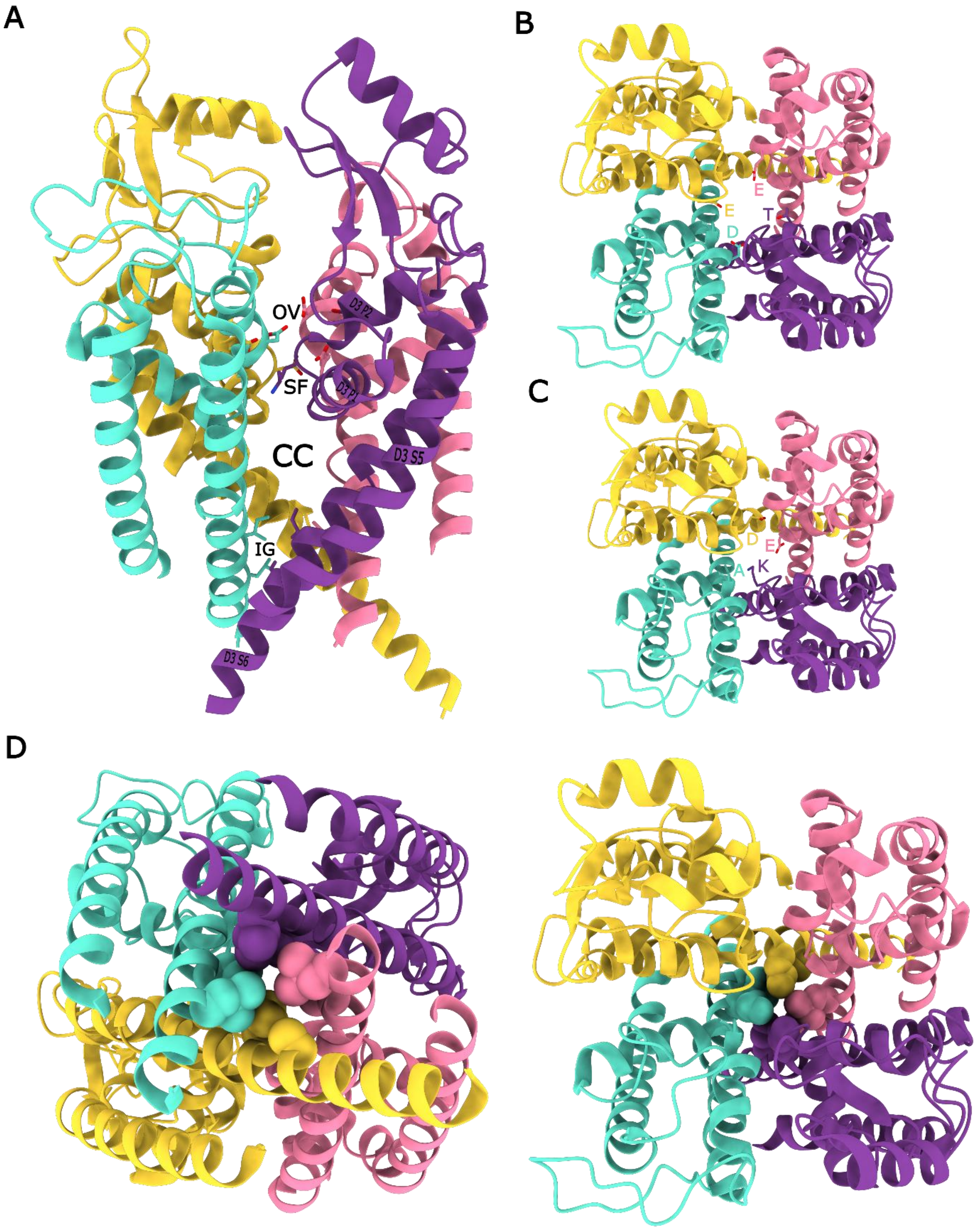

Intracellular view

Extracellular view

Figure 4 – PM of Na$_v$1.7 The PM is composed of the S5, S6, P1 and P2 helices. Here we use the structure from (G. Huang et al., 2022b) as an example (PDB ID 7XVF). **(A)** Side view of the PM. Only the S5, S6, P1 and P2 helices of D3 are labelled for clarity. The PM can be split vertically into four major regions. The outer vestibule (OV) attracts cations and funnels them into the narrow selectivity filter (SF). The SF only allows sodium to pass through into the largest part of the channel, the central cavity (CC). The CC leads to the intracellular gate (IG), that controls access of the ion to the inside of the cell. **(B)** Close-up of the OV residues in an extracellular view. Here we can see the OV is made of a ring of negatively charged residues (EETD). These help in ensuring attraction of cations rather than anions. **(C)** Close-up view of the SF residues in an extracellular view. The K in the DEKA motif is important for sodium selectivity. **(D)** Intra- and extra-cellular views of the IG. The IG residues are shown as spheres. As the structure has a closed pore, the hydrophobic residues face the inside of the pore.

the lysine is important for charge coordination (Zhorov, 2021). In recent cryo-EM structures of $Na_v1.7$ and $Na_v1.6$, the sodium ion can be seen coordinated by residues in the outer vestibule and selectivity filter (G. Huang et al., 2022a; Li et al., 2023). Such coordination could be part of a dehydration step before taking part in the dunking mechanism. Once the ion passes the selectivity filter, it enters the largest region of the ion channel – the central cavity region. This region is where many local anesthetics can bind, aptly termed “site C” (Li et al., 2024) .

When the VSDs activate, ion conduction occurs by the opening of the deepest region of the PM – the intracellular gate region. The intracellular gate consists of a set of hydrophobic residues that face the inside of the pore when closed and move away from the inside of pore when open (Fig 4D). These residues are found in the S6, which has been shown to change secondary structures in different states (Choudhury and Delemotte, 2023; Choudhury et al., 2022; G. Huang et al., 2022a; Lampert et al., 2008). Newer studies have also shown a second set of hydrophobic residues right above the primary ring, which not only plays a role in activation but also fast inactivation (Yichen Liu et al., 2024; Liu and Bezanilla, 2024).

1.3.3 The S4-S5 linkers

The opening of the PM (via the intracellular gate) and activation of the VSD are not mutually exclusive. The S4 of the VSD of one domain connects to both its own S5 and an adjacent domain’s S5 and S6 via the S4-S5. This is a transmembrane helix very close to the lower leaflet of the bilayer (Figure 5A, B). The S4-S5 has been shown to play a very important role in relaying information between the VSD and the intracellular gate via electro-mechanical coupling. This involves an “elbowing” motion of the S4-S5. When the VSD is deactivated, the S4-S5 is bent deep into the cytosol, compressing the S6 and keeping the intracellular gate closed (Figure 5A). During activation, the sliding of the S4 also pulls on the S4-S5, straightening it (Figure 5B). This straightening of the S4-S5 allows space for the S6 to move into, causing a rotation of the S6 and opening of the intracellular gate (G. Huang et al., 2022b; Wisedchaisri et al., 2019). Thus, the S4-S5 acts as a relay circuit, keeping the movements of the VSD and the intracellular gate synchronized to allow opening or closure of the pore.

1.3.4 The fast inactivation motif

The activation of the VSDs and opening of the pore subsequently leads to a swift closure of the pore within a few ms. This process – called fast inactivation – is facilitated by a set of hydrophobic amino acids (IFM motif). Initially thought to work by direct occlusion of the pore by the IFM motif (ball and chain mechanism), a host of literature encompassing functional and structural studies have shown that the fast inactivation occurs in an allosteric manner (Pan et al., 2018; Rühlmann et al., 2020). The IFM motif binds to a pocket formed by various segments of D3 and D4, which gets exposed when VSD3 and VSD4 activate (Figure 2D). This would allow the IFM motif to bind to its pocket, causing conformational changes that involve the pushing of the S6 helices towards the center of the pore and trigger deactivation of the VSDs.

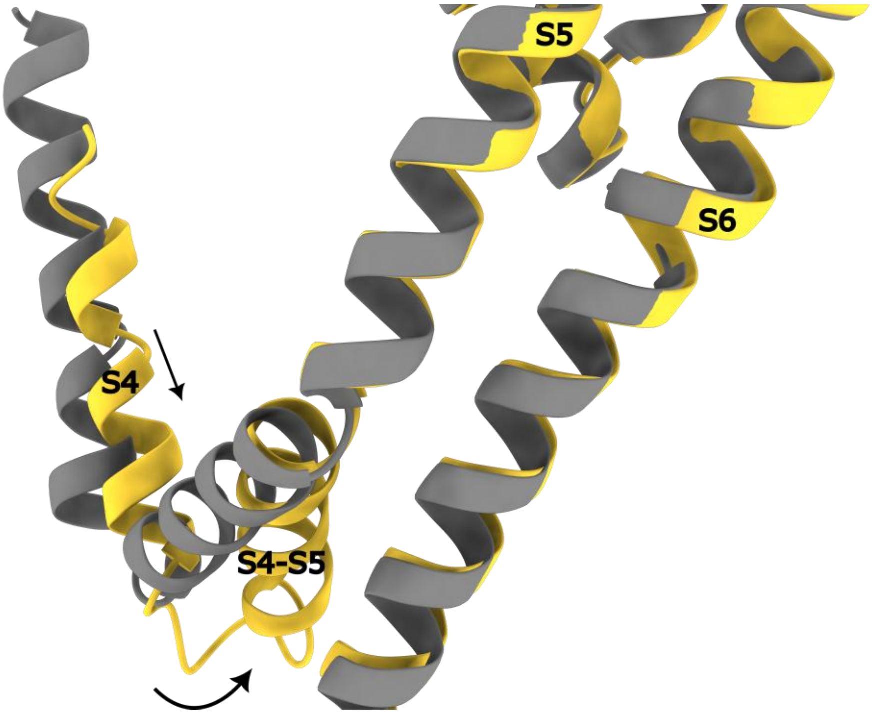

Figure 5 – Electromechanical coupling in Na$_v$1.7 The VSD is electromechanically coupled to the PM by the S4-S5 linker, a transmembrane helix. Here only D1 is shown for clarity. We use the structure from (G. Huang et al., 2022a) as a reference for a VSD1 conformation (PDB ID 7W9K, in **grey**), and the structure from (G. Huang et al., 2022b) as a reference for a VSD1 down conformation (PDB ID 7XVE, in **yellow**). When the S4 moves downward (straight downward arrow), the S4-S5 linker elbows into the pore (bent arrow), constricting the S6 and closing the intracellular gate. The reverse is also true – movement of the S4 upward straightens the S4-S5 linker and opens the pore.

(Clairfeuille et al., 2019) showed that the transition from an IFM-unbound to an IFM-bound state involved the breaking of two "switches" that get formed between VSD4, D3-D4 and the C-terminus. In short, the C-terminus forms ionic interactions with the gating charges of VSD4 (switch 1) and the D3-D4 forms further ionic interactions with the C-terminal end of D4 S6 (switch 2). In the resting state, switch 1 exists and stabilizes the binding of the C-terminus with the D4 S4-S5, which in turn stabilizes the binding of D3-D4 across the C-terminus and the C-terminal end of D4 S6 via switch 2. During VSD4 activation, switch 1 is broken due to the sliding movement of D4 S4. This causes the C-terminus to become more flexible, destabilizing D3-D4 and in turn releasing switch 2. This allows the D3-D4 to be flexible and the IFM motif moves toward the binding pocket and fast inactivates the channel. While this simplistic 2-step model for fast inactivation gives us insight into how the D34 can go from a bound to unbound state, it is yet to be experimentally validated. Also, the allostery involved in the closure of the pore is not well explained using this model. Recently, (Yichen Liu et al., 2024) showcased that the activation gate involves a set of not one but two rings of hydrophobic residues, that completely occlude the pore in a deactivated state. They propose the idea that the binding of the IFM motif triggers a rotation of these gates to occlude the pore, thus blocking ion conduction.

1.4 Structure-Function Relationship of Na$_v$s – Putting the Pieces Together

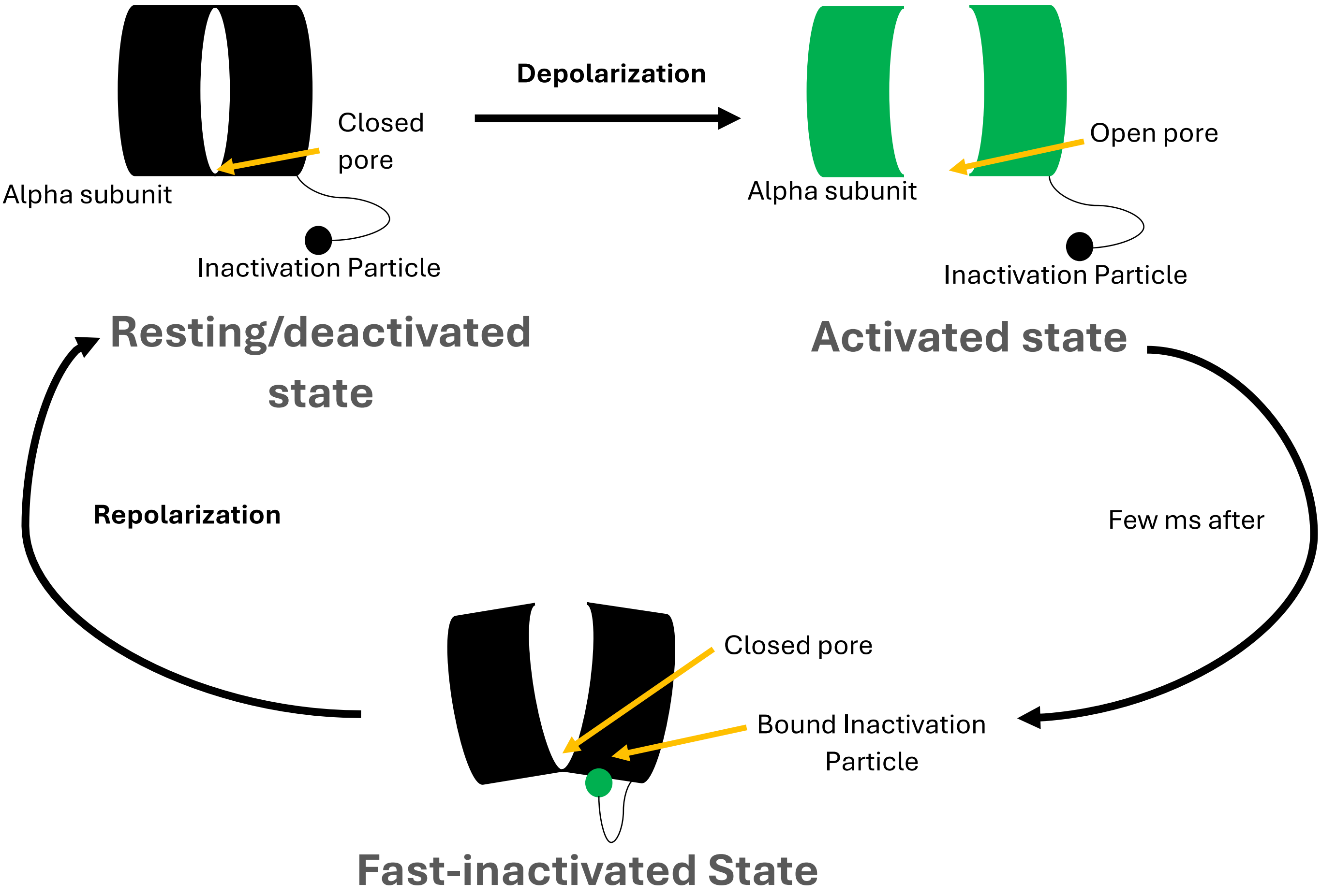

Figure 6 – A simplified representation of structure-function relationship in Na$_v$1.7 At resting state, the pore of Na$_v$s is closed due to the “down” conformation of the VSDs and an unbound fast inactivation motif. When depolarization beyond threshold occurs, the Na$_v$s open their pore due to the “up” conformation of the VSDs and allow sodium ion conduction, going into an activated state. In a few milliseconds (ms), the fast inactivation site is exposed and allows the fast inactivation motif to bind, closing the pore with the VSDs in an “up” conformation and entering the fast inactivated state. This closes ion conduction through Na$_v$s, during which the K$_v$s start to open and begin membrane repolarization. Repolarization allows the VSDs to go back into a “down” conformation, pushing the inactivation particle out and returning to a resting state.

The atomic structure and functional output do not exist in a mutually exclusive fashion. In fact, the gating transitions of the Na$_v$s at a structural level can be correlated to the phases of the action potential at a functional level. We will use the basic 3-state model to attempt such a mapping (Figure 6). At a state of rest or equilibrium, the RMP is negative, the VSDs are in a deactivated state due to the electrostatic gradient, keeping the S4-S5 elbowed and thus constricting the S6 to keep the pore closed (Figure 6, resting state). When depolarization causes the potential to go above the threshold, the gating charges of the S4 sense the change in the electrostatic gradient and thus slide and rotate towards the extracellular region. This straightens the S4-S5, releasing the locks on the S6. The S6 rotates and pushes away from the inside of the pore, with the rotations opening the hydrophobic ring and allowing flow of sodium ions into the cytosol (Figure 6, activated state). Shortly after, the activation of VSD4 is followed by the destabilization of switch 1 and subsequently switch 2. This causes the IFM motif to bind to its now exposed hydrophobic pocket, causing a conformational change allosterically that involves the rotation of the hydrophobic rings to close the pore (Figure 6, fast-inactivated state). The closure coincides with the opening of kinetically slower K_vs and a return to the RMP via re- and hyper-polarization. During this stage, the VSDs deactivate, causing the S4-S5 to elbow and push the IFM out of its pocket. This allows the Na_vs to return to their resting state and be ready for a subsequent round of gating transitions (and hence action potential generation). It is important to keep in mind that such a gating cycle is a simplified representation of a more complex cycle of conformations. For example, channels do not necessarily fast-inactivate after opening. Channels can undergo closed-state inactivation, whereby the channel pore is still closed but the binding pocket for the IFM motif is exposed, leading to fast inactivation of a closed-state structure (Armstrong, 2006). Another example involves kinetically slower forms of inactivation, aptly termed “slow” or “ultra slow” inactivation, whose exact mechanism is unclear but attributed to alterations in outer pore geometry (Silva, 2014).

1.5 Modulation of Na_vs

Na_vs normally undergo a set of physiological gating transitions at both a structural and functional level. However, internal or external factors can influence this structure-function relationship, causing alterations in Na_v gating. Altering Na_v gating in extreme scenarios can lead broadly to hyperexcitability (gain of function or GoF) or hypoexcitability (loss of function or LoF).

1.5.1 Mutations in the SCNxA gene

A natural way by which gating alterations occur is via mutations in the genes coding for Na_vs (SCN1A-SCN11A). These mutations usually occur randomly and are passed down through generations in a hereditary manner. Some common forms of mutations include point mutations (a single codon change results in a different amino acid), truncations (resulting in premature stop of the translation of the sequence) and frameshifts (occurring due to a shift in the codon triplets via insertions or deletions). The clinical manifestation of either GoF or LoF caused by these mutations depends on the Na_v subtype and by extension the region of the body affected. For example, GoF of $Na_v1.5$ results in 10-15% of long QT 3 syndrome (LQT3) cases (Kapplinger et al., 2015). LQT3 is a disease phenotype caused by irregularities in the cardiac repolarization that is observed in the surface electrocardiogram (ECG) as an elongation of the QT interval (Splawski et al., 2000). On the other hand, LoF of $Na_v1.5$ results in 20-30% of brugada syndrome (BrS) cases (Kapplinger et al., 2015). BrS is clinically observed as a ST segment elevation in the ECG, increasing the risk of cardiac arrest by ventricular fibrillations (Priori et al., 2002). Similarly, alterations of $Na_v1.1$ and $Na_v1.2$ gating cause various epileptic disorders (Mulley et al., 2005; Praticò et al., 2021), alteration of $Na_v1.4$ gating results in myopathies (McGowan et al., 2023) and alteration of $Na_v1.7$-$Na_v1.9$ gating results in neuropathies (Brouwer et al., 2014). Changes in $Na_v1.7$ gating can cause pain disorders due to the significant role $Na_v1.7$ plays in nociception.

1.5.1.1 GoF of $hNa_v1.7$

Mutations causing GoF of $Na_v1.7$ can lead to pain disorders such as inherited/primary erythromelagia (IEM) or paroxysmal extreme pain disorder (PEPD). IEM is an autosomal dominant disorder that is observed clinically as sporadic bouts of reddening and swelling of the extremities, usually the hand and feet, earning it the nickname “burning hand and feet” syndrome (Drenth et al., 2005). The attacks are normally induced by heat and begin from adolescence (Eberhardt et al., 2014; Lampert et al., 2010). Treatment of IEM poses a huge challenge, with the most common remedy being to submerge the extremities in cold water. This only abates the symptoms for a short time and comes with its own secondary complications such as infections (Eberhardt et al., 2014). PEPD normally begins during infancy and is characterized by debilitating pain in proximal body regions such as the rectum or jaw (Fertleman et al., 2006). These attacks are typically instigated by autonomic dysfunction, leading to poor feeding and vomiting (Eberhardt et al., 2014).

1.5.1.2 hNa$_v$1.7 p.M1628K causes PEPD

In 2008, a novel hNa$_v$1.7 mutation p.M1627K was characterized that caused PEPD in an English patient (Dib-Hajj et al., 2008). This residue was located in the S4-S5 of D4 and considerably altered various gating parameters when mutated to a lysine. A major finding was that the mutation depolarized voltage-dependence of steady-state fast inactivation, suggesting structurally that fast inactivation is destabilized (Dib-Hajj et al., 2008). A new heterozygous mutation of the SCN9A gene was found in a patient experiencing PEPD at the Uniklinik RWTH Aachen (Prof. Dr. Ingo Kurth Institute for Human Genetics and Genomic Medicine, Uniklinik RWTH Aachen, Germany). The patient experiences extreme pain episodes during bowel movements possibly triggered by exclusively tactile or mechanical stimuli (Prof. Dr. Michael Frosch, Vestische Kinder-Jugendklinik Kinderpalliativ-Zentrum, Datteln and Department of Pediatric Medicine, Uniklinik RWTH Aachen, Germany). The genetic sequencing showed a point mutation in the SCN9A gene, resulting in the protein amino acid mutation hNa$_v$1.7 p.M1628K (Prof. Dr. Ingo Kurth, Institute for Human Genetics and Genomic Medicine, Uniklinik RWTH Aachen, Germany). This residue is only one amino acid downstream of the M1627 residue described previously, with exact same substitution – methionine to lysine (Dib-Hajj et al., 2008).

The hNa$_v$1.7 p.M1628K mutant was electrophysiologically characterized by voltage-clamp experiments on HEK293t cells expressing hNa$_v$1.7 p.M1628K plasmids fused to the green fluorescent protein (GFP) (Aylin Kesdoğan, Institute for Neurophysiology, Uniklinik RWTH Aachen, Germany). This was done along with WT and hNa$_v$1.7 p.M1627K to ensure reproducibility of the phenotypes described previously (Dib-Hajj et al., 2008). Aylin Kesdoğan found that hNa$_v$1.7 p.M1628K and M1627K share a similar gating defect, namely the depolarizing shift in the voltage-dependence of fast inactivation (Figure 7A). Another observation was the altered kinetic properties of fast inactivation in both M1627K and M1628K, having slower onset of fast inactivation compared to the WT although to varying degrees (Figure 7B). Thus, M1628K also seems to disrupt the fast inactivation process as seen in M1627K. However, it was unclear how these functional differences manifest at a structural level.

1.5.1.3 LoF of hNa$_v$1.7

Mutations that result in a complete LoF of Na$_v$1.7 results in an inability to sense pain. Insensitivity to pain can be described as the inability to accurately code stimuli, that one is aware of being exposed to, as painful due to impaired nociception (Goldberg et al., 2007). Most times, the insensitivity to pain arises from birth congenitally as an autosomal recessive disorder (Cummins et al., 2007). This, however, is still a very rare disease with very few cases reported in literature. Whether this is due to a rarity in the mutations, lack of genetic screenings or early death of the patients is unclear. Congenital insensitivity to pain (CIP) does not show impairment in other sensory and motor regions, only in nociception (Goldberg et al., 2007). Although anosmia or hyposmia is seen in some patients, there is no clear correlation that they arise together (Goldberg et al., 2007). As a result of not being able to sense pain, children with CIP show oral and topical lesions that are self-afflicted. Other clinical observations include head trauma, untreated bone fractures that cause deformities and neuropathic joints (Goldberg et al., 2007). Even though the

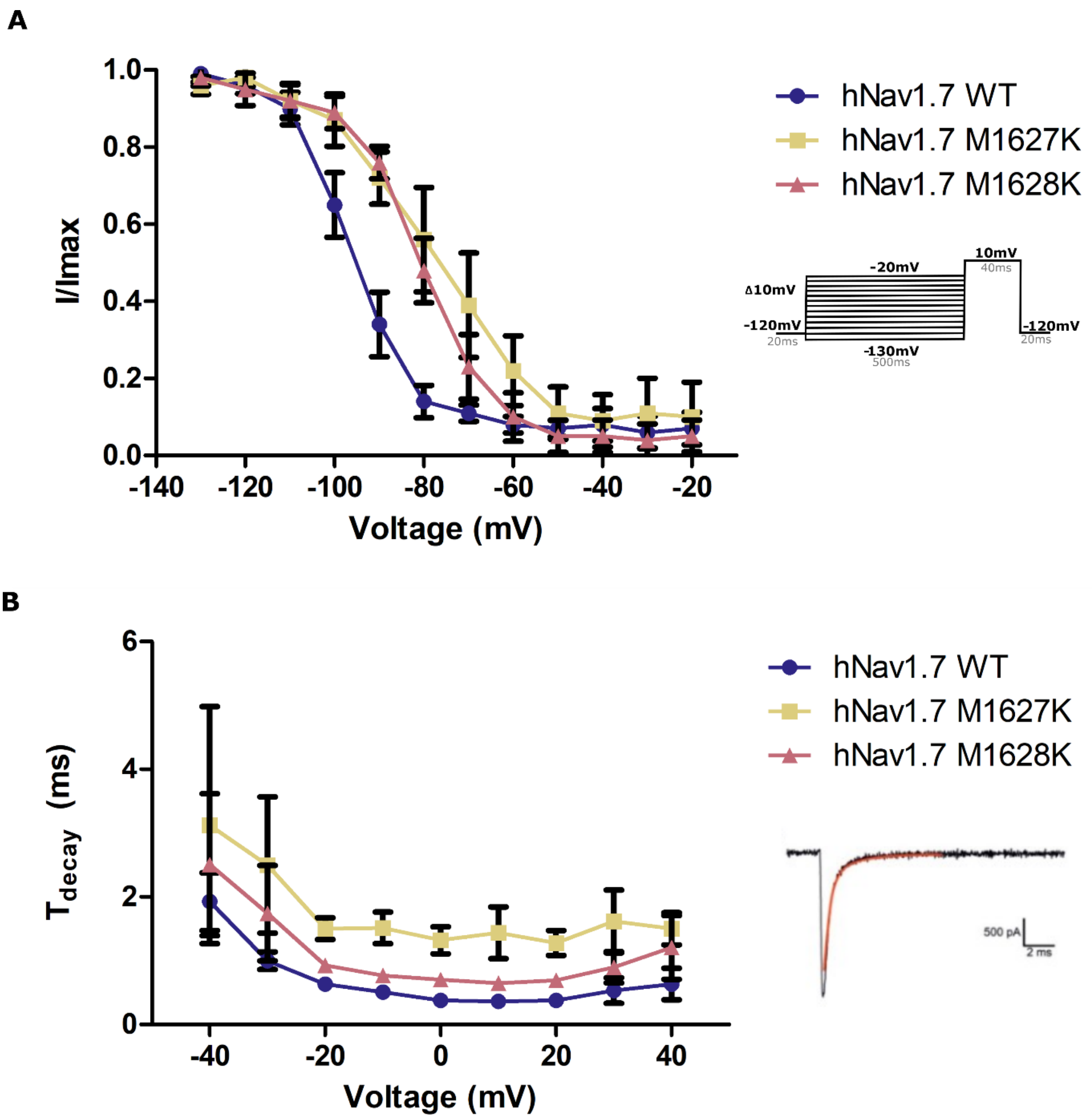

Figure 7 – hNa$_v$1.7 M1627K and M1628K alter fast inactivation properties and cause PEPD Na$_v$1.7 M1627K and M1628K fused to the green fluorescent protein (GFP) at the C-terminus were expressed in HEK293t cells and characterized electrophysiologically using whole-cell patch clamp. **(A)** Normalized current curves for hNa$_v$1.7 WT (**blue circles**), hNa$_v$1.7 M1627K (**yellow squares**) and hNa$_v$1.7 M1628K (**pink triangles**). The voltage-dependence of steady-state fast inactivation is shown in inset. No significant changes were observed for any properties of the voltage-dependence of steady-state fast inactivation. Voltages are shown in **bold** while durations are shown in grey. The protocol is composed of two major phases. In the pre-pulse phase, the voltage is varied from **-130mV** to **-20mV** in steps of 10mV for a duration of 500ms, starting from a holding potential of **-120mV**. This is followed by a test pulse phase, where a depolarizing stimulus to **10mV** for 40ms is used to test for how many channels are still in the fast-inactivated state, before being brought back to **-120mV**. We can clearly observe a depolarizing shift in the voltage dependence of steady-state fast inactivation in both hNa$_v$1.7 M1627K (n=10) and hNa$_v$1.7 M1628K (n=28) compared to hNa$_v$1.7 WT (n=21). **(B)** Onset of fast inactivation kinetics for hNa$_v$1.7 WT (**blue circles**), hNa$_v$1.7 M1627K (**yellow squares**) and hNa$_v$1.7 M1628K (**pink triangles**). The onset of fast inactivation can be obtained by first fitting the decaying phase of the trace to a single exponential function (red line) **(inset)**. The time constant of the fit represents the time for onset of fast inactivation. The inset figure was taken from Figure 6b from (Albani et al., 2024). Both hNa$_v$1.7 M1627K and hNa$_v$1.7 M1628K have a slower onset relative to hNa$_v$1.7 WT, with hNa$_v$1.7 M1627K even slower than hNa$_v$1.7 M1628K. All experiments and analyses were performed by Aylin Kesdoğan (Institute for Neurophysiology, Uniklinik RWTH Aachen, Germany).

focus of this thesis is in mutations of Nav1.7, it is important to keep in mind that $hNa_v1.8$ also plays a substantial role in nociception (Heinle et al., 2024; Kaluza et al., 2018; Kist et al., 2016; Faber et al., 2012).

1.5.1.4 Heterozygous mutation hNav1.7 p.M899I and c.1602+2delT causes CIP

In 2011, a Chinese patient was described as having CIP caused by a point mutation in the SCN9A gene. This resulted in amino acid 899 to be changed from methionine to isoleucine ($hNa_v1.7$ M899I or MI) (Yuan et al., 2011). Here I list some of the major clinical findings of the patient with MI from (Yuan et al., 2011):

1. The patient showed a lack of pain sensation while having normal proprioception, touch and temperature sensation.
2. The patient had bone fractures in his leg at the age of 4. Other complications include infections, repeated wounding and arthrosis.
3. The pain sensation was not completely lost and some mild perception remained.
4. No presence of anosmia or hyposmia.
5. The patient regained some level of pain sensation in adolescence

The study, however, did not delve more into the functional aspects of the mutation, and what the exact mechanism for the reduced pain sensation was. The authors of the study collaborated with the Uniklinik RWTH Aachen (Germany) to allow a thorough examination of the Chinese patient when he was age 19. The patient's parents did not show any symptoms of pain insensitivity. The patient had a normal neurological clinical examination, with normal nerve conduction velocities (Dr. Maike Dohrn, Department for Neurology, Uniklinik RWTH Aachen, Germany). Quantitative sensory testing (QST) is a set of tests to analyse various thresholds for detection of temperature (warm and cold), pain (thermal or mechanical) and vibrations (Rolke et al., 2006). QST in the patient showed no changes in warm or cold detection thresholds, as well as thermal pain thresholds (Prof. Dr. Roman Rolke, Department for Palliative Care, Uniklinik RWTH Aachen, Germany). Intraepidermal nerve fiber densities measured from skin biopsy of the lower leg showed a complete lack of fibers (Prof. Dr. J Weis, Department for Neuropathology, Uniklinik RWTH Aachen, Germany). Next generation sequencing (NGS) revealed that while one of the alleles showed the point mutation MI described in (Yuan et al., 2011), the other allele also showed a splice mutation $hNa_v1.7$ c.1602+2delT that alters the donor splice site of exon 11, likely skipping it (ex11del) (Prof. Dr. Ingo Kurth, Institute for Human Genetics and Genomic Medicine, Uniklinik RWTH Aachen, Germany). The mother carried the ex11del with one wild type (WT) allele, while the father carried MI with one WT allele (Figure 8). The hypothesis at this stage was that the patient had two alleles, one point mutation and one splice variant, both of which do not produce functional proteins and thus cause a loss of pain. It was unclear however, what the structural mechanism of action for the observed LoF of MI was and how the interplay between MI and ex11del causes the observed clinical phenotype of reduced sensitivity to pain and the subsequent regaining thereof.

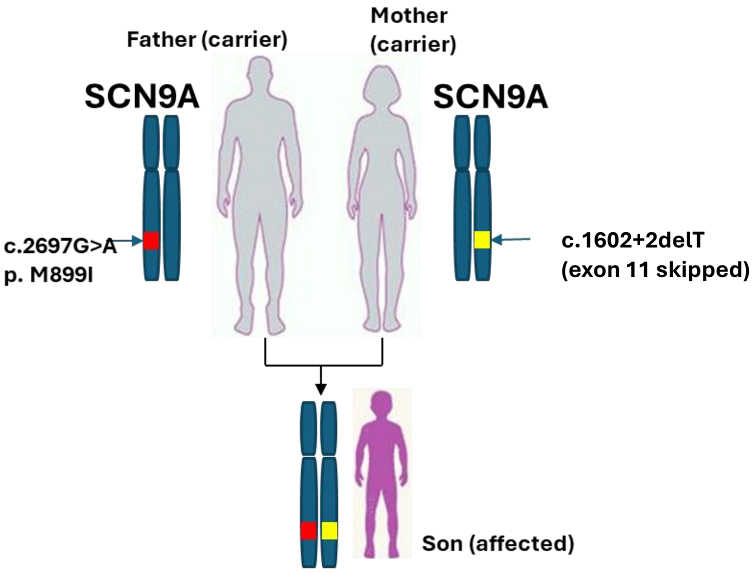

Figure 8 – A patient with congenital insensitivity to pain. The patient has a partial insensitivity to pain, due to inheriting two different mutations in each allele – one each from the mother and father. One causes a point mutation p.M899I, while the other results in a new splice variant c.1602+2delT. The parents are unaffected due to having one functional WT allele.

1.5.2 Other modulating agents of Na_v gating

While mutation of Na_v residues can directly impact the gating of these channels, other factors in the larger interactome can also alter Na_v gating by direct interactions or indirect allosterical modulation.

1.5.2.1 Modulation by membrane composition

Na_vs can be modulated indirectly by altering properties in the membrane. Various studies have shown that altering the elasticity of the membrane by changing cholesterol composition can also alter the gating properties of Na_vs (Amsalem et al., 2018; Lundbæk et al., 2004; Pristerà et al., 2012; Zakany et al., 2020).

Physiologically, lipid composition is unevenly distributed across the cell membrane with cholesterol-dense regions called “lipid rafts” playing a vital role in modulating excitability of neurons. $Na_v1.9$ for instance, is shown to likely partition from lipid rafts rich in cholesterol and sphingolipids to non-raft regions sparse in cholesterol (Amsalem et al., 2018). Such partitioning seems to drive neuronal sensitization during inflammatory pain. However, very little is known about such effects on $Na_v1.7$.

To predict *in silico* what effects on $Na_v1.7$ structure can occur due to differences in membrane composition, Simone Albani (IAS-5/INM-9, Forschungszentrum Jülich, Germany) performed coarse-grained molecular dynamics (CGMD) simulations of $hNa_v1.7$ embedded either in a single component (phosphatidylcholine or POPC) membrane, a complex membrane with cholesterol (raft-like), and a complex membrane without cholesterol (raft-like (-chol)). He found that the presence of cholesterol reduced the area taken up by each lipid molecule, altered the helix properties of VSD3 and VSD4 and changed the geometrical properties of the pore (Figure 9A, C,D and E) (Albani et al., 2024). He also found that cholesterol occupied regions around VSDs involved in activation and fast inactivation (Figure 9B) (Albani et al., 2024).Although the simulation results showcased that cholesterol could impact the regions important for the gating of $hNa_v1.7$, these predictions still needed to be experimentally validated.

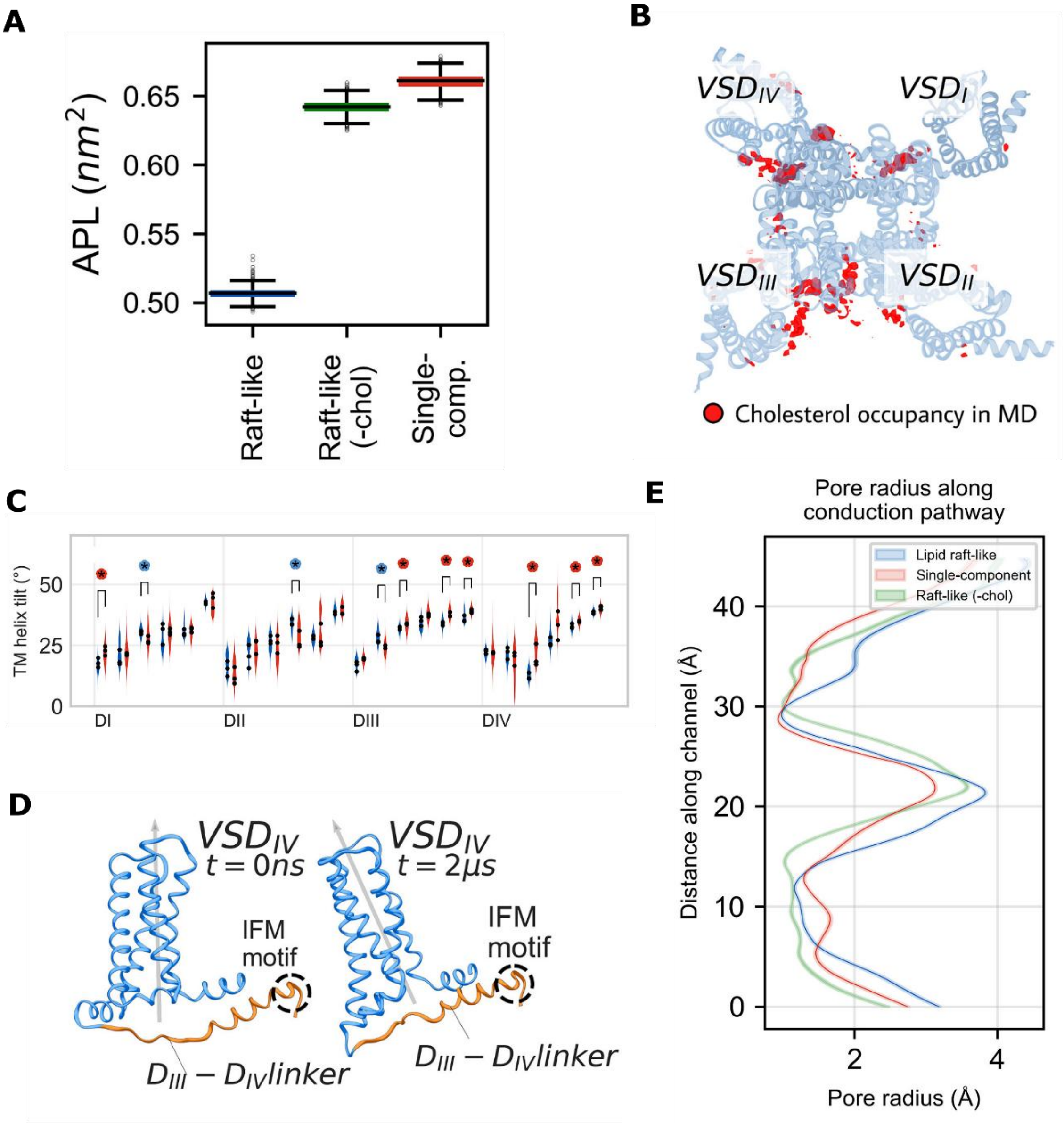

Figure 9 – Cholesterol modifies the structure of hNa$_v$1.7. (A) Area per lipid (APL) of raft-like (blue), raft-like without cholesterol (-chol, green) and single component membrane (red) simulated for 12µs. A lower APL suggests tighter packing of the membrane and vice-versa. The inclusion of cholesterol thus rigidifies the membrane as seen by the lowered APL in the raft-like membrane. **(B)** Cholesterol occupancy (red) around the simulated Na$_v$1.7 structure shown from an extracellular viewpoint. Cholesterol is observed to bind to regions involved in activation (VSD$_{I}$), fast-inactivation (VSD$_{III}$ and VSD$_{IV}$) and druggable regions (side fenestrations). **(C)** The tilt angles for all 24 transmembrane (TM) helices of the simulated Na$_v$1.7 channel in a raft-like (blue) and single component (red) membrane. **Black** dots represent the average. There are various TM helices both in the VSDs and PMs that alter their bending based on the presence or absence of cholesterol. * $p<0.05$. **(D)** Structural view of the VSD$_{IV}$ tilts in a single-component membrane. Absence of cholesterol allows for larger movements and tilts of the VSD$_{IV}$, a region heavily involved in fast inactivation of the channel. **(E)** Average pore radius of the simulated Na$_v$1.7 channel in a raft-like (blue), raft-like without cholesterol (-chol, green) or single component membrane (red). The fill around the average represents the bootstrapped 95% confidence interval of the mean. Presence of cholesterol alters the radius along the ion conduction pathway, likely leading to alterations in ion conductivity. Figure 9 is a combination of (in order from A-F) Fig. 2a, Fig. 2f, Fig. 3e, Fig. 3f and Fig. 4b published in (Albani et al., 2024). All simulations were performed by Simone Albani and other collaborators from IAS-5/INM-9, Forschungszentrum Jülich, Germany.

1.5.2.2 Modulation by small molecules

External compounds such as neurotoxins or anaesthetic drugs can alter the functionality of Na$_v$s. Neurotoxins are harmful, as they have been evolved to allow organisms to defend and capture prey by blocking the functionality of Na$_v$s. In fact, the neurotoxin tetrodotoxin (TTX) from the puffer fish was used to categorize the nine subtypes as TTX-sensitive (TTX-S; Na$_v$1.1-1.4, Na$_v$1.6-1.7) and TTX-resistant (TTX-R; Na$_v$1.5, Na$_v$1.8 and Na$_v$1.9). This however does not predispose neurotoxins to have no clinical purpose. Toxins that are known to block Na$_v$s have been suggested for potential clinical use in controlling pain in patients suffering from various neuropathies (Cardoso and Lewis, 2018). In this section however, we will focus only on drugs and their effects on Na$_v$s.

Drugs can help us control Na$_v$ functionality to help patients suffering from clinical pathologies. Some examples include the usage of local anaesthetics (LAs) that target Na$_v$1.7-Na$_v$1.9 for treating pain hypersensitivities, anti-epileptics that target Na$_v$1.1 or Na$_v$1.2 to prevent epileptic attacks, and anti-arrhythmics that target Na$_v$1.5 for treating cardiac disorders. Recent literature also show that cannabinoids can help with muscular pain by targeting Na$_v$1.4 and Na$_v$1.7 (Ghovanloo et al., 2021; Huang et al., 2021, 2023). Most of these compounds bind to similar regions in the channel, a site termed the local anaesthetic site. Access to this site can happen either directly through the intracellular pathway in a hydrophilic manner or via side fenestrations in a lipophilic manner (Körner et al., 2022). The binding of these drugs to a highly conserved region predisposes them to have side-effects when used. In other words, the same drug could bind to different sodium channel subtypes, thus having effects on various other parts of the body that did not intend to be targeted.

One such interesting drug is phentolamine, an α-adrenoreceptor blocker approved by the FDA to quickly reverse the effects of LAs post-surgery in dentistry by dilating the blood vessels for higher systemic absorption and redistribution of the LA away from the injected site (Prados-Frutos et al., 2015). However, studies have reported adverse cardiac effects when phentolamine was used (Laviola et al., 2008; Yasukawa et al., 2007). This hints at a possible effect on Na$_v$1.5. To better understand these effects of phentolamine, Idil Toklucu (Institute for Neurophysiology, Uniklinik RWTH Aachen, Germany) performed automated high-throughput voltage-clamp experiments on HEK293 cells stably expressing Na$_v$1.5 using the Synchropatch 384i (Nanion Technologies, Munich, Germany). The cells were either untreated (negative control), treated with 75μM phentolamine mesylate (Merck, Germany) or with 100μM mexiletine hydrochloride (Tokyo Chemical Industry, Japan) (Toklucu et al., 2025) . Mexiletine was used as a positive control as it is a known anti-arrhythmic that blocks Na$_v$1.5 (Wang et al., 2015). She showed that phentolamine blocks Na$_v$1.5 in both a tonic (i.e. the binding of the drug is independent on the state of the channel) and use-dependent manner (i.e. the binding of the drug is increased as more channels are pushed into a specific state), as is expected by traditional anti-arrhythmics like mexiletine (Figure 10A-D)(Toklucu et al., 2025). To see if the LA site is involved in this observed effect of phentolamine, the experiments were repeated with mutations in one of two major LA site residues – F1670A or N17565K. Both mutations completely abolished tonic and use-dependent block of the channel by phentolamine and mexiletine, suggesting that phentolamine likely binds to the LA site (Toklucu et al., 2025). However, a structural description of this binding mechanism was needed to elucidate on the possible mechanism of action.

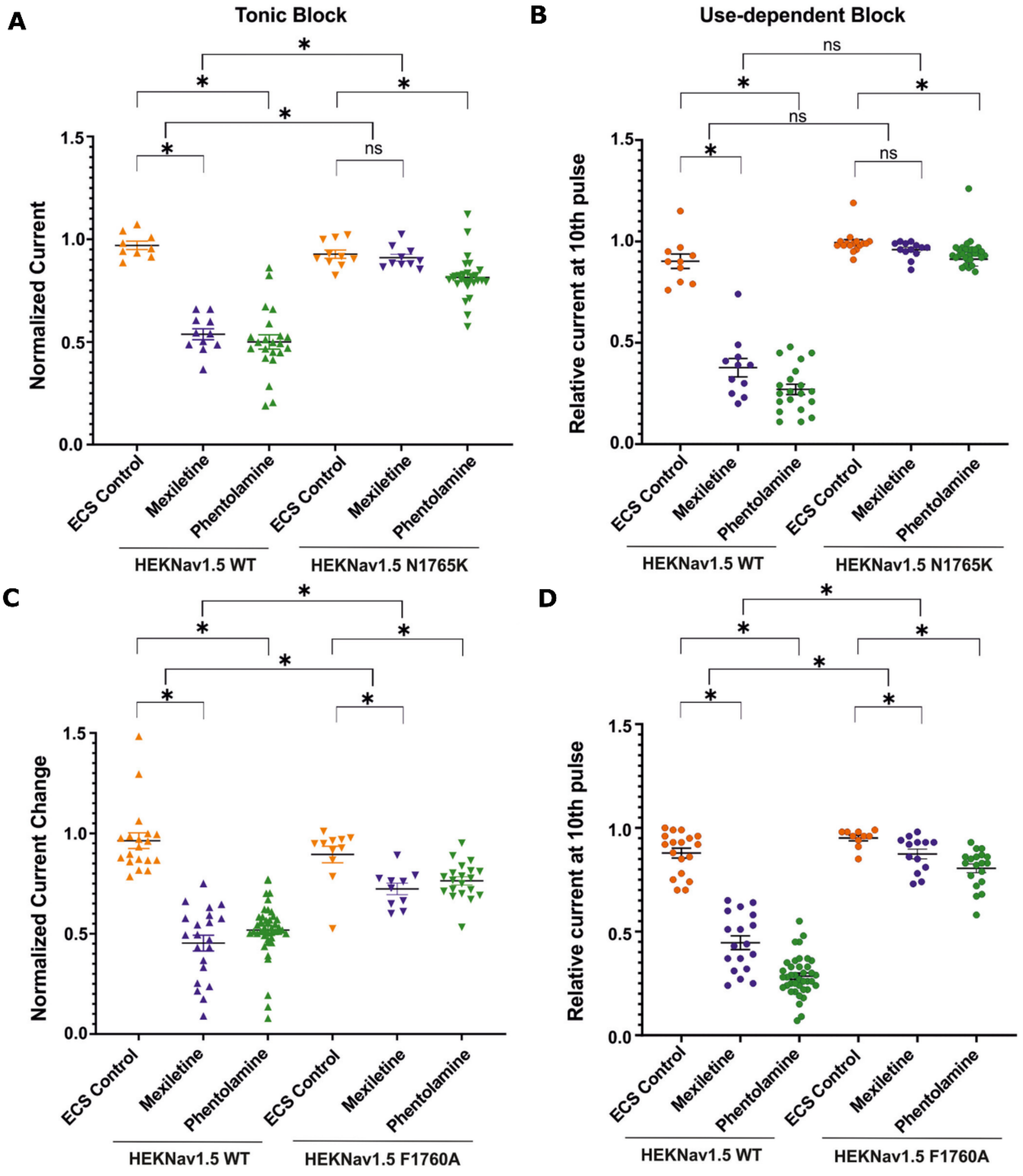

Figure 10 – Phentolamine, like mexiletine, blocks hNa$_v$1.5 at the local anaesthetic (LA) site both tonically and in a use-dependent manner. (A) Normalized current change for HEK293 cells stably expressing hNa$_v$1.5 WT or the local LA site residue mutation hNa$_v$1.5 N1765K treated with control, 100μM mexiletine or 75μM phentolamine in response to stimuli causing tonic block. (B) Relative current at the 10th pulse for HEK293 cells stably expressing hNa$_v$1.5 WT or the local LA site residue mutation hNa$_v$1.5 N1765K treated with control, 100μM mexiletine or 75μM phentolamine in response to stimuli causing use-dependent block. (C) Normalized current change for HEK293 cells stably expressing hNa$_v$1.5 WT or the local LA site residue mutation hNa$_v$1.5 F1760A treated with control, 100μM mexiletine or 75μM phentolamine in response to stimuli causing tonic block. (D) Relative current at the 10th pulse for HEK293 cells stably expressing hNa$_v$1.5 WT or the local LA site residue mutation hNa$_v$1.5 F1760A treated with control, 100μM mexiletine or 75μM phentolamine in response to stimuli causing use-dependent block. While phentolamine and mexiletine cause tonic and use-dependent block of hNa$_v$1.5 as shown by the reduction in the normalized current change and relative current values respectively, mutation of either of the two LA site residues abolished such block. This shows us that both phentolamine and mexiletine can block Na$_v$1.5 most likely via the LA site. Tonic block was measured by 30ms pulses to -10mV from the holding potential at 0.1Hz pre- and post-drug application. Normalized current changes were measured by normalizing the mean peak currents 180-270s after compound application to the mean peak currents of the last 15 sweeps before compound application. Use-dependent block was measured using ten 5ms high frequency pulses at 10Hz from the holding potential to 0mV. The current value at the 10th pulse was normalized to the current value at the 1st pulse (before compound application). * $p<0.05$. Image taken from Fig. 4 published in (Toklucu et al., 2025).

1.5.2.3 Modulation by secondary proteins and post-translational modifications

Na_vs are known to interact with various secondary proteins like the beta subunits (ß1-ß4), calmodulin and ankyrin (Balse and Eichel, 2018; Bouza and Isom, 2018; Chew et al., 2019). These interactions can influence both gating as well as expression of Na_vs. For example, ß1 has been shown to increase the expression of Na_v1.7 while also altering some of its gating properties (Bouza and Isom, 2018). Interaction of calmodulin with calcium ions can cause calcium-dependent inactivation of some sodium channel subtypes (Gabelli et al., 2016). The microtubule-associated protein 2 (MAP2) has been implicated in regulation of ion channel trafficking to the membrane (Chew et al., 2019). Nedd4-2, the E3 ubiquitin ligase, can control neuronal excitability and pain signaling by affecting the internalization of Na_v1.7 (Chew et al., 2019).

Post-translational modifications such as glycosylation, ubiquitination and phosphorylation can also alter gating properties of Na_vs (Pei et al., 2018). Phosphorylation is well studied in sodium channels, especially in Na_v1.5, with various serine/threonine (PKA and PKC) and tyrosine kinases (Fyn) modulating these channels via phosphorylation of residues in intracellular regions (Iqbal et al., 2018; Lorenzini et al., 2021). N-linked glycosylation have been shown to control the trafficking of Na_vs (Laedermann et al., 2013; Mercier et al., 2015). Ubiquitination is another common PTM whereby a ubiquitin molecule can attach itself to Na_vs via a motif intracellularly, most times inducing degradation of the protein (Pei et al., 2018). Other PTMs include SUMOylation (addition of small ubiquitin-like modifier protein to lysine residues), palmitoylation (addition of a palmitic acid chain to intracellular cysteine residues), methylation (via arginine residues) and S-nitrosylation (modification of channels by nitric oxide via cysteine residues flanked by charged residues) (Pei et al., 2018). In this thesis however, we will not discuss PTMs and modulation by secondary proteins.

1.6 How and why do we study Na_vs?

In the previous section, we already get a glimpse into the various methodologies researchers use to understand the functioning of these proteins. The methods range from *in silico* techniques such as molecular dynamics and structural visualization to *in vitro* methods such as whole-cell patch clamp that includes addition of various drugs and reagents that can control the gating of Na_vs. In **Chapter 2**, we will describe in detail the methods used in our thesis to better understand structure-function relationships of Na_vs.

Another aspect that becomes quite clear from the previous section is the need for combining structural, functional and clinical datasets to get a better picture of how these proteins function. For example, while we know the clinical and genetic picture of the patient with loss-of-pain harbouring Na_v1.7 mutations, we do not know what the structural mechanism for such a phenotype is and how it translates to the functioning of Na_v1.7. Similarly, the structural mechanism by which the GoF phenotype occurs in the patient with PEPD is not known. It thus becomes imperative to try and understand how these proteins work at an atomic level and the mechanism by which these mutations disrupt the gating processes. This must also be linked at a functional level to how atomistic changes in the protein conformation correspond to disruptions in the ionic conduction, which ultimately lead to diseased clinical phenotypes. Such multi-scale approaches can give us a larger picture also on other phenomena that control Nav gating. While we see cholesterol can impact the structural conformations of Na_vs, performing functional readouts can validate the predictions made. In a similar fashion, knowing the exact binding mechanism of phentolamine to the structure of Na_v1.5 can help us visualize the functional readouts to better understand the mechanism of action. The structure-function relationship of

Na_vs and its modulation in a multi-scale manner is deciphered in detail in the subsequent chapters.

The journey starts by first using the LoF patient harboring mutations in SCN9A (section 1.5.1.4) that alters the PM conformation of $Na_v1.7$, blocking ion conduction and reducing his sensitivity to pain **(Chapter 3.1)**. The other end of the coin is tackled by understanding how fast inactivation is altered by GoF mutations close to the IFM motif, describing the structural mechanism of action by which the GoF mutation $Na_v1.7$ M1628K (section 1.5.1.2) disrupts the voltage-dependence of steady-state fast inactivation and thereby causing PEPD **(Chapter 3.2)**. This is followed by moving to external regulators of Na_vs, with the most important being the bilayer membrane composition. The cholesterol content of the bilayer is shown to be an important factor in how $Na_v1.7$ gates *in vitro*, validating the predictions made *in silico* (section 1.5.2.1) **(Chapter 3.3)**. Another important external regulator of Na_v gating are drugs. While results point to the involvement of the LA site in the *in vitro* effects observed when $Na_v1.5$ is exposed to phentolamine, the structural picture of how this drug binds to the LA site is expanded upon and its possible mechanism of action to block $Na_v1.5$ is explored **(Chapter 3.4)**. The thesis ends by summarizing the various key takeaways from the different chapters, describing the importance to piece together how structure effects function in Na_vs, the importance of knowledge transfer between different subtypes, efficient strategies to uncover structure-function relationships, and the importance of visualization tools in understanding the implications of mutations in Na_vs **(Epilogue)**.

Chapter 2: Materials and Methods

Understanding Na$_v$s in a multi-scale perspective requires the use of various methodologies that are quite different from each other. This chapter describes all the methods used in this thesis to achieve its aims and objectives.

Before application of various experimental techniques, it is first crucial to be able to obtain a system where the protein of interest (in our case Na$_v$s) is expressed. **Section 2.1** discusses how one can achieve such systems by culturing of secondary cell lines and transfecting them with the plasmids of Na$_v$s. Once expressed, the functioning and gating of the channels can be described by measuring the electrical properties of the cell expressing these channels. **Section 2.2** describes the method of whole-cell patch clamp that allows effective characterization of the gating processes of Na$_v$s as electrical readouts. **Section 2.3** sheds light on how the cholesterol content of cells was altered, after which they were recorded for changes in their gating properties. Other than gating changes, imaging of the cells can be performed to understand the expression patterns of Na$_v$s in the transfected cells. **Section 2.4** deals with the technique of immunocytochemistry, where addition of various fluorophore-conjugated antibodies that target tags or Na$_v$s themselves can help visualize localization of these channels in the cell. **Sections 2.5-2-7** talk about various *in silico* methodologies that can better describe the structural determinants of various gating changes observed by mutations or addition of drugs. These include how to observe differences in the protein sequence and model the 3D structure of Na$_v$s with and without mutations (mutliple sequence alignment and homology modelling), dock various drugs in known binding sites of the channel (rigid body docking) and how to apply specialized force fields that can help understand more dynamic changes associated with mutant channels (coarse-grained molecular dynamics).

2.1 Cell culture and transfection

In this study, HEK293t cells were used for expression of all Na_v variants. The cells were grown in an incubator at 37°C with 5% CO_2 and passaged with accutase (Sigma-Aldrich, St.Louis, MO, USA). Cells were split either once or twice weekly depending on their confluence. The cells were kept in Dulbecco's Modified Eagle Medium F-12 (DMEM F-12; Thermo Fisher Scientific, Waltham, MA, USA) and 10% fetal bovine or calf serum (FBS/FCS).

All plasmids for transient transfection were generated by Petra Hautvast (Institute for Neurophysiology, Uniklinik RWTH Aachen, Germany). The $hNa_v1.7$ WT, M899I/A/V/C/F/L (WT, MI, MA, MV, MC, MF and ML respectively), F344A (FA_{D1}), F1378A (FA_{D3}), F1670A (FA_{D4}) and $hNa_v1.7$ c.1602+2delT (ex11del) were contained in a pCMV6neo vector (Origene, Rockville, MD, USA). The fusion proteins of green fluorescence protein (GFP) with the WT and mutants (WT_{GFP} and MI_{GFP}) were contained in a PCMV6-AC vector (Origene, Rockville, MD, USA). The $hNa_v1.2$ WT and M925T ($WT_{1.2}$ and $MT_{1.2}$) were contained in a pCMV6-XL5 vector (Addgene, plasmid #162279) while the $hNa_v1.5$ WT and M881I ($WT_{1.5}$ and $MI_{1.5}$) were contained in a pTracer™-SV40 vector (Thermo Fischer Scientific, Waltham, MA, USA). These plasmids were used for transient transfections, all of which were achieved using jetPEI® (Polyplus-transfection S.A., Illkirch, France). Fusion protein plasmids were transfected by using 1.5µg of the plasmid of interest. For expression of non-fusion protein plasmids, 1.25µg of the plasmid of interest was transfected along with 0.25µg of GFP. GFP was used as a marker to know which cells express the plasmid. The plasmids and jetPEI® were buffered in 150mM NaCl. Transient transfection was performed in HEK293t cells with atleast 70% confluency and incubated overnight after transfection in 37°C and 5% CO_2. For studying temperature effects on membrane trafficking, cells transfected with MI were incubated in 30°C and 5% CO_2 after transfection. For co-expression studies involving ex11del and MI, four different ratios were used. Ex11del:MI ratios were altered in the following manner: 1:0, 4:1, 1:1, 1:4 and 0:1. In all the ratios, the total plasmid quantity was kept constant at 1.5µg with 0.25µg always reserved for GFP. A summary of the transient transfection protocol is shown in Figure 11A.

Stable HEK293t Flp-in™ cell lines expressing various Tet-on (TO) sequence plasmids were generated by Prof. Dr. Ralf Hausmann, Amdiya Botchoi and Silvia Destro-Dassen (Institute for Clinical Pharmacology, Uniklinik RWTH Aachen, Germany). Stable cell line generation was achieved by using a HEK293 Flp-in™ cell line (Thermo Fischer Scientific, Waltham, MA, USA), which contains a modification at a transcriptionally active site. This allows for any Flp-in™ vectors to achieve very high expression stably. This was combined with a TO sequence, that allows for rapid expression of the plasmid only when induced by addition of doxycycline. To achieve this, the untagged $hNa_v1.7$ WT ($WT_{non\text{-}tagged,TO}$), untagged MI ($MI_{non\text{-}tagged,TO}$) and the three extracellular HA-tag locations ($WT_{HAext1,TO}$, $WT_{HAext2,TO}$, $WT_{HAext3,TO}$, $MI_{HAext1,TO}$, $MI_{HAext2,TO}$, $MI_{HAext3,TO}$) were contained in a pCDNA™5/FRT/TO vector (Thermo Fischer Scientific, Waltham, MA, USA) where the FRT provides compatibility with Flp-in (TM) and TO provides compatibility with Tet-on. The three extracellular locations for the HA tag insertion are as follows – between P148 and P149 in D1 S1-S2 (HAext1), between L280 and E281 in D1 S5-S6 (HAext2) and between L293 and E294 in D1 S5-S6 (HAext3). A C-terminal HA tag with the same vector was also generated in WT and MI ($WT_{HACterm,TO}$ and $MI_{HACterm,TO}$) as a control with the tag located intracellularly. Cells were incubated at 37°C and 5% CO_2. Maintenance of the cells was done with a modified DMEM-F12 medium containing 15µg/ml Blasticidin and 100µg/ml Hygromycin. Before running any experiments, the cells were induced for protein expression by addition of 1mg/ml of doxycycline and incubated for at least 18-24h. A summary of the stable transfection protocol is shown in Figure 11B.

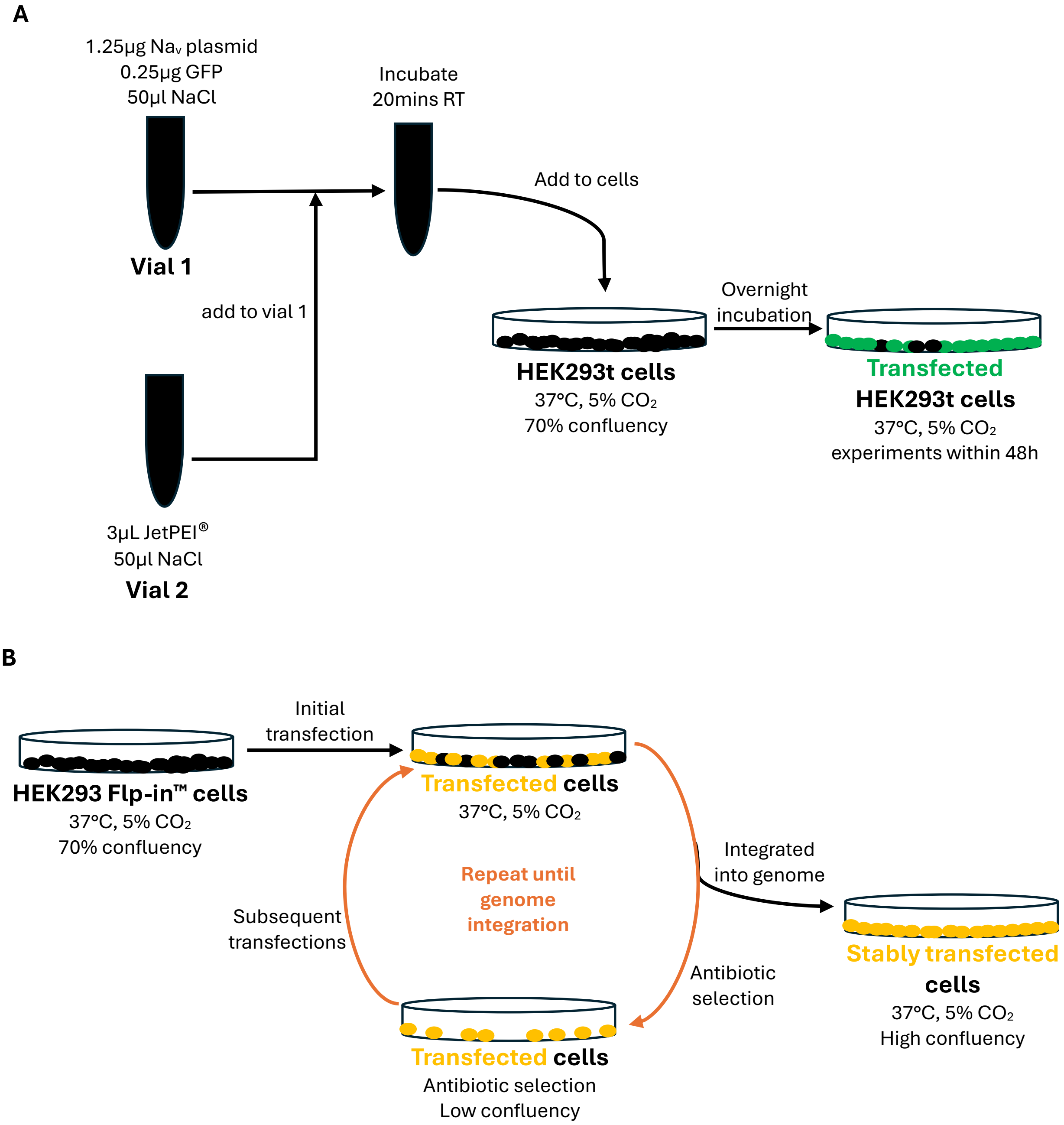

Figure 11 – Transient and stable transfection (A) Transient transfection of HEK293t cells was achieved using JetPEI®. Briefly, the plasmid mix (vial 1) and the JetPEI® working mix (vial 2) were aliquoted into separate Eppendorf tubes. The plasmid mix contains a total of 1.5µg of DNA, with 1.25µg of the Na_v plasmid and 0.25µg of the green fluorescent protein (GFP). The JetPEI® mix contains 3µL of JetPEI®. Both vials are diluted in 50µL of 150mM NaCl solution. The contents of the JetPEI® mix are added to the plasmid mix, and not the other way around. Once added, the resulting mixture is incubated for 20 minutes at room temperature (RT) to allow for formation of complexes. After 20 minutes, this is added into the dish containing HEK293t cells with at least 70% confluency and incubated overnight. Transfection is achieved when the cells show a green signal, due to expression of GFP and thus an indirect indication of Na_v plasmid expression. These cells are then taken for further experiments and used at the most 48h after the overnight incubation. **(B)** Stable transfection of HEK293t cells involves a repetitive cycle of transient transfection and antibiotic selection. First, the HEK293 Flp-in™ cell line is transfected as shown in the transient transfection protocol (without GFP) in Figure 11A. Post transfection, cells expressing the plasmid of interest are selected for by addition of neomycin or G418. As only the pCDNA™5/FRT/TO contains an antibiotic resistance sequence, the cells expressing this plasmid survive while the other cells die. This cycle is repeated until only the resistant cells remain in high confluency, showing that the cells have now integrated the plasmid into their genome and no longer require transient transfection.

2.2 Whole-cell patch clamp electrophysiology

Whole-cell voltage clamp experiments were performed in HEK293t/HEK293 Flp-in™ cells at room temperature using an EPC-10 USB amplifier and PatchMaster Next v1.2 software (HEKA Elektronik, Lambrecht, Germany). Borosilicate glass pipettes (Bio-medical Instruments, Zöllnitz, Germany) were pulled using a DMZ puller (Zeitz Instruments, Martinsried, Germany) to a resistance (R_{pip}) of 1 to 3MΩ. The series compensation was always set to atleast 70%. The V_{error} of analysed cells were always < 6mV. The composition of the intracellular solution (ICS) and extracellular solution (ECS), including the pH and osmolarities, are described in Table 2 and 3 respectively. Leak currents were subtracted online using a P/4 procedure after each test pulse. Signals were sampled with 100kHz and filtered at 10kHz.

Table 2: Composition of intracellular solution (ICS). ~310Osm, pH adjusted to 7.33 using CsOH

Components	Concentration (in mM)
NaCl	10
CsF	140
EGTA	1
HEPES	10
Sucrose	18

Table 3: Composition of physiological extracellular solution (ECS). ~298Osm, pH adjusted to 7.4 using NaOH or CsOH. * represents the additions or changes exclusive for a reduced sodium concentration.*

Components	Concentration (in mM)
NaCl	140 (40*)
Choline-Cl*	100*
KCl	3
$MgCl_2$	1
$CaCl_2$	1
HEPES	10
Glucose	20 (5*)
Sucrose*	10*

Before the start of the traditional pulses to measure activation and fast inactivation properties, a "monitor" pulse protocol was used to stabilize the currents recorded from the cells. To do so, a 100ms pulse to -10mV or 0mV from -120mV was used for 3 mins with an inter-pulse interval of 5s (Figure 12). This ensures that the cell reaches steady-state and that almost all channels are now ready to open with depolarizations.

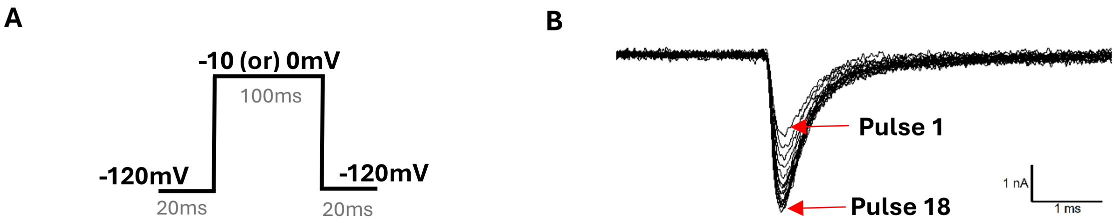

Figure 12 – The monitor protocol (A) The pulse shape of a monitor protocol. The voltages of each component are shown in **black** while the durations are shown in **grey**. A monitor protocol contains a short depolarizing stimuli (in my study to **-10mV**) for **100ms** from a holding potential of **-120mV**. This is then brought back to **-120mV** before repeating the stimuli after **5s** for a total of **3 minutes. (B)** The monitor protocol stabilizes the sodium currents in the cell, ensuring most of the channels in the cell respond to depolarizing stimuli. This is seen in recordings as a gradual increase in peak currents from pulse 1 to pulse 18 (red arrows).

Voltage-dependence of activation

Voltage-dependence of activation was recorded by firstly holding the cells at a hyperpolarized potential of -120mV. This is followed by a 40ms long pulse to various voltages between -90mV and +40mV in 10mV steps (Figure 13). The pulse then drops again to -120mV before repeating the sweep again. The inter-sweep interval was 5s. The conductance (G) of the specific sweep was calculated using equation 1:

$$G = \frac{I_{peak}}{(V - V_{rev,Na^+})} \qquad \textbf{\textit{Equation 1}}$$

Where V represents the applied voltage, $V_{rev,Na+}$ represents the reversal potential for sodium ions and I_{peak} denotes the peak current recorded for voltage V. The $V_{rev,Na+}$ was calculated by performing a linear regression on I_{max} values for the last 3-4 sweeps and calculating the intercept (i.e. the value at which $I_{max} = 0$). Theoretical $V_{rev,Na+}$ can be calculated using the Nerst equation, which results in a value of 67mV for 140mM Na^+ outside and 10mM Na^+ inside at 37°C. Once G is calculated for all sweeps, the G_{max} can be calculated and used to normalize G. This is then plotted against V. The G vs V curve can be fit with a Boltzmann function using equation 2:

$$\frac{G}{G_{max}} = \frac{G_{max} + (G_{max} - G_{min})}{(1 + e^{\frac{V_{1/2,act} - V}{k_{act}}})} \qquad \textbf{\textit{Equation 2}}$$

Where G_{min} and G_{max} represent the minimum and maximum conductance, V is the applied voltage, $V_{1/2,act}$ is the voltage at half-maximal channel activation (i.e. half the channel population is in an activated state at this voltage) and k_{act} is the slope factor that measures the steepness of the curve and is a measure of voltage sensitivity of the channel population.

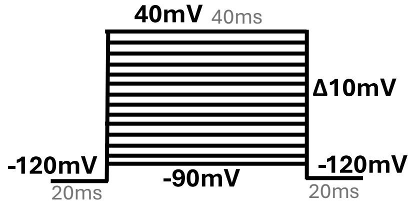

Figure 13 – The activation protocol Voltages are shown in **black** while durations are shown in **grey**. The protocol is composed of a series of depolarizing pulses starting and ending at a holding potential of **-120mV**. The depolarizing pulses last **40ms** and start from **-90mV** to **+40mV** in **10mV** steps. The inter-sweep interval is set to **5 seconds**.

Current densities

The current densities (CD) of the cell can be measured by equation 3:

$$CD = \frac{I_{peak}}{C_{slow}} \qquad \textbf{\textit{Equation 3}}$$

where CD is the current density (pA/pF) at voltage V, I_{peak} is the peak currents recorded at voltage V and C_{slow} is the membrane capacitance that is an indirect representation of the size of the cell. The maximal current density CD_{max} for each cell is calculated by choosing the CD with the highest absolute value.

For the co-expression studies with MI and ex11del in different ratios, the relationship between CD and MI concentration was achieved by first normalizing the average CD for each concentration to the average CD when only ex11del is expressed (1:0). The theoretical curves that represent the relationship between normalized current densities (CD) and the relative concentration of a non-functional channel (y) can be described by equation 4:

$$CD = (1 - y)^n$$ ***Equation 4***

where y represents the oligomeric setup of the channels. For instance, y = 2 would mean that the non-functional channel and functional channel form dimers. Error bars for each concentration represent the standard error of the mean for that concentration.

Time to peak and onset of fast inactivation

Time to peak is measured for each voltage step V as the time it takes from the start of the depolarizing pulse in the activation protocol to reach I_{peak} (Figure 14A). The onset of fast inactivation was measured by performing a single exponential fit on the decaying phase of the IV trace (Figure 14B), using equation 5:

$$I(t) = I_0 + A * e^{\left(\frac{t - t_0}{\tau}\right)}$$ ***Equation 5***

where I(t) is the current amplitude as function of time t, I_0 represents the current at t = 0, A is the amplitude coefficient for the decay time constant τ. τ was plotted against the applied voltage V.

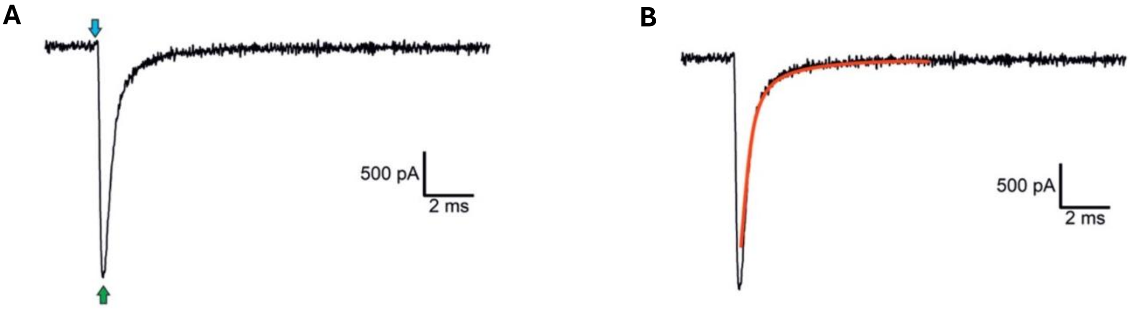

Figure 14 – Kinetic properties from activation protocol The activation protocol can be used to analyse much more than just the current densities and voltage-dependence of activation. **(A)** The time to peak is measured as the time it takes to reach peak currents (green arrow) from the start of the depolarizing pulse (blue arrow). **(B)** The onset of fast inactivation can be obtained by first fitting the decaying phase of the trace to a single exponential function (red line). The time constant of the fit represents the time for onset of fast inactivation. Figures taken from Figure 6a and 6b from (Albani et al., 2024).

Voltage-dependence of steady-state fast inactivation

Voltage-dependence of steady-state fast inactivation was measured by means of a two-pulse protocol. Cells were first held at -120mV, before applying a 500ms pre-pulse of varying voltages from -140mV to -10mV in 10mV increments (Figure 15). The long pulse ensures that channels enter the fast inactivated state, while at the same time avoiding the slow inactivated state (Meents and Lampert, 2016). Subsequently a 40ms depolarizing pulse to -10mV was applied to measure channel availability. A 10s inter-sweep interval was used to make sure that channels recovered from fast inactivation completely. The currents I recorded in the test pulse for each voltage V set in the pre-pulse were normalized to maximal current I_{max} and plotted against V. The normalized currents can be fit using a Boltzmann equation as given in equation 6:

$$\frac{I}{I_{max}} = \frac{I_{min} + (I_{max} - I_{min})}{(1 + e^{\frac{V_{1/2,ssfi} - V}{k_{ssfi}}})}$$ ***Equation 6***

where I_{min} represents the minimum currents at the test pulse, $V_{1/2,ssfi}$ represents the voltage at half-maximal channel inactivation (i.e. half the channel population is in a fast inactivated state at this voltage) and k_{ssfi} is the slope factor that measures the steepness of the curve and indirectly the voltage sensitivity of the channel population.

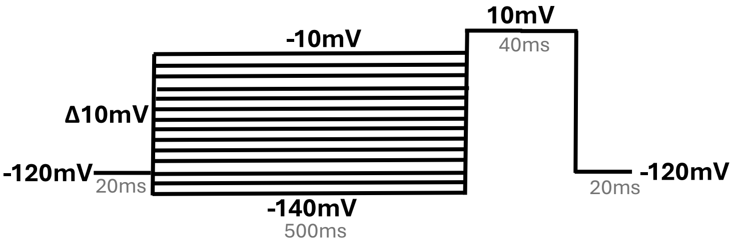

Figure 15 – The steady-state fast inactivation protocol Voltages are shown in **black** while durations are shown in **grey**. The protocol is composed of two major phases. In the pre-pulse phase, the voltage is varied from **-140mV** to **-10mV** in steps of 10mV for a duration of **500ms**, starting from a holding potential of **-120mV**. This is followed by a test pulse phase, where a depolarizing stimulus to **10mV** for **40ms** is used to test for how many channels are still in the fast-inactivated state, before being brought back to **-120mV**.

Recovery from fast inactivation

Recovery from fast inactivation was measured using a two-pulse protocol. Cells were first depolarized using a pre-pulse (I_{pre}) to +10 mV for 500 ms from -120mV to push the channels to enter fast inactivation. This was followed up by an inter-pulse to −120 mV with increasing durations in each sweep by a factor of two - from 0.1 ms to 1600 ms to allow recovery from fast inactivation. This inter-pulse was followed up with another depolarizing test pulse (I_{test}) to +10 mV for 40 ms to obtain the fraction of channels that could recover from fast inactivation (Figure 16). The current amplitudes at I_{test} were normalized to the current amplitude at I_{pre} and plotted against the inter-pulse durations to obtain the time course of recovery from fast inactivation.

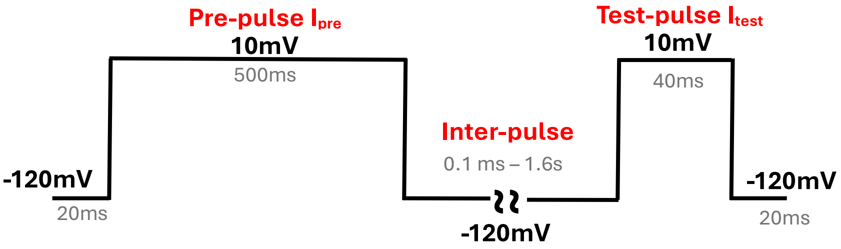

Figure 16 – The recovery from fast inactivation protocol Voltages are shown in **black** while durations are shown in **grey**. The names of the segments are shown in red. The protocol is composed of three major phases. In the **pre-pulse phase (I_{pre})**, the voltage is stepped to **+10mV** for a duration of **500ms** starting from a holding potential of **-120mV**. This is followed by an **inter-pulse** where the voltage is held at **-120mV** for times varying from **0.1ms** upto **1.6s** to allow for recovery from the fast inactivation phase. In the **test pulse phase (I_{test})**, another depolarizing stimulus to **10mV** for **40ms** is used to test for how many channels are still in the fast-inactivated state, before being brought back to **-120mV**.

Statistics

The raw data recorded was extracted for analysis with FitMaster software (HEKA Electronics, Lambrecht, Germany) and the traces were exported into Igor Pro (WaveMetrics, Portland, OR, USA) for extraction of the different parameters using in-house scripts generated by Dr. Stefanie Bothe (previous member of Institute for Neurophysiology, Uniklinik RWTH Aachen, Germany). The calculation of the Boltzmann fits, $V_{1/2,act}$, $V_{1/2,ssfi}$, slopes, graphs and statistical significance testing were done using GraphPad Prism 5 (GraphPad software Inc., La Jolla, CA, USA). The significance level was 95%, with various tests being run based on the number of independent groups and the normality of the distribution. Normality was checked for using the Shapiro-Wilk normality test. A student t-test was used for comparison of two groups when the samples were normal, one-way ANOVA with post-hoc Bonferroni corrections was used for comparison of multiple groups and normally distributed samples, Mann-whitney test was used for comparison of two groups when the samples were non-normal and the Kruskal-Wallis test with Dunn's post-hoc corrections was used for comparison of multiple groups when the samples were non-normal. All values and error bars are represented as mean±95% confidence interval of the mean, unless stated otherwise. * signifies statistical significance ($p < 0.05$).

2.3 Manipulation of cellular cholesterol content

To induce cholesterol depletion of HEK293t cells transfected with WT, a 5 mM working solution of the cholesterol chelating agent methyl-ß-cyclodextrin (MßCD) was added to the cells and incubated for 1 h at 37 °C and 5 % CO2 before being used for whole-cell patch clamp experiments. Briefly, 258.2 g of powdered MßCD (Sigma-Aldrich, C4555) was dissolved in 1 mL of distilled water and vortexed for 1–2 min to produce a 200 mM clear MßCD stock solution. A 5 mM MßCD working solution was made by diluting the stock solution with DMEM/F12 medium in a 1:40 ratio.

2.4 Immunocytochemistry

Immunostaining of MI and WT was performed by Li Yiu (Institute for Neurophysiology, Uniklinik RWTH Aachen, Germany). Briefly, HEK293t cells were transfected with either MI or WT with GFP as a marker protein. Cells were seeded into coverslips and incubated overnight for transfection. Once transfection is achieved, cover slips were fixed by incubation with 4% PFA at room temperature. Cells were then permeabilized by addition of 0.1% Triton X-100, exposed to the primary antibody targeting $Na_v1.7$ (Abcam, #ab85015) and incubated overnight in a wet chamber. Secondary antibodies with fluorophores that target the primary antibody (Life Technologies, #A-21434, Alexa Flour 555) were added the next day and used for imaging after 2 hours. DAPI (NucBlue Fixed Cell ReadyProbes Reagenz, Life Technologies, #R37606) was used to stain the nuclei.

Confocal imaging of WT_{GFP} and MI_{GFP} was performed by Li Yiu (Institute for Neurophysiology, Uniklinik RWTH Aachen, Germany). Briefly, HEK293t cells were transfected with either MI_{GFP} or WT_{GFP}. Cells were seed into coverslips and incubated overnight for transfection. Once transfection is achieved, cover slips were fixed by incubation with 4% PFA at room temperature. The GFP signal was used as a measure for channel expression. DAPI (NucBlue Fixed Cell ReadyProbes Reagenz, Life Technologies, #R37606) was used to stain the nuclei.

Immunostaining of WT_{TO}, $WT_{HAext1,TO}$, $WT_{HAext2,TO}$, $WT_{HAext3,TO}$, MI_{TO}, $MI_{HAext1,TO}$, $MI_{HAext2,TO}$, $MI_{HAext3,TO}$,$WT_{HACterm,TO}$ and $MI_{HACterm,TO}$ was performed by Dr. Anika Neureiter (Institute for Neurophysiology, Uniklinik RWTH Aachen, Germany). Briefly, stable cell lines were plated onto cover slips and induced using doxycycline for ~24h. After 24h, cover slips were fixed by incubation with 4% PFA at room temperature for 15 minutes. Afterwards the cover slips are washed with PBS to remove remnant PFA before staining. To allow for storage to stain at a later time-point, cover slips are exposed to 0.05% sodium azide (diluted in PBS) before being sealed with parafilm in a plate. Fixed coverslips are stored in the dark at 4°C. As all the tags are located extracellularly, this permeabilization step was completely skipped. Coverslips were then exposed to a blocking solution made up of PBS and 5% normal goat serum. After incubation at room temperature for 60 minutes, 200µL primary antibodies targeting the HA tag (Cell Signalling Technologies, #3742S) diluted in blocking solution was added to each cover slip. The cover slips are then incubated overnight at 2-8°C in a wet chamber. The next day, the samples are washed with PBS at room temperature to remove unbound primary antibodies. Then, secondary antibodies (Life Technologies, #A-21429, Alexa Flour 555) are added and incubated for 60 minutes at room temperature. As the fluorophores present in the secondary antibody are sensitive to light, this step was performed without exposure to light. Finally, samples are washed with PBS to remove unbound secondary antibodies and washed 2 times with DAPI (NucBlue Fixed Cell ReadyProbes Reagenz, Life Technologies, #R37606) to stain the nuclei. The slides are covered with 10µl mounting medium and stored at 4°C away from light until they are ready to be imaged.

Imaging of all stained cells was performed using a LSM 700 confocal microscope (Carl Zeiss) and captured using the Leica Zen Blue Suite software. Laser intensities were maintained constant throughout the samples to ensure comparability between the different plasmids. Where needed, only the brightness of the DAPI stain was increased in post-processing of the image. Post-processing, addition of scale bars and final image generation were done using ImageJ.

2.5 Multiple sequence alignment and homology modelling

Multiple sequence alignment of all nine human Na_v subtypes were performed using the T-Coffee package provided by JABAWS (Troshin et al., 2011). Alignments were visualized using Jalview (Waterhouse et al., 2009). Sequences for all the subtypes were taken from Uniprot (accession codes provided in Appendix Table S1).

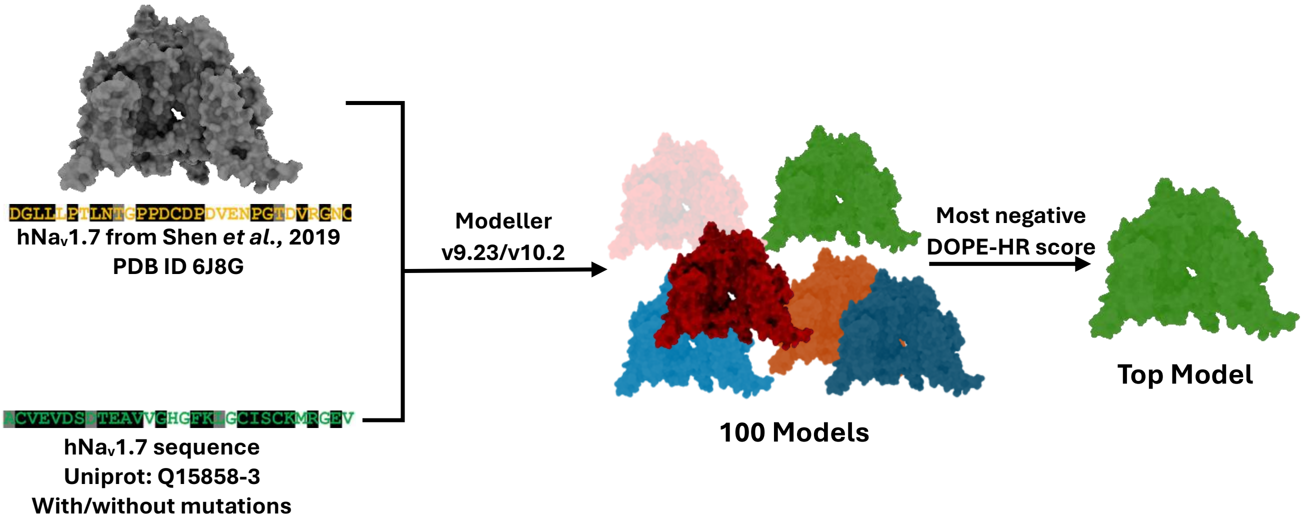

Figure 17 – Homology modelling of Na_v1.7 variants Homology modelling requires knowledge of a known structure (template) and an unknown sequence. The unknown sequence is aligned to the template sequence and fitted to the backbone positions of the template using Modeller v9.23 or v10.2. This included filling in missing atoms (WT and all mutants) and introducing the mutated amino acids (only mutants). Modeller generated a total of 100 models with various DOPE-HR energy scores. The top model was selected as the one with the most negative DOPE-HR score.

Homology modelling of hNa_v1.7 WT and M899I/A/C/V/L/F (WT, MI, MA, MC, MV, ML and MF respectively) was done using Modeller v9.23 or v10.2 (Webb and Sali, 2016) using the cryo-EM structure of hNa_v1.7 published by (Shen et al., 2019) (PDB ID 6J8G). Homology modelling of the HA tag insertions in hNa_v1.7 was done using Modeller v10.2 (Webb and Sali, 2016) using the cryo-EM structure of hNa_v1.7 published by (G. Huang et al., 2022a) (PDB ID 7W9K). Homology modelling of hNa_v1.5 F1760A and hNa_v1.5 N1765K ($FA_{1.5}$ and $NK_{1.5}$) was done using Modeller v10.2 (Webb and Sali, 2016) using the cryo-EM structure of hNa_v1.5 bound to quinidine published by (Li et al., 2021a) (PDB ID 6LQA). Firstly, the structure was prepared by removing the ß subunits and any drug molecules, ions and detergent molecules. The structure did not contain the N-terminus, intracellular linkers D1-D2 and D2-D3 and the C-terminus. Modeller was run to fill in the missing atoms between D2 S2 and D2 S3 in the $Na_v1.7$ structures (amino acids 815-818, isoform 3 numbering) and for the mutations the corresponding amino acid was changed in the sequence. A total of 100 models were generated for each mutant, and the best model was chosen using the Discrete Optimized Protein Energy Score (DOPE-HR) generated internally by Modeller. The best model was the one with the most negative DOPE-HR value. The top models were further used for molecular dynamics simulations. Molecular visualization and image/video generation was performed using UCSF ChimeraX v1.6 (Pettersen et al., 2021). A graphical representation of the homology modelling process is shown in Figure 17.

2.6 Rigid body docking of phentolamine and mexiletine

Rigid-body docking of phentolamine (pubchem CID: 5775) and mexiletine (pubchem CID: 4178) into the Cryo-EM structure of human $Na_V1.5$ ($WT_{1.5}$: PDB ID: 6LQA) and the selected homology models of $FA_{1.5}$ and $NK_{1.5}$ were performed using Autodock Vina v1.2 (Eberhardt et al., 2021). Hydrogen atoms and charges in the receptor ($hNa_V1.5$ structures) and the ligands (phentolamine and mexiletine) were added using the *AddH* and *Add Charges* tools in Chimera. Further preparation of the ligand and receptor was done using AutoDockTools4. Briefly, the rotatable roots of the ligand(s) were detected automatically and a 30x30x30A$^{\circ 3}$ grid with a 0.375A° spacing was generated with the center located around the F1760 and N1765 residues (or the mutated counterparts in $FA_{1.5}$ and $NK_{1.5}$) of the receptor structures. The search space of possible binding sites was constricted to the boundaries of the generated grid. A total of 100 poses were generated for each docking run, with an exhaustiveness value of 32. Five separate runs were performed for every ligand-receptor combination to control for the randomly generated starting points inside the grid, resulting in a total of 500 different binding poses for each combination. The poses were clustered in three dimensions using the K-means algorithm, with the 3D coordinates of the center-of-mass of the ligand as the feature. The optimal cluster size was calculated using a combination of the squared sum error minimization (elbow method), silhouette score and visual inspection of the individual clusters. After rejection of sparsely populated clusters, a total of five clusters were used for all our analyses. Clusters were ordered based on the population of the cluster and the top pose for the top cluster was selected based on the binding affinity score generated by Vina during the docking run. Interactomes of the top pose was predicted using PLIP (Adasme et al., 2021) and visualized using UCSF ChimeraX (Pettersen et al., 2021). Clustering and visualization of cluster populations were done using in-house python scripts written in Python 3.10.

2.7 Coarse-grained molecular dynamics

System setup and parameters

Molecular dynamics simulations of the top model for each mutant were performed using the coarse-grained approach. In coarse-grained molecular dynamics (CGMD), groups of atoms are bundled into “beads”, allowing for faster computational times at the cost of atomic resolution. CGMD was performed using GROMACS v2022 (Abraham et al., 2015; Bauer et al., 2022) and the Martini 3.0 forcefield (Souza et al., 2021, p. 3). Firstly, the top model from Modeller was aligned to the bilayer using PPM webserver (Lomize et al., 2012). This aligned all-atom structure was then coarse-grained, and its topology generated using Martinize2 (Kroon et al., 2023). As coarse-graining results in the loss of secondary structure information, elastic networks (EN) with a force constant of 700kJ/mol/nm^2 were added between non-bonded backbone beads at a distance between 0.3 and 0.9nm to ensure the maintenance of the secondary and tertiary folds of the protein. Side-chain corrections were introduced using the "-scfix" flag to improve the dynamics of the side-chain beads (Herzog et al., 2016) . Once coarse-grained and restrained, the structure was embedded in a 100% polyphosphatidylcholine (POPC) membrane with water in a 150mM NaCl solution using Insane (Wassenaar et al., 2015). Ions were added such that the total charge of the system is neutral. The system was kept in a cubic box of dimension 18x18x18nm^3, with a distance of at least 2.5nm between two periodic images of the protein. The system was minimized using the steepest-descent algorithm in two rounds, first with a maximal force cut-off of 1000 kJ mol^{-1} nm^{-1} and then with a lower cut-off of 500 kJ mol^{-1} nm^{-1}. The minimized system was then equilibrated shortly in an NPT ensemble for 2ns (2fs time steps with a total of 500000 steps) where the pressure and temperature are maintained at a constant value of 1 bar and 310K respectively. This allowed for the stabilization of the volume and box size of the system. This was followed by longer equilibrations first in a NVT ensemble for 200ns (20fs time steps with a total of 10000000 steps) where temperature is kept constant and then in an NPT ensemble for 50ns (20fs time steps with a total of 2500000 steps). Pressure was maintained using the Parrinello-Rahman barostat in a semi-isotropic manner, with a compressibility of 0.0003 bar^{-1} and time constant of 12. Temperature was maintained with a v-rescale thermostat with a time constant of 1. During all three equilibration phases, a backbone restraint of 1000kJ/mol was maintained. After the equilibration phase, an unrestrained and unbiased production run was generated using the "md" integrator for a total time of 4µs (20fs time steps with a total of 200000000 steps). To ensure that observations are not due to the random selection of the initial velocities, three separate replicas starting from the equilibration phase were generated. This resulted in a total simulation time of 12µs for each mutant. The steps are depicted graphically in Figure 18.

For simulation of the hNa$_v$1.7 M1627K and hNa$_v$1.7 M1628K, the hNa$_v$1.7 cryo-EM structure solved by (G. Huang et al., 2022a) (PDB ID 7W9K) was firstly aligned to the membrane bilayer using the PPM webserver (Lomize et al., 2012). This aligned all-atom structure was then coarse-grained, and its topology generated using Martinize2 (Kroon et al., 2023). Mutations (M1627K or M1628K) were introduced into the structure directly using the *-mutate* flag in martinize2. To better understand whether the mutation destabilizes binding of the IFM motif, the elastic networks were modified to allow flexibility in the D3-D4 by adopting the methodology used by (Lin et al., 2024). Briefly, the elastic networks between the backbone beads were generated with a force constant of 500kJ/mol/nm2 at a distance of 0.3 and 0.9nm. The generated networks between the D3-D4 and other parts of the protein were removed using a custom generated script. The rest of the workflow was similar to what was described before for simulation of MI. In brief, side chain corrections were introduced, a 100% POPC membrane was utilized with 150mM NaCl, minimization was performed followed by a short NPT, a longer NVT and a longer NPT equilibration with parameters as described before. The final unrestrained and unbiased production run was performed for 8µs (20fs time steps with a total of 400000000 steps). Three separate replicas starting from the equilibration phase was generated to account for randomness of the initial velocity generation.

Post-processing of trajectories

Post-processing of the simulated frames firstly involved down-sampling. Snapshots of the simulations were saved at intervals of 10ns. The first 1µs was discarded from further analyses as steady state was achieved around 1µs. In simulations with the hNa$_v$1.7 M1627K and hNa$_v$1.7 M1628K, all frames were considered without discarding. Periodic boundary effects were corrected for, including centering the protein and correcting for the rotation and translation of the protein. The final corrected trajectory was converted into a multi-state pdb file and used for further analyses. Root mean square deviations (RMSD) and root mean square fluctuations (RMSF) were calculated using the gmx rms and gmx rmsf commands respectively.

All post-processing of the simulations were run in Ubuntu 20.04 LTS. Analyses routines for the extracted frames were run in Windows 11 using Python3.10.

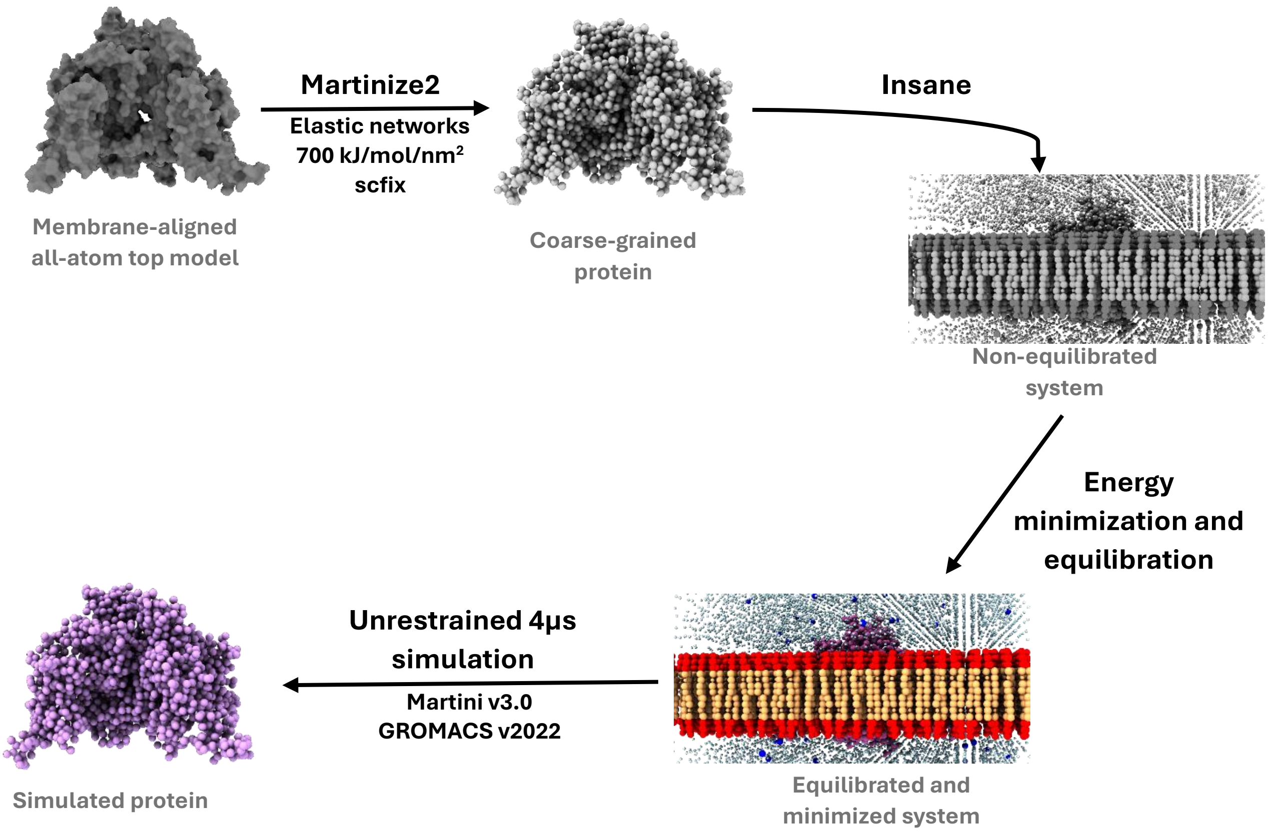

Figure 18 – CGMD of Na$_V$1.7 variants After the top model was aligned to the membrane using the PPM server (Lomize et al., 2012), the model was converted into a coarse-grained representation using Martinize2 (Kroon et al., 2023). Coarse graining included elastic bonds between backbone atoms at a distance of 0.3 to 0.9nm, with a force constant of 700 kJ/mol/nm^2. Side-chain dihedral fixes were introduced using scfix (Herzog et al., 2016). This coarse-grained protein was then embedded into a phosphatidylcholine (POPC) membrane surrounded by water and a salt solution made of 150mM NaCl using Insane (Wassenaar et al., 2015). The system was then energy minimized and equilibrated in both an NPT and NVT ensemble with positional restraints of the backbone atoms (1000 kJ/mol/nm^2). The equilibrated system was then run in an unbiased and unrestrained manner in the Martini v3 forcefield (Souza et al., 2021) using GROMACS v2022 (Abraham et al., 2015; Bauer et al., 2022). The trajectories were then post-processed, down sampled and used for further analyses.

Measurement of pore radius

The pore radius of each frame from the down-sampled trajectories for the MI/MC/MA/MF/ML/MV was calculated using HOLE 2.0 (Smart et al., 1993), with a modified radius file to account for the van-der-waal's radius of the martini beads (Appendix Table S2). The center-of-geometry of the protein backbone was used as the starting coordinate for pore radius calculations and the z axis was used as the coordinate direction along which the calculations are performed. Pore radius was calculated in steps of 0.25A°. Coordinates were limited to 16A° intracellularly and 15A°

extracellularly with respect to the center-of-geometry, generating a total of 125 pore coordinates. Average pore radius at each pore coordinate was calculated from the individual frames and plotted with respect to the normalized pore coordinate. To measure changes in the distribution of the pore radii in the mutants with respect to the WT at each pore coordinate, the Kullback-Leibler (KL) divergence was used as a metric. KL divergence between two discrete probability distributions P and Q can be measured using equation 7:

$$KL\ divergence\ (P||Q) = \sum_{x \in X} P(x) * log\left(\frac{P(x)}{Q(x)}\right)$$

Equation 7

where X represents the sample space that defines P and Q, and x is one such measure inside X (Kullback and Leibler, 1951). Thus, KL divergence is a measure of how two distributions differ from each other, with higher values representing higher divergence of the distributions. In our analysis, P is the WT distribution, Q is mutant distribution, and X is the range of pore radii values at pore point P. KL divergence was calculated using the sci-kit learn library in Python for each pore point and between each mutant with respect to the WT and plotted along with the mean pore radii using Python and matplotlib. Analyses routines for the extracted frames were run in Windows 11 using Python3.10.

Helix distance, IFM distance and helix rotation

The distance between the S4-S5 helix of D4 and the helical region in D3-D4 was calculated for each extracted frame of WT, hNa$_v$1.7 M1627K or hNa$_v$1.7 M1628K by measuring the Euclidean distance between the center-of-geometry of the backbone beads of D4 S4-S5 (residues 1619-1629, isoform 3 numbering) and the center-of-geometry of the backbone beads of the helical region in D3-D4 (residues 1464-1478, isoform 3 numbering). The distance between the IFM motif and the binding pocket was also measured as the Euclidean distance between the center-of-geometry of the IFM motif (residues 1461-1463, isoform 3 numbering) and the center-of-geometry of the binding pocket residues for the IFM motif (residues 1303 in D3 S4-S5, 1636 in D4 S5 and 1742 in D4 S6, isoform 3 numbering). The angle formed between the helical region of D3-D4 and D4 S4-S5 was calculated by measuring the angle between the vectors formed by the two regions. The probability density function (pdf) of each parameter for WT, hNa$_v$1.7 M1627K and hNa$_v$1.7 M1628K were calculated by fitting the histograms into a kernel density estimator. The measurement of the distances and angle and the fitting of the histograms were done using custom scripts written in Python 3.10. Graphs were plotted using matplotlib. Analyses routines for the extracted frames were run in Windows 11 using Python3.10.

Chapter 3: Results

3.1 Pore collapse as a patho-mechanism for Na$_v$1.7 mutations causing loss of pain

One approach towards understanding structure-function relationships of voltage-gated sodium channels (Na$_v$s) is to uncover mechanisms by which rare naturally occurring mutations cause disorders in Na$_v$ functioning. To this end, I use a heterozygous variant of hNa$_v$1.7 in a Chinese patient that causes partial insensitivity to pain and try to understand how this clinical phenotype is caused by dysfunction of Na$_v$ gating and the structural mechanisms by which loss of pain occur.

I show that one of the mutations hNa$_v$1.7 p.M899I (MI) is located deep in the pore module (PM) of D2 and causes complete loss of function (LoF) when expressed *in vitro* in HEK293t cells and electrophysiologically characterized using whole-cell patch clamp **(Section 3.1.1-3.1.2)**. This LoF phenotype is not limited to Na$_v$1.7, with mutation of the equivalent residue in hNa$_v$1.2 and hNa$_v$1.5 also causing LoF **(Section 3.1.3)**. Since LoF can either be due to defective trafficking to the cell membrane or defective gating at the cell membrane, I use various strategies to answer the question of membrane expression, using extracellular tagging to convincingly show that MI is expressed in the membrane **(Section 3.1.4)**. I next used coarse-grained molecular dynamics to show that MI alters the outer pore geometry, likely disrupting ion conduction and causing LoF **(Section 3.1.5)**. This residue, surprisingly, is robust to mutations, with various smaller or aromatic amino acids retaining functionality in correlation with the extent of the outer pore bottleneck **(Section 3.1.6)**. Such mutational robustness is not observed in the equivalent residue of other domains, causing complete LoF when these residues are mutated to alanine **(Section 3.1.7)**. The overall mechanism of the MI however does not fully answer the mechanism of partial insensitivity to pain phenotype observed in the patient. The other part of the puzzle requires us to understand the other allele, hosting the intronic mutation hNa$_v$1.7 c.1602+2delT (ex11del), which alters the donor splice site and skips exon 11. Exon 11 codes for 96 amino acids in the intracellular region of D1-D2, with many residues heavily implicated in channel dimerization **(Section 3.1.8)**. Deletion of these amino acids however did not alter expression of the channel and caused minor gating changes when compared to a wild type **(Section 3.1.9)**. Co-expression of the ex11del with MI reduced current densities linearly with respect to the amount of MI present in the cells **(Section 3.1.10)**.

Overall, our results suggest that the MI has a collapsed pore that leads to dysfunctional channels in the membrane, and a potential lack of dimerization with the functional ex11del likely reduces the patient's sensitivity to pain and could prevent any rescue mechanisms to enable the patient to sense pain at physiological levels.

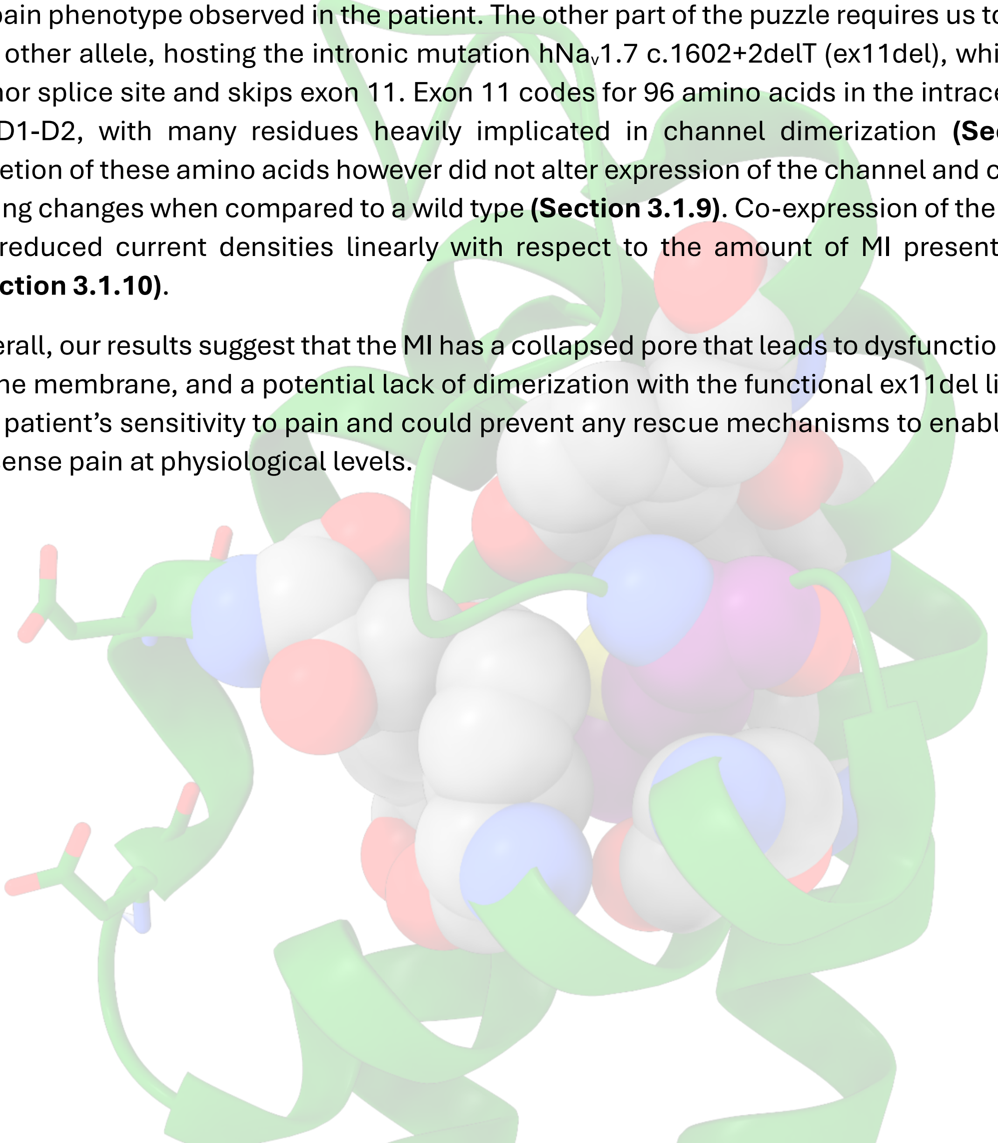

3.1.1 hNa$_v$1.7 p.M899I is located in the pore module of domain 2

Given that the patient manifests LoF clinically, the first step was to locate the M899 residue in the 3D structure of hNa$_v$1.7. I used the structure predicted by (Shen et al., 2019) (PDB ID 6J8G) and observed that the M899 residue is located in PM2, between the loop connecting D2 S5 and D2 P1 (Figure 19A and B). The residue is in close proximity to the selectivity filter and the interface formed between VSD1 and PM2 (Figure 19A and B). M899 is also highly buried, surrounded by various hydrophobic amino acids from D2 S5, D2 P1, D2 P2 and D2 S6.

3.1.2 hNa$_v$1.7 p.M899I shows complete loss of function *in vitro*

I proceed to test whether the point mutation MI causes LoF phenotype *in vitro*. I expressed either MI or WT in a homozygous manner in HEK293t cells using JetPEI® and recorded their current densities using whole-cell voltage clamp. GFP was used as a marker protein, and a negative control was made by transfecting GFP without WT or MI. While WT showed robust inward sodium currents, MI was indistinguishable from GFP, suggesting that MI causes complete LoF *in vitro* and any activity that can be due to MI is indistinguishable from the activity of the endogenous Na$_v$s present in HEK293t cells (Figure20A and B, Table 4).

3.1.3 hNa$_v$1.7 M899 is highly conserved

I employed multiple sequence alignment of the various human Na$_v$ sequences using Jalview to observed the conservation of the M899 residue (Waterhouse et al., 2009) (Uniprot codes in Appendix Table S1). M899 is fully conserved across the nine subtypes (Figure 21A). This hints at the possibility that a similar mutation in another subtype would also cause a LoF phenotype. I used the Clinvar database to search for missense variants of the M899-equivalent residue in other Na$_v$ subtypes. Hits were observed in Na$_v$1.1, Na$_v$1.2 and Na$_v$1.5. I used Na$_v$1.2 M925T (MT$_{1.2}$) as a representative for a Na$_v$ subtype in the CNS and Na$_v$1.5 M881I (MI$_{1.5}$) as a representative for a Na$_v$ subtype in the cardiac system. Clinvar entries suggested MT$_{1.2}$ caused epilepsies, while MI$_{1.5}$ caused Brugada syndrome – both primarily caused by a LoF of the respective Na$_v$ subtypes. I transfected MT$_{1.2}$ and MI$_{1.5}$ in HEK293t cells and measured their current densities using whole-cell patch clamp. Both MT$_{1.2}$ and MI$_{1.5}$ show complete LoF *in vitro*, indistinguishable from GFP (negative control) and MI (Figure 21B and C, Table 4). I concluded that mutation of the equivalent of M899 to I or T in any subtype can be expected to cause LoF of that subtype.

3.1.4 hNa$_v$1.7 p.M899I is expressed in the membrane

LoF can be caused either due to trafficking defects or gating defects. Trafficking defects involve improper trafficking of the channel to the membrane mostly due to improper folding caused by the mutation. Gating defects are due to properly folded channels having altered gating properties caused by the mutation. It is hence imperative to know if membrane expression is present in the mutated channel. The first step was to perform immunostainings on WT and MI. After transfecting HEK293t cells with either WT or MI (and GFP as a marker protein), primary antibodies targeting Na$_v$1.7 (Abcam, ab85015) and secondary antibodies with a fluorophore targeting the primary antibody (Life Technologies, A-21434, Alexa Flour 555) were used to detect Na$_v$1.7. Permeabilization of the cells using Triton-X was employed before staining to enable the antibodies to enter the cell and stain Na$_v$1.7. Both WT and MI have similar expression patterns of Na$_v$1.7 around the membrane region, although it is unclear if this is membrane expression or accumulation of transfected channels below the membrane in the cytosol (Figure 22).

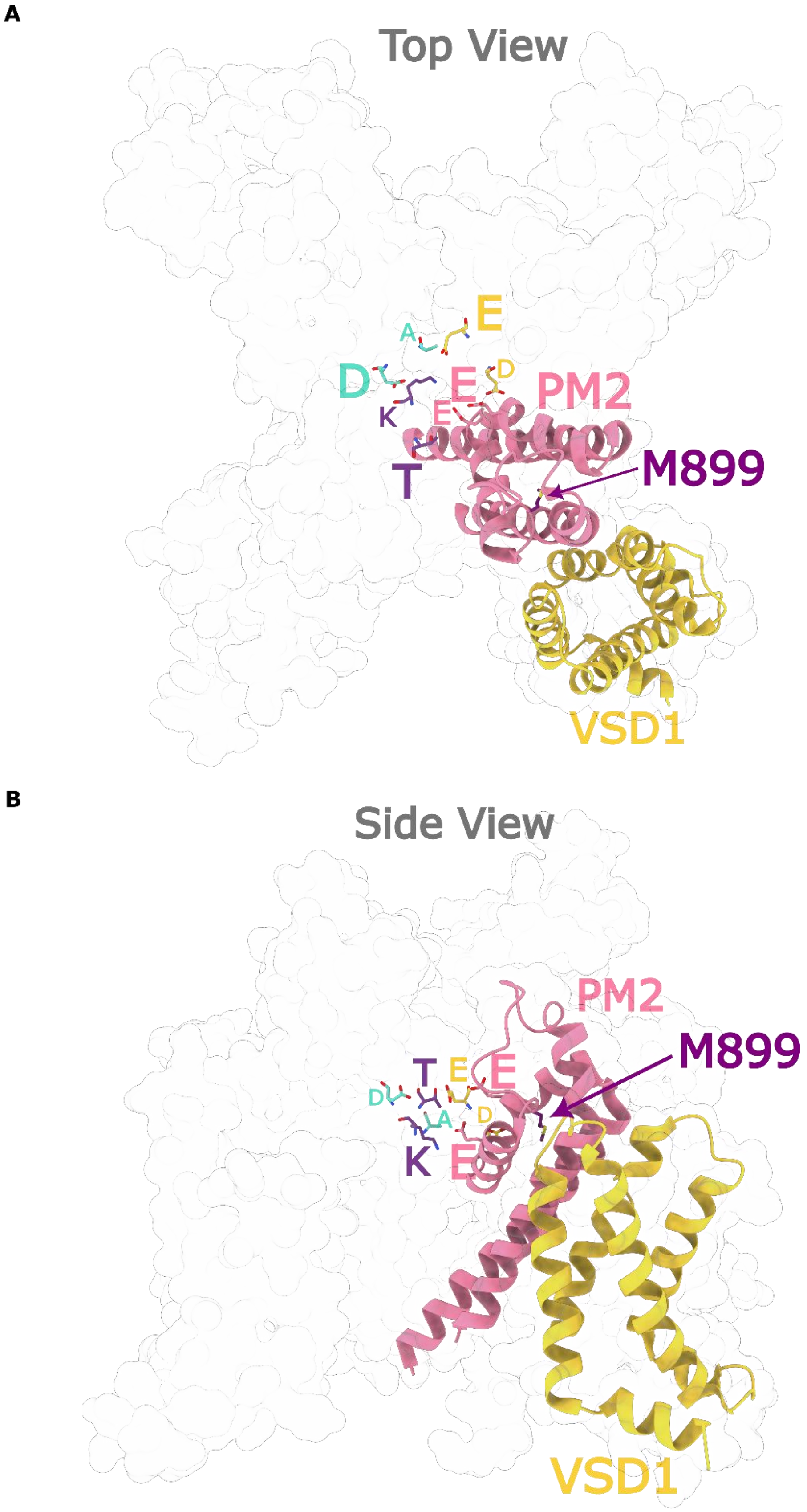

Figure 19 – M899 is located in PM2 Location of the M899 residue in the 3D structure of hNa$_v$1.7 published by (Shen et al., 2019) in the **(A)** top view and **(B)** side view. The residue is not only close to interface between PM2 and VSD1, but also to the outer pore lining residues including the selectivity filter (DEKA) and outer vestibule regions (EETD).

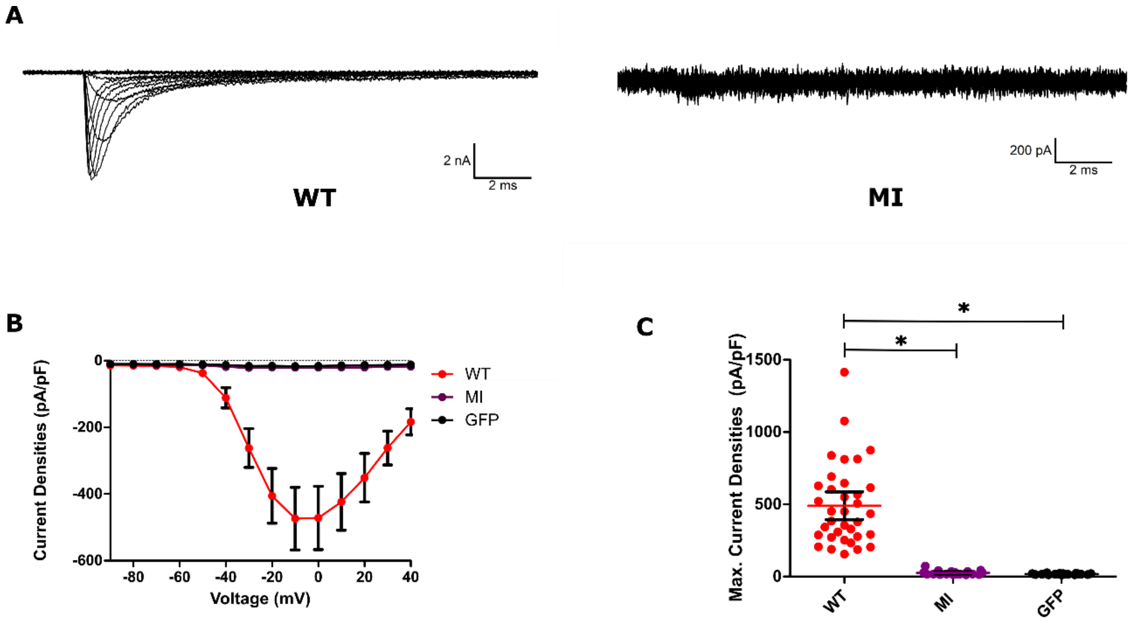

Figure 20 – M899I causes loss of function *in vitro* (A) Representative traces of hNa$_v$1.7 WT (WT) and hNa$_v$1.7 M899I (MI) obtained from whole-cell patch clamp of transfected HEK293t cells. While WT shows robust inward sodium currents, MI has a complete abolishment of function. **(B)** Current density vs voltage steps of HEK293t cells transfected with either WT, MI or fluorescent marker pMaxGFP (GFP, used as a negative control). WT has large inward currents, while MI is indistinguishable at all voltage ranges from GFP. **(C)** Absolute values of the maximum current densities of HEK293t cells transfected with WT, MI or GFP (used as a negative control). Maximum current densities are the maximal absolute value of the current densities observed at any of the applied voltage steps. WT has larger amplitudes, while MI is indistinguishable from GFP. * $p < 0.05$.

Table 4 – Current densities of hNa$_v$1.7, hNa$_v$1.2, hNa$_v$1.5 WT, corresponding M to I/T mutations or only the fluorescent protein GFP as a negative control transiently transfected in HEK293t cells. * $p<0.05$ compared to hNa$_v$1.7 WT. CI is 95% confidence interval of the mean. n is the number of patched cells used for analysis.

Channel	Current Densities (mean±95% CI, n)
hNa$_v$1.7 WT (WT)	490.3±96.4 pA/pF, n=35
hNa$_v$1.2 WT (WT$_{1.2}$)	598.5±739.5 pA/pF, n=5
hNa$_v$1.5 WT (WT$_{1.5}$)	1094.0±474.0 pA/pF, n=11
hNa$_v$1.7 M899I (MI)	26.1±6.4 pA/pF, n=21 *
hNa$_v$1.2 M925T (MT$_{1.2}$)	33.8±27.8 pA/pF, n=7 *
hNa$_v$1.5 M881I (MI$_{1.5}$)	21.8±8.8 pA/pF, n=9 *
pMaxGFP (GFP)	18.0±1.9 pA/pF, n=19 *

There were some major drawbacks with this method. Firstly, HEK293t cells express endogenous Na$_v$1.7 (He and Soderlund, 2010). Secondly, the cells must be permeabilized for the antibodies to function. Combined with the non-specificity of the antibodies, this means that the antibody will not only target and stain transfected channels, but also endogenous channels of HEK293t cells that may be Na$_v$1.7.

Indirect methods such as lowered temperature incubation was employed to overcome the drawbacks of antibodies targeting Na$_v$1.7. The reasoning behind this was that the functional output in the form of inward sodium currents can easily be quantified and attributed primarily to the expressed channels. Lowering incubation temperatures has also been shown to rescue trafficking in some mutations of Na$_v$s causing LoF (Bechi et al., 2015). In our hands however, hNa$_v$1.7 M889I was not rescued by incubation at 30°C before patching (Figure 23A and B, Table 5).

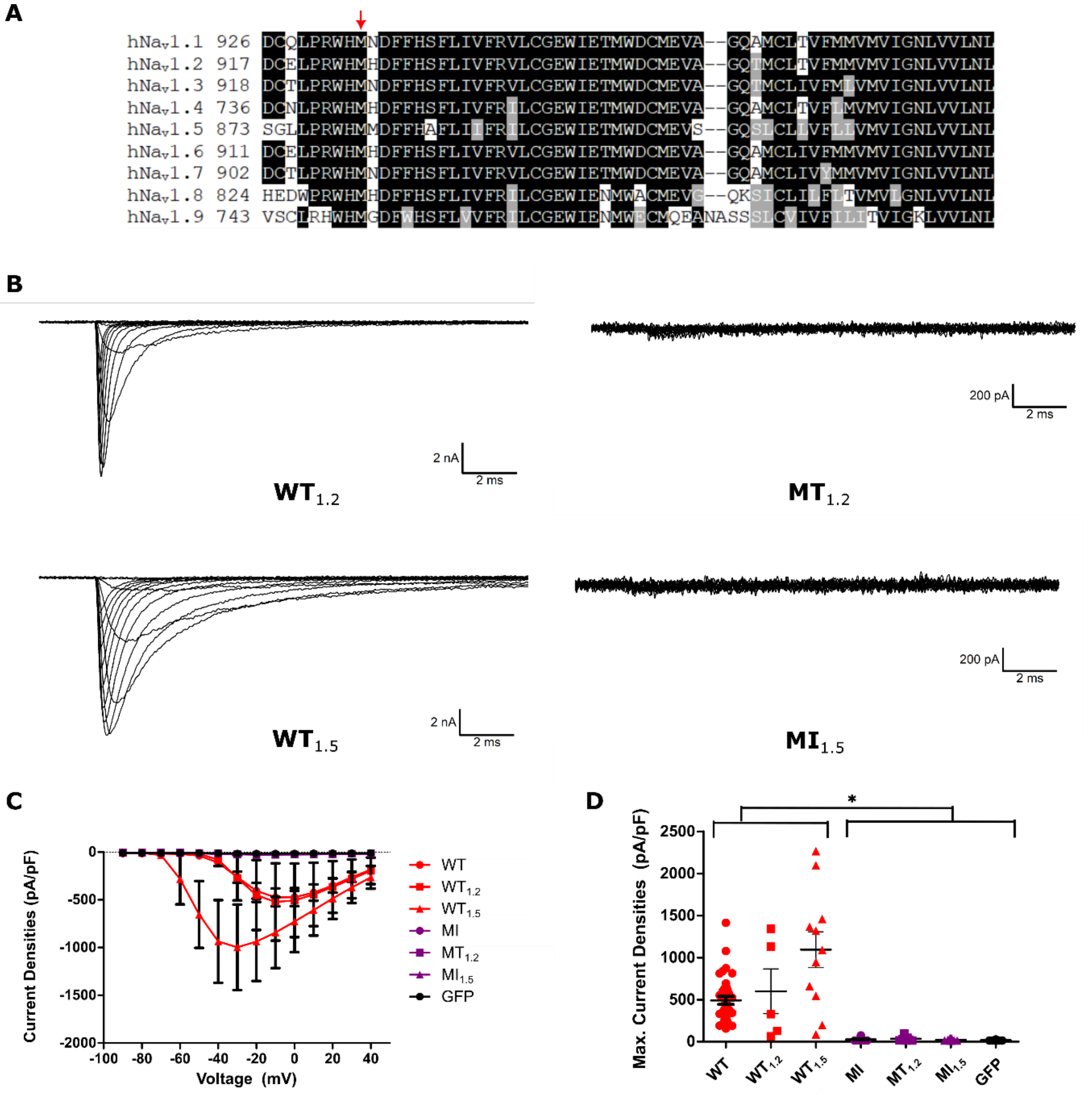

Figure 21 – M899 is a highly conserved residue (A) Multiple sequence alignment of the 9 human Na$_v$ subtypes (Na$_v$1.1 – Na$_v$1.9). The letters represent the one letter codes for each amino acid and the numbers represent the starting number of each sequence. Only the region around M899 is shown for clarity. **Dark** boxes show fully conserved residues, while **grey** boxes show partially conserved residues, and non-shaded boxes show non-conserved residues. M899 (red arrow) is a fully conserved residue. **(B)** Representative traces of hNa$_v$1.2 WT (WT$_{1.2}$), hNa$_v$1.2 M925T (MT$_{1.2}$), hNa$_v$1.5 WT (WT$_{1.5}$) and hNa$_v$1.5 M881I (MI$_{1.5}$) obtained from whole-cell patch clamp of transfected HEK293t cells. While WT$_{1.2}$ and WT$_{1.5}$ show robust inward sodium currents, MT$_{1.2}$ and MI$_{1.5}$ have a complete abolishment of function. **(C)** Current density vs voltage steps of HEK293t cells transfected with either hNa$_v$1.7 WT (WT), hNa$_v$1.7 M889I (MI), WT$_{1.2}$, MT$_{1.2}$, WT$_{1.5}$, MI$_{1.5}$ or fluorescent marker pMaxGFP (GFP, used as a negative control). WT, WT$_{1.2}$ and WT$_{1.5}$ have large inward currents, while MT$_{1.2}$ and MI$_{1.5}$ are indistinguishable at all voltage ranges from GFP and similar to the MI. **(D)** Absolute values of the maximum current densities of HEK293t cells transfected with either WT, MI, WT$_{1.2}$, MT$_{1.2}$, WT$_{1.5}$, MI$_{1.5}$ or GFP (used as a negative control). Maximum current densities are the maximal absolute value of the current densities observed at any of the applied voltage steps. WT, WT$_{1.2}$ and WT$_{1.5}$ have larger amplitudes, while MI, MT$_{1.2}$ and MI$_{1.5}$ are indistinguishable from GFP and from each other. * $p<0.05$.

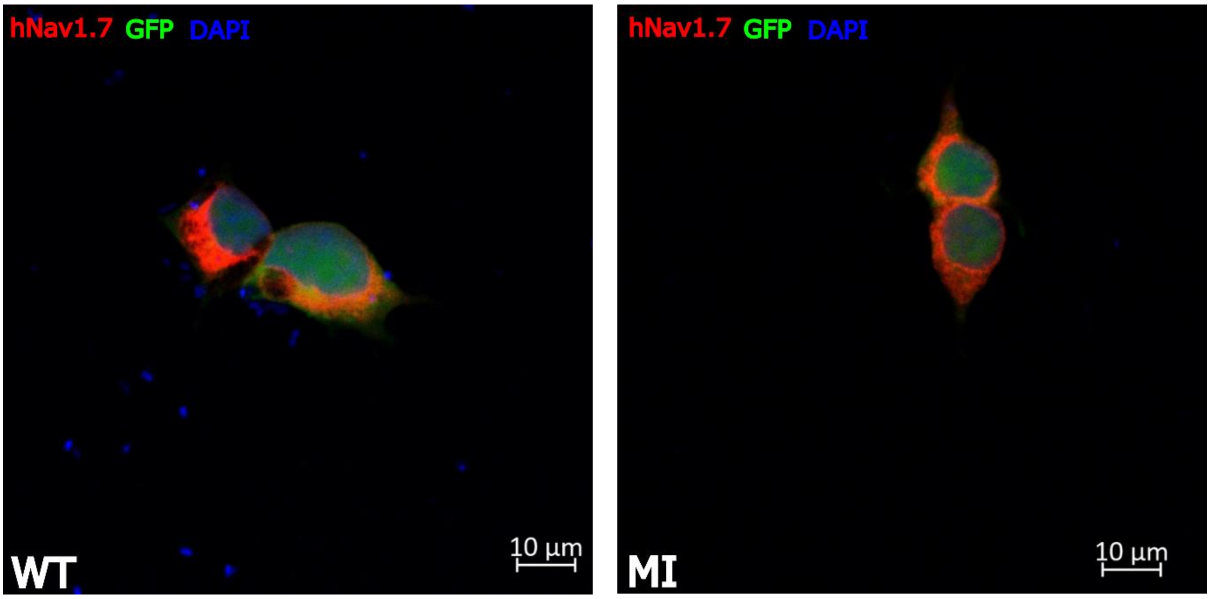

Figure 22 – Similar expression pattern of hNa$_v$1.7 WT and hNa$_v$1.7 M889I in HEK293t cells Immunostaining of HEK293t cells transfected with either hNa$_v$1.7 WT (WT) or hNa$_v$1.7 M889I (MI) were done using primary antibodies targeting Na$_v$1.7 and secondary antibodies with a fluorophore targeting the primary antibody. Permeabilization of the cells was done to allow for the antibodies to give access inside the cell membrane. **GFP** was used as a marker protein to ensure transfection of the cells was successful, while **DAPI** stains the nucleus of the cell. hNa$_v$1.7 is shown by **red** fluorescence. Scale bars are shown in the bottom right corner. Confocal images show no clear indication of membrane expression, although the expression patterns of both WT and MI are very similar. Staining and imaging performed by Li Yiu (Institute for Neurophysiology, Uniklinik RWTH Aachen, Germany).

Fusion proteins allow for fusing fluorescent probes to the protein, thus accurately attributing the intensity of the signal to the level of expression of the channel. Petra Hautvast (Institute of Neurophysiology, Uniklinik RWTH Aachen, Germany) generated WT and MI constructs fused at the C-terminus to GFP (WT$_{GFP}$, MI$_{GFP}$). However, the current densities of WT$_{GFP}$ were much less than WT, only marginally higher than the negative control transfected with GFP (Figure 24A, Table 5). Confocal imaging showed that both WT$_{GFP}$ and MI$_{GFP}$ showed clusters of green signals located intracellularly, resembling endoplasmic reticulum (ER) whorls observed when tagged channels dimerize and form internal clusters that prevent expression in the membrane (Costantini et al., 2012) (Figure 24B).This resulted in it being unclear if MI is expressed in the membrane.

Table 5 – Current densities of GFP-fused wild-type hNa$_v$1.7 or hNa$_v$1.7 M899I transiently transfected in HEK293t cells, of non-tagged hNa$_v$1.7 M899I incubated at 30°C or only the fluorescent protein GFP as a negative control. * p<0.05 compared to non-fused wild-type hNa$_v$1.7. CI is 95% confidence interval of the mean. n is the number of patched cells used for analysis.

Channel	Current Densities (mean±95% CI, n)
hNa$_v$1.7 WT (WT)	490.3±96.4 pA/pF, n=35
hNa$_v$1.7 WT-GFP (WT$_{GFP}$)	85.7±25.6 pA/pF, n=22 *
hNa$_v$1.7 M899I-GFP (MI$_{GFP}$)	19.5±3.5 pA/pF, n=11 *
hNa$_v$1.7 M899I @ 30°C (MI-30°C)	29.6±4.6 pA/pF, n=20 *
pMaxGFP (GFP)	18.0±1.9 pA/pF, n=19 *

Ultimately, I decided to employ a system in which the membrane expression of Na$_v$s can accurately be attributed to the channel of interest. To do so, I needed to overcome the two afore-mentioned problems – namely non-specificity of antibodies and permeabilization of the cell membrane. To get around the non-specificity of the Na$_v$ antibodies, we needed to use an external

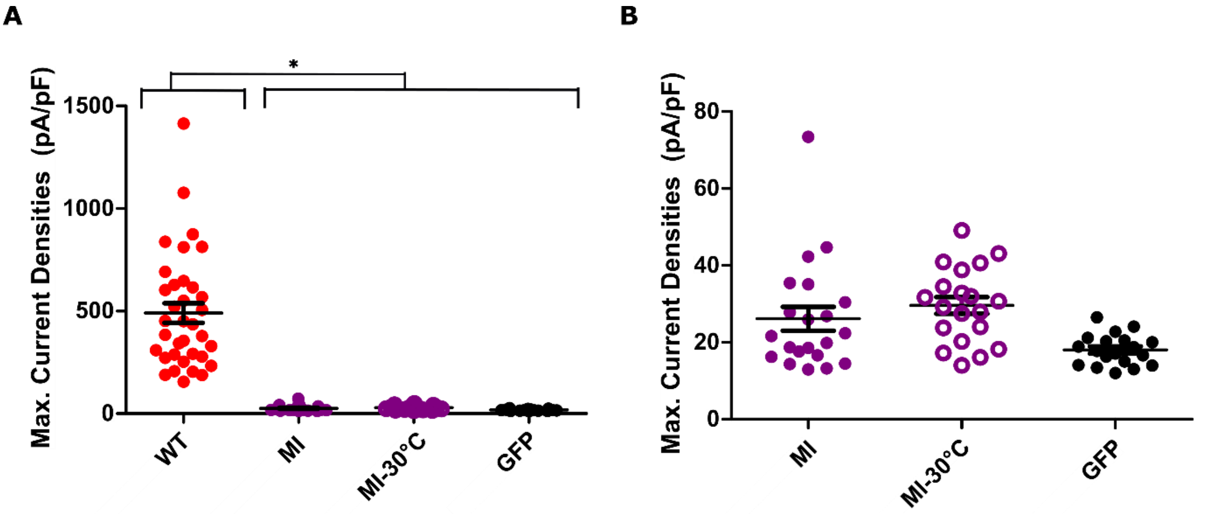

Figure 23 – Lowered temperature incubation does not rescue hNa$_v$1.7 M889I LoF phenotype (A) Absolute values of the maximum current densities of HEK293t cells transfected with hNa$_v$1.7 WT (WT), hNa$_v$1.7 M889I (MI), hNa$_v$1.7 M889I but incubated at 30°C (MI-30°C) or fluorescent marker pMaxGFP (GFP, used as a negative control). Maximum current densities are the maximal absolute value of the current densities observed at any of the applied voltage steps. Lowering the incubation temperature after transfection did not help in rescuing channel function. (B) A closer look at the absolute values of the maximum current densities of MI, MI-30°C and GFP. * $p<0.05$.

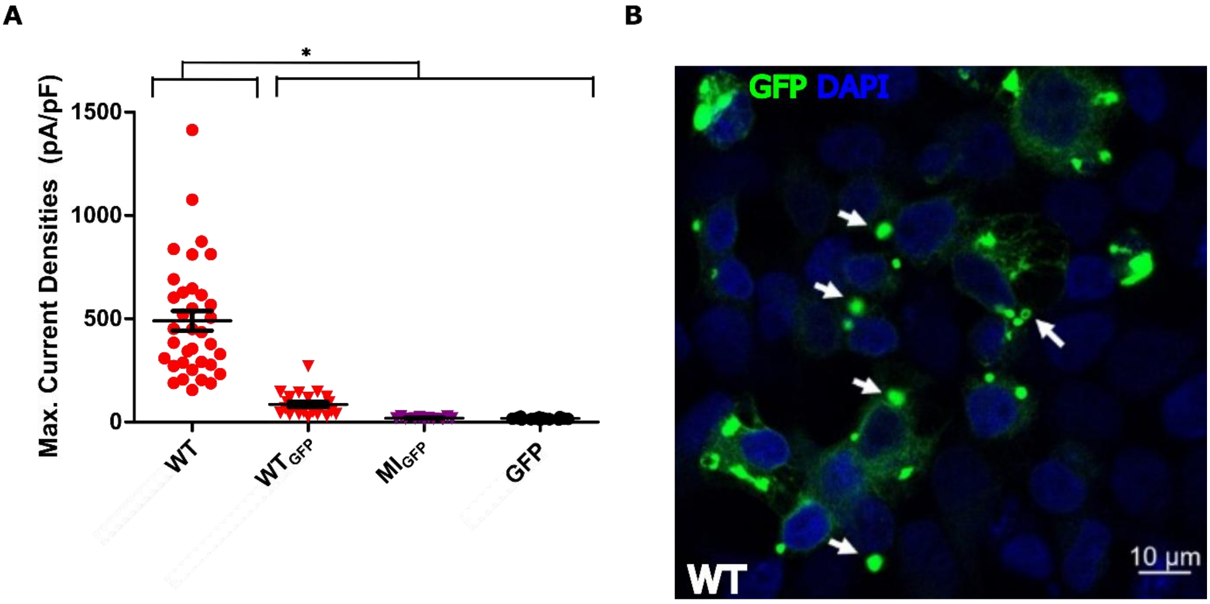

Figure 24 – GFP-tagging of hNa$_v$1.7 WT reduces channel expression (A) Absolute values of the maximum current densities of HEK293t cells transfected with either hNa$_v$1.7 WT (WT), hNa$_v$1.7 WT fused with GFP (WT$_{GFP}$), hNa$_v$1.7 M889I fused with GFP (MI$_{GFP}$) or fluorescent marker pMaxGFP (GFP, used as a negative control). Maximum current densities are the maximal absolute value of the current densities observed at any of the applied voltage steps. Addition of a GFP tag to the C-terminus of WT drastically reduces the expression of the channel. **(B)** Tagging of WT with GFP seems to create internal clusters that show up as bright green spots (white arrows) in confocal imaging. The internal clusters resemble endoplasmic reticulum whorls that can be caused by dimerization of the GFP-fused channels (Costantini et al., 2012). Imaging performed by Yi Liu (Institute for Neurophysiology, Uniklinik RWTH Aachen, Germany). * $p<0.05$.

tag that can be targeted in a more specific manner using antibodies for that specific tag. By introducing this tag in an extracellular position on the Na$_v$ channel, we can also do away with permeabilization as the antibodies can reach the tag without the need to disrupt and create pores in the membrane. For the tag, I used an HA tag. To determine the location, I first performed homology modelling of the hNa$_v$1.7 channel published by (G. Huang et al., 2022a) (PDB ID: 7W9K) with 3 different HA tag locations – one in-between P148 and P149 in the linker between D1 S1 and D1 S2 (ext1), one in-between L280 and E281 in the linker between D1 S5 and D1 P1 (ext2) and one in-between L293 and E294 in the linker between D1 S5 and D1 P1 (ext3). The HA tags are located extracellularly and do not interfere with any major secondary structures involved in the gating of the protein (Figure 25).

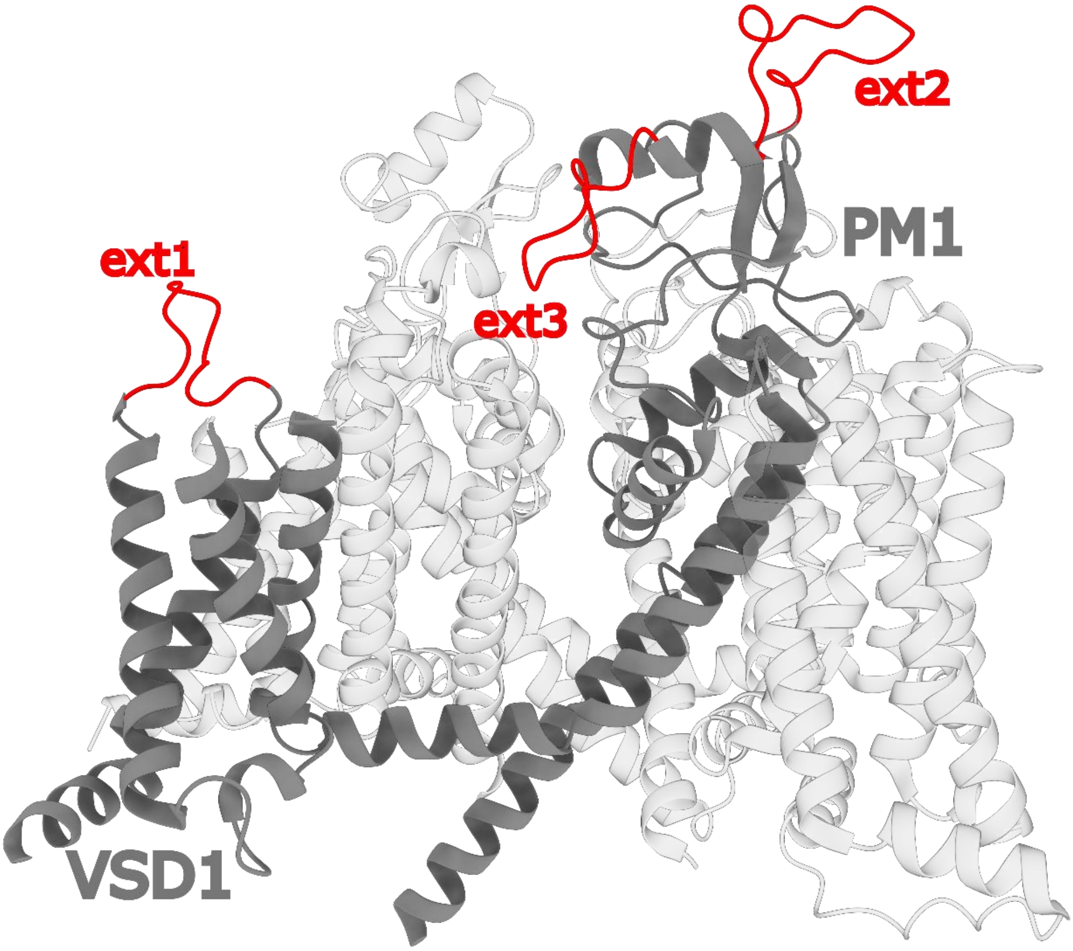

Figure 25 – Location of the extracellular HA tags. The three extracellular HA tags were all placed in D1. Only D1 is shown for clarity. The first HA tag position (ext1) is in the linker between S1 and S2 in VSD1 (red loop). The second (ext2) and third (ext3) HA tags are in the longer loop between S5 and P1 in PM1. All three locations are exposed to the extracellular side and do not seem to interfere with major gating regions. The structure used is the hNav1.7 structure solved by (G. Huang et al., 2022a)(PDB ID 7W9K).

Once a structural prediction was made regarding the positions of the HA tags, I obtained stable HEK293 Flp-in™ cells expressing untagged or HA-tagged WT or MI channels (WT$_{\text{non-tagged,TO}}$, WT$_{\text{HAext1,TO}}$, WT$_{\text{HAext2,TO}}$, WT$_{\text{HAext3,TO}}$, MI$_{\text{non-tagged,TO}}$, MI$_{\text{HAext1,TO}}$, MI$_{\text{HAext2,TO}}$, MI$_{\text{HAext3,TO}}$) with the help of Prof. Dr. Ralf Hausmann Amdiya Botchoi and Silvia Destro-Dassen (Institute for Clinical Pharmacology, Uniklinik RWTH Aachen, Germany). A C-terminal HA tag (WT$_{\text{HACterm,TO}}$ and MI$_{\text{HACterm,TO}}$) was also generated as a positive control. I used whole-cell patch clamp to validate that the WT channels were functional, and that the HA tag did not interfere with gating.

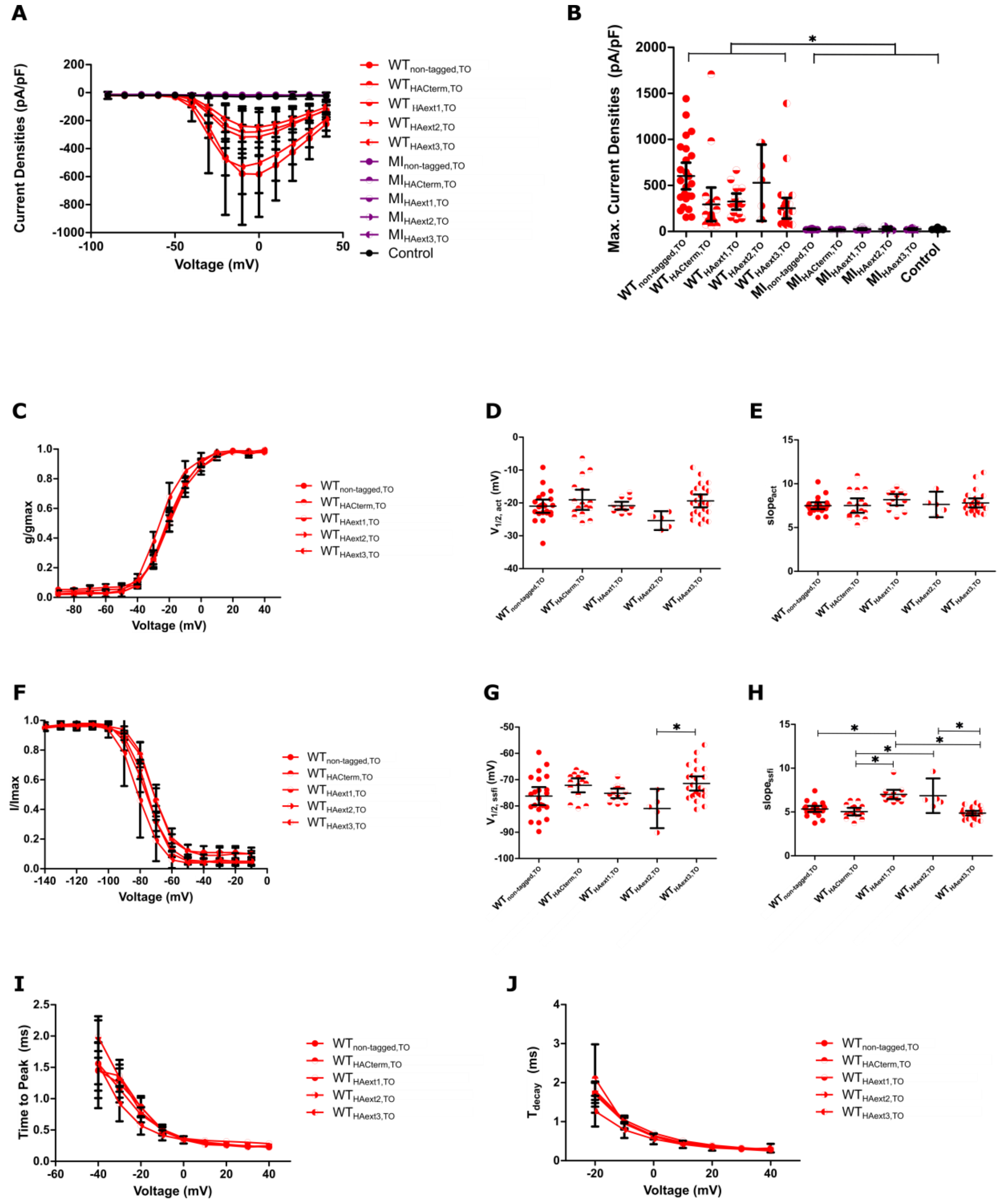

Figure 26 – HA-tagging does not alter electrophysiological properties of hNa$_V$1.7 WT TO. **(A)** Current densities vs applied voltage for untagged, C-terminally and extracellularly HA-tagged hNav1.7 WT TO and hNav1.7 MI TO constructs. HA-tagging does not affect the expression of the channel in the WT. **(B)** Maximal current densities for all stable cell lines. Maximum current densities are the maximal absolute value of the current densities observed at any of the applied voltage steps. **(C)** Normalized conductance curves, **(D)** $V_{1/2,act}$ and **(E)** $slope_{act}$ for the untagged and HA-tagged WT constructs. No significant changes were observed for any properties of the voltage-dependence of activation. **(F)** Normalized current curves **(G)** $V_{1/2,ssfi}$ and **(H)** $slope_{ssfi}$ for untagged and HA-tagged WT constructs. No significant changes were observed for any properties of the voltage-dependence of steady-state fast inactivation. **(I)** Time to peak and **(J)** onset of fast inactivation kinetics for untagged and HA-tagged WT constructs. No significant changes in the kinetic properties were observed. * $p<0.05$.

Current densities of all HA-tagged WT constructs were slightly reduced compared to non-tagged channels, but still large enough to suggest good membrane expression (Figure 26A and B, Table 6). Activation and steady-state fast inactivation properties of all tagged-channels did not differ from non-tagged channels, validating our *in-silico* predictions (Figure 26C-H, Table 7 and Table 8). None of the HA-tagged MI constructs showed currents (Figure 26B).

Table 6 – Current densities of wild-type hNa$_v$1.7 Tet-on or hNa$_v$1.7 M899I Tet-on with or without HA tags stably expressed in HEK293-Flp-in™ cells. * $p<0.05$ compared to non-fused wild-type hNa$_v$1.7 Tet-on. CI is 95% confidence interval of the mean. n is the number of patched cells used for analysis. Control are cells not activated by addition of doxycycline.

Channel	Current Densities (mean±95% CI, n)
hNa$_v$1.7 Tet-on (WT$_{TO}$)	602.4±144.8 pA/pF, n=25
hNa$_v$1.7 Tet-on HA-C terminus (WT$_{HACterm,TO}$)	294.7±182.2 pA/pF, n=15
hNa$_v$1.7 Tet-on P148-HA-P149 (WT$_{HAext1,TO}$)	325.3±87.8 pA/pF, n=15
hNa$_v$1.7 Tet-on L280-HA-E281 (WT$_{HAext2,TO}$)	529.7±415.2 pA/pF, n=5
hNa$_v$1.7 Tet-on L293-HA-E294 (WT$_{HAext3,TO}$)	252.5±112.2 pA/pF, n=26
hNav1.7 M899I Tet-on (MI$_{TO}$)	24.2±4.1 pA/pF, n=10 *
hNa$_v$1.7 M899I Tet-on HA-C terminus (MI$_{HACterm,TO}$)	20.4±2.4 pA/pF, n=4 *
hNa$_v$1.7 M899I Tet-on P148-HA-P149 (MI$_{HAext1,TO}$)	25.5±8.1 pA/pF, n=10 *
hNa$_v$1.7 Tet-on M899I L280-HA-E281 (MI$_{HAext2,TO}$)	26.4±24.2 pA/pF, n=5 *
hNa$_v$1.7 M899I Tet-on L293-HA-E294 (MI$_{HAext3,TO}$)	26.0±6.4 pA/pF, n=10 *
hNa$_v$1.7 Tet-on Φ doxycycline (Control)	32.2±3.7 pA/pF, n=21 *

Table 7 – Voltage-dependence of activation parameters of wild-type hNa$_v$1.7 Tet-on with or without HA tags stably expressed in HEK293-Flp-in™ cells. * $p<0.05$ compared to non-fused wild-type hNa$_v$1.7 Tet-on. CI is 95% confidence interval of the mean. n is the number of patched cells used for analysis.

Channel	$V_{1/2,act}$ (mean±95% CI, n)	$slope_{act}$ (mean±95% CI, n)
hNa$_v$1.7 Tet-on (WT$_{non\text{-}tagged,TO}$)	-21.0±2.0mV, n=22	7.5±0.4, n=22
hNa$_v$1.7 Tet-on HA-C terminus (WT$_{HACterm,TO}$)	-19.1±2.0mV, n=16	7.5±0.8, n=16
hNa$_v$1.7 Tet-on P148-HA-P149 (WT$_{HAext1,TO}$)	-20.9±1.2mV, n=13	8.2±0.6, n=13
hNa$_v$1.7 Tet-on L280-HA-E281 (WT$_{HAext2,TO}$)	-25.4±2.9mV, n=5	7.6±1.5, n=5
hNa$_v$1.7 Tet-on L293-HA-E294 (WT$_{HAext3,TO}$)	-19.4±2.0mV, n=24	7.8±0.5, n=24

Table 8 – Voltage-dependence of steady-state fast inactivation parameters of wild-type hNa$_v$1.7 Tet-on with or without HA tags stably expressed in HEK293-Flp-in™ cells. * $p<0.05$ compared to non-fused wild-type hNa$_v$1.7 Tet-on. CI is 95% confidence interval of the mean. n is the number of patched cells used for analysis.

Channel	$V_{1/2,ssfi}$ (mean±95% CI, n)	$slope_{ssfi}$ (mean±95% CI, n)
hNa$_v$1.7 Tet-on (WT$_{non\text{-}tagged,TO}$)	-76.2±3.4mV, n=22	5.4±0.3, n=22
hNa$_v$1.7 Tet-on HA-C terminus (WT$_{HACterm,TO}$)	-72.2±2.7mV, n=15	5.0±0.4, n=15
hNa$_v$1.7 Tet-on P148-HA-P149 (WT$_{HAext1,TO}$)	-75.2±1.8mV, n=13	7.0±0.5, n=13 *
hNa$_v$1.7 Tet-on L280-HA-E281 (WT$_{HAext2,TO}$)	-81.0±7.5mV, n=5	6.9±2.0, n=5
hNa$_v$1.7 Tet-on L293-HA-E294 (WT$_{HAext3,TO}$)	-71.4±2.7mV, n=24	4.9±0.3, n=24

After validating the expression of the tagged channels in the cells, immunostaining was performed by Dr. Anika Neureiter (Institute for Neurophysiology, Uniklinik RWTH Aachen, Germany) in a non-permeabilized manner using primary antibodies targeting the HA tag (Cell Signalling Technologies, #3742S) and secondary antibodies with a fluorophore targeting the primary antibody (Life Technologies, #A-21429, Alexa Flour 555). DAPI (NucBlue Fixed Cell

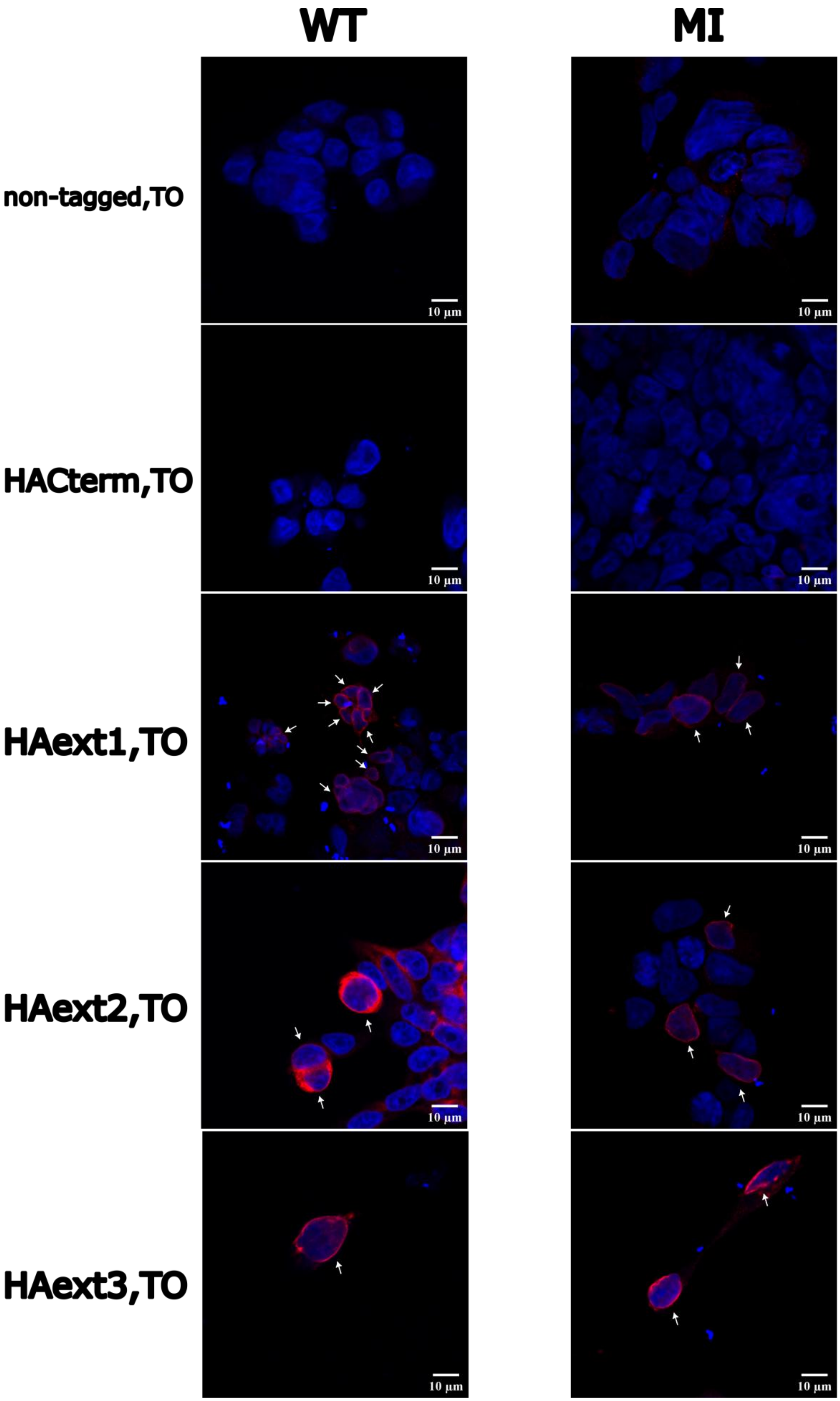
WT
MI
non-tagged,TO
HACterm,TO
HAext1,TO
HAext2,TO
HAext3,TO
10 µm

Figure 27 – hNa$_v$1.7 M899I is expressed in the cell membrane. Confocal imaging of HEK293 Flp-in™ stable cell lines expressing either hNa$_v$1.7 WT or hNa$_v$1.7 MI either without or with HA tags in the C-terminus or extracellular regions. The first column is hNa$_v$1.7 WT while the second column is hNav1.7 MI. The rows from the top represent untagged (non-tagged,TO), C-terminal HA tag (HACterm,TO) and extracellularly HA-tagged (HAext1,TO, HAext2,TO, HAext3,TO) channels. Immunostaining was done by Dr. Anika Neureiter (Institute for Neurophysiology, Uniklinik RWTH Aachen, Germany) without permeabilization using primary and secondary antibodies targeting the HA tag and the primary antibody respectively. The fluorophore of the secondary antibody emits red light. A **red color** represents the HA tag while a **blue color** represents the nucleus stained by DAPI. Untagged channels show no HA staining as expected. C-terminally tagged channels also show no staining since the membrane is not permeabilized, preventing antibodies from entering inside the cell to bind to the HA-tag. Extracellularly tagged WT and MI channels show good expression of channels in the membrane (red rings, marked with a white arrow). Thus, MI channels do not disrupt trafficking of the channel to the cell membrane.

ReadyProbes Reagenz, Life Technologies, #R37606) stained for the nucleus and is seen as a blue color in the confocal images (Figure 27). The $WT_{HAext1,TO}$, $WT_{HAext2,TO}$, and $WT_{HAext3,TO}$ were positive controls and $WT_{HACterm,TO}$ and $MI_{HACterm,TO}$ constructs acted as a negative control, since the HA tag is located intracellularly and cannot be accessed without permeabilization of the membrane. $WT_{non\text{-}tagged,TO}$ and $MI_{non\text{-}tagged,TO}$ also act as negative controls as they do not have any HA tags to target. No red signal is observed in the non-tagged and C-terminal tagged WT and MI cell lines (Figure 27). Extracellularly HA-tagged WT channels all showed good membrane staining, seen as red rims around the boundary of the cell (Figure 27, WT column, white arrows). Extracellularly HA-tagged MI channels also showed relatively good membrane staining (Figure 27, MI column, white arrows). This suggests that MI is expressed in the cell membrane and causes its LoF effect via gating defects.

3.1.5 hNa$_v$1.7 p.M899I causes pore collapse *in silico*

My experimental results show that MI is expressed in the membrane and thus causes its LoF effect most likely via alteration of Na$_v$ gating. To decipher the structural details of such a gating defect, I used coarse-grained molecular dynamics simulations (CG-MD) of the hNa$_v$1.7 structure solved by (Shen et al., 2019) (WT, PDB ID 6J8G) in the fast-inactivated state. In this structure, the VSDs were in the activated state, the pore was closed and the IFM motif bound. The mutation (MI) was introduced via Modeller v9.23 (Webb and Sali, 2016). The top model was chosen as the model with the most negative DOPE-HR score. MD simulations provide us with the tools to understand how mutations can alter the dynamic properties of a protein structure. CG-MD does this by increasing simulation time, at the expense of the resolution of the channel. Given the buried location of the residue in PM2, we decided to focus on global properties that describe the pore of the channel, namely the pore radius. This allowed us to overcome the limitation of not having an atomic resolution.

CG-MD was run using the Martini v3 forcefield (Souza et al., 2021) and GROMACS 2022 (Abraham et al., 2015; Bauer et al., 2022). WT was coarse-grained using Martinize2 and embedded into the membrane-solvent system (100% POPC, 150mM NaCl) using insane. To account for the randomness of the software, three separate unbiased production runs, each lasting 4µs were run for WT and MI. The protocol is described in detail in Section 2.7 (Figure 18). All six simulation runs underwent successful minimization and equilibration, with minimization of the potential energy and subsequent stabilization of temperature, pressure and volume at every step of equilibration. The average backbone RMSD of the structures also stabilized in the production run at ~ 3.5°, with no important differences in the average RMSF (Appendix Figure S1). The first 1µs was removed from analysis, and the last 3µs of each run was combined to give a total of 9µs for both structures (WT and MI each have a total of 9µs). The combined trajectory was corrected for periodic boundary conditions, roto-translations and down-sampled to give a total of 900 frames for each structure. The pore radius of each of the 900 frames in WT as well as MI were calculated using HOLE2.0 (Smart et al., 1993). Once calculated, the pore radii were plotted using an in-house script written in Python3.10. In the end, each individual frame was made up of 125 pore points each spaced at 0.25A°. The pore radius was measured starting from 17A° below the center-of-geometry (0A°) to 15A° above the center-of-geometry. This resulted in 125 different distributions of pore radii for each pore point, with each distribution representing the fitted gaussian kernel of the histogram of the 900 pore radii at that pore point. This means that showing the average pore radius will result in losing a lot of information corresponding to these distributions. To account for this, I used a Kullback-Leiber (KL) divergence (Chapter 2, equation 7) measure to understand if the distribution of the pore radius over time at a pore point in WT is different from that in MI. Using this measure, one can pinpoint the regions that showcase the maximum deviation in the distribution (magnitude of difference) and use the mean values to attribute the direction of this deviation (increase or decrease in pore radius).

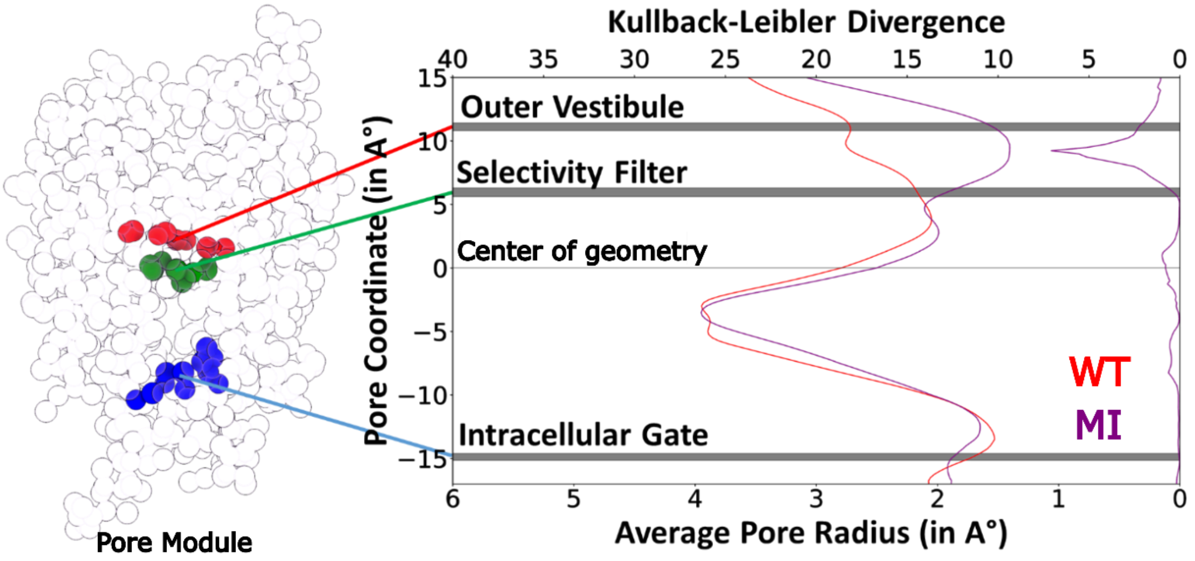

Figure 28 – hNa$_v$1.7 M899I disrupts the outer pore geometry. Mean pore radius (bottom x-axis) vs pore coordinate for the 900 frames obtained after downsampling the trajectories obtained by CGMD of hNa$_v$1.7 WT (WT, red line) and hNa$_v$1.7 M899I (MI, purple line). The pore module is shown on the far left to highlight where the outer vestibule (red spheres), selectivity filter (green spheres) and the intracellular gate (blue spheres) lie on the graph. The pore radius ranges from 0A° to 6A°, while the pore coordinate is centered at the center-of-geometry (0A°), going from 15A° extracellulary to 17A° (negative) intracellularly. The top x-axis represents the KL-divergence between the pore radius distributions at each pore point of MI against WT. This is shown as a purple line in the far right of the graph against the pore coordinate. A clear peak is observed at the outer pore near the outer vestibule, showcasing that the pore radius in this region of MI is significantly different from WT (magnitude of the KL-divergence) and is also much smaller (reduced average pore radius value near the outer vestibule).

The WT showed an average pore radius that is comparable to a fast-inactivated channel – a closed intracellular gate, a very large central cavity and a very narrow selectivity filter (Figure 28, **red line**). The outer vestibule opens to an almost funnel-like shape, showcasing how the geometry allows it to collect cations to push towards the selectivity filter. The MI, however had an altered pore geometry– while the radii at the intracellular gate, selectivity filter and central cavity region remained similar to WT, there was a large bottleneck observed in the average pore radius at the outer vestibule region (Figure 28, **purple line**). This can accurately be attributed to a difference in the distribution and not an artefact in the average due to outliers, as is shown by a very large KL-divergence value (Figure 28, **purple peak**). Our simulations seem to suggest that MI causes the rearrangement of the outer pore geometry and bottleneck the outer vestibule, preventing any ions from being able to reach the selectivity filter.

3.1.6 hNav1.7 M899 is robust to mutations

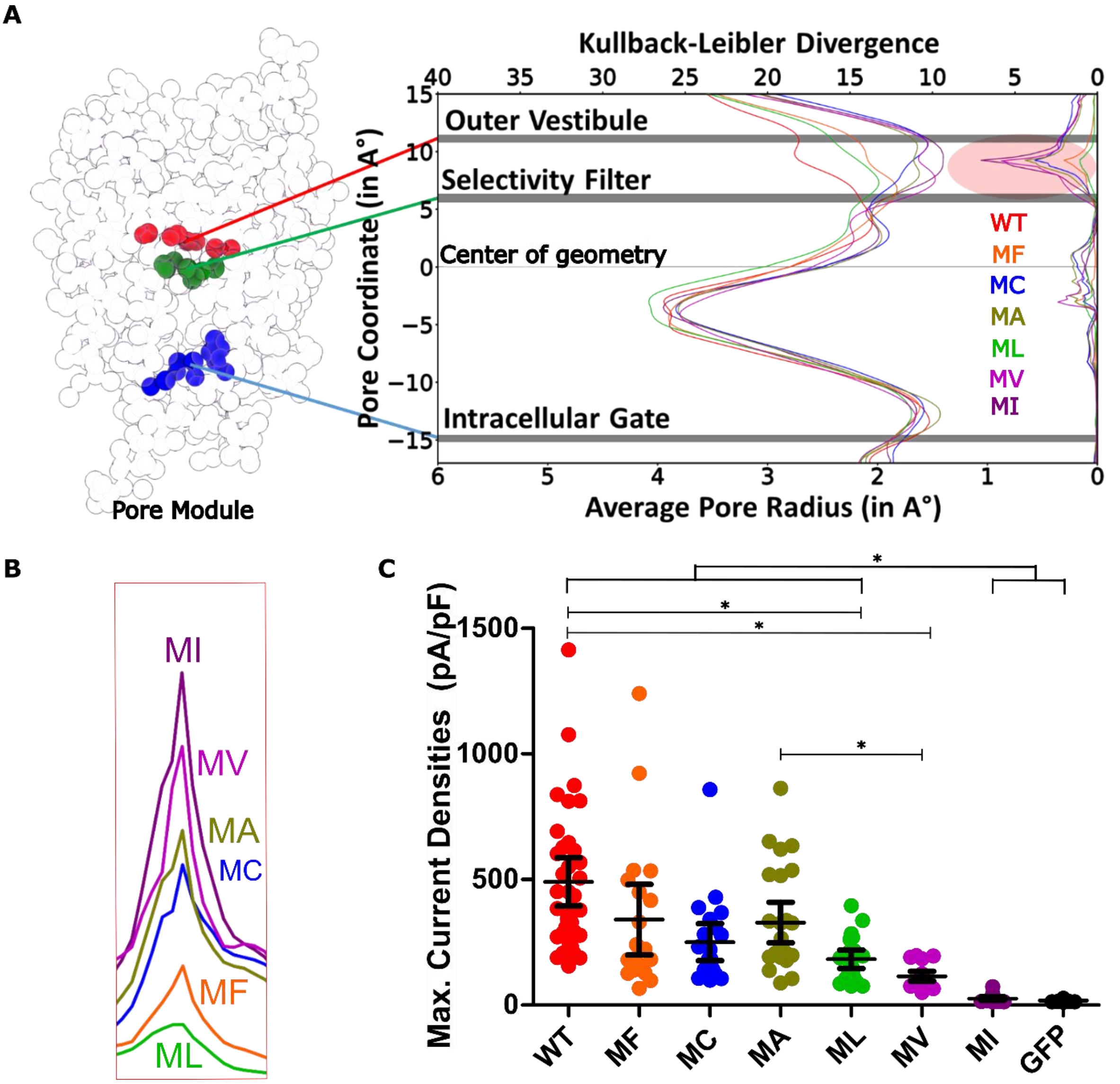

Figure 29 – hNa$_v$1.7 M899 is robust to mutations. (A) Mean pore radius (bottom x-axis) vs pore coordinate for the 900 frames obtained after downsampling the trajectories obtained by CGMD of hNa$_v$1.7 WT (WT) and all mutants hNa$_v$1.7 M899A/C/F/I/L/V (MA, MC, MF, MI, ML and MV respectively). The pore module is shown on the far left to highlight where the outer vestibule (red spheres), selectivity filter (green spheres) and the intracellular gate (blue spheres) lie on the graph. The pore radius ranges from 0A° to 6A°, while the pore coordinate is centered at the center-of-geometry (0A°), going from 15A° extracellulary to 17A° (negative) intracellularly. The top x-axis represents the KL-divergence between the pore radius distributions at each pore point of the various mutants against WT. This is shown as colored lines in the far right of the graph against the pore coordinate (red circle). Peaks of varying magnitudes are observed at the outer pore near the outer vestibule. **(B)** A close-up of the peaks near the outer vestibule showcasing that the pore radii of the mutants show varying magnitudes when compared against WT. MI has the largest deviation, followed by MV, MA and MC and MF and ML having the least deviation from the WT. **(C)** Absolute values of the maximum current densities of HEK293t cells transfected with either WT, any of the other six mutants or fluorescent marker pMaxGFP (GFP, used as a negative control). Maximum current densities are the maximal absolute value of the current densities observed at any of the applied voltage steps. The current densities closely follow the predicted bottleneck at the outer pore. MV has the second highest bottleneck and subsequently the lowest current densities other than MI. All other mutations show currents to varying magnitudes, with MF having the closest currents to WT. This showcases the robustness of the position to being mutated despite being a fully conserved residue. * $p<0.05$.

Given the fully conserved nature of this position and the collapse of the outer pore geometry observed in our simulations when replacing M with I, I wanted to test if such a collapse occurs by the introduction of other aliphatic amino acids that are small and linear (A, C), aromatic (F), or branched (V, L). I used the CGMD protocol described in section 2.7 (Figure 18) and measured pore radii and KL-divergence to check for pore geometry changes. All the 5 amino acids used (A, C, F, V, L) showed varying degrees of outer geometry collapse (Figure 29A and B). By observing the average pore radii, I saw that MI has the smallest radius at the outer vestibule region, followed by MV, MA, MC, ML and MF (Figure 29A). ML and MF were the closest to the WT, with the least bottlenecking at the outer pore. The KL-divergence gives us a better understanding of how different the distributions are (Figure 29A and B). A close-up of the KL-divergence shows that MI has the furthest deviation from the WT distribution, followed closely by MV. MC and MA seem to have a slight deviation that is not as strong as MV, and ML and MF have the least deviation, essentially similar as the WT (Figure 29B).

I hypothesized that if the extent of the bottleneck is positively correlated to the amount of current we can measure, then we should also see such a trend in our whole-cell patch clamp experiments. In other words, MV should have low but observable currents, followed by MC and MA, with ML and MV having currents similar to WT. To do so, I employed whole-cell patch clamping of HEK293t cells transfected with either of the mutants and the GFP as a marker protein. The activation protocol described in Section 2.2 Figure 10 was used to elicit current responses to voltage changes. I saw that the trend observed in our simulations is closely replicated in my experiments. All five mutants show currents, with MV being the lowest. ML however was the second lowest, with MC, MA and MF having currents not very different from WT (Figure 29C, Table 9). This validated my hypothesis that collapse of the outer pore is a proxy for blocking ion conduction and adds more credence to this as being a potential patho-mechanism of MI causing LoF of $Na_v1.7$.

Table 9 – Current densities of $hNa_v1.7$ WT, corresponding M to I,A,C,F,L or V mutations or only the fluorescent protein GFP as a negative control transiently transfected in HEK293t cells. * $p<0.05$ compared to $hNa_v1.7$ WT. CI is 95% confidence interval of the mean. n is the number of patched cells used for analysis.

Channel	**Current Densities (mean±95% CI, n)**
$hNa_v1.7$ WT (WT)	490.3±96.4 pA/pF, n=35
$hNa_v1.7$ M899I (MI)	26.1±6.4 pA/pF, n=21 *
$hNa_v1.7$ M899A (MA)	328.4±80.7 pA/pF, n=26
$hNa_v1.7$ M899C (MC)	250.4±74.0 pA/pF, n=22
$hNa_v1.7$ M899F (MF)	340.0±140.2 pA/pF, n=20
$hNa_v1.7$ M899L (ML)	182.6±36.6 pA/pF, n=23 *
$hNa_v1.7$ M899V (MV)	114.6±19.4 pA/pF, n=21 *
pMaxGFP (GFP)	18.0±1.9 pA/pF, n=19 *

3.1.7 FA_{D1}, FA_{D3} and FA_{D4} cause complete loss of function

Based on our results so far, I came to two observations regarding the M899 residue – (1) it is quite lenient to having any hydrophobic amino acid other than I and (2) it is fully functional when replaced with a phenylalanine (F). The second observation was especially interesting, since the corresponding residue in the other three domains are a F and located in a very similar position in the 3D structure (Figure 30A and B). I wanted to therefore test if the other three residues are also robust to mutations. Dawi Bajunaid (Institute for Neurophysiology, Uniklinik RWTH Aachen, Germany) used mutations that contain an alanine substitution of the three domains (FA_{D1}, FA_{D3}

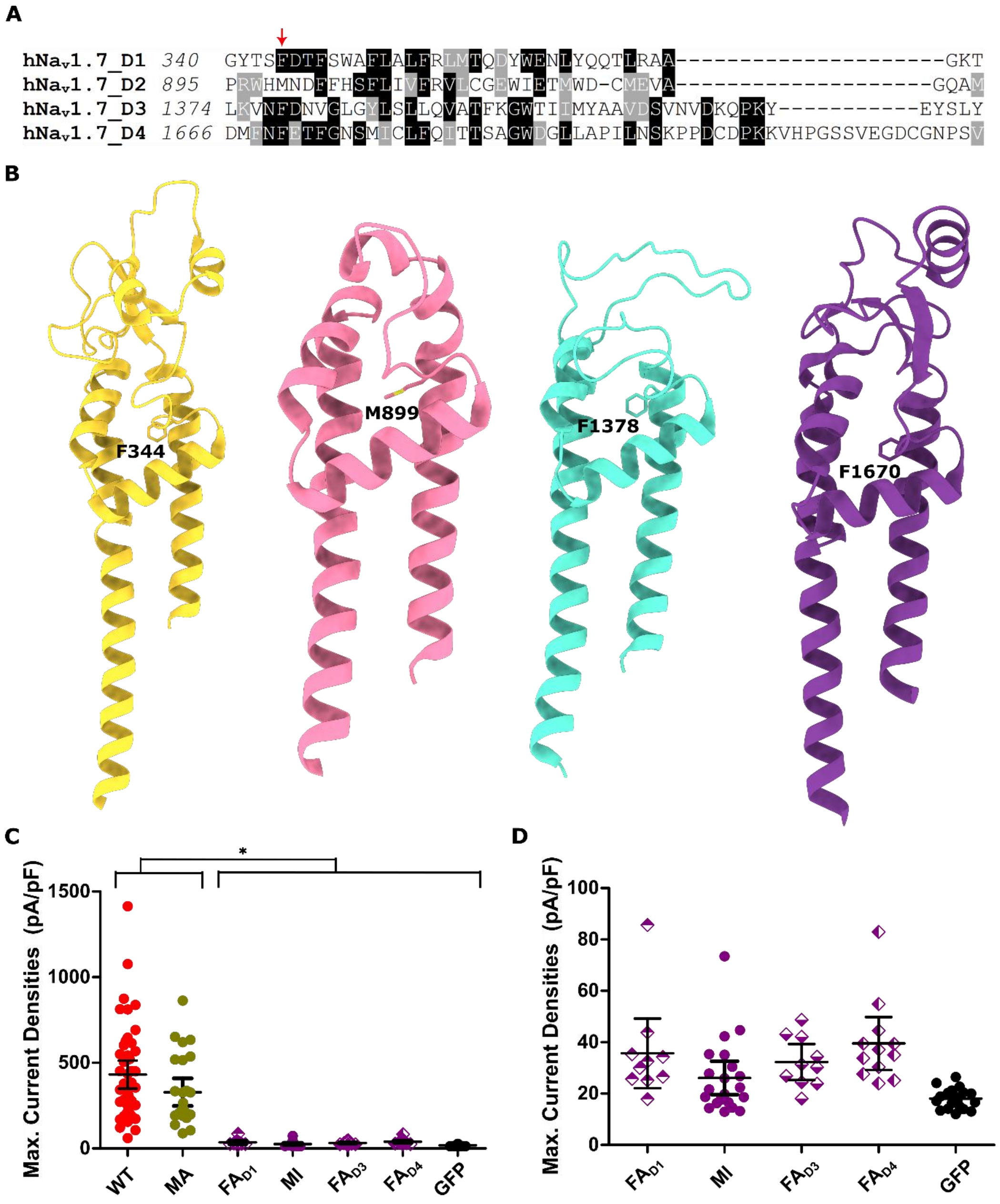

Figure 30 – hNa$_v$1.7 F344, F1378 and F1670 are very sensitive to mutations. (A) Multiple sequence alignment of the 4 domains (D1-D4) of the hNa$_v$1.7. Only the region around M899 and the equivalent residues in the other domains (**red arrow**) is shown for clarity. The letters represent the one letter codes for each amino acid and the numbers represent the starting number of each sequence. **Dark** boxes show fully conserved residues, while **grey** boxes show partially conserved residues, and non-shaded boxes show non-conserved residues. D2 contains a methionine (M899) while the other domains contain a phenylalanine (F344, F1378 and F1670). **(B)** 3D view of PM1 to PM4 showcasing the location of F344, M899, F1378 and F1670. All 4 residues are located in the disordered membrane re-entrant loop region immediately before the P1 helix. **(C)** Absolute values of the maximum current densities of HEK293t cells transfected with either hNa$_v$1.7 WT (WT), hNa$_v$1.7 M899A (MA), hNa$_v$1.7 F344A (FA$_{D1}$), hNa$_v$1.7 M889I (MI), hNa$_v$1.7 F1378A (FA$_{D3}$), hNa$_v$1.7 F1670A (FA$_{D4}$) or fluorescent marker pMaxGFP (GFP, used as a negative control). Maximum current densities are the maximal absolute value of the current densities observed at any of the applied voltage steps. Alanine mutation of M899 does not prevent channel function while alanine mutation of the equivalent residues in the other three domains completely abolish function. * $p<0.05$. **(D)** A closer look at the absolute values of the maximum current densities of FA$_{D1}$, MI, FA$_{D3}$, FA$_{D4}$ and GFP. Alanine mutations of the residues equivalent to M899 in the other three domains completely abolish function, similar to the LoF phenotype observed in MI. All experiments and analyses involving FA$_{D1}$, FA$_{D3}$ and FA$_{D4}$ were performed by Dawi Bajunaid (Institute for Neurophysiology, Uniklinik RWTH Aachen, Germany).

and FA_{D4}) to see using whole-cell patch clamp if they will still generate robust currents when expressed in HEK293t cells. Given that MA also showed currents, I expected a similar outcome in the other three domains. None of FA_{D1}, FA_{D3} or FA_{D4} showed significant currents when expressed in HEK293t cells (Figure 30C and D, Table 10). This points to a potential asymmetry that exists between the four different domains.

*Table 10 – Current densities of $hNa_v1.7WT$, M899I, M899A, alanine mutations of the corresponding residue in the other three domains or only the fluorescent protein GFP as a negative control transiently transfected in HEK293t cells. * $p<0.05$ compared to $hNa_v1.7$ WT. CI is 95% confidence interval of the mean. n is the number of patched cells used for analysis.*

Channel	Current Densities (mean±95% CI, n)
$hNa_v1.7$ WT (WT)	490.3±96.4 pA/pF, n=35
$hNa_v1.7$ M899I (MI)	26.1±6.4 pA/pF, n=21 *
$hNa_v1.7$ M899A (MA)	328.4±80.7 pA/pF, n=26
$hNa_v1.7$ F344A (FA_{D1})	35.7±13.5 pA/pF, n=10 *
$hNa_v1.7$ F1378A (FA_{D3})	32.3±7.0 pA/pF, n=10 *
$hNa_v1.7$ F1670A (FA_{D4})	39.5±10.3 pA/pF, n=12 *
pMaxGFP (GFP)	18.0±1.9 pA/pF, n=19 *

3.1.8 Ex11del removes 96 amino acids from D1-D2

MI causes a complete LoF of $Na_v1.7$, by disrupting the geometry of the outer pore while not affecting trafficking of the channel. The patient, however, also shows another allele with a splice

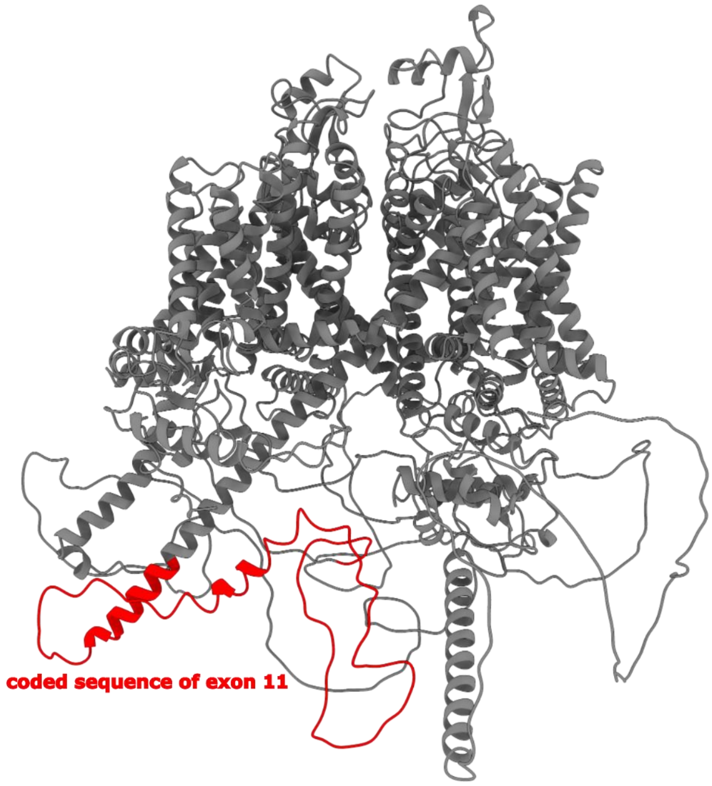

Figure 31 – deletion of exon 11 in $hNa_v1.7$ removes 96 amino acids from D1-D2. The full-length 3D structure of $hNa_v1.7$ obtained from the Alphafold Database (ID: AF-Q15858-F1). Alphafold3 solves the entire protein structure using deep learning methodologies (Abramson et al., 2024). The protein region translated from exon 11 is marked in red. Exon 11 translates for 96 amino acids in D1-D2. Skipping of exon 11 removes this part of the protein. This region contains amino acids shown to be involved in protein dimerization via the 14-3-3 protein (Clatot et al., 2017).

variant hNav1.7 c.1602+2del2, deleting the splice donor site and skipping exon 11 (ex11del). The codon sequence of exon 11 codes for 96 amino acids (residue 439-534) located in D1-D2 (Figure 31). These amino acids contain a set of residues whose equivalent locations in $Na_v1.5$ have been shown to be important for Na_v dimerization via the 14-3-3 protein (Clatot et al., 2017).

3.1.9 Ex11del is completely functional *in vitro*

To test if removal of a large chunk of the protein results in changes in gating properties, I transfected the ex11del plasmid in HEK293t cells with GFP as a marker protein and performed whole-cell patch clamp experiments. To my surprise, the ex11del showed highly robust inward currents, similar in magnitude to WT (Figure 32A and B, Table 11). A small but significant depolarizing shift of 3.7mV in the voltage-dependence of activation of ex11del compared to WT was observed (p<0.05; Figure 32C and D, Table 12). The voltage sensitivity, described by the slope of the G-V curve, was reduced in ex11del as seen by the shallow slope values (p<0.05; Figure 32E, Table 12). No changes in the voltage-dependence of steady-state fast inactivation were observed (Figure 32F-H, Table 13). Ex11del had a slower time to peak and a slower time constant for fast-inactivation decay at most of the voltage steps that elicited peak currents (p<0.05; Figure 32I-J). In summary, Ex11del was a fully functional channel with altered activation properties leaning towards a LoF phenotype.

*Table 11 – Current densities of $hNa_v1.7$WT, M899I, c.1602+2delT or only the fluorescent protein GFP as a negative control transiently transfected in HEK293t cells. * p<0.05 compared to $hNa_v1.7$ WT. CI is 95% confidence interval of the mean. n is the number of patched cells used for analysis.*

Channel	Current Densities (mean±95% CI, n)
$hNa_v1.7$ WT (WT)	490.3±96.4 pA/pF, n=35
$hNa_v1.7$ M899I (MI)	26.1±6.4 pA/pF, n=21 *
$hNa_v1.7$ c.1602+2delT (ex11del)	574.2±235.0 pA/pF, n=19
pMaxGFP (GFP)	18.0±1.9 pA/pF, n=19 *

*Table 12 – Voltage-dependence of activation parameters of wild-type $hNa_v1.7$ or $hNa_v1.7$ c.1602+2delT transiently transfected in HEK293t cells. * p<0.05 compared to wild-type $hNa_v1.7$. CI is 95% confidence interval of the mean. n is the number of patched cells used for analysis.*

Channel	$V_{1/2,act}$ (mean±95% CI, n)	$slope_{act}$ (mean±95% CI, n)
$hNa_v1.7$ WT (WT)	-23.5±2.2mV, n=35	8.6±0.4, n=35
$hNa_v1.7$ c.1602+2delT (ex11del)	-19.8±2.0mV, n=19 *	7.7±0.5, n=19

*Table 13 – Voltage-dependence of steady-state fast inactivation parameters of wild-type $hNa_v1.7$ or $hNa_v1.7$ c.1602+2delT transiently transfected in HEK293t cells. * p<0.05 compared to wild-type $hNa_v1.7$. CI is 95% confidence interval of the mean. n is the number of patched cells used for analysis.*

Channel	$V_{1/2,ssfi}$ (mean±95% CI, n)	$slope_{ssfi}$ (mean±95% CI, n)
$hNa_v1.7$ WT (WT)	-87.9±2.5mV, n=17	6.6±0.8, n=17
$hNa_v1.7$ c.1602+2delT (ex11del)	-83.5±5.2mV, n=11	8.2±1.8, n=11

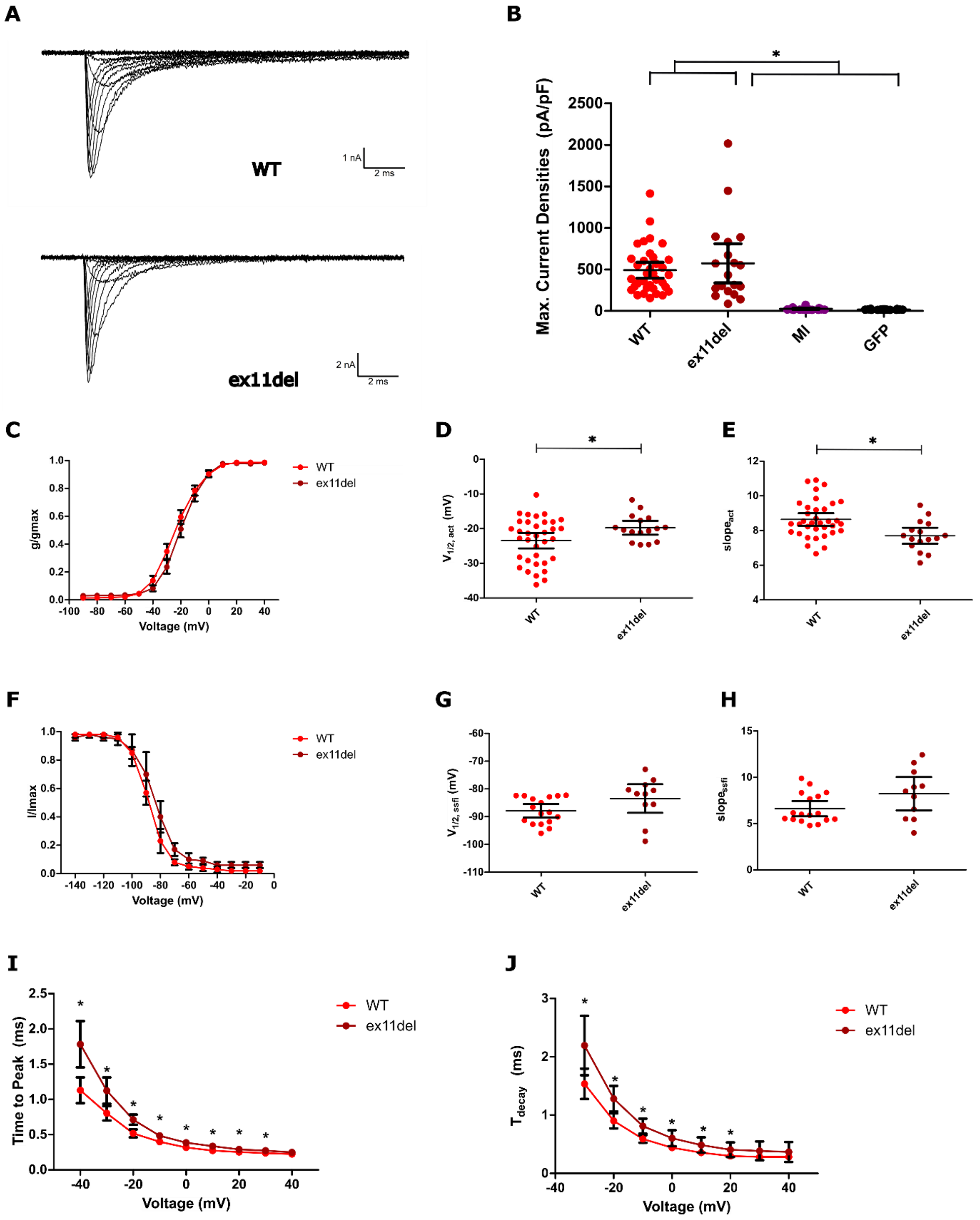

Figure 32 – Exon11del is highly functional with altered activation properties. (A) Representative traces of hNa$_V$1.7 WT (WT) and hNa$_V$1.7 c.1602+2delT that results in the skipping of exon 11 (ex11del) obtained from whole-cell patch clamp of transfected HEK293t cells. Both WT and ex11del show robust inward sodium currents that are indistinguishable by eye. **(B)** Absolute values of the maximum current densities of HEK293t cells transfected with WT, ex11del, hNa$_V$1.7 M889I (MI) or only fluorescent marker pMaxGFP (GFP, used as a negative control). Maximum current densities are the maximal value of the current densities observed at any of the applied voltage steps. Ex11del does not alter the expression levels of Na$_V$1.7, being similar to WT and much higher than MI and GFP. * $p<0.05$. **(C)** Normalized conductance curves, **(D)** V$_{1/2,act}$ and **(E)** slope$_{act}$ for WT and ex11del. Loss of exon11 resulted in a depolarized V$_{1/2,act}$ and a relatively shallower slope$_{act}$. * $p<0.05$. **(F)** Normalized current curves **(G)** V$_{1/2,ssfi}$ and **(H)** slope$_{ssfi}$ for WT and ex11del. No significant changes were observed for any properties of the voltage-dependence of steady-state fast inactivation. **(I)** Time to peak and **(J)** onset of fast inactivation kinetics for WT and ex11del. No significant changes in the kinetic properties were observed. * $p<0.05$.

3.1.10 Co-expression of ex11del and MI reduces current levels *in vitro*

The functionality of ex11del raised an important question – will co-expression of ex11del and MI reduce current densities *in vitro* in a manner observed clinically in the patient as reduced pain sensitivity? To do this, I performed experiments where I co-transfected both ex11del and MI in varying proportions. The proportions were either 100% ex11del : 0% MI, 75% ex11del : 25% MI, 50% ex11del : 50% MI, 25% ex11del : 75% MI or 0% ex11del : 100% MI. The first condition acted as the positive control, while the last condition acted as a negative control.

Increasing amounts of MI decreased current densities, with a 50% increase in MI decreasing the current densities by ~50% (Figure 33, Table 14). Such decreases in current densities due to expression of a LoF variant can be caused by a "dominant negative effect" as a result of dimerization between the functional and non-functional protein (Clatot et al., 2017). The relationship between the increasing concentration of the non-functional protein (in our study the MI) and normalized current densities (between 0 and 1, with 1 representing the average current densities of only expressing the functional protein – in our study the ex11del) can be used to deduce if the reduction happens due to existence of monomeric forms of the protein, dimerization or oligomerization of the protein (for exact calculation see Section 2.4 Equation 4).

The reduction of current densities observed with increasing MI concentrations closely follows a linear form of decrease, suggesting that dimerization might not play a role in the observed reduction (Figure 33, Table 14).

Table 14 – Variation of normalized current densities when varying the quantity of hNa$_v$1.7 M899I co-transfected transiently with hNa$_v$1.7 c.1602+2delT in HEK293t cells. Quantities of the plasmid are normalized as ratios. Normalized current densities are normalized for each ratio to the highest value observed during recordings. Errors represent the standard error of mean (SEM). n represents the number of cells patched and used for analysis.

Ratio of hNa$_v$1.7 M899I (MI)	Ratio of hNa$_v$1.7 c.1602+2delT (ex11del)	Current densities (mean±SEM, n)	Normalized current densities (mean±SEM, n)
0 (0%)	1 (100%)	574.2±235.0 pA/pF, n=19	1.00±0.19, n=19
1 (25%)	4 (75%)	444.6±206.5 pA/pF, n=11	0.77±0.21, n=11
1 (50%)	1 (50%)	322.8±119.4 pA/pF, n=20	0.56±0.18, n=20
4 (75%)	1 (25%)	232.1±78.4 pA/pF, n=15	0.40±0.16, n=15
1 (100%)	0 (0%)	26.13±6.5 pA/pF, n=21	0.04±0.12, n=21

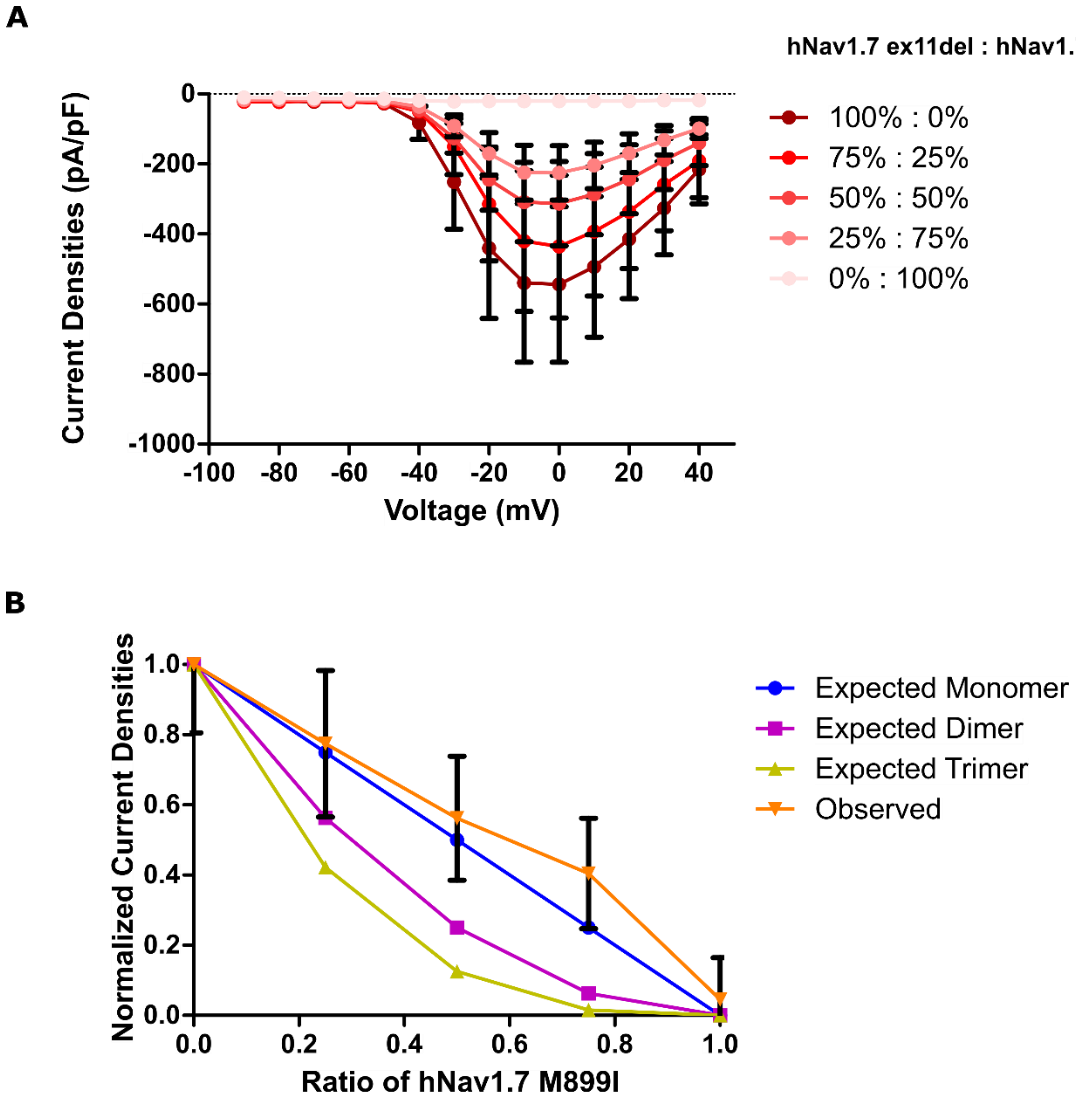

Figure 33 – Co-expression of ex11del and MI replicates clinical phenotype. (A) Current densities vs applied voltage for hNa$_v$1.7 c.1602+2delT that results in skipping of exon 11 (ex11del) and hNa$_v$1.7 M899I (MI) in the following ratios – 1:0 (100% ex11del and 0% MI), 1:4 (75% ex11del and 25% MI), 1:1 (50% ex11del and 50% MI), 4:1 (25% ex11del and 75% MI) and 0:1 (0% ex11del and 100% MI). Increasing the quantity of the LoF mutation MI reduced the mean current densities. **(B)** Normalized current densities vs normalized ratio of MI. The normalized average current densities were obtained by normalizing the maximal average current densities of each ratio group by the value obtained when only ex11del was transfected (1:0 ratio). Errors bars represent the standard error of mean. Theoretical relations between the two are shown for monomeric, dimeric and trimeric configurations of a protein as calculated by Equation 4. Dominant negative effects can only take place when Na$_v$s interact in a dimeric manner. The observed relation between current densities and quantity of a LoF variant (in our case the MI) follows closely the theoretical line for a monomeric configuration, suggesting that the decrease in the current densities is likely not linked to dimerization of the Na$_v$s.

3.2 hNa$_v$1.7 p.M1628K Disrupts Fast-Inactivation by Preventing IFM Motif Binding

Having uncovered details on how naturally occurring mutations prevent channel functioning and ultimately lead to a loss of channel function (LoF), it is also important to look at the other side of the coin. There also exist naturally occurring mutations that can pathologically increase the functionality of the channel (gain of function or GoF), causing pain disorders where patients feel extreme levels of pain with physiologically benign stimuli. Such GoF mutations work via different mechanisms and uncovering them can help us better understand channel gating. To move along this direction, I utilize another naturally occurring mutation hNav1.7 p.M1628K, that causes paroxysmal extreme pain disorder (PEPD) in a patient, with Aylin Kesdoğan (Institute for Neurophysiology, Uniklinik RWTH Aachen, Germany) showing the mutation impaired fast inactivation when electrophysiologically characterized *in vitro*.

I show first with the utilization of molecular visualization that the M1628 residue is fully conserved along with the other PEPD-causing M1627 residue located one amino acid downstream across all nine human Na$_v$ subtypes, with both being located in the S4-S5 linker of D4 (D4 S4-S5), in close proximity to the helical part of D3-D4 and forming various hydrophobic interactions **(Section 3.2.1)**. To better understand dynamic properties of these mutants, I utilize coarse-grained molecular dynamics with modified restraints to enable increased flexibility. I show that M1627K and M1628K exert their effects through two different mechanisms, altering the orientation and distance between the helical region of D3-D4 and D4 S4-S5 respectively **(Section 3.2.2-3.2.3)**. Both inevitably are predicted to lead to the same result, disrupting the binding of the IFM motif - the motif important for fast inactivation -to its binding site **(Section 3.2.4)**.

In summary, I show that both helix distance and orientation are important pre-requisites to enable strong binding of the IFM motif, and disruption of either of the two properties can lead to impaired fast inactivation.

3.2.1 hNa$_v$1.7 M1627 and M1628 form multiple interactions with D3-D4

hNa$_v$1.7 M1628K was shown to depolarize the voltage-dependence of steady-state fast inactivation by Aylin Kesdoğan (Institute for Neurophysiology, Uniklinik RWTH Aachen, Germany), hinting at a disruption of the fast inactivation process (Figure 7). This was a gating change comparable to hNa$_v$1.7 M1627K (Dib-Hajj et al., 2008). Given the proximity of both residues and the similarity in the gating changes, I aimed to understand the structural location of these residues. Both M1627 and M1628 are fully conserved across all nine human Na$_v$ subtypes (Figure 34A) and located in the S4-S5 helix in D4 (D4 S4-S5), pointing their sidechains towards the helical region of D3-D4 (Figure 34B inset). Both residues make extensive interactions with various hydrophobic residues in the helical region of D3-D4. A mutation to lysine could disrupt this hydrophobic stacking between the two helices.

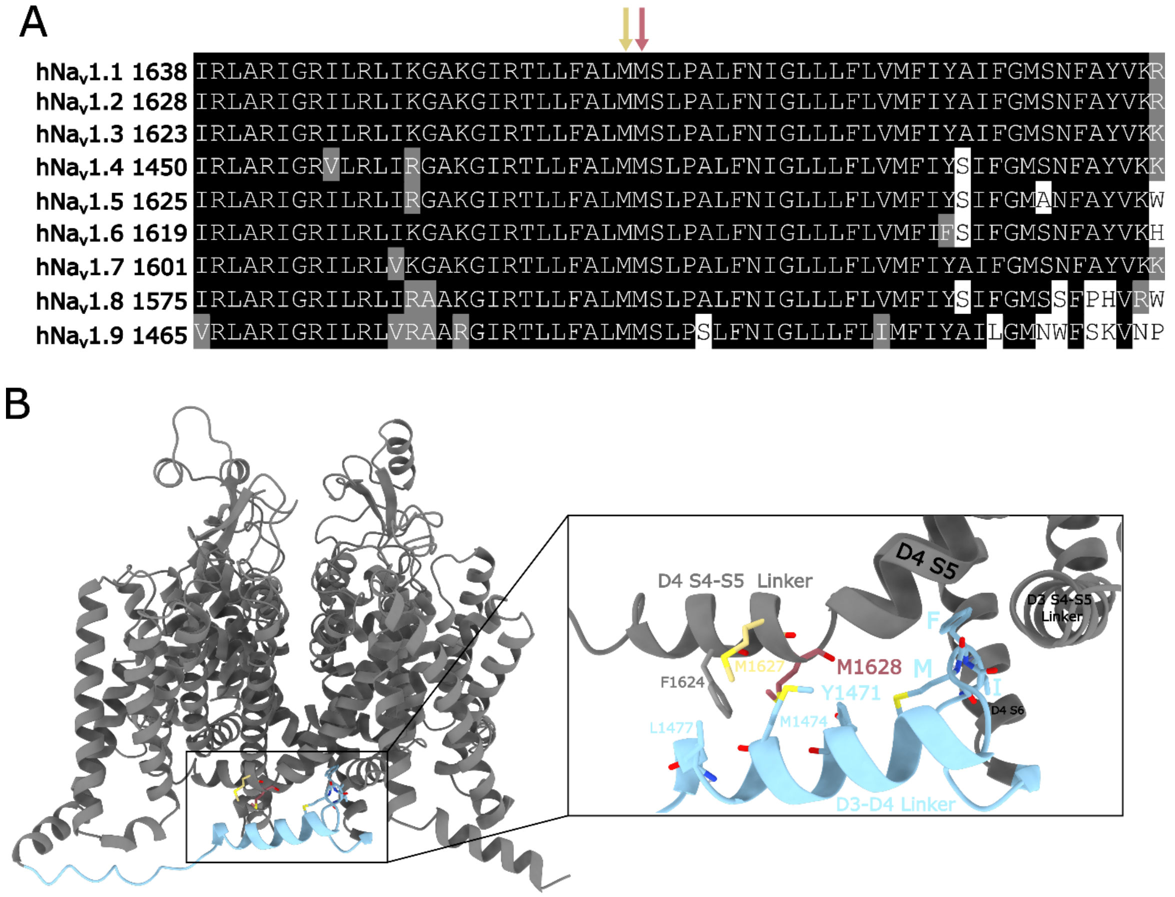

```
hNav1.1 1638 IRLARIGRILRLIKGAKGIRTLLFALMMSLPALFNIGLLLFLVMFIYAIFGMSNFAYVKR
hNav1.2 1628 IRLARIGRILRLIKGAKGIRTLLFALMMSLPALFNIGLLLFLVMFIYAIFGMSNFAYVKR
hNav1.3 1623 IRLARIGRILRLIKGAKGIRTLLFALMMSLPALFNIGLLLFLVMFIYAIFGMSNFAYVKK
hNav1.4 1450 IRLARIGRVLRLIRGAKGIRTLLFALMMSLPALFNIGLLLFLVMFIYSIFGMSNFAYVKK
hNav1.5 1625 IRLARIGRILRLIRGAKGIRTLLFALMMSLPALFNIGLLLFLVMFIYSIFGMANFAYVKW
hNav1.6 1619 IRLARIGRILRLIKGAKGIRTLLFALMMSLPALFNIGLLLFLVMFIFSIFGMSNFAYVKH
hNav1.7 1601 IRLARIGRILRLVKGAKGIRTLLFALMMSLPALFNIGLLLFLVMFIYAIFGMSNFAYVKK
hNav1.8 1575 IRLARIGRILRLIRAAKGIRTLLFALMMSLPALFNIGLLLFLVMFIYSIFGMSSFPHVRW
hNav1.9 1465 VRLARIGRILRLVRAARGIRTLLFALMMSLPSLFNIGLLLFLIMFIYAILGMNWFSKVNP
```

Figure 34 - hNa$_v$1.7 M1627 and M1628 are located close to the fast inactivation region. (A) Multiple sequence alignment of all nine human subtypes of voltage-gated sodium channels (hNa$_v$1.1-1.9). A **black shade** represents full conservation, **grey shade** represents partial conservation, and no shade represents non-conservation. The sequences were loaded from the Uniprot database. The previously studied M1627 (Dib-Hajj et al., 2008) and the novel M1628 residue characterized in this study highlighted by a **yellow** and **pink** arrow respectively. Both residues are fully conserved across all the human subtypes. **(B)** Location of the mutations in the recent high resolution cryo-EM structure of hNa$_v$1.7 in the fast-inactivated state (Huang et al., 2022; PDB ID 7W9K). The residues **M1627** and **M1628** are in the S4-S5 linker of domain 4 (D4 S4-S5). These residues also pack with the helical region of the linker between domain 3 and 4 (D3-D4 Linker or D3-D4). Inset shows the hydrophobic residues in the proximity of **M1627** and **M1628** like **Y1471, M1474** and **L1477** in the helical region of D3-D4 and **F1624**, **M1627** and **M1628** in the D4 S4-S5 would form hydrophobic interactions, allowing for tight packing of these two regions and in turn, the IFM motif. **M1627K** and **M1628K** would disrupt this packing due to hydrophobic mismatch, thus destabilizing the fast-inactivated state.

3.2.2 hNa$_v$1.7 p.M1628K disrupts helix stacking

To better understand how the mutation from methionine to lysine can impact this hydrophobic interactome, I utilized coarse-grained molecular dynamics simulations (CGMD) to capture dynamic changes in this region. While CGMD allows for longer simulation time, it compromises on the resolution of the protein structure. This is due to the creation of “beads” by combining two to four heavy atoms. Such coarse graining also leads to a loss of secondary structure information. However, global changes to protein dynamics can still be accurately captured. Elastic networks between various backbone beads are introduced to ensure that the secondary and tertiary structure of the protein remains intact. This, however, introduces restraints that limit the flexibility of the protein. One way to overcome this limitation is to precisely remove the elastic networks in regions where we plan to introduce flexibility, a strategy utilized by (Lin et al., 2024) to understand how phosphoinositide binds to Na$_v$s. I adopted a similar strategy to understand my mutation, by removing elastic networks of the backbone beads of the helical region of D3-D4 to and from other parts of the structure. The internal contacts within this region were retained to maintain helicity (Appendix Figure S2). Mutations were introduced via martinize2 and the systems were simulated in a single component phosphatidylcholine (POPC) bilayer for a total of 8μs using the protocol described in Section 2.7 (Figure 18). Three replicates were simulated to account for the randomness of the velocities generated. The RMSD and RMSF of the backbone beads of hNa$_v$1.7 M1627K and M1628K showed differences when compared to hNa$_v$1.7 WT, although differences could be observed when focusing only on the D3-D4 linker (Appendix Figure S3 and S4).

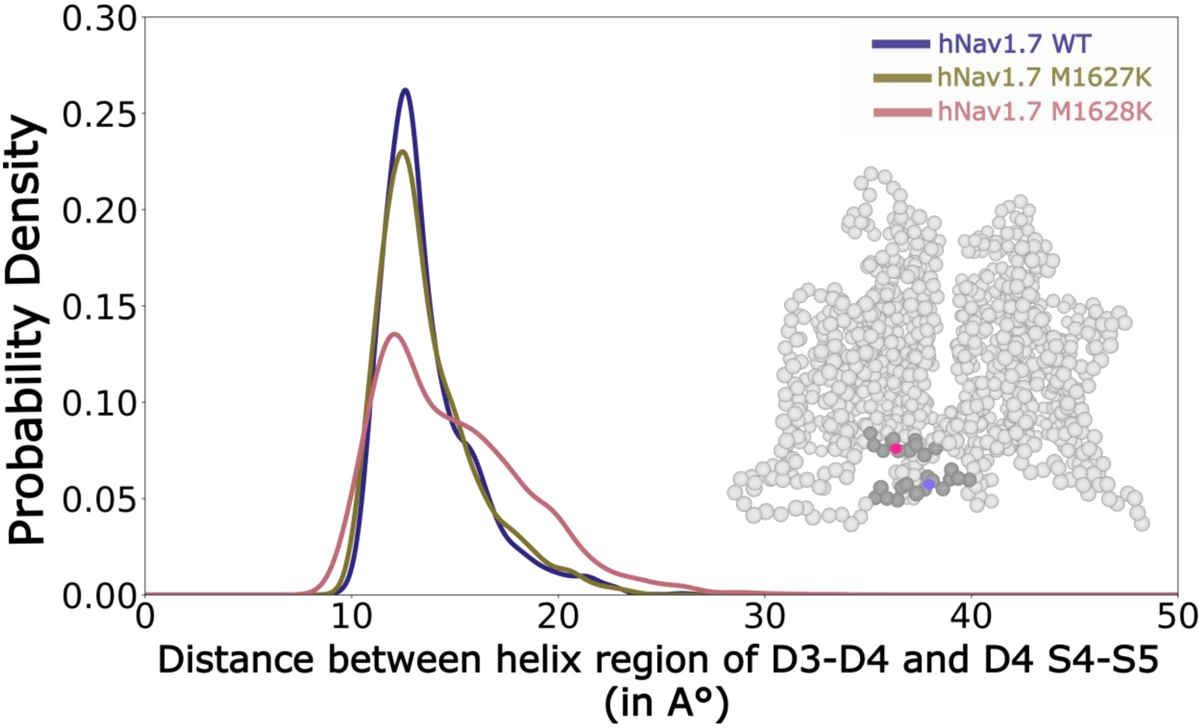

Figure 35 - hNa$_v$1.7 M1628K disrupts stacking of the helical region of D3-D4 and D4 S4-S5. The probability density distribution of the distance between the helical region of D3-D4 and D4 S4-S5. (Inset) The starting frame of **hNa$_v$1.7 WT** shown for reference. The distances are calculated between the center-of-geometries of the helical region of D3-D4 (residues 1465-1479, **purple dot**) and D4 S4-S5 (1619-1629, **pink dot**). For each group, probability distributions were calculated for a total of 2400 frames (800 downsampled frames x 3 replicates) using a gaussian kernel density estimator. While **hNa$_v$1.7 WT** shows a narrow distribution with a clear peak at ~15A°, **hNa$_v$1.7 M1628K** has a broad distribution with a smaller peak and a larger tail. **hNa$_v$1.7 M1627K** has a distribution similar to hNa$_v$1.7 WT, with a slightly lowered peak.

As a first step, I looked at the distances between the helical region of D3-D4 and the D4 S4-S5. To do this, I first downsampled the simulated trajectories to obtain a snapshot every 10ns, resulting in 800 snapshots or frames per simulation run. This ultimately gives us 2400 frames (800 frames x 3 replicates) for every structure. For every downsampled frame, I calculated the distance between the center-of-geometry of the helical part of D3-D4 (residues 1465-1479) and D4 S4-S5 (residues 1619-1629) (Figure 35 inset, purple and pink dots respectively). The distances were then used to estimate the probability densities using a gaussian kernel density estimator. While the distance of the helices remained stable for hNa$_v$1.7 WT with a clear peak at ~15A°, the hNa$_v$1.7 M1628K showed a reduced peak at this point with a broader tail leading to distances above 20A° (Figure 35, **blue** and **pink** line respectively). The hNa$_v$1.7 M1627K also had a distribution similar to hNa$_v$1.7 WT, although the peak density was lower compared to hNav1.7 WT (Figure 35, **yellow** line). Thus, distance between the two helices is disturbed quite strongly by hNa$_v$1.7 M1628K, with hNa$_v$1.7 M1627K having minimal effects.

3.2.3 hNa$_v$1.7 p.M1627K disrupts helix orientation

While the distance with the helices already suggests a disruption in the helix packing, hNa$_v$1.7 M1627K did not show much change in this parameter. This does not answer why both hNa$_v$1.7 M1627K and hNa$_v$1.7 M1628K disrupt fast inactivation. I decided to analyse the relative angles of the two helices, which informs us about the rotational aspect of the helices and hence their

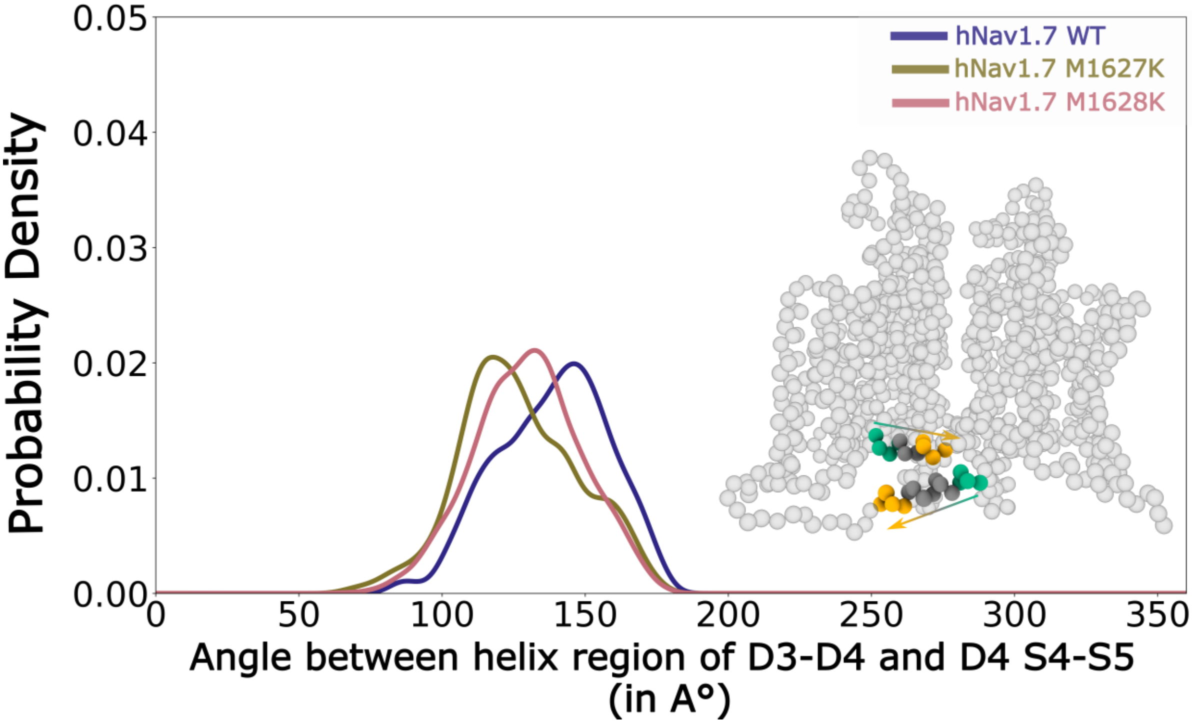

Figure 36 - hNa$_v$1.7 M1628K disrupts the orientation between the helical part of D3-D4 and D4 S4-S5. The probability density distribution of the angles between the helical region of D3-D4 and D4 S4-S5. (Inset) The starting frame of **hNa$_v$1.7 WT** shown for reference. The angles are calculated by first defining the vectors of the helical region of D3-D4 and D4 S4-S5 that connect the center-of-geometry of the first three residues (**orange** spheres) to the center-of-geometry of the last three residues (**green** spheres). Parallel angles are 180° in this scenario since the two helices run in opposite directions. For each group, probability density distributions were calculated for a total of 2400 frames (800 downsampled frames x 3 replicates) using a gaussian kernel density estimator. While all three groups have very broad distributions, hNa$_v$1.7 WT takes up angles closer to 180° while hNa$_v$1.7 M1627K has angles close to 90°. hNa$_v$1.7 WT M1628K sites in-between the other two. This suggests that hNa$_v$1.7 WT prefers parallel orientations, hNa$_v$1.7 M1627K prefers perpendicular orientations and hNa$_v$1.7 M1628K can take intermediary angles.

relative orientation. To analyse the orientation, I calculated the angles between the vector describing the direction of the D4 S4-S5 and the vector describing the direction of the helical segment of D3-D4 (Figure 36, inset). A visually noticeable observation was the broad distributions observed in all 3 groups (Figure 36). However, while the hNa$_v$1.7 WT had a peak and a tail more towards (anti-)parallel angles (180°) (Figure 36, **blue** line), hNa$_v$1.7 M1627K had a peak and tail closer to perpendicular angles (90°) (Figure 36, **yellow** line). hNa$_v$1.7 M1628K was sat between the other two (Figure 36, **pink** line). This shows that while hNa$_v$1.7 M1628K causes a disruption in the distance between the helices, hNa$_v$1.7 M1627K significantly alters the orientation between the helices.

3.2.4 Both M1627K and M1628K disrupt IFM binding

We see clear differences in the geometrical properties concerning the helical region of D3-D4 and D4 S4-S5. However, fast-inactivation is ultimately set into place by the binding of the IFM motif. I decided to test if these geometrical changes in the helix stacking correspond to a difference in IFM binding.

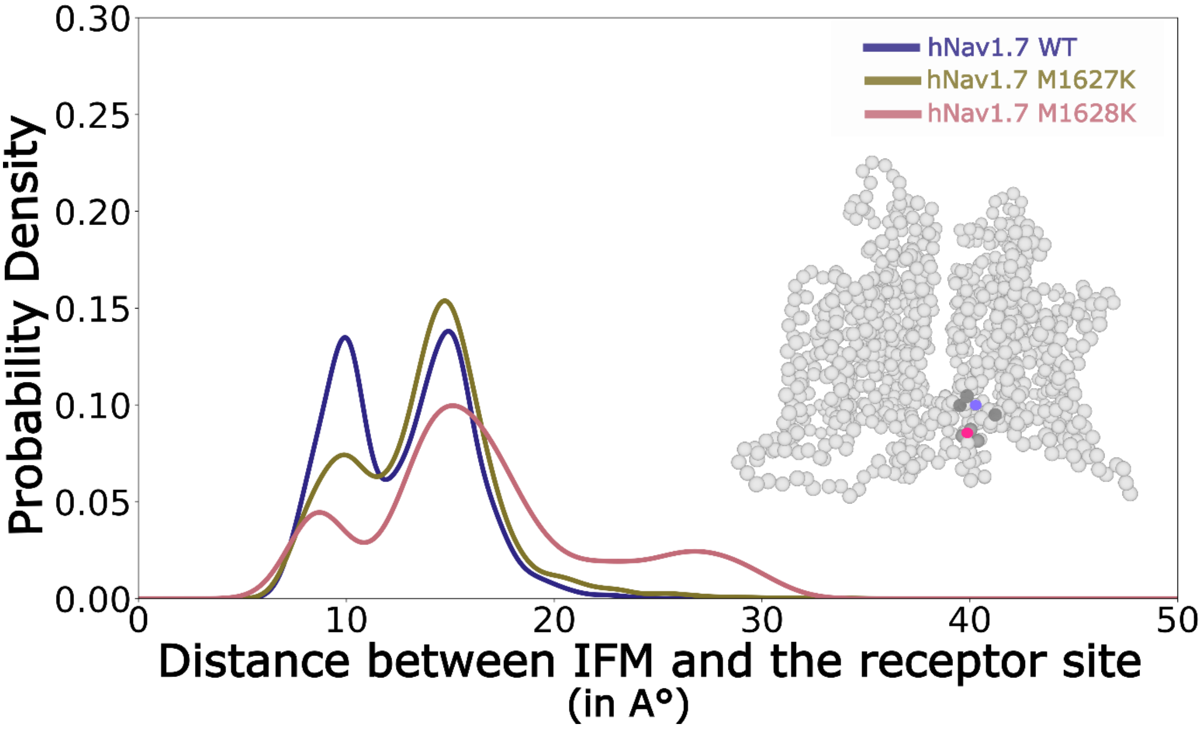

Figure 37 - hNa$_v$1.7 M1627K and hNa$_v$1.7 M1628K disrupt binding of the IFM motif. The probability density distribution of the distance between the IFM motif and its binding site. (inset) The starting frame of **hNa$_v$1.7 WT** shown for reference. The distances are calculated between the center-of-geometries of the IFM motif (residues 1461-1463, **pink dot**) and the residues majorly involved in IFM binding (residue 1303 in D4 S4-S5, residue 1636 in D4 S4-S5 and residue 1742 in D4 S6, **purple dot**). For each group, probability density distributions were calculated for a total of 2400 frames (800 downsampled frames x 3 replicates) using a gaussian kernel density estimator. The hNa$_v$1.7 WT shows an equally split bimodal distribution, which showcases a 50% chance for the IFM motif to either be in the binding pocket or not. Such a distribution is most likely due to the relaxed constraints in this region. The hNa$_v$1.7 M1627K and hNa$_v$1.7 M1628K both also have bimodal distributions, but with a significantly reduced peak at lower distances (that correlate to IFM binding) and significantly higher peak at larger values (that correlate to IFM unbinding). Both also show larger tails, with the largest tail shown by hNa$_v$1.7 M1628K.

To do this, I determined the distance between the center-of-geometry of the IFM motif (residues 1461-1463) and the center-of-geometry of key residues involved in the binding of the IFM motif (residue 1303 in D4 S4-S5, residue 1636 in D4 S4-S5 and residue 1742 in D4 S6) (Figure 37 inset,

purple and **pink** dots respectively). In the hNa$_v$1.7 WT, there was an equal split in the binding mode of the IFM motif, observed by the bimodal distribution resulting in peaks at ~8-9A° and at ~15A° which relate to IFM binding and unbinding respectively (Figure 37, **blue** line). In hNa$_v$1.7 M1627K, the bimodal distribution persists, but with a significantly reduced peak at lower distances and significantly higher peak at larger distances with a longer tail than the hNa$_v$1.7 WT (Figure 37, **yellow** line). hNa$_v$1.7 M1628K also continued the trend of the bimodal distribution, with once again a reduced peak at lower distances, a relatively elevated peak at higher distances and a very long tail with values >30A°, showcasing the complete unbinding of the IFM motif (Figure 37, **pink** line). My results overall suggest that the increased probability for unbinding of the IFM motif to occur happens via two different mechanisms – in hNa$_v$1.7 M1627K via disruption of helix closeness and in hNa$_v$1.7 M1628K via disruption of helix orientation. These results are also in congruence with the electrophysiological data on these two mutants – the change in the geometrical properties of helical stacking results in destabilization of IFM motif binding, which ultimately causes the depolarizing shift in the voltage-dependence of steady-state fast inactivation.

3.3 Cholesterol Depletion Alters Gating of hNa$_v$1.7

While naturally occurring mutations give us a glimpse into how Na$_v$s function, the gating of Na$_v$s is also controlled in a very significant manner by its environment. One of the major players in Nav environment is the lipid bilayer. Alterations of the lipid bilayer properties or composition can thus impact the functioning of Na$_v$s. Simone Albani (IAS-5/INM-9, Forschungszentrum Jülich, Germany) showed *in silico* that altering the cholesterol composition of the lipid bilayer changes the conformational dynamics of Na$_v$1.7. I utilized whole-cell patch clamp to show that these conformational changes in the structure can accurately be translated into functional changes *in vitro*.

To do this, I performed whole-cell patch clamp in HEK293t cells transfected with hNa$_v$1.7 in either a control condition (WT ctrl) or by pre-incubating in 5mM methyl-ß-cyclodextrin (WT MßCD) for 1 hour to deplete the cholesterol content of the cell. Depleting cholesterol increases the functionality of the channel population in the cell, as shown by increased current densities (Section 3.3.1). This is also accompanied by hyperpolarizing shifts in voltage dependence of both activation and steady-state fast inactivation (Section 3.3.2-3.3.3). While cholesterol depletion did not alter the recovery times from fast inactivation, it hastened both the time to peak and the onset of fast inactivation (Section 3.3.4-3.3.5).

The effects of depleting cholesterol from the membrane observed in the structure *in silico* are validated *in vitro*, with functional changes hinting at hyperactivity-like phenotypes and a possible mechanism through which physiological sensitization at a region experiencing pain can occur.

This work was published in part as a joint first author in the International Journal of Biological Macromolecules (Elsevier).

Albani, S., **Eswaran, V.S.B.***, Piergentili, A., De Souza, P.C.T., Lampert, A. and Rossetti, G., 2024. Depletion of membrane cholesterol modifies structure, dynamic and activation of Nav1. 7. *International Journal of Biological Macromolecules*, *278*, p.134219.

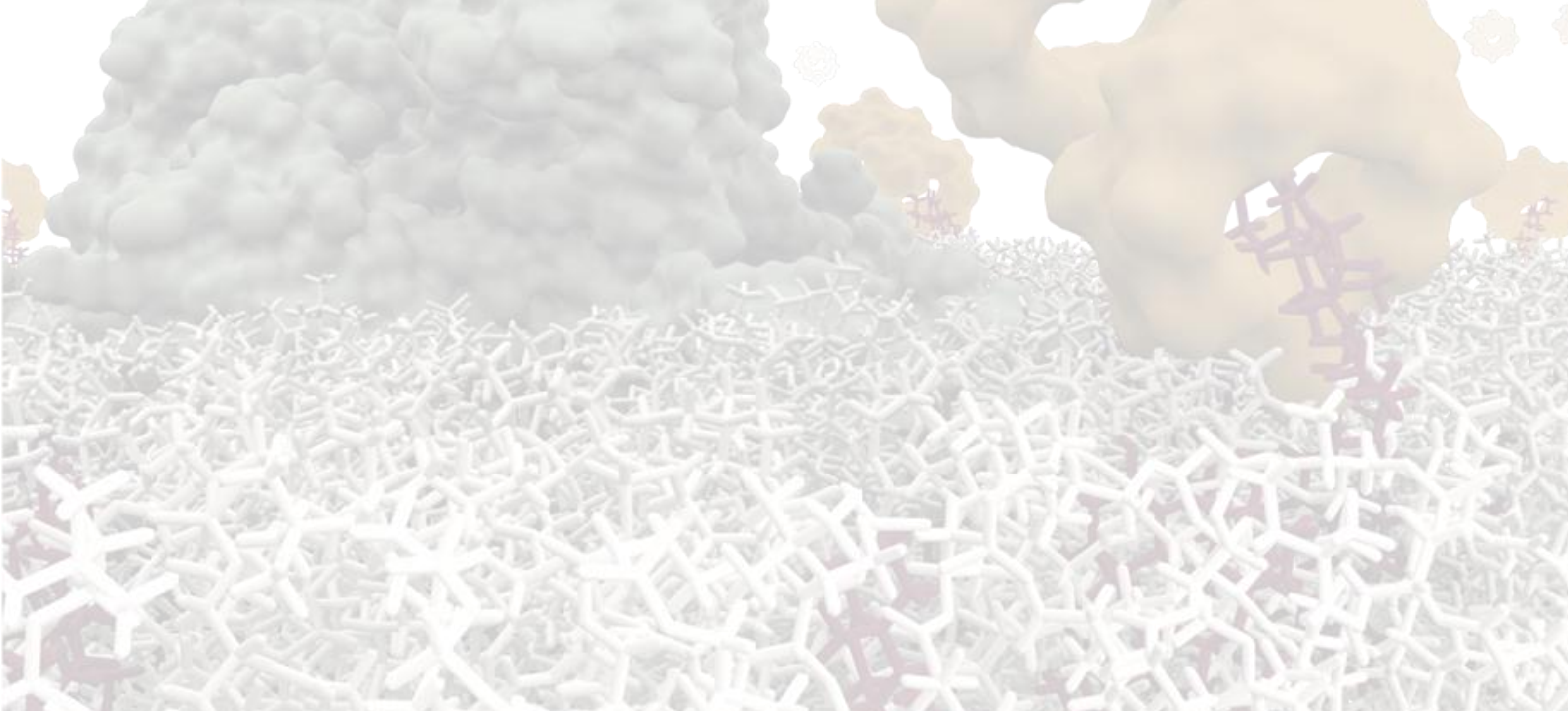

3.3.1 Depletion of cholesterol alters current densities

The absence of cholesterol was found to influence a lot of geometrical parameters of Na$_v$s that ultimately can alter the various gating phases (activation and fast inactivation) and also their druggability (Figure 9) (Albani et al., 2024). However, we needed to validate the *in-silico* results via experimental techniques. To mimic the depletion of cholesterol from the membrane as done in our simulations, we used 5mM methyl-ß-cyclodextrin (MßCD) to sequester cholesterol from the membrane. MßCD is commonly used in various experimental methods for the removal of cholesterol from the cell membrane (Amsalem et al., 2018; Lundbæk et al., 2004). HEK293t cells transfected with hNa$_v$1.7 WT (WT) were either not treated (WT ctrl) or incubated with 5mM MßCD for approximately 1 hour (WT MßCD) before patching.

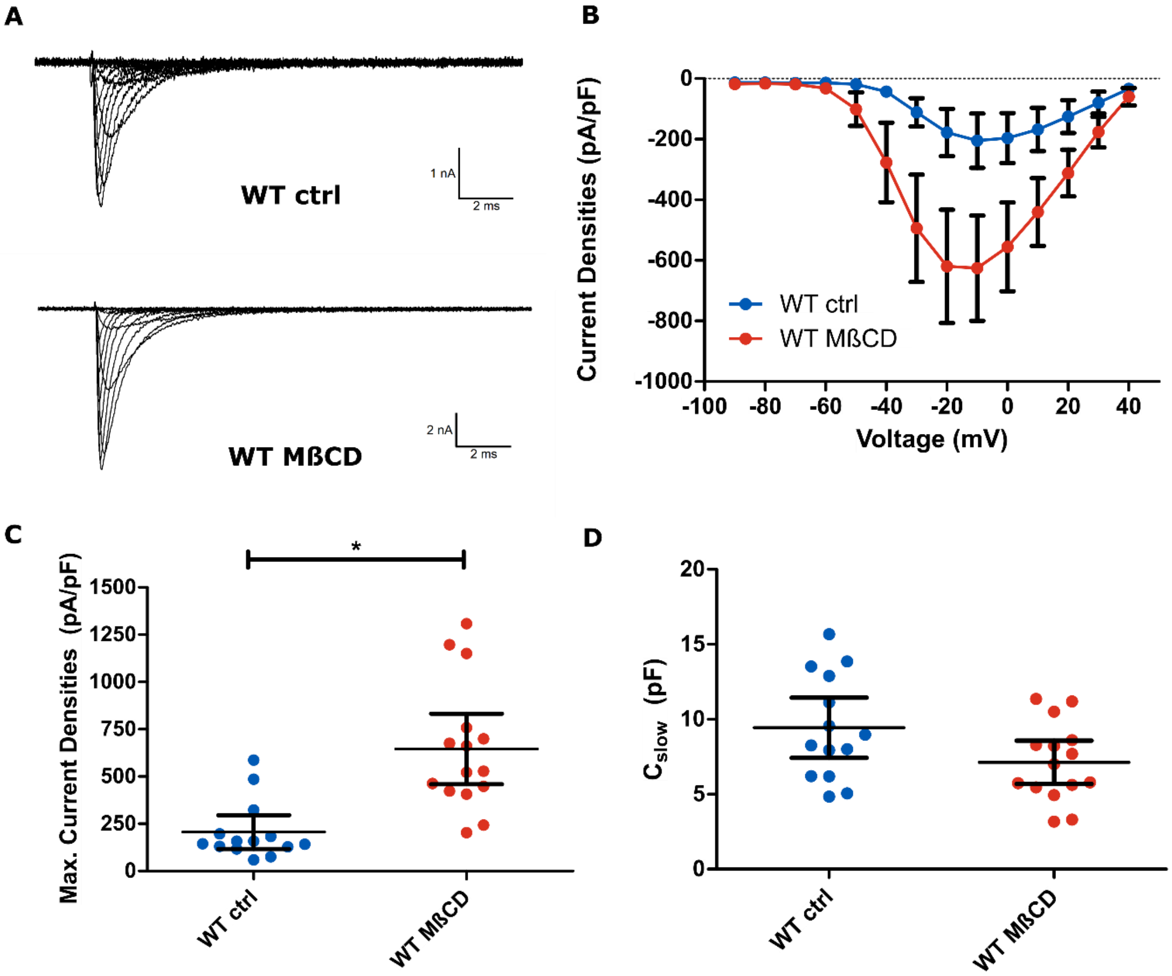

Figure 38 – Cholesterol depletion by MßCD causes an increase in current densities. (A) Representative traces of hNa$_v$1.7 WT obtained from whole-cell patch clamp of transfected HEK293t cells in either an untreated condition (WT ctrl) or incubated with 5mM methyl-ß-cyclodextrin 1 hour before patching to deplete cholesterol from the cell membrane (WT MßCD). WT ctrl and WT MßCD both show robust inward currents, with cholesterol depletion by MßCD causing an increase in the currents. **(B)** Current density vs voltage steps of WT ctrl and WT MßCD obtained during the activation protocol. We can clearly observe the larger current densities at almost every voltage step in MßCD. **(C)** Absolute values of the maximum current densities of WT ctrl and WT MßCD. Maximum current densities are the maximal absolute value of the current densities observed at any of the applied voltage steps. Cholesterol depletion by MßCD increases the current densities. **(D)** C$_{slow}$ values of WT ctrl and WT MßCD. C$_{slow}$ is a measure of the capacitance of the cell and hence an indicator of cell size. All cells patched are observed to have similar cell sizes. * $p < 0.05$.

A reduced sodium concentration of the extracellular solution was used to ensure that cells could be accurately clamped by lowering the currents. During the test pulses of the activation protocol

(Figure 13), I first measured the current densities for every cell using Equation 3. The current densities give us an idea about channel activity in the cells. A higher current density represents higher Na_v activity in the cell. Depletion of cholesterol caused a significant increase in current densities, even while the patched cells were of similar size distributions (Figure 38A-D, Table 15).

*Table 15 – Current densities of $hNa_v1.7$ wild-type transiently transfected in HEK293t cells either untreated (ctrl) or incubated with 5mM methyl-ß-cyclodextrin (MßCD) 1 hour before patching. * $p<0.05$ compared to $hNa_v1.7$ WT ctrl. CI is 95% confidence interval of the mean. n is the number of patched cells used for analysis.*

Channel	*Current densities* (mean±95% CI, n)
$hNa_v1.7$ WT ctrl (WT ctrl)	206.3±89.0 pA/pF, n=14
$hNa_v1.7$ WT MßCD (WT MßCD)	645.8±186.0 pA/pF, n=15 *

3.3.2 Depletion of cholesterol alters voltage-dependence of activation

The activation protocol (Figure 13) can give us an idea about the voltage-dependence of the activation phase of Na_vs. This is measured using the voltage at half-maximal channel activation i.e. the voltage at which 50% of channels remain activated ($V_{1/2,act}$), which can be obtained by the current traces using the activation protocol, measuring the conductance using equation 1 and using the normalized conductance to fit the curve using a Boltzmann fit as described in equation 2 to obtain the $V_{1/2,act}$ and also the slope of the curve ($slope_{act}$). The slope represents the sensitivity to voltage steps.

Depletion of cholesterol shifted the $V_{1/2,act}$ in a hyperpolarizing direction, meaning a cholesterol-depleted condition required less depolarized voltages to push channel populations into activation (Figure 39A-B, Table 16). The sensitivity to voltage changes remained unchanged in both conditions, as shown by the indifference in slope values (Figure 39C, Table 16).

*Table 16 – Voltage-dependence of activation parameters of $hNa_v1.7$ wild-type transiently transfected in HEK293t cells either untreated (ctrl) or incubated with 5mM methyl-ß-cyclodextrin (MßCD) 1 hour before patching. * $p<0.05$ compared to $hNa_v1.7$ WT ctrl. CI is 95% confidence interval of the mean. n is the number of patched cells used for analysis.*

Channel	$V_{1/2,act}$ (mean±95% CI, n)	$slope_{act}$ (mean±95% CI, n)
$hNa_v1.7$ WT ctrl (WT ctrl)	-21.1±1.8mV, n=14	9.3±0.7, n=14
$hNa_v1.7$ WT MßCD (WT MßCD)	-28.3±3.4mV, n=15 *	9.0±0.6, n=15

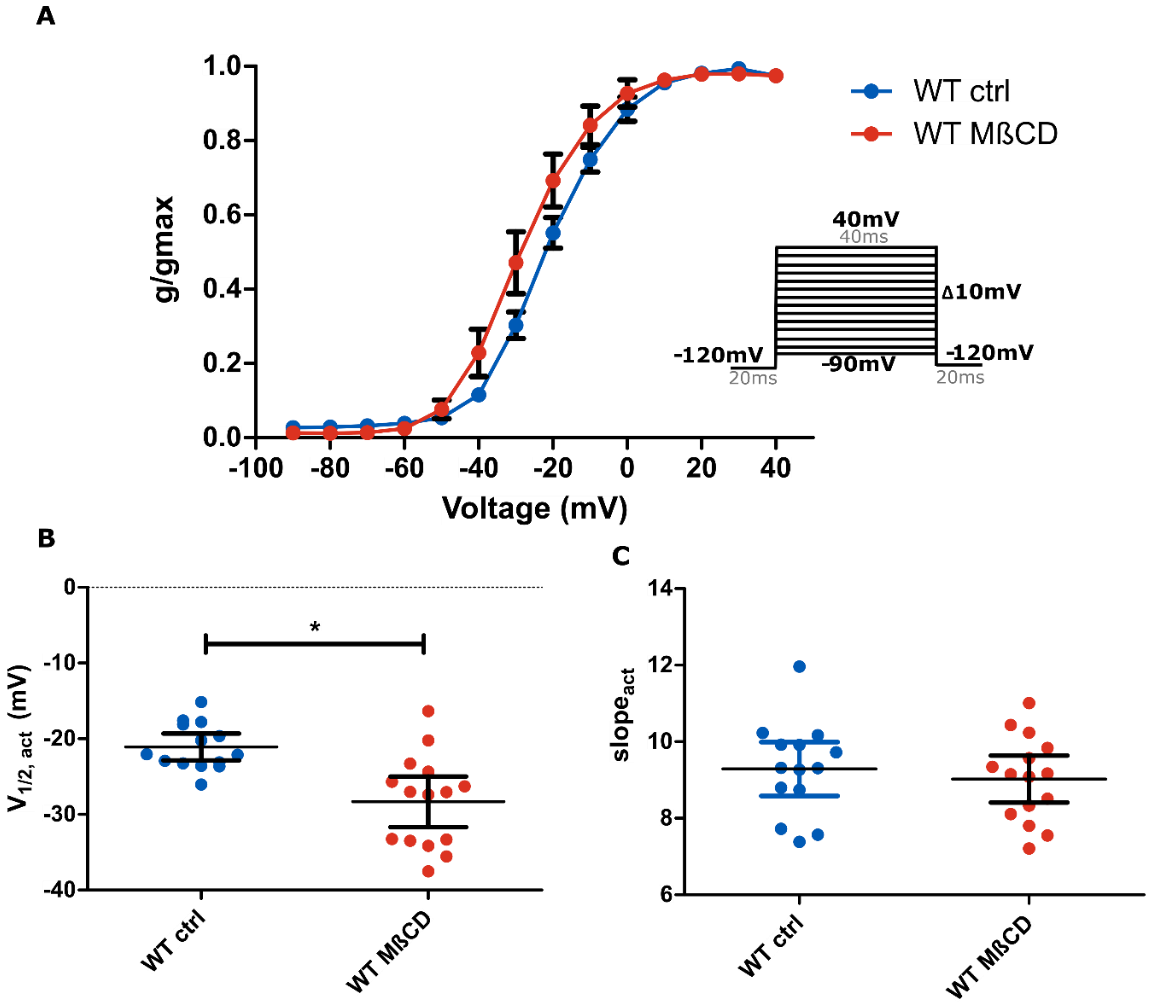

Figure 39 – Cholesterol depletion by MßCD alter voltage-dependence of activation. (A) Normalized conductance curves vs voltage for the hNa$_v$1.7 WT channels transfected in HEK293t cells either in an untreated condition (WT ctrl) or incubated with 5mM methyl-ß-cyclodextrin 1 hour before patching to deplete cholesterol from the cell membrane (WT MßCD). (inset) Conductance curves were obtained by using an activation protocol as described in section 2.2 Figure 13 and fitting the traces to a Boltzmann fit described in equation 2. Cholesterol depletion by MßCD shifts the conductance curves in a hyperpolarizing direction. **(B)** $V_{1/2,act}$ and **(C)** slope$_{act}$ of WT ctrl and WT MßCD. Cholesterol depletion by MßCD causes a hyperpolarizing shift in the $V_{1/2,act}$ but does not change the slope of the curves (and hence the voltage sensitivity). * $p<0.05$.

3.3.3 Depletion of cholesterol alters voltage-dependence of steady-state fast inactivation

Fast inactivation is another important gating process that allows Na$_v$s to stop ion conduction within a few ms (Körner and Lampert, 2020). To measure the voltage dependence of steady-state fast inactivation, I used the protocol described in Section 2.2 (Figure 15). Similar to activation, the peak currents are normalized to the maximal currents for each recorded cell, and the curves are fitted with a Boltzmann equation described in equation 6. The fitting results in the voltage at half-maximal channel fast inactivation i.e. the voltage at which 50% of channels remain fast inactivated ($V_{1/2,ssfi}$) and also the slope of the curve that explains the voltage sensitivity (slope$_{ssfi}$).

Cholesterol depletion resulted in a hyperpolarizing shift of $V_{1/2,ssfi}$, meaning that a cholesterol depleted condition caused channels to start entering fast inactivation at more hyperpolarized potentials (Figure 40A-B, Table 14). This was accompanied by no changes in the voltage-sensitivity to fast inactivation, as observed by the similar values in slope$_{ssfi}$ (Figure 40C, Table 17).

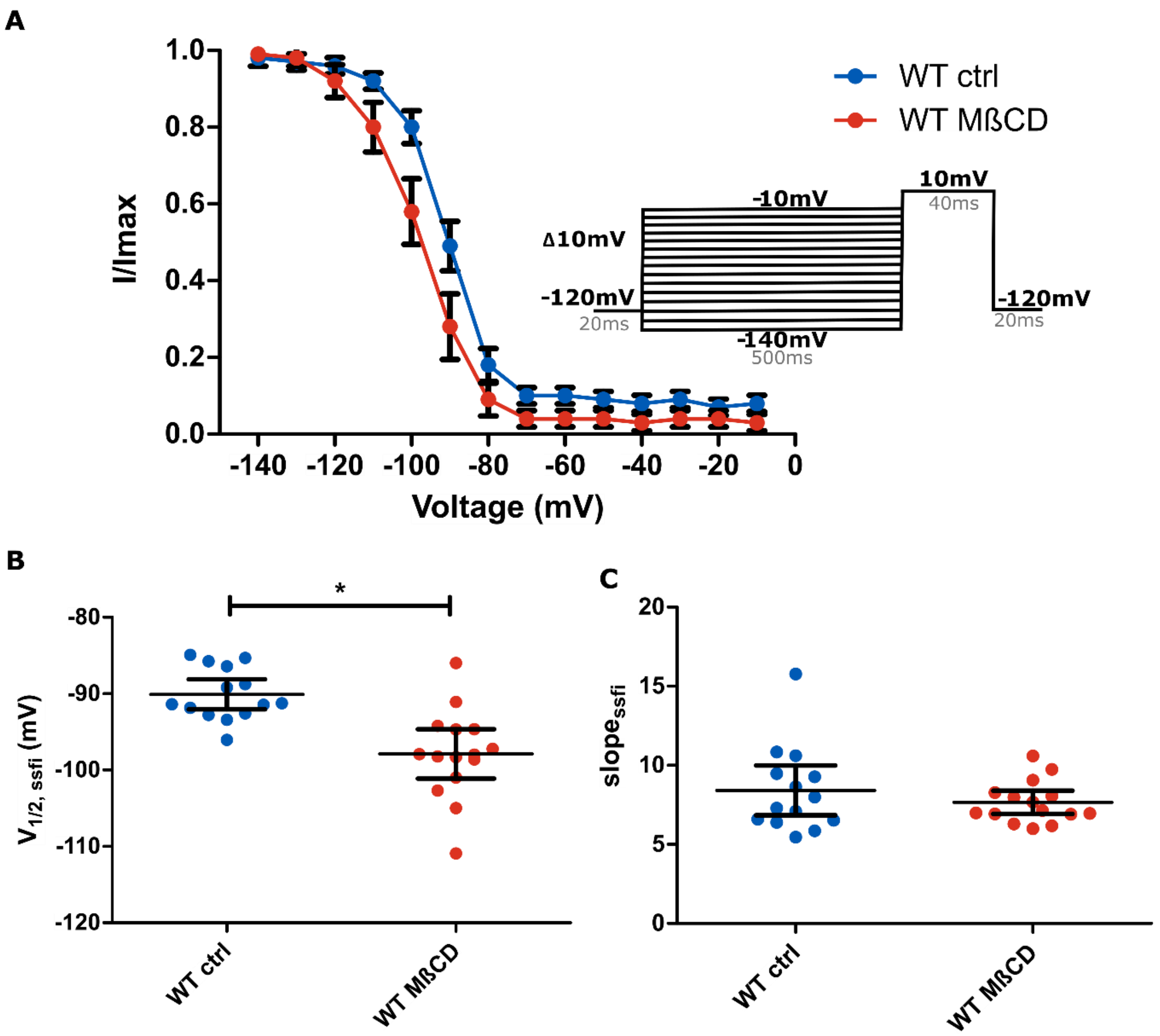

Figure 40 – Cholesterol depletion by MßCD alter voltage-dependence of steady-state fast inactivation. (A) Normalized current curves vs voltage for the hNa$_v$1.7 WT channels transfected in HEK293t cells either in an untreated condition (WT ctrl) or incubated with 5mM methyl-ß-cyclodextrin 1 hour before patching to deplete cholesterol from the cell membrane (WT MßCD). (inset) The curves were obtained by using a steady-state fast inactivation protocol as described in section 2.2 figure 15 and fitting the traces to a Boltzmann fit described in equation 6. Cholesterol depletion by MßCD shifts the current curves in a hyperpolarizing direction. **(B)** V$_{1/2,ssfi}$ and **(C)** slope$_{ssfi}$ of WT ctrl and WT MßCD. Cholesterol depletion by MßCD causes a hyperpolarizing shift in the V$_{1/2,ssfi}$ but does not change the slope of the curves (and hence the voltage sensitivity). * p<0.05.

Table 17 – Voltage-dependence of steady-state fast inactivation parameters of hNa$_v$1.7 wild-type transiently transfected in HEK293t cells either untreated (ctrl) or incubated with 5mM methyl-ß-cyclodextrin (MßCD) 1 hour before patching. * p<0.05 compared to hNa$_v$1.7 WT ctrl. CI is 95% confidence interval of the mean. n is the number of patched cells used for analysis.

Channel	***V$_{1/2,ssfi}$* (mean±95% CI, n)**	***slope$_{ssfi}$* (mean±95% CI, n)**
hNa$_v$1.7 WT ctrl (WT ctrl)	-90.1±2.0mV, n=14	8.4±1.6, n=14
hNa$_v$1.7 WT MßCD (WT MßCD)	-97.9±3.2mV, n=15*	7.7±0.7, n=15

3.3.4 Depletion of cholesterol causes faster time to peak and onset of fast inactivation

While voltage-dependence of gating processes allow us to understand how cholesterol affects these processes, some kinetic features can also change and ultimately alter the gating processes of Na_vs. Two such kinetic features include the time to peak and the onset of fast inactivation. Both these features can be measured from the activation protocol in a manner described in section 2.2 (Figure 14). Time to peak measures the time taken at various voltage steps to reach peak current values. The onset of fast inactivation measures the time it takes for a channel to start and reach fast inactivation after channel activation. This is measured by fitting the decaying phase of the current traces obtained in the activation protocol to a single exponential as described in equation 5. ´

Cholesterol depletion caused a speeding up of both kinetic features, with time to peak and onset of fast inactivation much faster at most voltage ranges where peak currents are observed (Figure 41). This, in combination with the voltage-dependence changes suggest that cholesterol depletion allows for Na_vs to undergo their gating cycles faster.

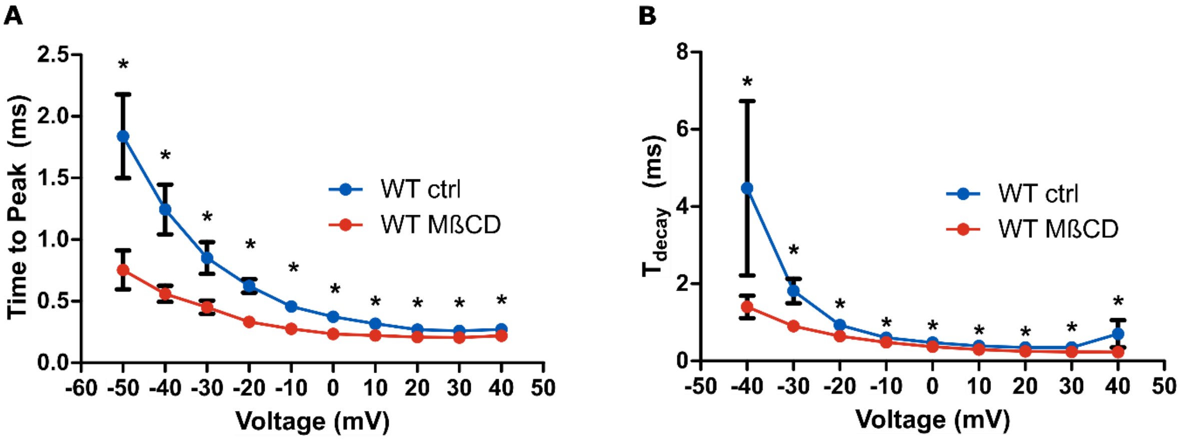

Figure 41 – Cholesterol depletion by MßCD hastens time to peak and onset of fast inactivation. (A) Time to peak and **(B)** time constant (T_{decay}) of the decay of fast-inactivation (or onset of fast inactivation) of $hNa_v1.7$ WT channels transfected in HEK293t cells either in an untreated condition (WT ctrl) or incubated with 5mM methyl-ß-cyclodextrin one hour before patching to deplete cholesterol from the cell membrane (WT MßCD). Time to peak is calculated as the time from the start of the test pulse in the activation protocol to achieve peak currents. The T_{decay} for the onset of fast inactivation is obtained by fitting the decaying phase of the current traces during the activation protocol to an exponential function described in equation 5. Depletion of cholesterol by MßCD causes both kinetic parameters to become quicker at most voltage steps where peak currents are observed. * $p < 0.05$.

3.3.5 Depletion of cholesterol did not change recovery rates from fast inactivation

Another important kinetic feature to consider is how long it takes for channels to go from a fast-inactivated state back to a resting state. This is done using a recovery from fast inactivation protocol, where changing the duration of the inter-pulse allows us to see how many channels still remain in a fast-inactivated state after a test-pulse (Figure 16). The peak current values during the test-pulse is normalized to those during the pre-pulse and plotted against the various durations of the inter-pulse.

Depleting cholesterol interestingly did not alter recovery times of WT from fast inactivation except at an inter-pulse duration of 1.6s (Figure 42). This suggests that while the onset of fast inactivation is hastened by cholesterol depletion, the recovery from it remains unchanged.

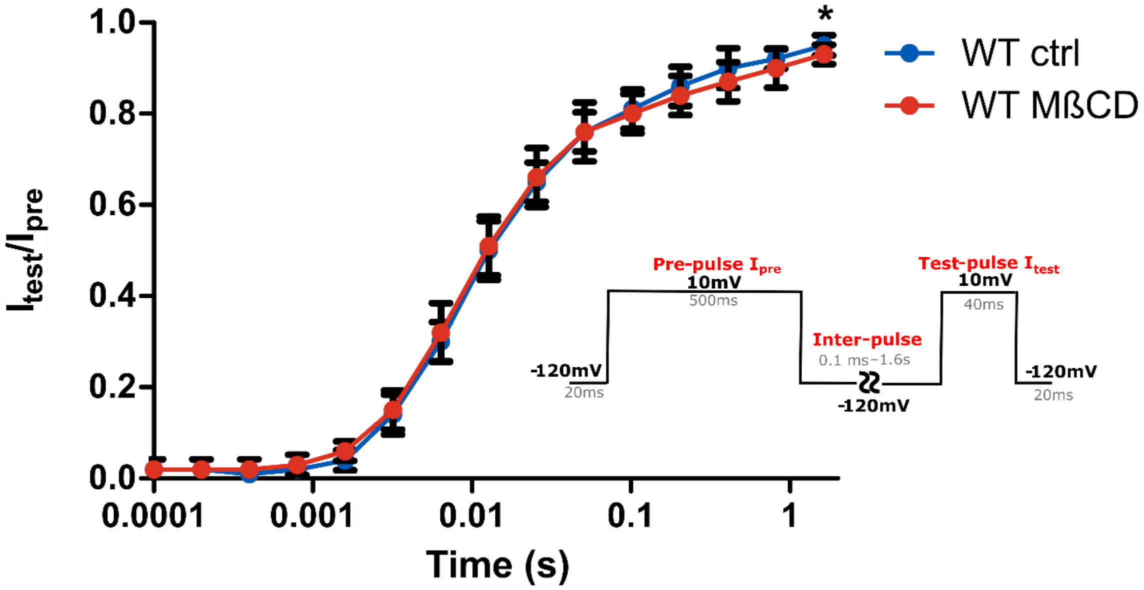

Figure 42 – Cholesterol depletion by MßCD does not alter recovery times from fast inactivation. The time course of recovery from fast inactivation of hNa$_v$1.7 WT channels transfected in HEK293t cells either in an untreated condition (WT ctrl) or incubated with 5mM methyl-ß-cyclodextrin 1 hour before patching to deplete cholesterol from the cell membrane (WT MßCD). (Inset) Recovery from fast inactivation was measured using a specialized protocol as described in section 2.2 Figure 16. The currents measured during the test-pulse (I_{test}) were normalized to the currents measured during the pre-pulse (I_{pre}) and plotted against the various durations of the inter-pulse. Cholesterol depletion did not alter the recovery from fast inactivation at almost all inter-pulse durations. * $p<0.05$.

3.4 Phentolamine Binds to the Local Anaesthetic Site

Recent decades have seen the rise in usage of external compounds or artificially designed drugs to effectively control aberrant Na$_v$ gating and relive clinically pathogenic phenotypes. Local anesthetics are one such compound which acts by blocking Na$_v$ function, helpful either in the context of controlling pain phenotypes or in the context of surgeries. To help patients' recovery from surgical application of local anaesthetics in a quick manner, the drug phentolamine is used as it causes vasodilation at the injection site by blocking the α-adrenergic receptors, resulting in subsequent increase in systemic absorption and redistribution of the local anaesthetic away from the application site (Prados-Frutos et al., 2015). However, phentolamine comes with various side-effects that include a sensation of numbness and in severe cases cardiac arrhythmias. Idil Toklucu (Institute for Neurophysiology, Uniklinik RWTH Aachen, Germany) investigated the effects of phentolamine on both hNa$_v$1.5 and hNa$_v$1.7 using an automated patch clamp system and showed that phentolamine blocked both channels in a tonic and use-dependent manner. She also found that mutating either of two residues important for local anesthetic binding abolished the effects of phentolamine. Her effects were almost a replica of the effects she observed when using the known local anti-arrhythmic mexiletine.

I use this *in vitro* information to better understand the structural picture of phentolamine and mexiletine binding to hNa$_v$1.5. For this, I utilized rigid-body docking methodologies to bind phentolamine and mexiletine to the hNa$_v$1.5 structure published by (Li et al., 2021b). To mimic the functional effects of point mutations to the two residues involved in phentolamine binding (F1760 and N1765), I also performed docking on homology models with the point mutations F1760A and N1765K. I found that while both phentolamine and mexiletine bind to hNa$_v$1.5 in five major regions, the highest population occurs close to the LA binding site in the center of the channel **(Section 3.4.1)**. This distribution is shifted to the peripheral regions of the channel when mutations F1760A or N1765K are introduced **(Section 3.4.2)**. The likely mechanism of phentolamine and mexiletine was predicted to occur by first binding beneath the selectivity filter and hindering the movement of the lysine residue of the selectivity filter – a residue crucial for sodium selectivity in Na$_v$s **(Section 3.4.3)**.

Thus, phentolamine binds to Na$_v$s at the LA site and likely blocks ion permeation via disruption of sodium ion coordination. Such a molecular mechanism showcases the non-specificity of these compounds and the importance of computational drug design methodologies to improve drug selectivity and avoid side-effects.

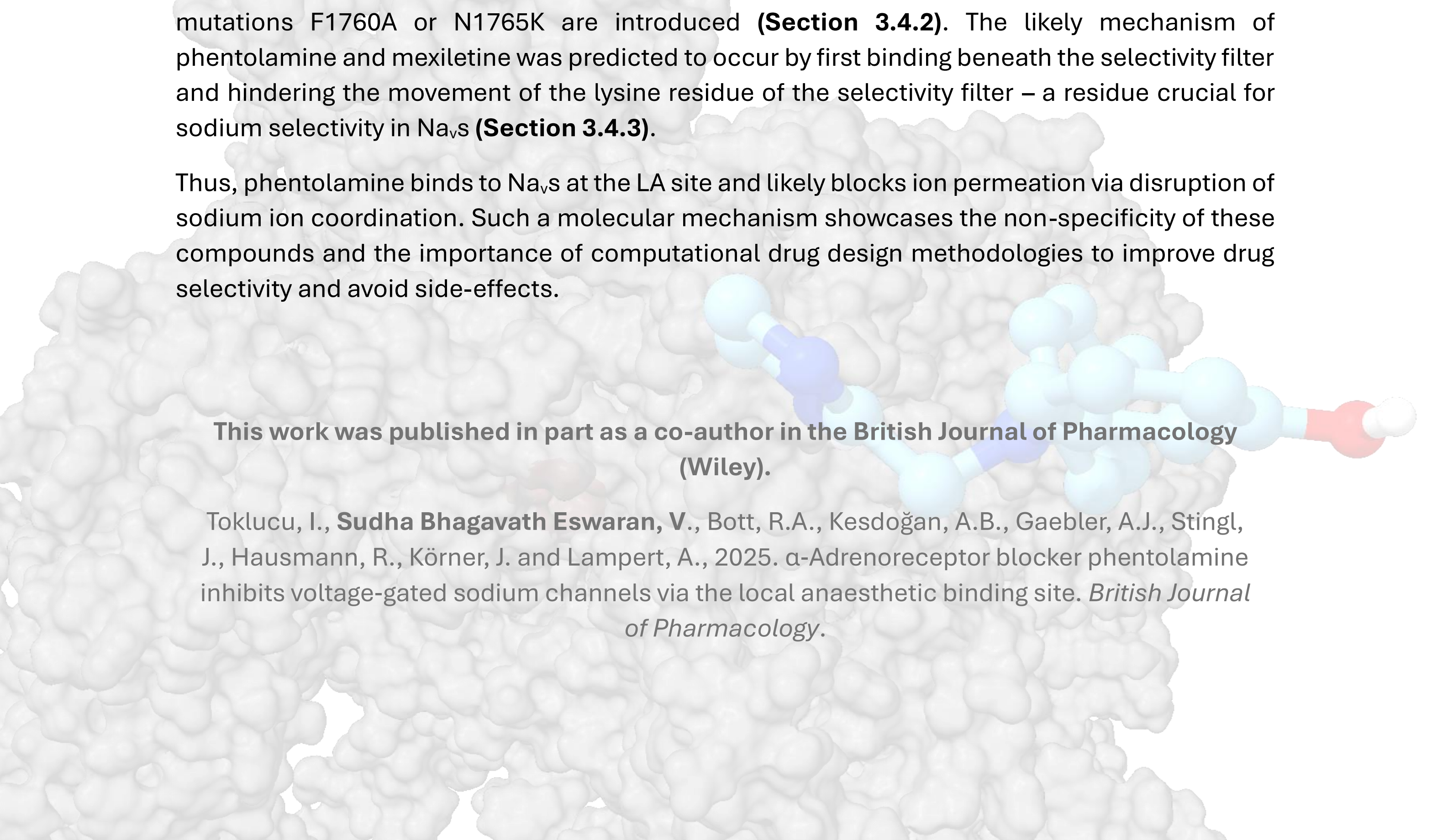

This work was published in part as a co-author in the British Journal of Pharmacology (Wiley).

Toklucu, I., **Sudha Bhagavath Eswaran, V.**, Bott, R.A., Kesdoğan, A.B., Gaebler, A.J., Stingl, J., Hausmann, R., Körner, J. and Lampert, A., 2025. α-Adrenoreceptor blocker phentolamine inhibits voltage-gated sodium channels via the local anaesthetic binding site. *British Journal of Pharmacology*.

3.4.1 Phentolamine binds to the LA site

Idil Toklucu (Institute for Neurophysiology, Uniklinik RWTH Aachen, Germany) showed that phentolamine has effects similar to other local anesthetics (LA) and anti-arrhythmics on Na_vs, blocking their conduction in both a tonic and use-dependent manner (Figure 10) (Toklucu et al., 2025). She also showed that mutation of either of two residues heavily implicated in LA binding (F1760 and N1765) prevented the blocking effect of phentolamine (Figure 10). Given this experimental evidence, we wanted to know the possible binding locations phentolamine in the Nav structure and what the molecular mechanism for the blocking action can be.

To do this, I utilized rigid-body docking via Autodock Vina on the $hNa_v1.5$ cryo-EM structure ($WT_{1.5}$) solved by (Li et al., 2021a)(PDB ID 6QLA). The structure was chosen since it was resolved with a local arrhythmic quinidine already bound to the channel. Thus, the channel structure is closer to the conformation one could expect when a LA binds to the channel. I used a grid centered around the F1760 and N1765 residues that were shown *in vitro* to control the binding of phentolamine and performed a docking run with 100 poses being generated. To account for randomness in the starting point inside the grid, I performed five independent runs, resulting in a total of 500 poses. The 500 poses were clustered using a K-means clustering algorithm. The 3-dimensional vectors representing the center-of-mass of phentolamine was used as the feature for the clustering, and the optimal number of clusters were chosen based on a combination of three techniques - the minimization of the least squared error, the maximization of the silhouette score, and visual inspection to remove spurious binding poses. Based on this combination, I observed a total of five clusters – one in a site close to where quinidine was found to bind in the cryo-EM structure of $hNa_v1.5$ solved by (Li et al., 2021b) (Qdn-like), one in a site close to where the anti-arrhythmic flecanide was found to bind in the cryo-EM structure of rat $Na_v1.5$ solved by (Jiang et al., 2020) (Flec-like), a site in the periphery of the side fenestration between D3 and D4 (III-IV fen), a site in the periphery of the side fenestration between D1 and D4 (I-IV fen) and a site deeper in the pore center (Pore center) (Figure 43). Of the 500 total poses, 46.8% was found to bind at the Qdn-like site, followed in second by the Flec-like site (24.2%) (Figure 44A and Table 18).

To act as a control, we used a known anti-arrhythmic mexiletine and performed the same methodology as described previously for phentolamine. Mexiletine also bound to the five major clusters in $WT_{1.5}$, with a large portion of the poses clustering at the Qdn-like site (20.4%) (Figure 44B and Table 18).

3.4.2 Mutations FA and NK reduce binding affinity to the LA site

As a next step, I decided to mutate the F1760 and N1765 to an alanine ($FA_{1.5}$) and lysine ($NK_{1.5}$) respectively to see if this alters the binding site clustering of phentolamine. This was done via homology modelling in Modeller v10.2 using the cryo-EM structure of $hNa_v1.5$ solved by (Li et al., 2021a) as a starting template. Mutation of the either of the two residues completely shifted the clustering distribution of phentolamine poses. $FA_{1.5}$ had the highest clustering in the III-IV fen (54.4%) followed by the I-IV fen (21.2%). Clustering at the Qdn-like site dropped significantly (8.6%) when compared to $WT_{1.5}$ (Figure 44A). A similar trend was observed for $NK_{1.5}$, with the highest clustering in the III-IV fen (39%) and a significantly lowered clustering in the Qdn-like (16.2%) and Flec-like (4%) sites when compared to $WT_{1.5}$ (Figure 44A). Similar changes were observed when mexiletine was docked, with zero binding poses at the Qdn-like site in both $FA_{1.5}$ and $NK_{1.5}$, and a majority of the clusters at III-IV fen (46% and 49% respectively) (Figure 44B).

A

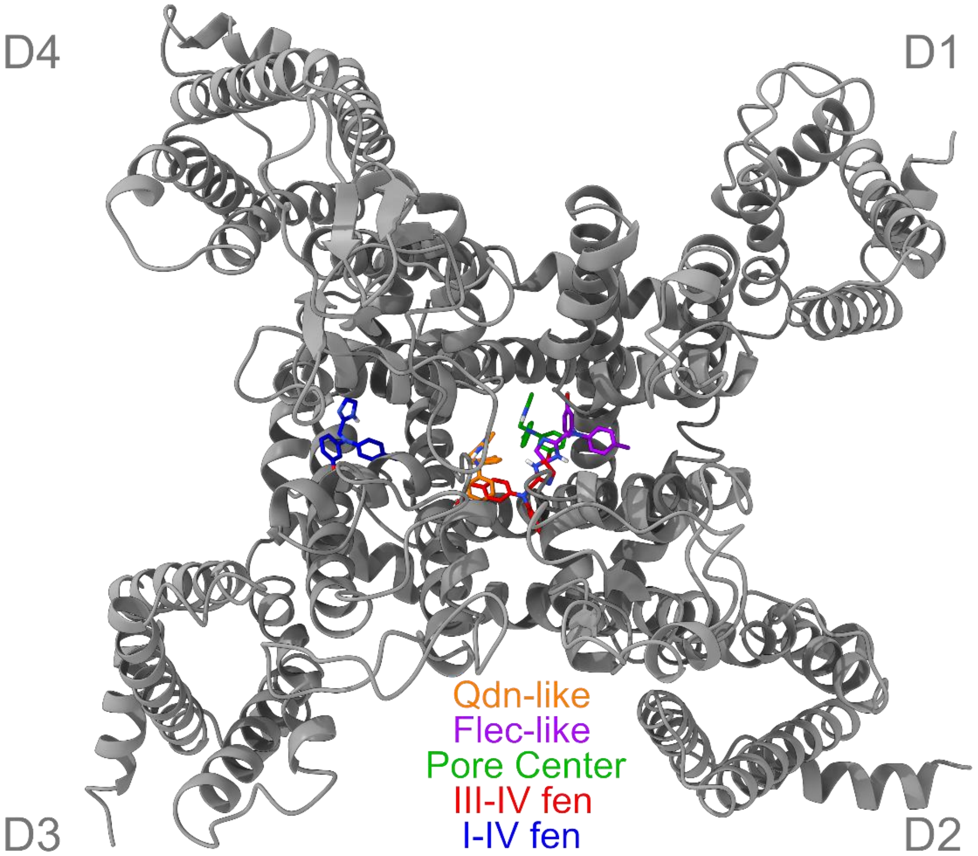
D4
D1
D3
D2
Qdn-like
Flec-like
Pore Center
III-IV fen
I-IV fen

B

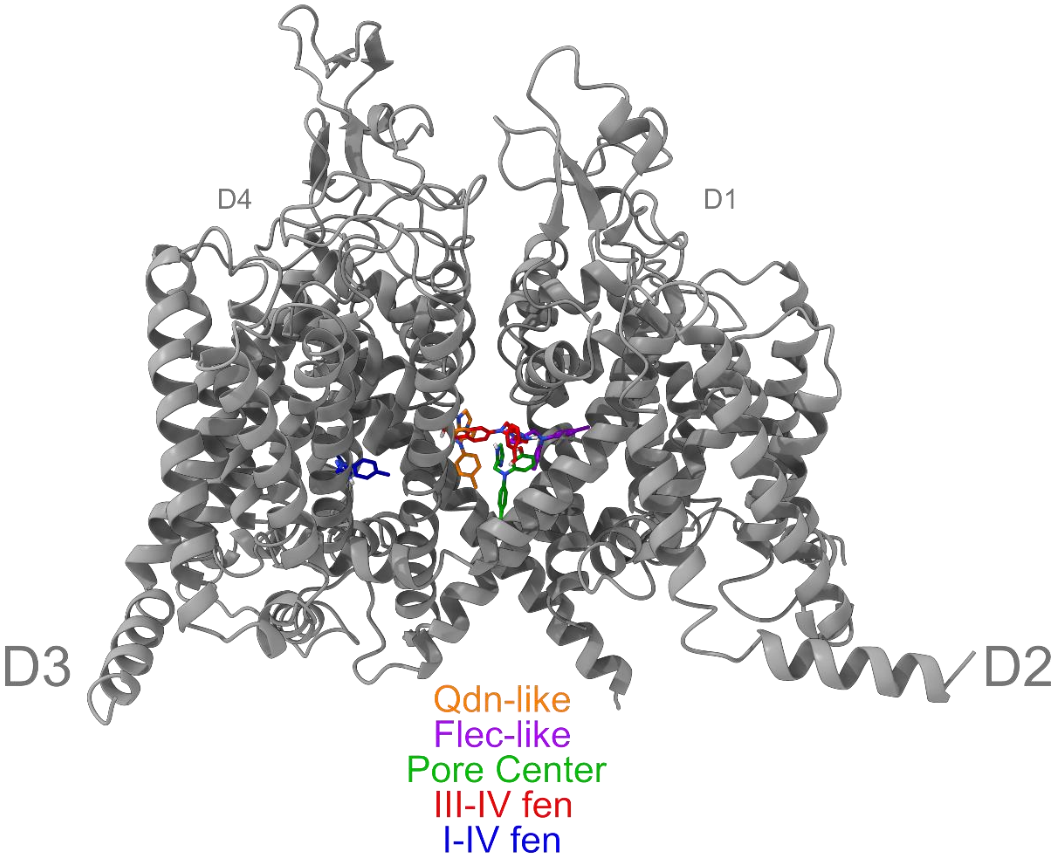
D4
D1
D3
D2
Qdn-like
Flec-like
Pore Center
III-IV fen
I-IV fen

Figure 43 – Clustering sites of phentolamine in hNa$_v$1.5. (A) Extracellular and **(B)** side view of the 5 major clustering sites of phentolamine in hNa$_v$1.5 as predicted by Autodock Vina. Rigid body docking of phentolamine was done by creating a grid around the F1760 and N1765 residues. A total of 100 poses and five independent runs produced 500 poses, which were clustered using the K-means clustering algorithm. The top pose for each cluster was chosen based on the lowest binding affinity score output by Autodock Vina. The top pose of phentolamine in each cluster is represented by sticks. The five clusters are as follows - one in a site close to where quinidine was found to bind in the cryo-EM structure of hNa$_v$1.5 solved by (Li et al., 2021b)(**Qdn-like**), one in a site close to where the anti-arrhythmic flecanide was found to bind in the cryo-EM structure of rat Na$_v$1.5 solved by (Jiang et al., 2020) (**Flec-like**), a site in the side fenestration between D3 and D4 (**III-IV fen**), a site in the side fenestration between D1 and D4 (**I-IV fen**) and a site deeper in the pore center (**Pore center**).

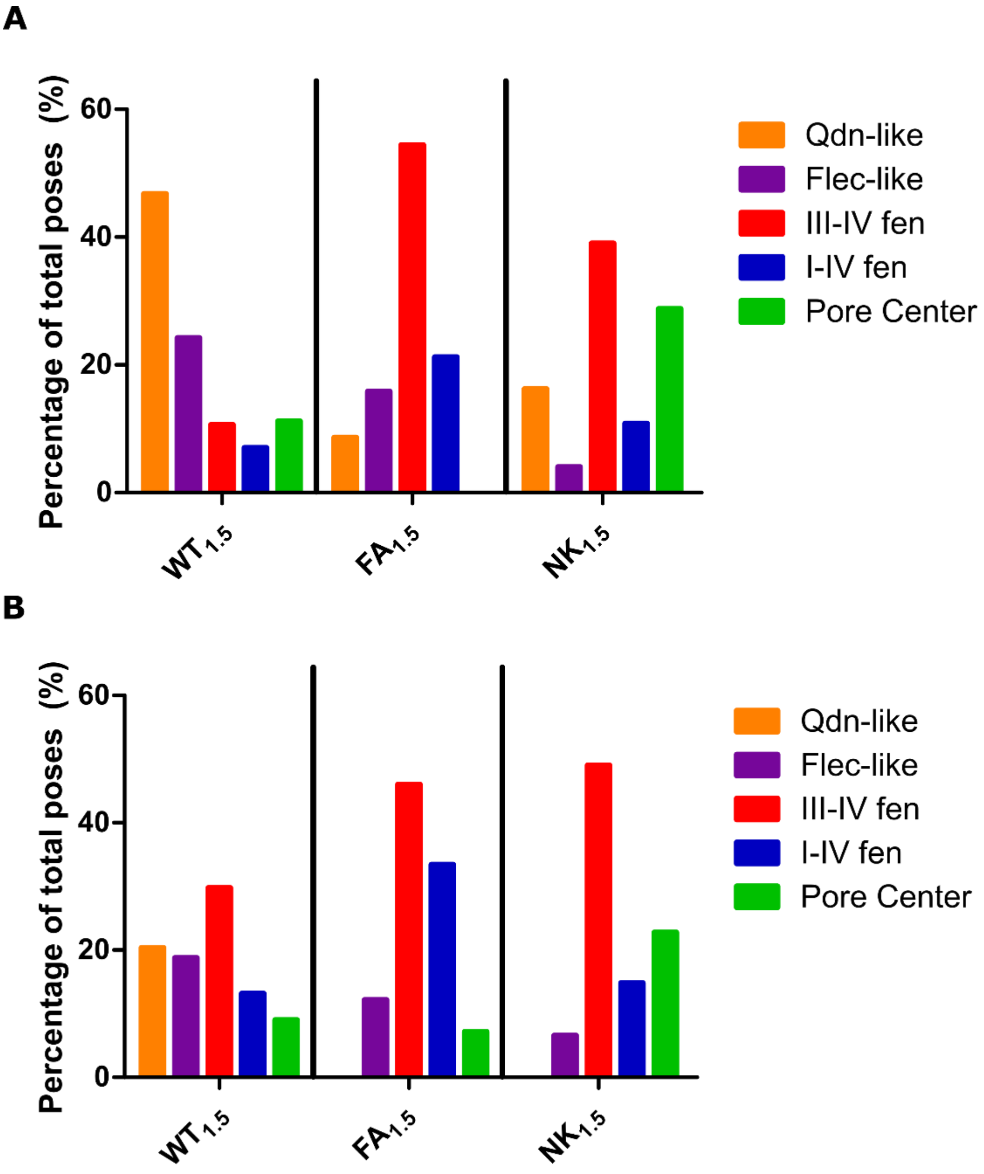

Figure 44 – Cluster distribution of phentolamine and mexiletine. (A) Grouped bar graph representing the population of phentolamine poses in each cluster as a percentage of 500 poses in WT$_{1.5}$, FA$_{1.5}$ and NK$_{1.5}$. While WT$_{1.5}$ shows a larger population in the Qdn-like site, FA$_{1.5}$ and NK$_{1.5}$ reduce this cluster population and shift them to the III-IV fen. **(B)** Grouped bar graph representing the population of mexiletine poses in each cluster as a percentage of 500 poses in WT$_{1.5}$, FA$_{1.5}$ and NK$_{1.5}$. While WT$_{1.5}$ has a somewhat equally distributed cluster population in Qdn-like, Flec-like and III-IV fen, FA$_{1.5}$ and NK$_{1.5}$ have no poses in the Qdn-like site.

Table 18 – Percentage of total poses in different clusters when phentolamine or mexiletine were docked on hNa$_v$1.5 Wild Type (WT$_{1.5}$), F1760A (FA$_{1.5}$) and N1765K (NK$_{1.5}$) structures. The numbers are given as a percentage of total poses (n=500).

Ligand	Structure	Qdn-like	Flec-like	III-IV fen	I-IV fen	Pore Center
Phentolamine	WT$_{1.5}$	46.8%	24.2%	10.6%	7.0%	11.2%
	FA$_{1.5}$	8.6%	15.8%	54.4%	21.2%	0.0%
	NK$_{1.5}$	16.2%	4.0%	39.0%	10.8%	28.8%
Mexiletine	WT$_{1.5}$	20.4%	18.8%	29.8%	13.2%	9.0%
	FA$_{1.5}$	0.0%	12.2%	46.0%	33.4%	7.2%
	NK$_{1.5}$	0.0%	6.6%	49.0%	14.8%	22.8%

3.4.3 Phentolamine blocks ion conduction via the lysine residue in the selectivity filter

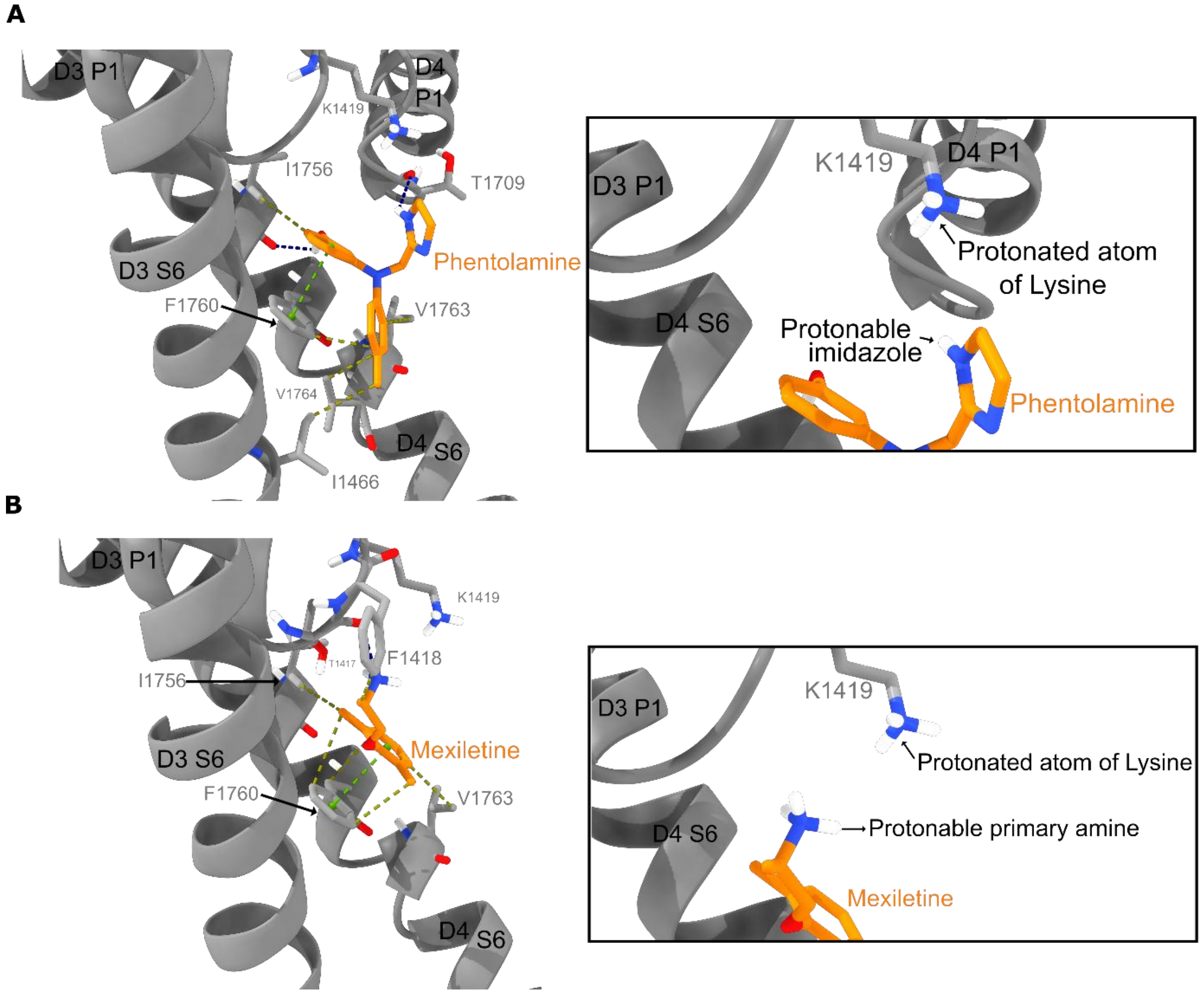

Figure 45 – Phentolamine and mexiletine block the central pore conduction pathway. **(A)** The interactome of the top pose of phentolamine in the Qdn-like cluster. The top pose was chosen based on the binding affinity scores generated by Autodock Vina. Phentolamine makes an important π-stack interaction with F1760, and various other hydrogen bonds and van-der-Waal's interactions. **(Inset)** The imidazole group of phentolamine pokes towards the central pore axis and underneath the lysine residue of the selectivity filter, likely blocking ion conduction. **(B)** The interactome of the top pose of mexiletine in the Qdn-like cluster. The top pose was chosen based on the binding affinity scores generated by Autodock Vina. Mexiletine also makes an important π-stack interaction with F1760, and various other hydrogen bonds and van-der-Waal's interactions. **(Inset)** The protonable amine group of phentolamine pokes towards the central pore axis and underneath the lysine residue of the selectivity filter, likely blocking ion conduction in a manner similar to phentolamine.

Given the clustering results, I proceeded to see how the interactome looked like at the binding site. To do this, I first chose the best pose from the Qdn-like cluster by choosing the lowest binding affinity score generated by AutoDock Vina. The top pose of phentolamine was found to form π-stack interactions between the phenyl ring of phentolamine and the F1760 residue (Figure 45A). Further stabilizing bounds were seen in the form of hydrogen bonds and other van-der-Waal's interactions (Figure 45A). On a closer look, the imidazole ring of phentolamine was found to point towards the central axis and position right below the protonated lysine of the selectivity filter (Figure 45A inset). Such interactions were also found in the top pose of mexiletine, with the protonable amine positioned similarly under the lysine of the selectivity filter (Figure 45B and inset). Such an orientation of these groups likely blocks the lysine residue from conducting ions, thus blocking ion conduction.

Chapter 4: Discussion

Mutations, membrane and externally applied synthetic drugs: All are shown to modulate the gating of Na_vs to varying degrees, via multiple mechanisms. Mechanistic insights can help in understanding structure and function from different perspectives and ultimately translate them to clinical findings.

This chapter puts the results of this thesis into perspective. I start by highlighting an extracellular tagging methodology that can effectively help us visualize and quantify membrane expression of Na_vs **(Section 4.1)**. Membrane-trafficking LoF Na_vs must exert their phenotype via a gating mechanism, and the collapse of the outer pore is most likely a more general patho-mechanism for mutations in the PM **(Section 4.2)**. Na_vs are folded from a single polypeptide into four homologous domains. This means that the four domains, though similar, are not equivalent. My results highlighted this inherent asymmetry in the Na_v pore modules, which may be an important feature of eukaryotic Na_vs **(Section 4.3)**. My results showcasing the absence of substantial effects on gating upon deletion of an entire exon raises the question on whether these inter-domain linkers are only sufficient but not necessary for normal Na_v gating **(Section 4.4)**. While dominant negative effects might arise from dimerization of WT with an aberrantly gating channel, an alternate mechanism– a “dominant positive effect” - that might exist between WT and membrane-trafficking gating-deficient LoF channels is explored **(Section 4.5)**. Recent years have seen a massive and rapid development in our understanding of fast inactivation. One part of the structure that is often overlooked when studying fast inactivation is the helical region of the D3-D4 and the D4 S4-S5, whose geometrical features might govern binding of the IFM motif and consequently fast inactivation **(Section 4.6)**. As membrane proteins, Na_vs are also subject to regulation by the bilayer membrane. While direct interaction of lipid species with the alpha subunit exists, cholesterol depletion likely causes its exerted effects indirectly by controlling the fluidity of the membrane and raises the possibility for other secondary proteins to use membrane fluidity as a mechanism to control gating **(Section 4.7)**. On top of physiological modulators, artificially synthesized drugs can also modulate Na_v gating. While the binding mode of phentolamine I observe to the local anaesthetic site is in line with current consensus of literature, the presence of other binding modes highlights the possibility for more than one molecule of phentolamine to bind to the same channel and for two or more different drugs to bind to the Na_v channel at the same time **(Section 4.8)**. The experimental design throughout most parts of the thesis was supported by the usage of protein visualization tools, allowing me to make educated guesses on expected phenotype differences of mutations before creating experimental strategies. I highlight the importance of this tool for computational experts and non-experts alike, with some examples on how we can make educated guesses on mechanism of action of various naturally occurring mutations **(Section 4.9)**.

4.1 A robust system for Na_v membrane expression studies

Whole-cell voltage clamp of MI shows that the current densities are indistinguishable from untransfected HEK293t cells, most likely suggesting an extreme LoF phenotype. However, LoF of Na_vs can broadly be caused either because the protein does not exist in the membrane (ER retention, degradation etc.) or because it does not function once inserted into the membrane (gating defects). Thus, it is crucial to accurately determine whether a LoF phenotype *in vitro* is due to improper membrane expression of the channel. Immunostaining methodologies are commonly employed to test for Na_v expression (Aiba et al., 2014; Bechi et al., 2015; Cox et al., 2010). Na_vs, however, have the unique problem that the antibodies targeting the Na_v subtype of interest are not accurate, due to the very high similarity between the nine subtypes. Biochemical methods can also be used for determination of membrane proportions of the protein (Gallego-Delgado et al., 2024; Mercier et al., 2015; Laedermann et al., 2013). However, biochemistry of $Na_v1.7$ is complicated by the afore mentioned non-specificity of the antibodies, the necessity for high expression, and the large size of the protein.

A more recent approach involves addition of various tags that can be attached to the channel and targeted by specific antibodies with relatively high precision (Tyagi et al., 2023; Dulsat et al., 2017; Mercier et al., 2012). However, deciding the position of the tag in the protein is a non-trivial task. Tags can be inserted either intracellularly (Reinhard et al., 2013) or extracellularly (Mercier et al., 2012; Baroudi et al., 2001). Extracellular tagging prevents the need to permeabilize the membrane to allow antibodies to function against the tag. Utilizing the advantage that Na_v subtypes are highly similar in their sequence, locations of the extracellular tags found in $Na_v1.5$ were mapped into $Na_v1.7$. These locations were all present in D1. With previous work from (Yi Liu et al., 2024) showing HA-tagging of $Na_v1.7$ at the C-terminus is possible, a HA tag was inserted into the protein at three extracellular locations (Figure 25).

The three extracellular positions used for HA tagging only minimally interfere with the gating of the channels and show substantial expression to allow for validating membrane expression without permeabilizing the membrane (Figure 27). One of the positions HAext3 (between L293-E294) was mapped from the position used for insertion of a FLAG tag in $Na_v1.5$ (Reinhard et al., 2013). While the insertion of a FLAG tag in $Na_v1.5$ resulted in a 5mV depolarizing shift in $V_{1/2,act}$, changed selectivity as observed in the altered reversal potential and a 4-fold reduction in current densities (Reinhardt et al., 2013), no such differences were observed in the HA-tagged $Na_v1.7$ used in this thesis (Figure 26). One possible explanation could be the sequence difference between the two tags. The FLAG tag sequence “DYKDDDDK“ is highly polar while the HA tag sequence "YPYDVPDYA“ is relatively more hydrophobic. The extracellular loop between S5 and P1 have been postulated to control the electrostatic field near the VSD, thereby altering gating properties of Na_vs (Bennett et al., 1997). Addition of such highly charged tags can thus alter the electrostatic surface of the extracellular region, ultimately resulting in changed gating properties. While more studies are needed to confirm such an effect, the selection of tags and their positioning extracellularly should be performed keeping in mind the possibility of interfering with gating processes far from the site on which the tag is introduced. Another limitation is the extent to which subtype transferability can work. The extracellular loops are quite non-conserved across the nine subtypes and thus may play a vital role in subtype-specific gating differences via the above-mentioned electrostatic mechanism. Utilizing similar positions in other subtypes can cause unexpected changes to their gating properties.

The three positions used in my thesis highlight D1 as a robust region for introduction of tags for membrane expressions studies. It however raises the question if equivalent positions in other domains can tolerate the addition of any tag. Domains such as D4 are important for fast inactivation of the channel (Capes et al., 2013), and alteration of electrostatic fields close to this VSD could change fast inactivation properties. All experiments involving the HA tag did not utilize co-expression of ß subunits, which have been shown to alter expression and gating of Na_vs (Bouza and Isom, 2018). Although this may not alter the results observed in this study, it is a possibility that the HA tags can interfere with the binding of the ß1/ß3 subunit. Though not statistically significant, a trend emerged wherein the addition of the HA tag caused a reduction in current densities compared to untagged channels (Figure 26A). Even though this was not to the extent of adding a GFP molecule (Figure 24A), it is important to keep in mind that expression levels may reduce when additional tags are inserted into Na_vs in any position.

In my case, the selection of the HA tag was rooted more in the fact that it is widely used for immunostaining, is small and was previously used in our institute successfully for insertion in the C-terminus and understanding the development of Na_v1.7 in iPSC-derived sensory neurons (Yi Liu et al., 2024). HA tags are small, hydrophobic and hence have a minimal chance of interfering with Na_v gating and expression. The specificity of the antibody that targets these tags also allows them to be easily used with secondary cell lines like HEK cells. This does not necessitate that only HA tags be extracellularly inserted into Na_vs. Various other tags such as Halotags that can be targeted by nanobodies exist and can be utilized for studies on ion channels in primary cultures like DRG neurons and also iPSC-derived neurons (Higerd-Rusli et al., 2023).

The immunostaining results also showed that both extracellularly HA-tagged WT and MI both express in the membrane (Figure 27). While the power settings of the laser and analysis of the images were consistent to ensure comparison between WT and MI, immunostaining does not give accurate quantification of Na_vs in the membrane. Biochemical techniques such as surface biotinylation are necessary for this and provide a next step in quantification of membrane expression. While permeabilization was avoided to ensure that the signal observed is most likely due to membrane-bound Na_vs, the fixing process can induce damage to the cells, causing some cells to allow antibodies to also go into the cell and stain intracellularly. Fixing also prevents us from making any time-related inferences. One possible avenue could be to use live-cell staining to understand the turn-over rate of the mutant once transfected.

Even with all limitations considered, the extracellular tagging strategy used in my thesis provides three robust locations to test for membrane expression of LoF mutations in Na_v1.7 and a pipeline by which knowledge from other subtypes can be used to predict possible locations in Na_v1.7 that can minimally affect the gating of the protein.

4.2 Pore collapse as a patho-mechanism of LoF

CGMD was used as an *in silico* tool to understand dynamic changes to structure upon introduction of the MI mutation. Unlike all-atom simulations, CGMD allows for longer, computationally less intensive simulations at the expense of a loss of resolution. Given the location of M899 residue in the pore module and the LoF phenotype observed *in* vitro, I expected more global changes to the geometry of the pore and hence decided the loss of resolution was acceptable given the advantage of relatively longer and computationally inexpensive simulations. The MI was shown to collapse the outer pore, by causing a bottleneck at the level of the outer vestibule (Figure 28). Many of the recently published human Na_v cryo-EM structures show the radius at the selectivity filter as being one of the bottlenecks in the permeation pathway

(G. Huang et al., 2022a; Li et al., 2021b; Shen et al., 2019). The selectivity filter is composed of the “DEKA” motif, a filter that controls for sodium selectivity over other monovalent cations. The selectivity comes specifically due to the lysine (K), a crucial evolution in eukaryotic Na_vs (Spafford, 2023; Sun et al., 1997). However, the attraction of cations occurs before the SF region through a set of negatively charged residues above the SF region, called the outer vestibule (Noreng et al., 2021). The outer vestibule region residues are also implicated in the non-trivial task of coordinating hydrated Na^+ ions with the DEKA residues (Li et al., 2023; Pan et al., 2019). The bottleneck caused by MI could thus cause this coordination to be disrupted, preventing dehydration and subsequent movement of the ion into the central cavity. Another possible mechanism for MI causing LoF could be the permanent trapping of the channels in a slow inactivated state due to alteration of the outer pore geometry. The latter may however be less convincing, since a possible mechanism for slow inactivation was shown to be caused by outer pore dilation rather than constriction in Na_v channels of the coccolithophore *Emiliania huxleyi*, and suggested as a possible mechanism of slow inactivation (Chen et al., 2024). Neverthless, pore geometry disruption – irrespective of pore collapse or dilation – may be a common mechanism by which channels slow inactivate in mammalian Na_vs.

While the simulations show interesting insights into structural changes to the protein when MI is introduced, it still has its limitations. To understand these, it is important to keep in mind two major limitations that CGMD possesses when looking at my results. The first is that it is a technique that is highly sensitive to the starting state of the structure used (Marrink et al., 2023, p. 3). In the context of Na_vs, this means that results can vary based on whether we use a fast-inactivated state or an open state. In my thesis, I utilized the fast-inactivated state published in (Shen et al., 2019) where all the VSDs are in the activated state but the pore is closed. This is an important point in the context of the second drawback – unbiased usage of CGMD will always result in oscillations around a local energy minimum due to the presence of elastic bonds. This means that if we start with a fast inactivated state with the pore closed and VSDs up, we will not observe any up-down transition of the VSDs or sudden opening-closing events of the inner pore. This limits us from looking at the possibility that MI disrupts the interface of the PM2 with VSD1. VSD1 is important for activation of Na_vs and the PM2-VSD1 interface is plastic and was shown to change in Na_v1.8 based on whether the VSD1 is activated on deactivated (X. Huang et al., 2022). The MI could alter the connections made in the PM2-VSD1 interface via local disruption of its neighborhood, preventing the flow of information from the VSD to the PM. In other words, MI may “disconnect” the movements of the VSD from the PM, preventing opening of the pore when the VSDs move up. This may be the root cause of the final effect of pore collapse observed in my simulations. Computationally intensive biasing of the simulations via metadynamics may help uncovering if such structural changes can explain the LoF phenotype caused by MI. To better elucidate the pore collapse hypothesis, application of electric fields can help understand the free energy landscape of ion flow through the pore in the presence or absence of the MI mutation. A final and non-trivial consideration is the composition of the bilayer. In this study, a single component POPC membrane was utilized for reducing complexity and due to lack of a coarse-grained representation of cholesterol at the time of study. However, the membrane composition can significantly impact the dynamics of Na_v1.7 (Albani et al., 2024).

Utilization of various amino acids in the M899 location showed a varying tendency to cause outer pore bottleneck *in silico* which could be correlated to the current densities observed *in vitro (Figure 29)*. Of these, the observation that leucine did not disrupt ion flow while its isomer isoleucine did, highlights the possible role atomic packing plays in maintaining pore geometry. Isoleucine could cause local rearrangement of the packing in PM2, rearranging the outer pore geometry and causing a bottleneck. Leucine instead could fit better in this pocket, causing minimal to no change in atomic packing in the region. Other amino acids also show no specific trend towards size, since a bulky amino acid like phenylalanine works just as well as a small amino acid like alanine. These results showcase the extremely tight packing of the pore module, and the sensitivity it possesses to changes in this packing. However, the computational results observed must be considered with the limitation of structural sensitivity in mind. All mutations are introduced via Modeller, which utilizes an energy minimization routine at the end to relax the structures (Webb and Sali, 2016). This means that each model is a little different from each other with respect to the positioning of its side chains. This invariably affects the restraints of the simulation due to its high sensitivity to the starting structure. The usage of experimental techniques, however, can offset this disadvantage since they provide validation of whether the observed computational results are indeed true. This highlights a pipeline whereby I can offset the limitations of *in silico* techniques by combining them with *in vitro* techniques to provide validation of results and ultimately get closer to finding the physiological mechanism of various mutations.

4.3 Inherent asymmetry of Na_v pore modules

While extreme scenarios of MI and MA showcase the sensitivity of atom packing in the PM2, the LoF caused by alanine mutations of equivalent residues of the other three domains calls into question whether D2 is more robust to changes in atom packing while D1, D3 and D4 are highly sensitive to these changes. D1, D3 and D4 are the only domains to have a phenylalanine in the equivalent position of M899 in D2 (Figure 30A).

To try and hypothesize the reason, differences in the four domains in $hNa_v1.7$ were investigated. D2 is the only domain that has a short extracellular loop between S5 and P1 and an extended S5, while the other three (especially D1) have very long and complex S5-P1 loops and a shorter S5 (Figure 46A). These extracellular regions are stabilized by the help of disulfide bonds (Figure 46B). However, D2 is the only domain to contain two disulfide bonds that do not exist in these long loops – one between S5 and the loop between S5 and P1, and one between P2 and S6. Putting together the shortest extracellular S5-P1 loop among the four domains and the unique disulfide bonds, D2 can easily stabilize the pore geometry. On the other hand, D1, D3 and D4 lack sufficient disulfide bridges near S5, P1 and P2 to stabilize the geometry. The disulfide bridges are all towards the long loops that are positioned extracellularly (Figure 46B). Thus, a mutation such as an alanine can rearrange the packing significantly, causing LoF of the channel.

A second observation by Dawi Bajunaid (Institute for Neurophysiology, Uniklinik RWTH Aachen, Germany) lies in the density of aromatic residues in each domain. While D1, D3 and D4 are packed from S5 to S6 with various aromatic residues, D2 is the domain with the least number of aromatic residues in the PM (Figure 47). The F344, F1378 and F1670 could thus form pi-pi interactions for stabilizing the bonds with many of the aromatic residues present in these PMs. While M899 is also surrounded by aromatic residues, it does not have the density of aromatic residues observed in the other domains (Figure 47). This would mean that the loss of methionine to an alanine would not alter how the aromatic rings pack and thus not do much to alter the pore geometry. Such asymmetries between the domains must be kept in mind so that one can efficiently take findings about LoF pathomechanisms from one domain and map it to another. However, it is unclear if larger amino acids like methionine or other aromatic amino acids like tyrosine in D1, D3 and D4 can still function normally without disrupting pore packing. Further mutagenesis experiments can help in understanding the extent of the asymmetries between the domains.

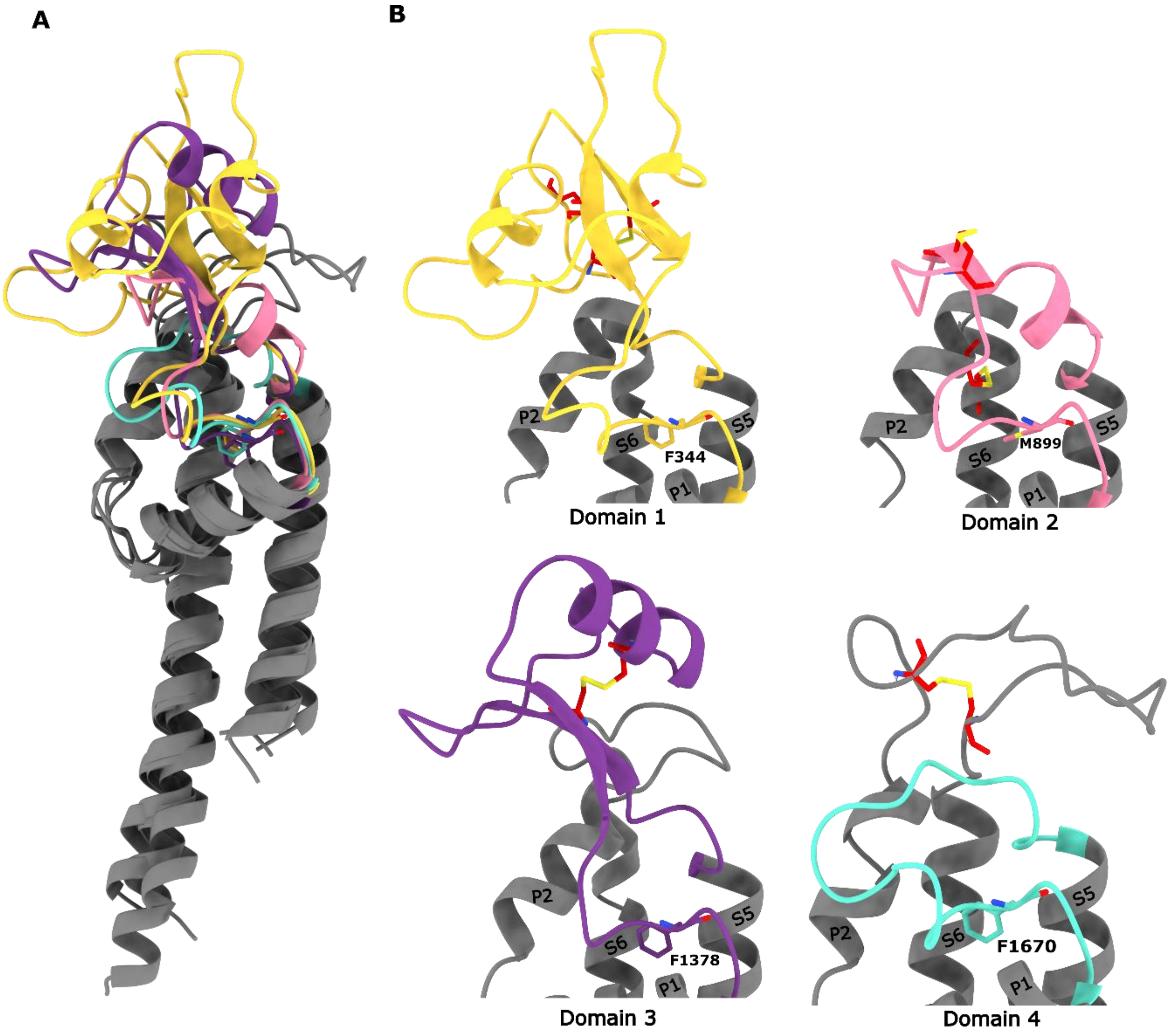

Figure 46 – Structural asymmetries in the pore module architecture between the four domains of hNa$_v$1.7. (A) Structural alignment of the four pore modules in each domain (PM1-PM4). Only the extracellular loop connecting S5 and P1 are shown in domain specific colors (**D1**, **D2**, **D3**, **D4**). **PM2** contains the smallest linker between the different helices, while **PM1**, **PM3** and **PM4** have large linkers of varying secondary structures. **(B)** Close-up of the extracellular loops of the four PMs. The **F344**, **M899**, **F1378** and **F1670** residues are shown as sticks. Various disulfide bonds between cysteine residues **(red sticks)** exist to stabilize the long loops. **PM2** is the only domain with a disulfide bridge stabilizing the P2 and S6 helices directly. The shorter loops and extra disulfide bridges close to the hydrophobic core of **PM2** allow it to be more forgiving of mutations. **PM1**, **PM3** and **PM4** have disulfide bridges stabilizing the longer loops and hence could be more sensitive to mutations.

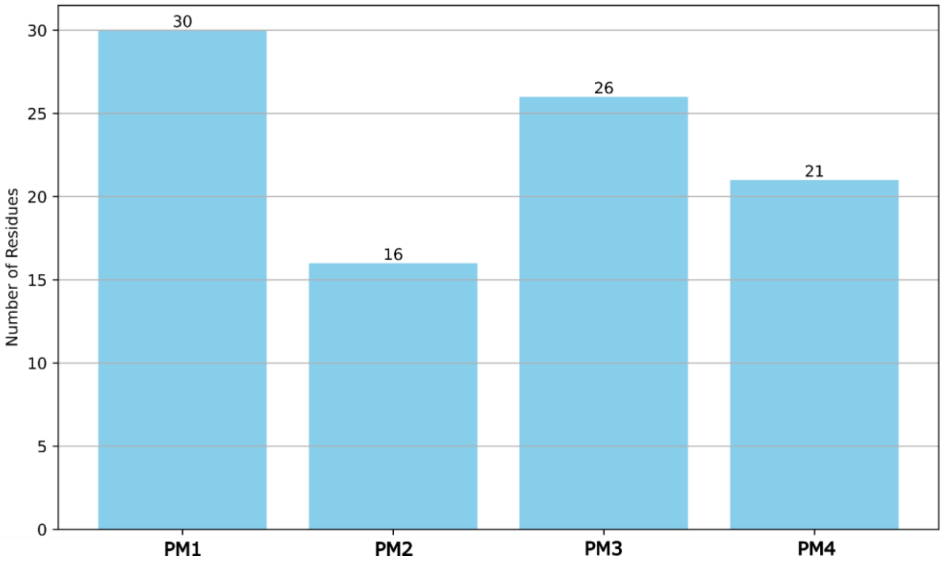

Figure 47 – PM2 has the least number of aromatic amino acids compared to other domains. The number of aromatic amino acids (y-axis) in pore modules of domain 1-4 (PM1-PM4) in the hNa$_v$1.7 structure published by (G. Huang et al., 2022a). The aromatic amino acids are phenylalanine, tyrosine, histidine or tryptophan. The pore module consists of the S5, P1, P2, S6 and all extracellular and membrane re-entrant loops connecting these helices. The graph was generated using Python3. While PM1, PM3 and PM4 have more than 20 aromatic amino acids, PM2 has the least number of these residues. Analysis performed by Dawi Bajunaid (Institute for Neurophysiology, Uniklinik RWTH Aachen, Germany).

4.4 Usefulness of D1-D2 and its role in dimerization

The inter-domain linkers D1-D2 and D2-D3 are important for a host of interactions intracellularly with secondary proteins and undergo various post translational modifications (Lorenzini et al., 2021; Chew et al., 2019; Iqbal et al., 2018). The D1-D2 in Na$_v$1.7 is 310 amino acids long and contains various motives including the conserved ER retention motif (Tyagi et al., 2023) and equivalent residues that make-up a putative dimerization site involving the 14-3-3 protein in Na$_v$1.5 (Clatot et al., 2017). However, I show that removal of exon 11 which codes for 96 amino acids in D1-D2 minimally alters gating of Na$_v$1.7 (Figure 31 and 32). This is in line with a previous study of exon 11 deletion in Na$_v$1.8, where no gating changes were observed (Schirmeyer et al., 2014, p. 11). Exon 11 is also a region with splice variants of Na$_v$1.7, with a long form having 11 amino acids and a short form lacking 11 amino acids in D1-D2 (Chatelier et al., 2008). A more recent pre-print did a study of the D1-D2 in Na$_v$1.5, showcasing that deletion of most sections of the D1-D2 did not alter gating of Na$_v$1.5 in HEK293t cells (Wagner et al., 2024). Put together with my results, this raises the question about the usefulness of the D1-D2 linker across all subtypes and by extension also the D2-D3 to the overall gating cycle of Na$_v$s and the evolutionary role behind splicing of exon 11. Given the disordered nature of most of these regions, many cryo-EM structures cannot resolve these regions. However, structure prediction tools like Alphafold offer an opportunity to better understand the role these linkers play in Na$_v$ gating. This is currently still a challenge given the conformational plasticity of Na$_v$s and the lack of conformational diversity in human Na$_v$ structures published thus far.

Regardless, one interesting correlation that can be made regarding the loss of exon 11 is the possible loss of dimerization between Nav subunits. Na$_v$s have been hypothesized to form dimeric units, connecting with each other via the 14-3-3 protein and possibly coupling their gating (Clatot et al., 2017). The region exon 11 codes for in hNa$_v$1.7 contains the equivalent set of residues involved in 14-3-3 binding in hNa$_v$1.5 (Clatot et al., 2017). Although more recent studies call into question whether such dimerization between wild-type channels can happen physiologically (Selimi et al., 2023) and if the 14-3-3 is really important for such dimerization events (Iamshanova et al., 2024), many studies agree that dimerization is highly likely in diseased states involving heterozygous mutations (Iamshanova et al., 2023). For example, mutated Na_vs causing LoF can dimerize with wild-type Na_vs and exert their "negative" effect on the latter. This dominant negative effect is observed in the case of LoF as a 75% reduction in current densities when the ratio of wild-type to LoF mutant is 50%:50% (O'Neill et al., 2022). In this thesis, however, we observe that the current densities of ex11del reduce linearly with increasing amounts of MI (Figure 33). This hints towards a possibility that dimerization is lacking due to exon 11 being deleted. While the results could potentially point towards why the patient has only a partial and not complete loss of pain – one allele functions while the other doesn't – it fails to do so convincingly due to two major unanswered questions.

Firstly, it has been postulated that an almost 80-90% block of Navs is necessary to achieve complete analgesia (Mulcahy et al., 2019). If we assume a 50-50 expression of the ex11del and MI in the patient, our results suggest a lack of the dominant negative effect, but 50% of the ex11del must be enough to sustain nociception without any drop in sensitivity. A possible explanation for this question could be the regulation of the alleles through development. During the patient's early years, the MI may be over-expressed relative to the ex11del, causing almost 80-90% of the channels to cause complete LoF and clinically manifesting as loss of pain. Over adolescence, the splicing variant (ex11del) starts to express more, decreasing the MI channels present in the membrane and slightly increasing nociception. Such mechanisms can happen at a translation level via anti-sense RNAs towards Na_vs (Koenig et al., 2015) or via more general transcriptional interference phenomena (Shearwin et al., 2005). This would however require more physiological systems such as iPSCs of the patient or human DRGs and advanced transcriptomic approaches to quantify RNA levels.

Secondly, my results show-casing the almost similar gating of ex11del and WT raises the following question - if the ex11del could gate in a similar way to WT, why would the father of the patient not have a reduced sensitivity to pain? The father also has a heterozygous split in the Na_v gene, with one allele containing the WT and the other containing the point mutation MI (Figure 8). This could be explained by considering the lack of dimerization. While LoF variants cause a dominant negative effect via reduction in current levels *in vitro*, GoF mutants can also exert their "positive" effect onto WT channels via dimerization (Rühlmann et al., 2020). If we consider the WT to be a GoF mutant in relation to the MI, then we could postulate a reason as to why the father does not have loss of pain while the patient does. In the father, WT has the residues necessary for dimerization due to presence of exon 11 and could exert its "positive" gating effect onto the MI, rescuing it and preventing LoF (Figure 48A). The mother has two functional alleles that do not dimerize due to the lack of exon 11 in one allele. However, since both are functional and gate similarly, there is no LoF induced (Figure 48B). The patient however contains MI and ex11del. Since ex11del cannot dimerize, it cannot exert its "positive" gating effect onto the LoF-causing MI, preventing the rescue of MI and possibly reducing nociceptive capabilities (Figure 48C). Co-expression studies involving varying ratios of WT and MI, and ex11del and MI could answer whether this is possible. If the hypothesis is true, increasing MI should cause only minimal change to current levels of WT due to rescue by dimerization. However, this explanation does not consider the possibility for physical dimerization of Na_vs and assumes that dimerization primarily happens via the 14-3-3 protein. Also, transient transfection strategies over-express the protein of interest. Thus, varying ratios of two different DNAs might not necessarily mean those specific amounts of protein are expressed in the cell, resulting in a degree of variability that reduces the effect size of the phenomenon and prevents us from accurately gauging if dimerization exists. This is also visually observable from my results co-expressing MI and ex11del, where the error bars representing the SEM are large (Figure 33). One possible counter strategy could involve utilizing the extracellular tagging approach mentioned previously, tagging each of the WT/ex11del or MI with two different tags and using high-resolution imaging to see if dimerization events can happen at the membrane. This is however beyond the scope of the thesis but offers further avenues to understand what real role dimerization plays to the overall functioning of Na$_v$s.

All things considered, my results involve the usage of secondary cell lines such as HEK293t cells. While these systems allow us to understand how Na$_v$s function and what the effect of various mutants are, they are still not a system close to the physiological reality of the body. To better understand how exactly the mutants affect neuronal functioning in the patient, usage of iPSC-derived sensory neurons from the patient can help us understand the effects of this heterozygous mutation and how it alters AP generation.

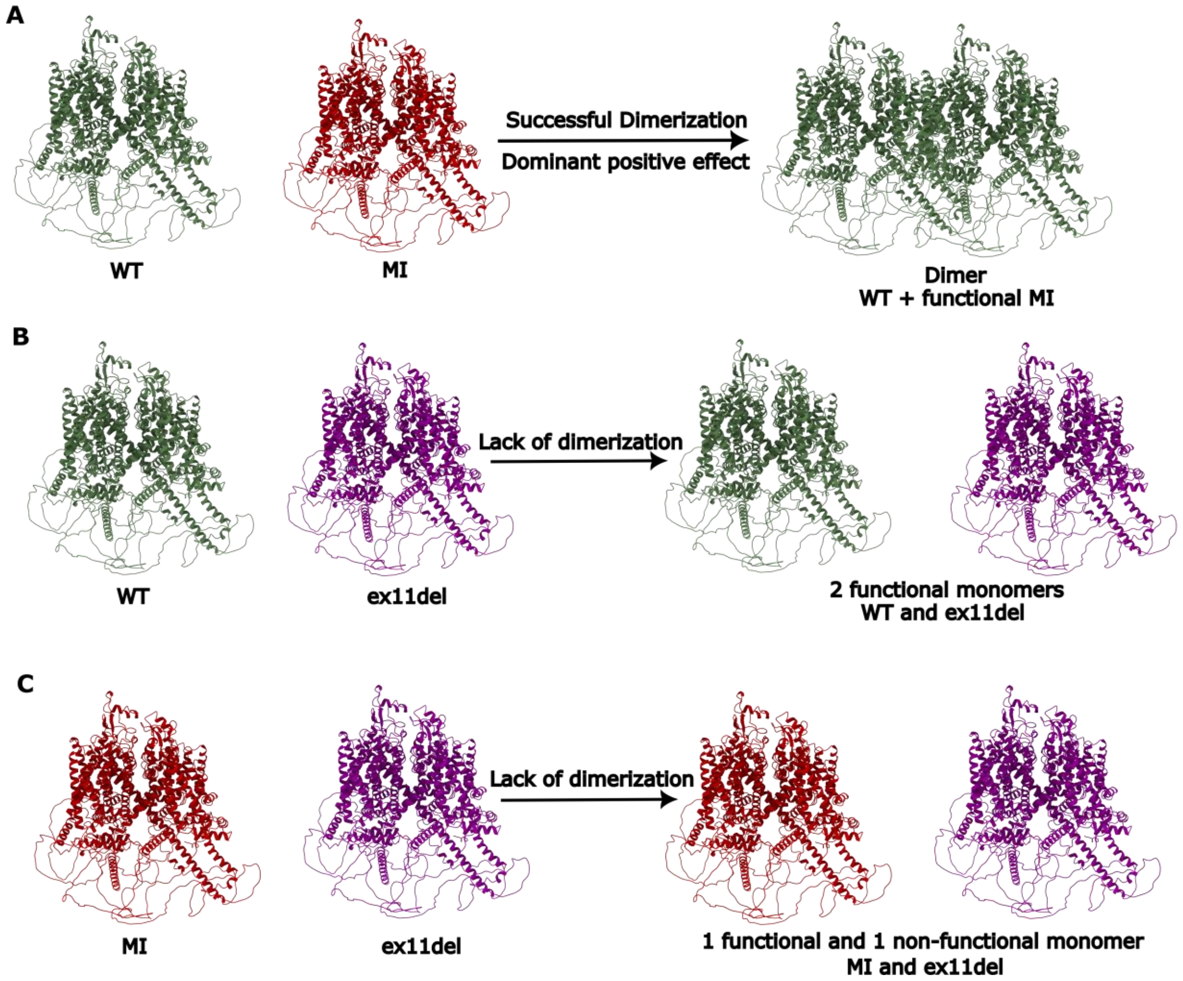

Figure 48 – The "dominant positive effect" can drive phenotypical differences between the patient suffering from insensitivity to pain and his parents. **(A)** The father of the patient carries a **hNa$_v$1.7 wildtype (WT)** allele along with the point mutation **hNa$_v$1.7 p.M899I (MI)** in the other allele. As the dimerization site is intact, membrane bound **MI** channels dimerize with **WT**, and the **WT** rescues the **MI** pore collapse by coupled gating – a phenomenon dubbed "dominant positive effect" in this study. **(B)** The mother carries **WT** and an intronic variant **hNav1.7 c.1602+2delT that skips exon 11 (ex11del)**. Exon 11 codes for residues involved in dimerization, preventing any dimerization between the two channels. However, **WT** and **ex11del** are both functional and hence does not translate to LoF phenotypes. **(C)** The patient carries **MI** and **ex11del**. Since **ex11del** cannot dimerize, the patient has expression of one functional and one non-functional channel, causing a partial insensitivity to pain.

4.5 Two mechanisms, similar outcome – geometrical properties of the helix region of D3-D4 and D4 S4-S5 control fast inactivation

While the PM is important for control of ion flow and the root of potential LoF mechanisms, the IFM motif is another important region that controls fast inactivation of the channel. Fast inactivation is an important gating process evolved in mammalian Na_vs, to quickly stop the conduction of Na^+ in a few ms after opening (Körner and Lampert, 2020). Many GoF mutations of $Na_v1.7$ cause pain disorders resulting in hyperactivity and intense burning pain to physiological stimuli (Drenth et al., 2005; Eberhardt et al., 2014). Paroxysmal extreme pain disorder (PEPD) is one such disease phenotype, typically observed to start during infancy (Fertleman et al., 2006). (Dib-Hajj et al., 2008) showed via electrophysiological characterization that a novel mutation $hNa_v1.7$ p.M1627K in a PEPD patient disrupted the voltage-dependence of steady-state fast inactivation by causing a depolarizing change. Aylin Kesdoğan (Institute for Neurophysiology, Uniklinik RWTH Aachen, Germany) electrophysiologically characterized another novel PEPD-causing mutation $hNa_v1.7$ p.M1628K, which showed a similar large depolarizing shift in voltage-dependence of steady-state fast inactivation (Figure 7). With both mutations showing a disruption of fast inactivation, it was imperative to understand the structural mechanism of this disruption.

With the goal of uncovering a coarse mechanism for fast inactivation disruption, the CGMD approach was utilized. However, CGMD requires the introduction of restraints to maintain the secondary and tertiary structure of the protein (Marrink et al., 2023). This causes unwanted loss of flexibility of the protein. (Lin et al., 2024) provided an improved methodology to overcome this limitation, by targeted removal of restraints to increase local flexibility of the region. This could be applied in the current study by removing the restraints between the D3-D4 and other parts of the protein. This would increase the flexibility of the D3-D4 and capture any mutational effects on IFM binding. The D3-D4 contains a short helical region, whose internal restraints were maintained to ensure the helicity of the region is not lost.

As expected, simulations showed that the overall probability of IFM binding is shifted to unbound conformations in both $hNa_v1.7$ M1627K and $hNa_v1.7$ M1628K (Figure 37). The more interesting difference was in how this shift was achieved in the two mutations. While $hNa_v1.7$ M17628K altered the distance between the helical region of D3-D4 and the D4 S4-S5 helix, $hNa_v1.7$ M1627K changed the relative orientation of the two helices to more perpendicular angles (Figure 35 and Figure 36 respectively). The first change is easier to explain – the packing of the two helices is seen in multiple cryo-EM structures of $hNa_v1.7$ in the fast inactivated state to be quite tight (G. Huang et al., 2022a, 2022b; Shen et al., 2019). Lysine thus causes hydrophobic mismatch in the region, preventing efficient packing of the helix and ultimately leading to IFM unbinding. Such hydrophobic mismatches in the D3-D4 is not uncommon, as shown by the IEM-causing mutation $hNa_v1.7$ p.A1632E that also causes hydrophobic mismatch in the IFM binding pocket *in* silico (Rühlmann et al., 2020). The second observation is a more interesting one, since most eukaryotic cryo-EM structures are solved in one of many fast-inactivated conformations. Although an "open" state structure and an "weakened" IFM-bound structure exists, they do not show huge changes in the orientation of the two helices (Jiang et al., 2021b, 2021a). The only solid evidence for helix orientation driving fast inactivation comes from the chimeric cryo-EM structure of the Nav from the American cockroach (Na_vPaS) combined with the VSD4 of $hNa_v1.7$ (Clairfeuille et al., 2019). In this structure, the relative orientation of the helical region of D3-D4 is almost perpendicular to the D4 S4-S5, in stark contrast to the fully fast inactivated state where the orientations are more parallel (Appendix Figure S5). I hypothesize that fast inactivation requires the fulfilment of two geometrical constraints – the tight packing of the two helices and the parallel orientation of the two helices. Disruption of any one of these geometrical restraints can alter the probability for IFM binding to more unbound conformations. This, however, must be understood with the caveat that no human Na_v structure is published showcasing a possible non-inactivated state. Our understanding that rotation of the helices could be important stems from the only known non-inactivated-like structure from the American cockroach (Clairfeuille et al., 2019). While one can easily verify disruption of fast inactivation predicted *in silico* as gating changes to fast inactivation parameters (for e.g. depolarized steady-state fast inactivation curves) *in vitro*, it is a challenge using this method to pinpoint the effect to either disruption of translation or rotation of the helices as electrophysiological techniques lack the temporal resolution to capture such events. Discerning and validating these geometric properties experimentally will heavily rely on structural prediction methodologies such as NMR spectroscopy or cryo-EM techniques.

A mechanism not explored in this thesis is the fast inactivation “switch” mechanism described by (Clairfeuille et al., 2019). A limitation of our simulation models is the lack of the C-terminal region. (Clairfeuille et al., 2019) argued that the fast inactivation process requires the breaking of two switches – one between the gating charges of VSD4 and C-terminus, and another between D34 and C-terminus. Aylin Kesdoğan (Institute for Neurophysiology, Uniklinik RWTH Aachen, Germany) showed that the onset of fast inactivation is slower for the $hNa_v1.7$ M1627K compared to the $hNa_v1.7$ M1628K, with both much slower than $hNa_v1.7$ WT (Figure 7B). A possible hypothesis could be related to the positioning of the two amino acid side chains close to switch 1. VSD4 activation has been shown to be very important for the initiation of fast inactivation (Capes et al., 2013). Thus, strengthening this switch by either M1627K or M1628K to varying degrees can make it harder for the VSD4 to break switch 1, thus slowing the activation of VSD4 and the initiation of fast inactivation. Researching into such a mechanism however requires extensive mutagenesis and MD studies that are an avenue for further research.

4.6 Membrane rigidity controls Na_v gating

Cholesterol as a lipid species has been shown to influence the gating of a variety of membrane proteins (Zakany et al., 2020) and also control the fluidity of the bilayer (Lundbæk et al., 2004). In the context of inflammatory pain, this was seen as a shift in the population of $Na_v1.9$ from cholesterol-rich lipid rafts to cholesterol-poor regions of the membrane (Amsalem et al., 2018). However, such effects have not been studied in detail for $Na_v1.7$. Simone Albani (IAS-5/INM-9, Forschungszentrum Jülich, Germany) showed *in silico* that reduction of the cholesterol composition in the membrane generated the expected effects of decreased membrane fluidity, but also interestingly altered the geometrical properties of $Na_v1.7$ (Figure 9). Having observed *in-silico* changes, an *in vitro* validation of these predictions was necessary.

An important part of designing such an experiment was to find a method to accurately mimic the depletion of cholesterol from the bilayer. A commonly used agent is methyl-ß-cyclodextrin (MßCD), a cyclic compound that can chelate cholesterol out of the membrane (Kilsdonk et al., 1995). By using 5mM of MßCD, cholesterol content of HEK293t cells transfected with $hNa_v1.7$ WT were depleted by incubating them for 1 hour before patching. Due to the over-expression of these channels, a reduced sodium concentration extracellularly (40mM compared to a physiological extracellular solution with 140mM sodium; Table 2) was used to control the magnitude of the inward sodium currents and clamp the voltage accurately. Depleting cholesterol increased current densities, shifted voltage-dependences of both activation and steady-state fast inactivation in a hyperpolarizing direction, hastened time to peak and onset of fast inactivation without altering recovery from fast inactivation (Figures 38-40, Tables 15-17). The usage of MßCD for cholesterol sequestration is not without limitations. While there is high specificity for MßCD to remove cholesterol from the bilayer, it has also been shown to remove other phospholipids from the membrane (Zidovetzki and Levitan, 2007). Thus, the extent to which the removal of other phospholipids contributes to the gating effects observed is unclear. Cyclodextrins have also been observed to interact with various transmembrane receptors (Zidovetzki and Levitan, 2007). Due to its hydrophobic composition, it is not surprising that MßCD could interact with hydrophobic pockets in various transmembrane proteins. Na_vs also have such hydrophobic regions, namely the side fenestrations, where uncharged and lipophilic compounds can enter and bind to the channel (Körner et al., 2022). It could be likely that MßCD also binds to these fenestrations, although the extent to which this can happen and its contribution to the effects is unclear. Cholesterol sequestration can also decrease the quality of the patch of the cells, introducing noise into the system. While the current levels in my study are much higher than the noise introduced, it prevents us from looking into properties such as persistent/late currents which require a low-noise recording for accurate measurements. This is however a weaker argument, which can be negated due to the gating changes observed – the channel when cholesterol-depleted starts fast inactivation quicker and require relatively lower depolarization to push channel populations into complete fast inactivation without altering recovery kinetics (Figures 38-42). Even with the limitations in mind, I argue that the usage of MßCD results majorly in the sequestration of cholesterol, and the gating changes can be attributed primarily to this sequestration. A future step to convincingly answer such a question would involve lipidomic profiling of the cells before and after addition of MßCD to observe changes in cholesterol content of the cells.

The plethora of changes observed are hard to bucket as either GoF or LoF. For instance, while increased current densities and hyperpolarizing shift in activation are considered GoF effects, hyperpolarizing shifts in fast inactivation are considered LoF effects. Such effects on the channel can be mediated by both direct and indirect effects of cholesterol. Cholesterol is shown to alter membrane fluidity, and Na_vs undergo many conformational transitions throughout its gating cycle. A combination of these two phenomena – i.e. easier conformational movements across a fluid membrane - can be used to explain the changes observed – (1) A fluid membrane means that more of the channel population's VSD1, 2 and 3 can transition faster to "up" states thus requiring less depolarized voltages to achieve activation and achieving peak currents faster (2) more of the channel population's VSD4 can transition faster to "up" states thus requiring less depolarized voltages to achieve fast inactivation and less time to start fast inactivation and (3) more of the channel population is active at a given voltage, increasing current densities. Thus, a fluid membrane could drive hyperexcitability-like phenotypes, while cholesterol-rich domains like the lipid-rafts have more control on the gating transitions of $hNa_v1.7$. Direct effects, however, cannot be ruled out since cholesterol was found to bind directly to the side fenestrations and VSDs of $hNa_v1.7$ *in silico* (Figure 9B).

The indirect effects of cholesterol depletion also raise another intriguing possibility. Previous studies have shown that shear stress of the cell membrane can alter gating of $hNa_v1.7$ and $hNa_v1.5$, with effects similar to effects observed when depleting cholesterol (Maroni et al., 2019; Körner et al., 2018).These effects were reversed by the co-expression of the ß1 subunit in $hNa_v1.7$ but not in $hNa_v1.5$ (Maroni et al., 2019). Such a subtype-specific difference raises the question – are effects of ß-subunits on Na_v channels mediated via localized alterations in the membrane fluidity?

The ß subunits can either bond covalently via a disulfide bond (ß2 and ß4) or non-covalently via various interactions (ß1 and ß3) to the alpha subunit (Bouza and Isom, 2018). Although the effects of various ß subunits are seen across all nine subtypes, recent cryo-EM structures have allowed an interesting observation to be made between TTX-S (Na$_v$1.1-1.4, Na$_v$1.6-1.7) and TTX-R channels (Na$_v$1.5, Na$_v$1.8-1.9). TTX-S channels have a cysteine residue that can disulfide bond with a cysteine residue in the Ig-domain of ß2 or ß4, a residue not present in TTX-R channels (Jiang et al., 2020). ß1 was observed in various cryo-EM structures of Na$_v$1.7 (TTX-S), with the Ig-domain making a host of interactions with the extracellular regions of Na$_v$1.7 (G. Huang et al., 2022a, 2022b; Shen et al., 2019). Not much was known regarding the binding interactions of ß1 with TTX-R channels, until (Jiang et al., 2020) showed that a possible reason for ß1 not co-crystallizing with rat Nav1.5 is due to the presence of an additional glycosylation site only observed in TTX-R channels that can hinder the binding of the Ig domain. Such a difference, along with the concept of membrane fluidity, can help explain why stress-mediated effects on hNa$_v$1.7, but not Na$_v$1.5, are rescued by ß1. The ß1 Ig-domain is an important mediator in this mechanism – (1) during shear stress, the membrane has an increase in its fluidity, allowing channels (both TTX-R and TTX-S) to cycle faster through their various conformations. (2) Upon presence of the ß1, the Ig domain can effectively bind to TTX-R channels, restricting the local fluidity of the membrane and movements of the channel. This reverses the stress-mediated effect. (3) In TTX-S channels, such binding of the Ig-domain cannot occur and hence cannot reverse the effects of membrane stress. This hypothesis is summarized in Figure 49. A recent pre-print has shown that other secondary proteins like the FGF-13 can also alter Na$_v$ gating via membrane-mediated effects (Gade et al., 2025).

Testing this hypothesis allows us to really understand the mechanism of action of ß-subunits on Na$_v$s, the role the Ig-domain really plays in mediating these effects and the physiological and clinical relevance of any subtype-specific differences that can exist. Testing such a hypothesis would require multiple mutagenesis studies – various constructs of the ß-subunit to pinpoint the role of the Ig domain, chimeric mutations between TTX-S and TTX-R channels to find the exact binding site of the Ig-domain and if such effects are indeed subtype specific, cholesterol enrichment studies to understand if such effects are reversible, and lipidomic analyses to quantify better the amount of cholesterol present or absent in the cell. This represents an avenue for research to better understand the functioning of Na$_v$s and their interactome and push towards a possibility for subtype-specific drug design.

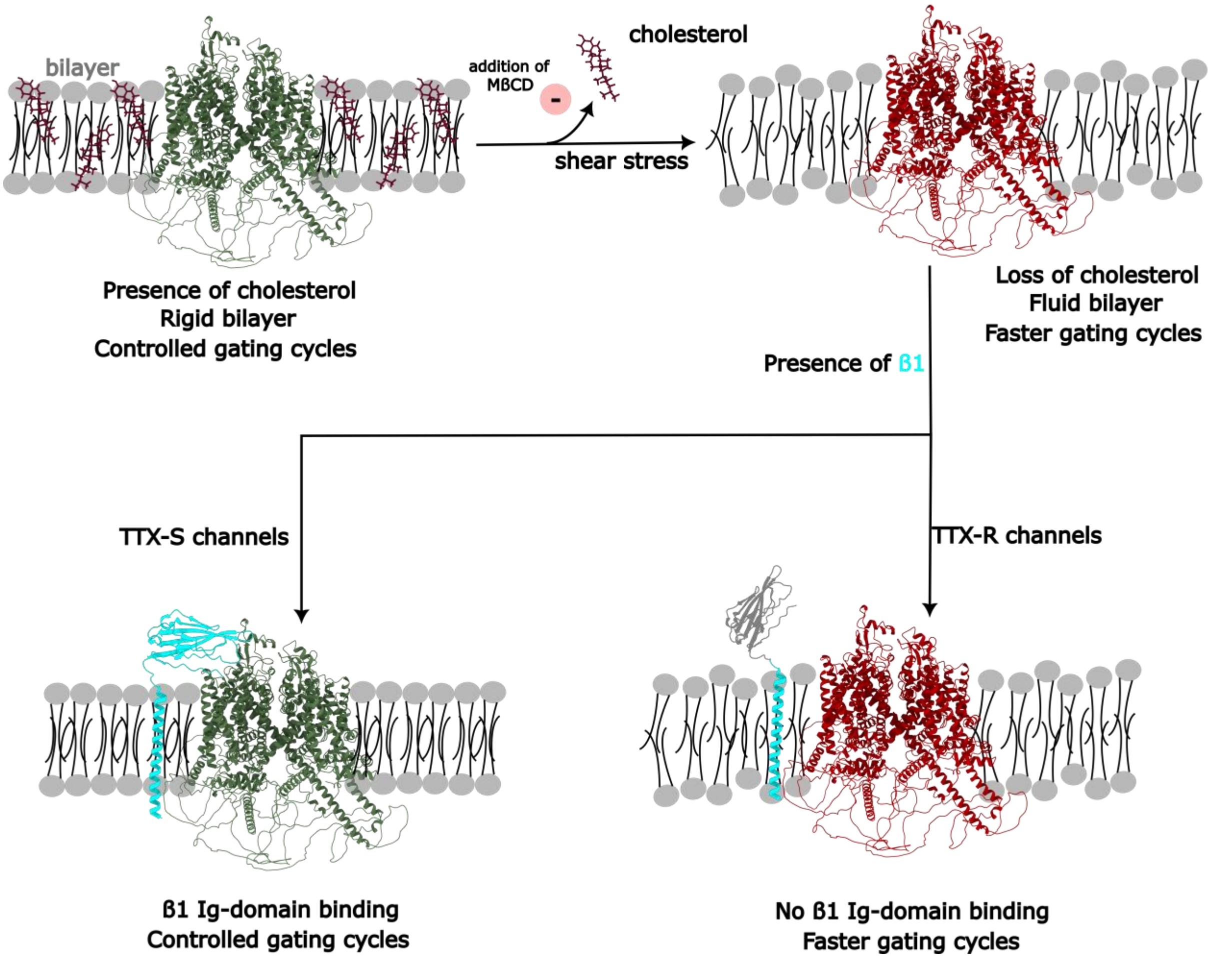

Figure 49 – Membrane-fluidity as a subtype-specific control mechanism for ß1 rescue effects of membrane stress on Na$_v$ gating. In a bilayer with cholesterol molecules **(red sticks)**, the membrane fluidity is controlled and thus restricts the rate at which Na$_v$s undergo their gating transitions. With the addition of either methyl-ß-cyclodextrin to remove cholesterol or application of shear stress to mechanically alter membrane shape, membrane fluidity is increased, allowing Na$_v$ channels to now increase the rate of their gating transitions and subsequent activity. Presence of **ß1** can rescue these effects in a subtype-specific manner. In TTX-S channels, binding of the Ig-domain of **ß1** is possible, and hence restricts gating movements, rescuing them. In TTX-R channels, Ig-domain of ß1 cannot bind and cannot rescue these channels from stress-mediated effects.

4.7 Local anaesthetic mechanism of action and secondary sites for drug binding

Local anaesthetics work by acting on Na$_v$s, blocking their ionic conduction and hence inducing a loss of sensation of pain. Binding of LAs are typically thought to occur via a binding site close to the center of the channel, in the pore axis (Körner et al., 2022). This LA site is a primary target, that may also be utilized by drugs previously not thought to induce anaesthesia.

Phentolamine is one such drug, previously utilized to reverse effects of anaesthesia in dental surgeries (Prados-Frutos et al., 2015). Phentolamine was shown using rigid body docking in the current study to paradoxically bind to the LA site *in silico* (Figure 45), in a spot similar to where the anti-arrhythmic quinidine was shown to bind in hNa$_v$1.5 (Li et al., 2021b). Rigid body docking involves the binding of a “flexible” drug of interest to a location in a “rigid” structure – meaning the structure does not change its conformation or side chain positions upon binding of the drug (Pujadas et al., 2008). While drug molecules are flexible and can rotate around a torsion site, protein binding sites are also plastic and can change when a drug binds in that location (Pujadas et al., 2008). Rigid body docking also requires the generation of a grid where the drug can search for the best binding position onto the structure. A larger grid while allowing for a "blind" search increases computational expenditure while reducing the accuracy of the results. Thus selecting the right grid is also crucial for obtaining accurate binding poses of the drug. The way in which I circumvented the first problem is by using a drug-bound structure of $hNa_v1.5$, where the anti-arrhythmic quinidine was present in the LA site (Li et al., 2021a). This meant that the conformation of the channel is highly likely to be close to if a LA was to bind to it. The second problem of grid selection was solved by utilizing experimental evidence which showed two residues F1760 and N1765 that majorly control binding of phentolamine and mexiletine (Toklucu et al., 2025). I used these two residues to build a grid cube of $30x30x30A^{o3}$ to allow for binding pose searches in the side fenestrations and the intracellular gate. Such a search space enabled a good compromise between computational resources and accuracy of the predictions.

Even so, using only the best structure requires a high level of accuracy which rigid body docking cannot offer despite the measures mentioned above to mitigate some of the limitations. A further step was utilized to ensure all the results were used and multiple runs of the docking procedure were done to account for computational variability. For this, I performed five different runs of the same docking procedure and used K-means clustering as an unsupervised machine learning tool to cluster the poses. The 3D spatial location of the center-of-mas of the drug was used as features for clustering. Such a measure allowed to really understand trends in drug binding, rather than solely focusing on one specific affinity score. The mutations were introduced via homology modelling to see if the *in vitro* changes of reduced drug effect can be captured as varying trend in drug binding in mutated structures. We do observe that phentolamine and mexiletine binding vary from $WT_{1.5}$ to $FA_{1.5}$ and $NK_{1.5}$, with the mutations changing binding from the Qdn-like to other regions farther away from the pore axis (Figure 44). The Qdn-like site is likely high in $WT_{1.5}$ due to us using a $Na_v1.5$ structure bound to Quinidine. However, it is highly likely that LAs are likely bind at this site due to the high resolution of this structure and the existence of non-covalent interactions between the drug and F1760 (Figure 45). This can easily explain why $FA_{1.5}$ causes a drastic movement of drug clustering from this Qdn-like site to fenestration sites outside the pore axis (Figure 44). The N1765 residue, however, is not seen in any of the binding poses to directly be involved in drug binding. It is likely that the $NK_{1.5}$ acheives alterations in drug binding allosterically by changing access to the binding pocket. Homology modelling via Modeller introduces some level of noise due to energy minimization routines that exist within its procedures. This means that the shift in trends we observed may well have been considered a complete chance occurrence, if not for experimental evidence showing the importance of the residue. However, more dynamic approaches are needed to discern if this allosteric mechanism exists and how it achieves alterations in drug binding. Nevertheless, phentolamine likely achieves its effect via blocking the pore axis and disrupting the movement of the lysine residue that makes up the selectivity filter (Figure 45). The lysine residue of the selectivity filter has been shown to be involved in a "dunking" process, a necessary step to coordinate the sodium ion into the central cavity via charge displacement (Jiang et al., 2020). Binding to this primary site allows for protonable regions of the drug to hinder the "dunking" of the lysine of the SF region, preventing efficient ion coordination, blocking conduction. Deciphering such a mechanism in detail, however, necessitates the usage of advance computational techniques like MD simulations to understand how ion conduction is blocked by phentolamine.

While we focus on the Qdn-like site due to the existence of a quinidine-bound structure, the observation of the existence of various "secondary" sites, where phentolamine and mexiletine are predicted to bind, is non-trivial (Figures 43-44). Recently, a cryo-EM structure of hNa$_v$1.7 with lacosamide was published, where two lacosamide molecules can bind simultaneously to one channel (Wu et al., 2023). Such binding is also seen with pyrethroids, a chemical family of pesticides (Du et al., 2013). This could present the possibility that more than one drug molecule (phentolamine or mexiletine) can bind to the same channel via multiple “low affinity” binding sites other than the “high affinity” primary binding site where quinidine is shown to bind. Another possibility could be the binding of two different drugs to two different sites – one at the “high” affinity site and one at the “low affinity” site. For instance, Idil Tokclucu (Institute for Neurophysiology, Uniklinik RWTH Aachen, Germany) found that usage of phentolamine after application of mexiletine enhanced tonic block but not use-dependent block (Toklucu et al., 2025). This can be understood in relation to the drug docking results in the following manner. When mexiletine is already applied, it binds first to the Qdn-like “high affinity” site, inducing both tonic and use-dependent block. When phentolamine is now applied, it has already been outcompeted for binding to the Qdn-like site by mexiletine. It thus proceeds to bind to other secondary sites, enhancing tonic block. Use-dependent block is attributed to the fact that drug binding sites are changing both their accessibility and affinity with conformational transitions (Körner et al., 2022). Tonic block instead is less dependent on these changes and can be accessed regardless of the conformation. This may mean that the secondary sites such as the side fenestrations are available for access regardless of the state, allowing application of a second drug to enhance tonic but not use-dependent block due to the first drug outcompeting the second for access to the high affinity use-dependent binding site. A newer review annotating various druggable sites in Na$_v$s highlight the vast number of areas where drugs can interact with Na$_v$s, lending credence to the idea of the secondary sites observed in my study being non-trivial (Li et al., 2024). More experiments and computational simulations, however, are necessary to elucidate this mechanism.

4.8 Protein visualization – a useful tool in structure-function analyses

With the release of a various number of cryo-EM structures in the PDB database, visualization of the 3D structures allows for educated guesses on the effects of mutations based on the spatial location of the residue. Knowing that M899 is located at a buried, tightly packed region in PM2 allowed us to predict a complete LoF as an initial hypothesis and focus on the pore region. Without knowledge of the spatial location, the experimental designs would have been less specific on the pore and hence take more effort and time to accomplish. The knowledge that ex11del causes removal of residues intracellularly relating to dimerization allowed for the experimental design of co-expression studies to test for potential loss of channel dimerization. Visualization of Na$_v$1.7 structures enabled cost-effective *in-silico* methodologies to add extracellular tags, ensuring that the tags do not interfere with gating regions and hence have a higher likelihood of having success when implemented experimentally. Knowing hNav1.7 M1627 and M1628 residues are located in the D4 S4-S5 close to the D3-D4 made it easier to perform targeted removal of restraints, making it feasible to use CGMD and understand disruption of fast inactivation. The use-case of molecular visualization is not limited to the projects described in this thesis.

In 2019, a PEPD mutation hNa$_v$1.7 p.N1245S was found electrophysiologically to not have any impact on the gating when compared to wild-type (Le Cann et al., 2021). Visualization of the protein structure of hNa$_v$1.7 published by (Shen et al., 2019) (PDB ID:6J8G) allowed us to understand why – the N1245 residue is a completely exposed residue that does not interact with any important residue either in the VSD or the PM (Figure 1 in (Le Cann et al., 2021)).

Recently, the mutation hNa$_v$1.9 p.Y66S was seen in two carriers with small fiber neuropathy, who showed clinically distinct phenotypes (Van den Braak *et al., 2025*). Although structures of hNa$_v$1.9 do not exist, the rise of artificial intelligence allowed Alphafold3 to generate accurate protein structures given the sequence (Abramson et al., 2024). Using the hNa$_v$1.9 model from Alphafold3 (ID: AF-Q9UI33-F1), the residue can be localized to the N-terminal region, exposed intracellularly (Van den Braak *et al.,* 2025). Exposed intracellular serine, threonine and tyrosine residues are commonly implicated in phosphorylation (Lorenzini et al., 2021). Thus, altered post-translational modification of this mutated serine residue in the two carriers can help account for the varied phenotypes.

Understanding of Na$_v$ modulation requires in some capacity information on the spatial location of either mutants, residues or the environment. However, this does not mean that visualization is a replacement for rigorous experimental techniques. Experimental techniques remain the gold standard to precisely understand molecular mechanisms and validate any predicted hypotheses. However, experimental techniques consume time, effort and money. Using *in-silico* tools helps us to better design experiments to target specific predictions (rather than a large array of hypotheses) and reduce the costs incurred while exponentially increasing the chances of uncovering likely mechanisms.

3D visualization is not a technique that must be limited to structural biologists and computational experts– it is a technique that holds massive potential if used in a large-scale manner by experts and non-experts alike and this thesis is proof of the inter-disciplinary potential such protein visualization tools hold.

Chapter 5: Conclusion

Na_vs are membrane proteins whose proper gating is crucial for the physiological functioning of the body. Channelopathies can cause devasting disease phenotypes, that are currently incurable and take a toll on the quality of life of the affected individual. Understanding how these channels function and the mechanisms by which one can modulate their gating can help us make crucial inroads into potential treatment strategies.

This thesis takes a small step in this direction by viewing the gating via multiple scales of study (either atomic or cellular) and via various agents (natural/physiological or artificial) and putting them together to get a more holistic view of Na_v biophysics. We see that LoF of the channel can also occur via gating defects, with the possible patho-mechanism being the collapse of the outer pore. GoF of the channel meanwhile can occur via disruption of the fast inactivation process, by changing either of two crucial geometric features between the helical region of the D3-D4 and the D4 S4-S5. The membrane composition also plays an important role in tuning $Na_v1.7$ function, with removal of cholesterol showing hyperexcitability-like phenotypes. Artificial application of compounds can also modulate Nav function, as shown by the paradoxical effects of the drug phentolamine and its likely binding to the local anesthetic site blocking ion coordination and hence conduction.

These insights were achieved by the combination of findings in the molecular scale via *in silico* methodologies such as molecular dynamics, drug docking and structural visualization and findings in the cellular scale via *in vitro* methodologies such as whole-cell patch clamp and immunostaining. These combinatory approaches showcase a potential methodology for successful and logical experimental design that can improve our understanding of Na_v gating and whose findings can be utilized for improving both diagnostics and treatment strategies.

References

1. Abraham, M.J., Murtola, T., Schulz, R., Páll, S., Smith, J.C., Hess, B., Lindahl, E., 2015. GROMACS: High performance molecular simulations through multi-level parallelism from laptops to supercomputers. SoftwareX 1–2, 19–25. https://doi.org/10.1016/j.softx.2015.06.001

2. Abramson, J., Adler, J., Dunger, J., Evans, R., Green, T., Pritzel, A., Ronneberger, O., Willmore, L., Ballard, A.J., Bambrick, J., Bodenstein, S.W., Evans, D.A., Hung, C.-C., O'Neill, M., Reiman, D., Tunyasuvunakool, K., Wu, Z., Žemgulytė, A., Arvaniti, E., Beattie, C., Bertolli, O., Bridgland, A., Cherepanov, A., Congreve, M., Cowen-Rivers, A.I., Cowie, A., Figurnov, M., Fuchs, F.B., Gladman, H., Jain, R., Khan, Y.A., Low, C.M.R., Perlin, K., Potapenko, A., Savy, P., Singh, S., Stecula, A., Thillaisundaram, A., Tong, C., Yakneen, S., Zhong, E.D., Zielinski, M., Žídek, A., Bapst, V., Kohli, P., Jaderberg, M., Hassabis, D., Jumper, J.M., 2024. Accurate structure prediction of biomolecular interactions with AlphaFold 3. Nature 630, 493–500. https://doi.org/10.1038/s41586-024-07487-w

3. Adasme, M.F., Linnemann, K.L., Bolz, S.N., Kaiser, F., Salentin, S., Haupt, V.J., Schroeder, M., 2021. PLIP 2021: expanding the scope of the protein–ligand interaction profiler to DNA and RNA. Nucleic Acids Research 49, W530–W534. https://doi.org/10.1093/nar/gkab294

4. Aiba, T., Farinelli, F., Kostecki, G., Hesketh, G.G., Edwards, D., Biswas, S., Tung, L., Tomaselli, G.F., 2014. A Mutation Causing Brugada Syndrome Identifies a Mechanism for Altered Autonomic and Oxidant Regulation of Cardiac Sodium Currents. Circulation: Cardiovascular Genetics 7, 249–256. https://doi.org/10.1161/CIRCGENETICS.113.000480

5. Albani, S., Eswaran, V.S.B., Piergentili, A., de Souza, P.C.T., Lampert, A., Rossetti, G., 2024. Depletion of membrane cholesterol modifies structure, dynamic and activation of Nav1.7. International Journal of Biological Macromolecules 278, 134219. https://doi.org/10.1016/j.ijbiomac.2024.134219

6. Amsalem, M., Poilbout, C., Ferracci, G., Delmas, P., Padilla, F., 2018. Membrane cholesterol depletion as a trigger of Nav1.9 channel-mediated inflammatory pain. The EMBO Journal 37, e97349. https://doi.org/10.15252/embj.201797349

7. Angsutararux, P., Kang, P.W., Zhu, W., Silva, J.R., 2021. Conformations of voltage-sensing domain III differentially define NaV channel closed- and open-state inactivation. The Journal of General Physiology 153, e202112891. https://doi.org/10.1085/jgp.202112891

8. Armstrong, C.M., 2006. Na channel inactivation from open and closed states. Proceedings of the National Academy of Sciences 103, 17991–17996. https://doi.org/10.1073/pnas.0607603103

9. Ashcroft, F.M., 1999. Ion Channels and Disease. Academic Press.

10. Balse, E., Eichel, C., 2018. The Cardiac Sodium Channel and Its Protein Partners, in: Chahine, M. (Ed.), Voltage-Gated Sodium Channels: Structure, Function and Channelopathies. Springer International Publishing, Cham, pp. 73–99. https://doi.org/10.1007/164_2017_45

11. Baroudi, G., Pouliot, V., Denjoy, I., Guicheney, P., Shrier, A., Chahine, M., 2001. Novel Mechanism for Brugada Syndrome. Circulation Research 88, e78–e83. https://doi.org/10.1161/hh1201.093270

12. Bauer, P., Hess, B., Lindahl, E., 2022. GROMACS 2022 Source code. https://doi.org/10.5281/zenodo.6103835

13. Bechi, G., Rusconi, R., Cestèle, S., Striano, P., Franceschetti, S., Mantegazza, M., 2015. Rescuable folding defective NaV1.1 (*SCN1A*) mutants in epilepsy: Properties, occurrence, and novel rescuing strategy with peptides targeted to the endoplasmic reticulum. Neurobiology of Disease 75, 100–114. https://doi.org/10.1016/j.nbd.2014.12.028

14. Bennett, E., Urcan, M.S., Tinkle, S.S., Koszowski, A.G., Levinson, S.R., 1997. Contribution of Sialic Acid to the Voltage Dependence of Sodium Channel Gating : A Possible Electrostatic Mechanism. Journal of General Physiology 109, 327–343. https://doi.org/10.1085/jgp.109.3.327

15. Bouza, A.A., Isom, L.L., 2018. Voltage-Gated Sodium Channel β Subunits and Their Related Diseases, in: Chahine, M. (Ed.), Voltage-Gated Sodium Channels: Structure, Function and Channelopathies. Springer International Publishing, Cham, pp. 423–450. https://doi.org/10.1007/164_2017_48

16. Brouwer, B.A., Merkies, I.S.J., Gerrits, M.M., Waxman, S.G., Hoeijmakers, J.G.J., Faber, C.G., 2014. Painful neuropathies: the emerging role of sodium channelopathies. Journal of the Peripheral Nervous System 19, 53–65. https://doi.org/10.1111/jns5.12071

17. Capes, D.L., Goldschen-Ohm, M.P., Arcisio-Miranda, M., Bezanilla, F., Chanda, B., 2013. Domain IV voltage-sensor movement is both sufficient and rate limiting for fast inactivation in sodium channels. Journal of General Physiology 142, 101–112. https://doi.org/10.1085/jgp.201310998

18. Cardoso, F.C., Lewis, R.J., 2018. Sodium channels and pain: from toxins to therapies. British Journal of Pharmacology 175, 2138–2157. https://doi.org/10.1111/bph.13962

19. Catterall, W.A., 2023. Voltage gated sodium and calcium channels: Discovery, structure, function, and Pharmacology. Channels 17, 2281714. https://doi.org/10.1080/19336950.2023.2281714

20. Cervenka, R., Zarrabi, T., Lukacs, P., Todt, H., 2010. The Outer Vestibule of the Na+ Channel–Toxin Receptor and Modulator of Permeation as Well as Gating. Marine Drugs 8, 1373–1393. https://doi.org/10.3390/md8041373

21. Chatelier, A., Dahllund, L., Eriksson, A., Krupp, J., Chahine, M., 2008. Biophysical Properties of Human Nav1.7 Splice Variants and Their Regulation by Protein Kinase A. Journal of Neurophysiology 99, 2241–2250. https://doi.org/10.1152/jn.01350.2007

22. Chen, H., Xia, Z., Dong, J., Huang, B., Zhang, J., Zhou, F., Yan, R., Shi, Y., Gong, J., Jiang, J., Huang, Z., Jiang, D., 2024. Structural mechanism of voltage-gated sodium channel slow inactivation. Nat Commun 15, 3691. https://doi.org/10.1038/s41467-024-48125-3

23. Chew, L.A., Bellampalli, S.S., Dustrude, E.T., Khanna, R., 2019. Mining the Nav1.7 interactome: Opportunities for chronic pain therapeutics. Biochemical Pharmacology 163, 9–20. https://doi.org/10.1016/j.bcp.2019.01.018

24. Choudhury, K., Delemotte, L., 2023. Modulation of Pore Opening of Eukaryotic Sodium Channels by π-Helices in S6. J. Phys. Chem. Lett. 14, 5876–5881. https://doi.org/10.1021/acs.jpclett.3c00803

25. Choudhury, K., Kasimova, M.A., McComas, S., Howard, R.J., Delemotte, L., 2022. An open state of a voltage-gated sodium channel involving a π-helix and conserved pore-facing asparagine. Biophysical Journal 121, 11–22. https://doi.org/10.1016/j.bpj.2021.12.010

26. Clairfeuille, T., Cloake, A., Infield, D.T., Llongueras, J.P., Arthur, C.P., Li, Z.R., Jian, Y., Martin-Eauclaire, M.-F., Bougis, P.E., Ciferri, C., Ahern, C.A., Bosmans, F., Hackos, D.H., Rohou, A., Payandeh, J., 2019. Structural basis of α-scorpion toxin action on Na $_v$ channels. Science 363, eaav8573. https://doi.org/10.1126/science.aav8573

27. Clatot, J., Hoshi, M., Wan, X., Liu, H., Jain, A., Shinlapawittayatorn, K., Marionneau, C., Ficker, E., Ha, T., Deschênes, I., 2017. Voltage-gated sodium channels assemble and gate as dimers. Nat Commun 8, 2077. https://doi.org/10.1038/s41467-017-02262-0

28. Costantini, L.M., Fossati, M., Francolini, M., Snapp, E.L., 2012. Assessing the Tendency of Fluorescent Proteins to Oligomerize Under Physiologic Conditions. Traffic 13, 643–649. https://doi.org/10.1111/j.1600-0854.2012.01336.x

29. Cox, J.J., Sheynin, J., Shorer, Z., Reimann, F., Nicholas, A.K., Zubovic, L., Baralle, M., Wraige, E., Manor, E., Levy, J., Woods, C.G., Parvari, R., 2010. Congenital Insensitivity to Pain: Novel SCN9A Missense and In-Frame Deletion Mutations. Hum Mutat 31, 1670–1686. https://doi.org/10.1002/humu.21325

30. Cummins, T.R., Sheets, P.L., Waxman, S.G., 2007. The roles of sodium channels in nociception: Implications for mechanisms of pain. PAIN 131, 243–257. https://doi.org/10.1016/j.pain.2007.07.026

31. Dib-Hajj, S.D., Estacion, M., Jarecki, B.W., Tyrrell, L., Fischer, T.Z., Lawden, M., Cummins, T.R., Waxman, S.G., 2008. Paroxysmal Extreme Pain Disorder M1627K Mutation in Human Nav1.7 Renders DRG Neurons Hyperexcitable. Mol Pain 4, 1744-8069-4–37. https://doi.org/10.1186/1744-8069-4-37

32. Drenth, J.P.H., te Morsche, R.H.M., Guillet, G., Taieb, A., Lee Kirby, R., Jansen, J.B.M.J., 2005. *SCN9A* Mutations Define Primary Erythermalgia as a Neuropathic Disorder of Voltage Gated Sodium Channels. Journal of Investigative Dermatology 124, 1333–1338. https://doi.org/10.1111/j.0022-202X.2005.23737.x

33. Du, Y., Nomura, Y., Satar, G., Hu, Z., Nauen, R., He, S.Y., Zhorov, B.S., Dong, K., 2013. Molecular evidence for dual pyrethroid-receptor sites on a mosquito sodium channel. Proceedings of the National Academy of Sciences 110, 11785–11790. https://doi.org/10.1073/pnas.1305118110

34. Dubin, A.E., Patapoutian, A., 2010. Nociceptors: the sensors of the pain pathway. J Clin Invest 120, 3760–3772. https://doi.org/10.1172/JCI42843

35. Dulsat, G., Palomeras, S., Cortada, E., Riuró, H., Brugada, R., Vergés, M., 2017. Trafficking and localisation to the plasma membrane of Nav1.5 promoted by the β2 subunit is defective due to a β2 mutation associated with Brugada syndrome. Biology of the Cell 109, 273–291. https://doi.org/10.1111/boc.201600085

36. Eberhardt, J., Santos-Martins, D., Tillack, A.F., Forli, S., 2021. AutoDock Vina 1.2.0: new docking methods, expanded force field, and Python bindings. J Chem Inf Model 61, 3891–3898. https://doi.org/10.1021/acs.jcim.1c00203

37. Eberhardt, M., Nakajima, J., Klinger, A.B., Neacsu, C., Hühne, K., O'Reilly, A.O., Kist, A.M., Lampe, A.K., Fischer, K., Gibson, J., Nau, C., Winterpacht, A., Lampert, A., 2014. Inherited Pain: SODIUM CHANNEL NAV1.7 A1632T MUTATION CAUSES ERYTHROMELALGIA DUE TO A SHIFT OF FAST INACTIVATION* *This work was supported by Deutsche Forschungsgemeinschaft (DFG) Grant LA2740/2-1 (to A. L.), by ELAN-Fonds (Erlanger Leistungsbezogene Anschubfinanzierung und Nachwuchsförderung, Fonds für Forschung und Lehre des Klinikums der Friedrich-Alexander-Universität Erlangen-Nürnberg, Ref. No.: 11.05.30.1) (to A. L. and C. N.), and by the Dr. Ernst und Anita Bauer Stiftung (to M. E.). Journal of Biological Chemistry 289, 1971–1980. https://doi.org/10.1074/jbc.M113.502211

38. Faber, C.G., Lauria, G., Merkies, I.S.J., Cheng, X., Han, C., Ahn, H.-S., Persson, A.-K., Hoeijmakers, J.G.J., Gerrits, M.M., Pierro, T., Lombardi, R., Kapetis, D., Dib-Hajj, S.D., Waxman, S.G., 2012. Gain-of-function Nav1.8 mutations in painful neuropathy. Proceedings of the National Academy of Sciences 109, 19444–19449. https://doi.org/10.1073/pnas.1216080109

39. Fertleman, C.R., Baker, M.D., Parker, K.A., Moffatt, S., Elmslie, F.V., Abrahamsen, B., Ostman, J., Klugbauer, N., Wood, J.N., Gardiner, R.M., Rees, M., 2006. SCN9A Mutations in Paroxysmal Extreme Pain Disorder: Allelic Variants Underlie Distinct Channel Defects and Phenotypes. Neuron 52, 767–774. https://doi.org/10.1016/j.neuron.2006.10.006

40. Gabelli, S.B., Yoder, J.B., Tomaselli, G.F., Amzel, L.M., 2016. Calmodulin and Ca2+ control of voltage gated Na+ channels. Channels 10, 45–54. https://doi.org/10.1080/19336950.2015.1075677

41. Gade, A., Malvezzi, M., Das, L.T., Matsui, M., Ma, C.-I.J., Mazdisnian, K., Marx, S.O., Maxfield, F.R., Pitt, G.S., 2025. The Na$_V$1.5 auxiliary subunit FGF13 modulates channels by regulating membrane cholesterol independent of channel binding. bioRxiv 2025.03.19.644183. https://doi.org/10.1101/2025.03.19.644183

42. Gallego-Delgado, M., Cámara-Checa, A., Rubio-Alarcón, M., Heredero-Jung, D., de la Fuente-Blanco, L., Rapún, J., Plata-Izquierdo, B., Pérez-Martín, S., Cebrián, J., Moreno de Redrojo, L., García-Berrocal, B., Delpón, E., Sánchez, P.L., Villacorta, E., Caballero, R., 2024. Variable Penetrance and Expressivity of a Rare Pore Loss-of-Function Mutation (p.L889V) of Nav1.5 Channels in Three Spanish Families. International Journal of Molecular Sciences 25, 4686. https://doi.org/10.3390/ijms25094686

43. Gamal El-Din, T.M., Lenaeus, M.J., Catterall, W.A., 2018. Structural and Functional Analysis of Sodium Channels Viewed from an Evolutionary Perspective, in: Chahine, M. (Ed.), Voltage-Gated Sodium Channels: Structure, Function and Channelopathies. Springer International Publishing, Cham, pp. 53–72. https://doi.org/10.1007/164_2017_61

44. Ghovanloo, M.-R., Choudhury, K., Bandaru, T.S., Fouda, M.A., Rayani, K., Rusinova, R., Phaterpekar, T., Nelkenbrecher, K., Watkins, A.R., Poburko, D., Thewalt, J., Andersen, O.S., Delemotte, L., Goodchild, S.J., Ruben, P.C., 2021. Cannabidiol inhibits the skeletal muscle Nav1.4 by blocking its pore and by altering membrane elasticity. Journal of General Physiology 153, e202012701. https://doi.org/10.1085/jgp.202012701

45. Goldberg, Y., MacFarlane, J., MacDonald, M., Thompson, J., Dube, M.-P., Mattice, M., Fraser, R., Young, C., Hossain, S., Pape, T., Payne, B., Radomski, C., Donaldson, G., Ives, E., Cox, J., Younghusband, H., Green, R., Duff, A., Boltshauser, E., Grinspan, G., Dimon, J., Sibley, B., Andria, G., Toscano, E., Kerdraon, J., Bowsher, D., Pimstone, S., Samuels, M., Sherrington, R., Hayden, M., 2007. Loss-of-function mutations in the Nav1.7 gene underlie congenital indifference to pain in multiple human populations. Clinical Genetics 71, 311–319. https://doi.org/10.1111/j.1399-0004.2007.00790.x

46. He, B., Soderlund, D.M., 2010. Human embryonic kidney (HEK293) cells express endogenous voltage-gated sodium currents and Nav1.7 sodium channels. Neuroscience Letters 469, 268–272. https://doi.org/10.1016/j.neulet.2009.12.012

47. Heinle, J.W., Dalessio, S., Janicki, P., Ouyang, A., Vrana, K.E., Ruiz-Velasco, V., Coates, M.D., 2024. Insights into the voltage-gated sodium channel, NaV1.8, and its role in visceral pain perception. Front. Pharmacol. 15. https://doi.org/10.3389/fphar.2024.1398409

48. Herzog, F.A., Braun, L., Schoen, I., Vogel, V., 2016. Improved Side Chain Dynamics in MARTINI Simulations of Protein–Lipid Interfaces. J. Chem. Theory Comput. 12, 2446–2458. https://doi.org/10.1021/acs.jctc.6b00122

49. Higerd-Rusli, G.P., Tyagi, S., Liu, S., Dib-Hajj, F.B., Waxman, S.G., Dib-Hajj, S.D., 2023. The fates of internalized NaV1.7 channels in sensory neurons: Retrograde cotransport with other ion channels, axon-specific recycling, and degradation. Journal of Biological Chemistry 299, 102816. https://doi.org/10.1016/j.jbc.2022.102816

50. Hodgkin, A.L., Huxley, A.F., 1952. A quantitative description of membrane current and its application to conduction and excitation in nerve. J Physiol 117, 500–544.

51. Huang, C.-W., Lin, P.-C., Chen, J.-L., Lee, M.-J., 2021. Cannabidiol Selectively Binds to the Voltage-Gated Sodium Channel Nav1.4 in Its Slow-Inactivated State and Inhibits Sodium Current. Biomedicines 9, 1141. https://doi.org/10.3390/biomedicines9091141

52. Huang, G., Liu, D., Wang, W., Wu, Q., Chen, J., Pan, X., Shen, H., Yan, N., 2022a. High-resolution structures of human Nav1.7 reveal gating modulation through α-π helical transition of S6IV. Cell Reports 39. https://doi.org/10.1016/j.celrep.2022.110735

53. Huang, G., Wu, Q., Li, Z., Jin, X., Huang, X., Wu, T., Pan, X., Yan, N., 2022b. Unwinding and spiral sliding of S4 and domain rotation of VSD during the electromechanical coupling in Nav1.7. Proceedings of the National Academy of Sciences 119, e2209164119. https://doi.org/10.1073/pnas.2209164119

54. Huang, J., Fan, X., Jin, X., Jo, S., Zhang, H.B., Fujita, A., Bean, B.P., Yan, N., 2023. Cannabidiol inhibits Nav channels through two distinct binding sites. Nat Commun 14, 3613. https://doi.org/10.1038/s41467-023-39307-6

55. Huang, X., Jin, X., Huang, G., Huang, J., Wu, T., Li, Z., Chen, J., Kong, F., Pan, X., Yan, N., 2022. Structural basis for high-voltage activation and subtype-specific inhibition of human Nav1.8. Proceedings of the National Academy of Sciences 119, e2208211119. https://doi.org/10.1073/pnas.2208211119

56. Iamshanova, O., Hämmerli, A.-F., Ramaye, E., Seljmani, A., Ross-Kaschitza, D., Schärz, N., Essers, M., Guichard, S., Rougier, J.-S., Abriel, H., 2024. The dispensability of 14-3-3 proteins for the regulation of human cardiac sodium channel Nav1.5. PLOS ONE 19, e0298820. https://doi.org/10.1371/journal.pone.0298820

57. Iamshanova, O., Rougier, J.-S., Abriel, H., 2023. Exploring the Oligomerization of Nav1.5 and Its Implication for the Dominant-Negative Effect. Bioelectricity 5, 279–289. https://doi.org/10.1089/bioe.2023.0014

58. Iqbal, S.M., Aufy, M., Shabbir, W., Lemmens-Gruber, R., 2018. Identification of phosphorylation sites and binding pockets for modulation of NaV1.5 channel by Fyn tyrosine kinase. The FEBS Journal 285, 2520–2530. https://doi.org/10.1111/febs.14496

59. Jiang, D., Banh, R., El-Din, T.M.G., Tonggu, L., Lenaeus, M.J., Pomès, R., Zheng, N., Catterall, W.A., 2021a. Open-state structure and pore gating mechanism of the cardiac sodium channel. Cell 184, 5151-5162.e11. https://doi.org/10.1016/j.cell.2021.08.021

60. Jiang, D., Shi, H., Tonggu, L., El-Din, T.M.G., Lenaeus, M.J., Zhao, Y., Yoshioka, C., Zheng, N., Catterall, W.A., 2020. Structure of the Cardiac Sodium Channel. Cell 180, 122-134.e10. https://doi.org/10.1016/j.cell.2019.11.041

61. Jiang, D., Tonggu, L., Gamal El-Din, T.M., Banh, R., Pomès, R., Zheng, N., Catterall, W.A., 2021b. Structural basis for voltage-sensor trapping of the cardiac sodium channel by a deathstalker scorpion toxin. Nat Commun 12, 128. https://doi.org/10.1038/s41467-020-20078-3

62. Jiang, D., Zhang, J., Xia, Z., 2022. Structural Advances in Voltage-Gated Sodium Channels. Front. Pharmacol. 13. https://doi.org/10.3389/fphar.2022.908867

63. Kaluza, L., Meents, J.E., Hampl, M., Rösseler, C., Hautvast, P.A.I., Detro-Dassen, S., Hausmann, R., Schmalzing, G., Lampert, A., 2018. Loss-of-function of Nav1.8/D1639N linked to human pain can be rescued by lidocaine. Pflugers Arch - Eur J Physiol 470, 1787–1801. https://doi.org/10.1007/s00424-018-2189-x

64. Kapplinger, J.D., Giudicessi, J.R., Ye, D., Tester, D.J., Callis, T.E., Valdivia, C.R., Makielski, J.C., Wilde, A.A., Ackerman, M.J., 2015. Enhanced Classification of Brugada Syndrome–Associated and Long-QT Syndrome–Associated Genetic Variants in the SCN5A-Encoded Nav1.5 Cardiac Sodium Channel. Circulation: Cardiovascular Genetics 8, 582–595. https://doi.org/10.1161/CIRCGENETICS.114.000831

65. Kilsdonk, E.P.C., Yancey, P.G., Stoudt, G.W., Bangerter, F.W., Johnson, W.J., Phillips, M.C., Rothblat, G.H., 1995. Cellular Cholesterol Efflux Mediated by Cyclodextrins *. Journal of Biological Chemistry 270, 17250–17256. https://doi.org/10.1074/jbc.270.29.17250

66. Kist, A.M., Sagafos, D., Rush, A.M., Neacsu, C., Eberhardt, E., Schmidt, R., Lunden, L.K., Ørstavik, K., Kaluza, L., Meents, J., Zhang, Z., Carr, T.H., Salter, H., Malinowsky, D., Wollberg, P., Krupp, J., Kleggetveit, I.P., Schmelz, M., Jørum, E., Lampert, A., Namer, B., 2016. SCN10A Mutation in a Patient with Erythromelalgia Enhances C-Fiber Activity Dependent Slowing. PLOS ONE 11, e0161789. https://doi.org/10.1371/journal.pone.0161789

67. Koenig, J., Werdehausen, R., Linley, J.E., Habib, A.M., Vernon, J., Lolignier, S., Eijkelkamp, N., Zhao, J., Okorokov, A.L., Woods, C.G., Wood, J.N., Cox, J.J., 2015. Regulation of Nav1.7: A Conserved SCN9A Natural Antisense Transcript Expressed in Dorsal Root Ganglia. PLOS ONE 10, e0128830. https://doi.org/10.1371/journal.pone.0128830

68. Körner, J., Albani, S., Eswaran, V.S.B., Roehl, A.B., Rossetti, G., Lampert, A., 2022. Sodium Channels and Local Anesthetics—Old Friends With New Perspectives. Frontiers in Pharmacology 13. https://doi.org/10.3389/fphar.2022.837088

69. Körner, J., Lampert, A., 2020. Sodium Channels☆, in: Fritzsch, B. (Ed.), The Senses: A Comprehensive Reference (Second Edition). Elsevier, Oxford, pp. 120–141. https://doi.org/10.1016/B978-0-12-809324-5.24208-9

70. Körner, J., Meents, J., Machtens, J.-P., Lampert, A., 2018. β1 subunit stabilises sodium channel Nav1.7 against mechanical stress. The Journal of Physiology 596, 2433–2445. https://doi.org/10.1113/JP275905

71. Kroon, P.C., Grunewald, F., Barnoud, J., Tilburg, M. van, Souza, P.C.T., Wassenaar, T.A., Marrink, S.J., 2023. Martinize2 and Vermouth: Unified Framework for Topology Generation. eLife 12. https://doi.org/10.7554/eLife.90627.1

72. Kullback, S., Leibler, R.A., 1951. On Information and Sufficiency. The Annals of Mathematical Statistics 22, 79–86. https://doi.org/10.1214/aoms/1177729694

73. Laedermann, C.J., Syam, N., Decosterd, I., Abriel, H., 2013. β1- and β3- voltage-gated sodium channel subunits modulate cell surface expression and glycosylation of Nav1.7 in HEK293 cells. Front. Cell. Neurosci. 7. https://doi.org/10.3389/fncel.2013.00137

74. Lampert, A., O'Reilly, A.O., Dib-Hajj, S.D., Tyrrell, L., Wallace, B.A., Waxman, S.G., 2008. A Pore-blocking Hydrophobic Motif at the Cytoplasmic Aperture of the Closed-state Nav1.7 Channel Is Disrupted by the Erythromelalgia-associated F1449V Mutation *. Journal of Biological Chemistry 283, 24118–24127. https://doi.org/10.1074/jbc.M802900200

75. Lampert, A., O'Reilly, A.O., Reeh, P., Leffler, A., 2010. Sodium channelopathies and pain. Pflugers Arch - Eur J Physiol 460, 249–263. https://doi.org/10.1007/s00424-009-0779-3

76. Laviola, M., McGavin, S.K., Freer, G.A., Plancich, G., Woodbury, S.C., Marinkovich, S., Morrison, R., Reader, A., Rutherford, R.B., Yagiela, J.A., 2008. Randomized Study of Phentolamine Mesylate for Reversal of Local Anesthesia. J Dent Res 87, 635–639. https://doi.org/10.1177/154405910808700717

77. Le Cann, K., Meents ,Jannis E., Sudha Bhagavath Eswaran ,Vishal, Dohrn ,Maike F., Bott ,Raya, Maier ,Andrea, Bialer ,Martin, Hautvast ,Petra, Erickson ,Andelain, Rolke ,Roman, Rothermel ,Markus, Körner ,Jannis, Kurth ,Ingo, and Lampert, A., 2021. Assessing the impact of pain-linked Nav1.7 variants: An example of two variants with no biophysical effect. Channels 15, 208–228. https://doi.org/10.1080/19336950.2020.1870087

78. Li, Y., Yuan, T., Huang, B., Zhou, F., Peng, C., Li, X., Qiu, Y., Yang, B., Zhao, Y., Huang, Z., Jiang, D., 2023. Structure of human NaV1.6 channel reveals Na+ selectivity and pore blockade by 4,9-anhydro-tetrodotoxin. Nat Commun 14, 1030. https://doi.org/10.1038/s41467-023-36766-9

79. Li, Z., Jin, X., Wu, T., Huang, G., Wu, K., Lei, J., Pan, X., Yan, N., 2021a. Structural Basis for Pore Blockade of the Human Cardiac Sodium Channel Nav1.5 by the Antiarrhythmic Drug Quinidine**. Angewandte Chemie International Edition 60, 11474–11480. https://doi.org/10.1002/anie.202102196

80. Li, Z., Jin, X., Wu, T., Huang, G., Wu, K., Lei, J., Pan, X., Yan, N., 2021b. Structural Basis for Pore Blockade of the Human Cardiac Sodium Channel Nav1.5 by the Antiarrhythmic Drug Quinidine. Angewandte Chemie 133, 11575–11581. https://doi.org/10.1002/ange.202102196

81. Li, Z., Wu, Q., Yan, N., 2024. A structural atlas of druggable sites on Nav channels. Channels 18, 2287832. https://doi.org/10.1080/19336950.2023.2287832

82. Lin, Y., Tao, E., Champion, J.P., Corry, B., 2024. A binding site for phosphoinositides described by multiscale simulations explains their modulation of voltage-gated sodium channels. eLife 12, RP91218. https://doi.org/10.7554/eLife.91218

83. Liu, Yi, Balaji, R., de Toledo, M.A.S., Ernst, S., Hautvast, P., Kesdoğan, A.B., Körner, J., Zenke, M., Neureiter, A., Lampert, A., 2024. The pain target NaV1.7 is expressed late during human iPS cell differentiation into sensory neurons as determined in high-resolution imaging. Pflugers Arch - Eur J Physiol 476, 975–992. https://doi.org/10.1007/s00424-024-02945-w

84. Liu, Yichen, Bassetto, C., Pinto, B., Bezanilla, F., 2024. A mechanistic reinterpretation of fast inactivation in voltage-gated Na+ channel. Biophysical Journal 123, 107a. https://doi.org/10.1016/j.bpj.2023.11.766

85. Liu, Y., Bezanilla, F., 2024. Comparison of two fast-inactivation deficient mutants in voltage-gated sodium channel. Biophysical Journal 123, 106a–107a. https://doi.org/10.1016/j.bpj.2023.11.765

86. Lomize, M.A., Pogozheva, I.D., Joo, H., Mosberg, H.I., Lomize, A.L., 2012. OPM database and PPM web server: resources for positioning of proteins in membranes. Nucleic Acids Research 40, D370–D376. https://doi.org/10.1093/nar/gkr703

87. Lorenzini, M., Burel, S., Lesage, A., Wagner, E., Charrière, C., Chevillard, P.-M., Evrard, B., Maloney, D., Ruff, K.M., Pappu, R.V., Wagner, S., Nerbonne, J.M., Silva, J.R., Townsend, R.R., Maier, L.S., Marionneau, C., 2021. Proteomic and functional mapping of cardiac NaV1.5 channel phosphorylation sites. Journal of General Physiology 153, e202012646. https://doi.org/10.1085/jgp.202012646

88. Lundbæk, J.A., Birn, P., Hansen, A.J., Søgaard, R., Nielsen, C., Girshman, J., Bruno, M.J., Tape, S.E., Egebjerg, J., Greathouse, D.V., Mattice, G.L., Koeppe, R.E., II, Andersen, O.S., 2004. Regulation of Sodium Channel Function by Bilayer Elasticity : The Importance of Hydrophobic Coupling. Effects of Micelle-forming Amphiphiles and Cholesterol. Journal of General Physiology 123, 599–621. https://doi.org/10.1085/jgp.200308996

89. Maroni, M., Körner, J., Schüttler, J., Winner, B., Lampert, A., Eberhardt, E., 2019. β1 and β3 subunits amplify mechanosensitivity ofthe cardiac voltage-gated sodium channel Nav1.5. Pflugers Arch - Eur J Physiol 471, 1481–1492. https://doi.org/10.1007/s00424-019-02324-w

90. Marrink, S.J., Monticelli, L., Melo, M.N., Alessandri, R., Tieleman, D.P., Souza, P.C.T., 2023. Two decades of Martini: Better beads, broader scope. WIREs Computational Molecular Science 13, e1620. https://doi.org/10.1002/wcms.1620

91. McGowan, B.R., Schwaede, A.N., De Simone, L., Rao, V.K., 2023. Muscle channelopathies: A review. Annals of the Child Neurology Society 1, 273–288. https://doi.org/10.1002/cns3.20040

92. Meents, J.E., Lampert, A., 2016. Studying Sodium Channel Gating in Heterologous Expression Systems, in: Korngreen, A. (Ed.), Advanced Patch-Clamp Analysis for Neuroscientists. Springer, New York, NY, pp. 37–65. https://doi.org/10.1007/978-1-4939-3411-9_3

93. Mercier, A., Clément, R., Harnois, T., Bourmeyster, N., Bois, P., Chatelier, A., 2015. Nav1.5 channels can reach the plasma membrane through distinct *N*-glycosylation states. Biochimica et Biophysica Acta (BBA) - General Subjects 1850, 1215–1223. https://doi.org/10.1016/j.bbagen.2015.02.009

94. Mercier, A., Clément, R., Harnois, T., Bourmeyster, N., Faivre, J.-F., Findlay, I., Chahine, M., Bois, P., Chatelier, A., 2012. The β1-Subunit of Nav1.5 Cardiac Sodium Channel Is Required for a Dominant Negative Effect through α-α Interaction. PLOS ONE 7, e48690. https://doi.org/10.1371/journal.pone.0048690

95. Mulcahy, J.V., Pajouhesh, H., Beckley, J.T., Delwig, A., Du Bois, J., Hunter, J.C., 2019. Challenges and Opportunities for Therapeutics Targeting the Voltage-Gated Sodium Channel Isoform NaV1.7. J. Med. Chem. 62, 8695–8710. https://doi.org/10.1021/acs.jmedchem.8b01906

96. Mulley, J.C., Scheffer, I.E., Petrou, S., Dibbens, L.M., Berkovic, S.F., Harkin, L.A., 2005. SCN1A mutations and epilepsy. Human Mutation 25, 535–542. https://doi.org/10.1002/humu.20178

97. Nishino, A., Okamura, Y., 2018. Evolutionary History of Voltage-Gated Sodium Channels, in: Chahine, M. (Ed.), Voltage-Gated Sodium Channels: Structure, Function and Channelopathies. Springer International Publishing, Cham, pp. 3–32. https://doi.org/10.1007/164_2017_70

98. Noreng, S., Li, T., Payandeh, J., 2021. Structural Pharmacology of Voltage-Gated Sodium Channels. Journal of Molecular Biology, Ion channels : Intersection of Structure, Function, and Pharmacology 433, 166967. https://doi.org/10.1016/j.jmb.2021.166967

99. O'Neill, M.J., Muhammad, A., Li, B., Wada, Y., Hall, L., Solus, J.F., Short, L., Roden, D.M., Glazer, A.M., 2022. Dominant negative effects of *SCN5A* missense variants. Genetics in Medicine 24, 1238–1248. https://doi.org/10.1016/j.gim.2022.02.010

100. Pan, X., Li, Z., Huang, X., Huang, G., Gao, S., Shen, H., Liu, L., Lei, J., Yan, N., 2019. Molecular basis for pore blockade of human Na+ channel Nav1.2 by the μ-conotoxin KIIIA. Science 363, 1309–1313. https://doi.org/10.1126/science.aaw2999

101. Pan, X., Li, Z., Zhou, Q., Shen, H., Wu, K., Huang, X., Chen, J., Zhang, J., Zhu, X., Lei, J., Xiong, W., Gong, H., Xiao, B., Yan, N., 2018. Structure of the human voltage-gated sodium channel Nav1.4 in complex with β1. Science 362, eaau2486. https://doi.org/10.1126/science.aau2486

102. Pei, Z., Pan, Y., Cummins, T.R., 2018. Posttranslational Modification of Sodium Channels, in: Chahine, M. (Ed.), Voltage-Gated Sodium Channels: Structure, Function and Channelopathies. Springer International Publishing, Cham, pp. 101–124. https://doi.org/10.1007/164_2017_69

103. Pettersen, E.F., Goddard, T.D., Huang, C.C., Meng, E.C., Couch, G.S., Croll, T.I., Morris, J.H., Ferrin, T.E., 2021. UCSF ChimeraX: Structure visualization for researchers, educators, and developers. Protein Science 30, 70–82. https://doi.org/10.1002/pro.3943

104. Prados-Frutos, J.C., Rojo, R., González-Serrano, J., González-Serrano, C., Sammartino, G., Martínez-González, J.M., Sánchez-Monescillo, A., 2015. Phentolamine mesylate to reverse oral soft-tissue local anesthesia: A systematic review and meta-analysis. The Journal of the American Dental Association 146, 751-759.e3. https://doi.org/10.1016/j.adaj.2015.04.018

105. Praticò, A.D., Giallongo, A., Arrabito, M., D'Amico, S., Gauci, M.C., Lombardo, G., Polizzi, A., Falsaperla, R., Ruggieri, M., 2021. SCN2A and Its Related Epileptic Phenotypes. Journal of Pediatric Neurology 21, 173–185. https://doi.org/10.1055/s-0041-1727097

106. Priori, S.G., Napolitano, C., Gasparini, M., Pappone, C., Bella, P.D., Giordano, U., Bloise, R., Giustetto, C., De Nardis, R., Grillo, M., Ronchetti, E., Faggiano, G., Nastoli, J., 2002. Natural History of Brugada Syndrome. Circulation 105, 1342–1347. https://doi.org/10.1161/hc1102.105288

107. Pristerà, A., Baker, M.D., Okuse, K., 2012. Association between Tetrodotoxin Resistant Channels and Lipid Rafts Regulates Sensory Neuron Excitability. PLOS ONE 7, e40079. https://doi.org/10.1371/journal.pone.0040079

108. Pujadas, G., Vaque, M., Ardevol, A., Blade, C., Salvado, M.J., Blay, M., Fernandez-Larrea, J., Arola, L., 2008. Protein-ligand Docking: A Review of Recent Advances and Future Perspectives. Current Pharmaceutical Analysis 4, 1–19. https://doi.org/10.2174/157341208783497597

109. Reinhard, K., Rougier, J.-S., Ogrodnik, J., Abriel, H., 2013. Electrophysiological properties of mouse and epitope-tagged human cardiac sodium channel Na v1.5 expressed in HEK293 cells. F1000Res 2, 48. https://doi.org/10.12688/f1000research.2-48.v2

110. Rolke, R., Magerl, W., Campbell, K.A., Schalber, C., Caspari, S., Birklein, F., Treede, R.-D., 2006. Quantitative sensory testing: a comprehensive protocol for clinical trials. European Journal of Pain 10, 77–88. https://doi.org/10.1016/j.ejpain.2005.02.003

111. Rühlmann, A.H., Körner, J., Hausmann, R., Bebrivenski, N., Neuhof, C., Detro-Dassen, S., Hautvast, P., Benasolo, C.A., Meents, J., Machtens, J.-P., Schmalzing, G., Lampert, A., 2020. Uncoupling sodium channel dimers restores the phenotype of a pain-linked Nav1.7 channel mutation. British Journal of Pharmacology 177, 4481–4496. https://doi.org/10.1111/bph.15196

112. Sands, Z., Grottesi, A., Sansom, M.S.P., 2005. Voltage-gated ion channels. Current Biology 15, R44–R47. https://doi.org/10.1016/j.cub.2004.12.050

113. Schirmeyer, J., Szafranski, K., Leipold, E., Mawrin, C., Platzer, M., Heinemann, S.H., 2014. Exon 11 skipping of SCN10A coding for voltage-gated sodium channels in dorsal root ganglia. Channels (Austin) 8, 210–215. https://doi.org/10.4161/chan.28146

114. Selimi, Z., Rougier, J.-S., Abriel, H., Kucera, J.P., 2023. A detailed analysis of single-channel Nav1.5 recordings does not reveal any cooperative gating. The Journal of Physiology 601, 3847–3868. https://doi.org/10.1113/JP284861

115. Shearwin, K.E., Callen, B.P., Egan, J.B., 2005. Transcriptional interference – a crash course. Trends in Genetics 21, 339–345. https://doi.org/10.1016/j.tig.2005.04.009

116. Shen, H., Liu, D., Wu, K., Lei, J., Yan, N., 2019. Structures of human Nav1.7 channel in complex with auxiliary subunits and animal toxins. Science 363, 1303–1308. https://doi.org/10.1126/science.aaw2493

117. Silva, J., 2014. Slow Inactivation of Na+ Channels, in: Ruben, P.C. (Ed.), Voltage Gated Sodium Channels. Springer, Berlin, Heidelberg, pp. 33–49. https://doi.org/10.1007/978-3-642-41588-3_3

118. Smart, O.S., Goodfellow, J.M., Wallace, B.A., 1993. The pore dimensions of gramicidin A. Biophysical Journal 65, 2455–2460. https://doi.org/10.1016/S0006-3495(93)81293-1

119. Souza, P.C.T., Alessandri, R., Barnoud, J., Thallmair, S., Faustino, I., Grünewald, F., Patmanidis, I., Abdizadeh, H., Bruininks, B.M.H., Wassenaar, T.A., Kroon, P.C., Melcr, J., Nieto, V., Corradi, V., Khan, H.M., Domański, J., Javanainen, M., Martinez-Seara, H., Reuter, N., Best, R.B., Vattulainen, I., Monticelli, L., Periole, X., Tieleman, D.P., de Vries, A.H., Marrink, S.J., 2021. Martini 3: a general purpose force field for coarse-grained molecular dynamics. Nat Methods 18, 382–388. https://doi.org/10.1038/s41592-021-01098-3

120. Spafford, J.D., 2023. A governance of ion selectivity based on the occupancy of the “beacon” in one- and four-domain calcium and sodium channels. Channels 17, 2191773. https://doi.org/10.1080/19336950.2023.2191773

121. Splawski, I., Shen, J., Timothy, K.W., Lehmann, M.H., Priori, S., Robinson, J.L., Moss, A.J., Schwartz, P.J., Towbin, J.A., Vincent, G.M., Keating, M.T., 2000. Spectrum of Mutations in Long-QT Syndrome Genes. Circulation 102, 1178–1185. https://doi.org/10.1161/01.CIR.102.10.1178

122. Sun, Y.-M., Favre, I., Schild, L., Moczydlowski, E., 1997. On the Structural Basis for Size-selective Permeation of Organic Cations through the Voltage-gated Sodium Channel : Effect of Alanine Mutations at the DEKA Locus on Selectivity, Inhibition by Ca2+ and H+, and Molecular Sieving. Journal of General Physiology 110, 693–715. https://doi.org/10.1085/jgp.110.6.693

123. Toklucu, I., Sudha Bhagavath Eswaran, V., Bott, R.A., Kesdoğan, A.B., Gaebler, A.J., Stingl, J., Hausmann, R., Körner, J., Lampert, A., 2025. α-Adrenoreceptor blocker phentolamine inhibits voltage-gated sodium channels via the local anaesthetic binding site. British Journal of Pharmacology n/a. https://doi.org/10.1111/bph.17450

124. Troshin, P.V., Procter, J.B., Barton, G.J., 2011. Java bioinformatics analysis web services for multiple sequence alignment—JABAWS:MSA. Bioinformatics 27, 2001–2002. https://doi.org/10.1093/bioinformatics/btr304

125. Tyagi, S., Sarveswaran, N., Higerd-Rusli, G.P., Liu, S., Dib-Hajj, F.B., Waxman, S.G., Dib-Hajj, S.D., 2023. Conserved but not critical: Trafficking and function of NaV1.7 are independent of highly conserved polybasic motifs. Front. Mol. Neurosci. 16. https://doi.org/10.3389/fnmol.2023.116102

126. van den Braak, W.M.N., Kuehs, S., Peschke, Z.G., Namer, B., Lischka, A., Eggermann, K., Dumke, C., Eswaran, S.B.V., Nikolin, S., Weis, J., Schulz, B.J., Lampert, A., Kurth, I., Rolke, R., Leipold, E., Dohrn, M.F., 2025. Altered $\mathrm{Na_v}$1.9 channel activity in two Tyr66Ser variant carriers with small fiber dysfunction. Journal of General Physiology, 157(6), e202413691. https://doi.org/10.1085/jgp.202413691

127. Wagner, E., Marras, M., Kumar, S., Kelley, J., Ruff, K., Silva, J., 2024. Investigating the Functional Role of the DI-DII Linker in Nav1.5 Channel Function. bioRxiv 2024.12.01.626264. https://doi.org/10.1101/2024.12.01.626264

128. Wang, Y., Mi, J., Lu, K., Lu, Y., Wang, K., 2015. Comparison of Gating Properties and Use-Dependent Block of Nav1.5 and Nav1.7 Channels by Anti-Arrhythmics Mexiletine and Lidocaine. PLOS ONE 10, e0128653. https://doi.org/10.1371/journal.pone.0128653

129. Wassenaar, T.A., Ingólfsson, H.I., Böckmann, R.A., Tieleman, D.P., Marrink, S.J., 2015. Computational Lipidomics with insane: A Versatile Tool for Generating Custom Membranes for Molecular Simulations. J. Chem. Theory Comput. 11, 2144–2155. https://doi.org/10.1021/acs.jctc.5b00209

130. Waterhouse, A.M., Procter, J.B., Martin, D.M.A., Clamp, M., Barton, G.J., 2009. Jalview Version 2—a multiple sequence alignment editor and analysis workbench. Bioinformatics 25, 1189–1191. https://doi.org/10.1093/bioinformatics/btp033

131. Webb, B., Sali, A., 2016. Comparative Protein Structure Modeling Using MODELLER. Current Protocols in Bioinformatics 54, 5.6.1-5.6.37. https://doi.org/10.1002/cpbi.3

132. Wisedchaisri, G., Tonggu, L., El-Din, T.M.G., McCord, E., Zheng, N., Catterall, W.A., 2021. Structural Basis for High-Affinity Trapping of the NaV1.7 Channel in Its Resting State by Tarantula Toxin. Molecular Cell 81, 38-48.e4. https://doi.org/10.1016/j.molcel.2020.10.039

133. Wisedchaisri, G., Tonggu, L., McCord, E., El-Din, T.M.G., Wang, L., Zheng, N., Catterall, W.A., 2019. Resting-State Structure and Gating Mechanism of a Voltage-Gated Sodium Channel. Cell 178, 993-1003.e12. https://doi.org/10.1016/j.cell.2019.06.031

134. Wu, Q., Huang, J., Fan, X., Wang, K., Jin, X., Huang, G., Li, J., Pan, X., Yan, N., 2023. Structural mapping of Nav1.7 antagonists. Nat Commun 14, 3224. https://doi.org/10.1038/s41467-023-38942-3

135. Yasukawa, M., Yasukawa, K., Kamiizumi, Y., Yokoyama, R., 2007. Intravenous phentolamine infusion alleviates the pain of abdominal visceral cancer, including pancreatic carcinoma. J Anesth 21, 420–423. https://doi.org/10.1007/s00540-007-0528-8

136. Yuan, R., Zhang, X., Deng, Q., Si, D., Wu, Y., Gao, F., Zhou, B., 2011. Two Novel SCN9A Gene Heterozygous Mutations May Cause Partial Deletion of Pain Perception. Pain Medicine 12, 1510–1514. https://doi.org/10.1111/j.1526-4637.2011.01237.x

137. Zakany, F., Kovacs, T., Panyi, G., Varga, Z., 2020. Direct and indirect cholesterol effects on membrane proteins with special focus on potassium channels. Biochimica et Biophysica Acta (BBA) - Molecular and Cell Biology of Lipids 1865, 158706. https://doi.org/10.1016/j.bbalip.2020.158706

138. Zhorov, B.S., 2021. Possible Mechanism of Ion Selectivity in Eukaryotic Voltage-Gated Sodium Channels. J. Phys. Chem. B 125, 2074–2088. https://doi.org/10.1021/acs.jpcb.0c11181

139. Zidovetzki, R., Levitan, I., 2007. Use of cyclodextrins to manipulate plasma membrane cholesterol content: Evidence, misconceptions and control strategies. Biochimica et Biophysica Acta (BBA) - Biomembranes 1768, 1311–1324. https://doi.org/10.1016/j.bbamem.2007.03.026

Appendices

***Table S1.** Uniprot accession codes for the nine human Na_v subtypes*

Subtype	Gene	Accession code
Na_v1.1	SCN1A	Q8NEY1
Na_v 1.2	SCN2A	Q99250
Na_v1.3	SCN3A	Q9NY46
Na_v1.4	SCN4A	P35499
Na_v1.5	SCN5A	Q14524
Na_v1.6	SCN8A	Q9UQD0
Na_v1.7	SCN9A	Q15858
Na_v1.8	SCN10A	Q9Y5Y9
Na_v1.9	SCN11A	Q9UI33

***Table S2.** Updated van-der-waal's radii for HOLE2.0 adapted to the martini3 forcefield*

Bead Size	Radius
Regular (R)	2.640
Backbone (B)	2.640
Small (S)	2.300
Tiny (T)	1.910

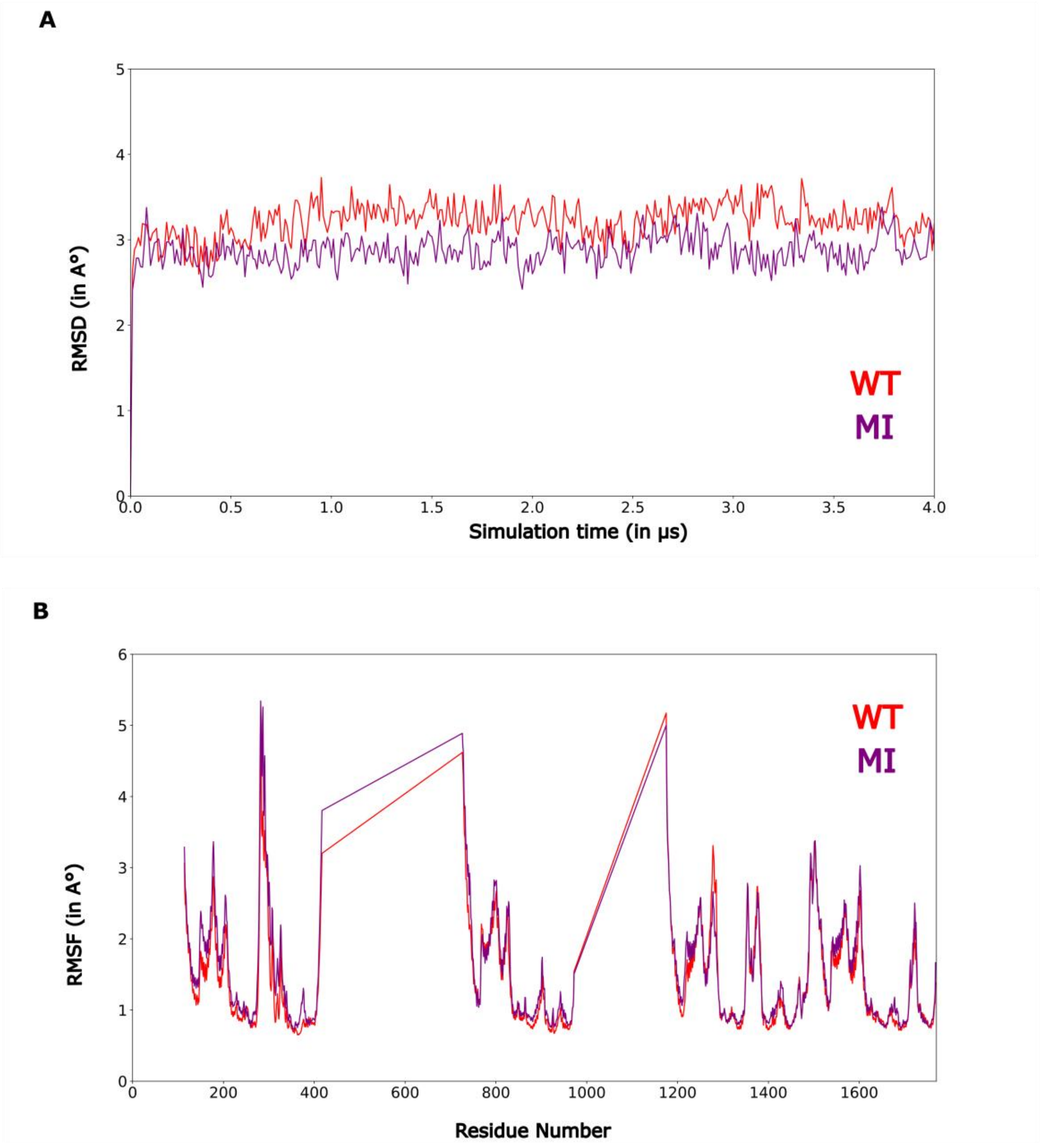

Figure S1 Average **(A)** RMSD and **(B)** RMSF of the simulated frames of hNa$_v$1.7 WT (WT) and hNa$_v$1.7 M899I (MI). RMSD is plotted against the simulation time, while RMSF is plotted against the residue number.

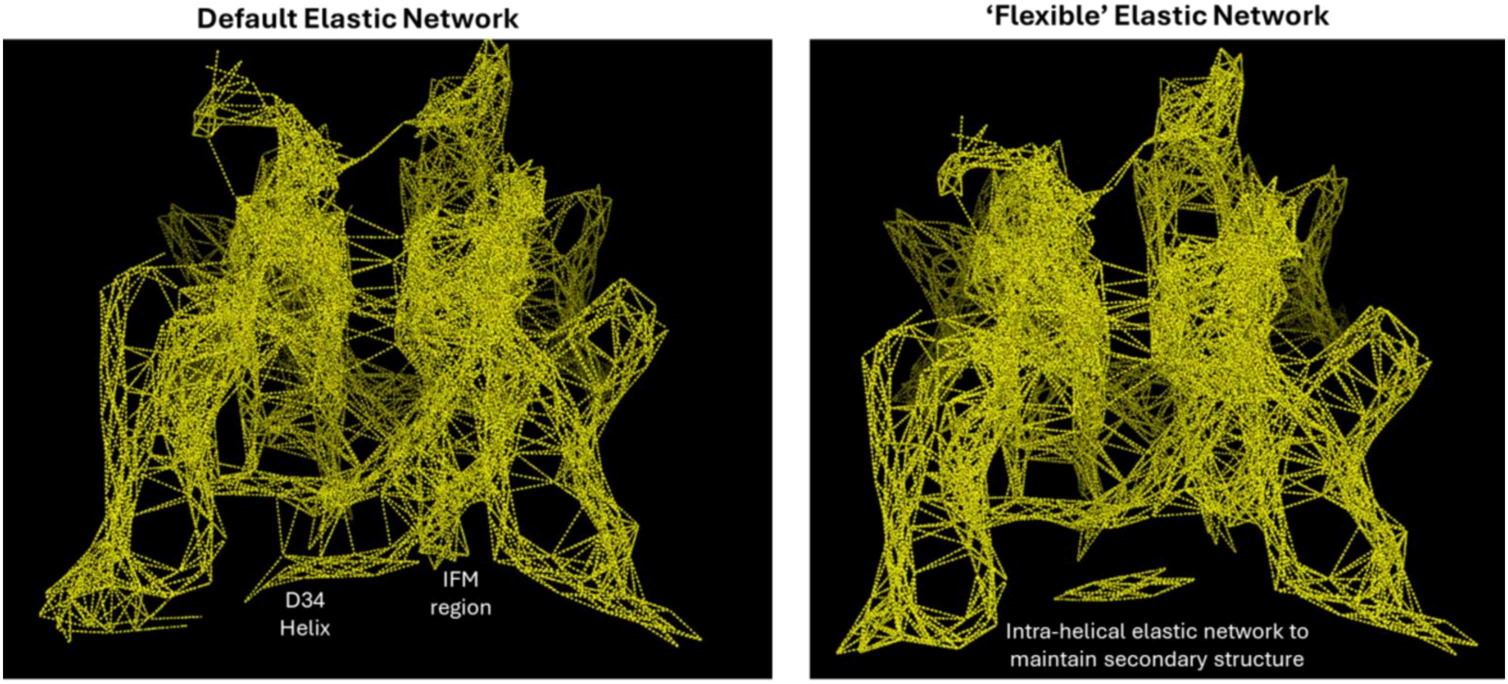

Default Elastic Network

‘Flexible’ Elastic Network

Figure S2 The elastic networks generated in the default and the modified “flexible” elastic network as performed in (Lin et al., 2024). While elastic networks are generated between the D34 and other parts of the protein in the default network, these are removed in the “flexible” network. The elastic networks within the helical region of D34 are kept to preserve its secondary structure.

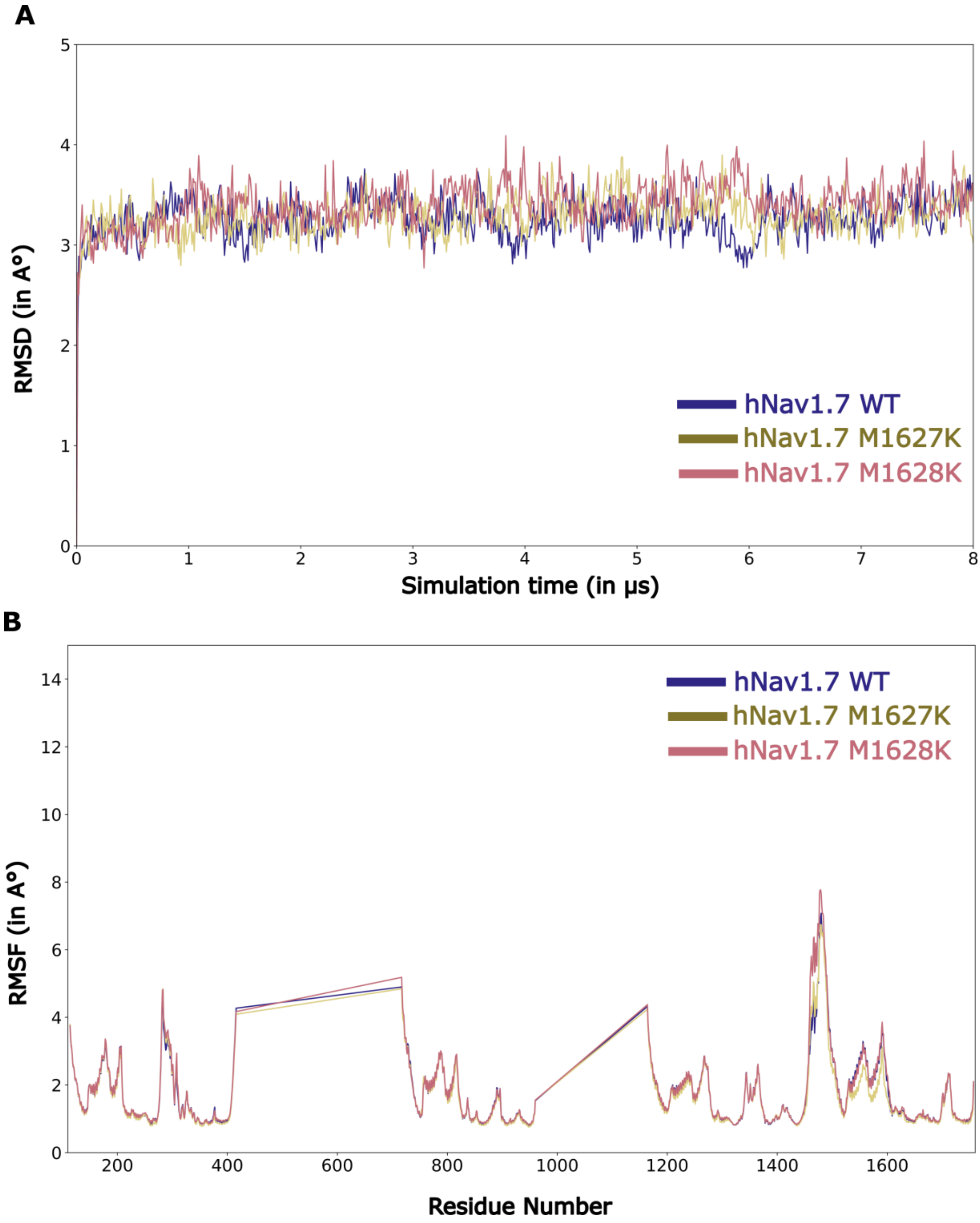

Figure S3 The average **(A)** RMSD and **(B)** RMSF of the backbone beads of the simulated frames of hNa$_v$1.7 WT, hNa$_v$1.7 M1627K and hNa$_v$1.7 M1628K. RMSD is plotted against the simulation time, while RMSF is plotted against the residue number. No difference in both can be visually observed.

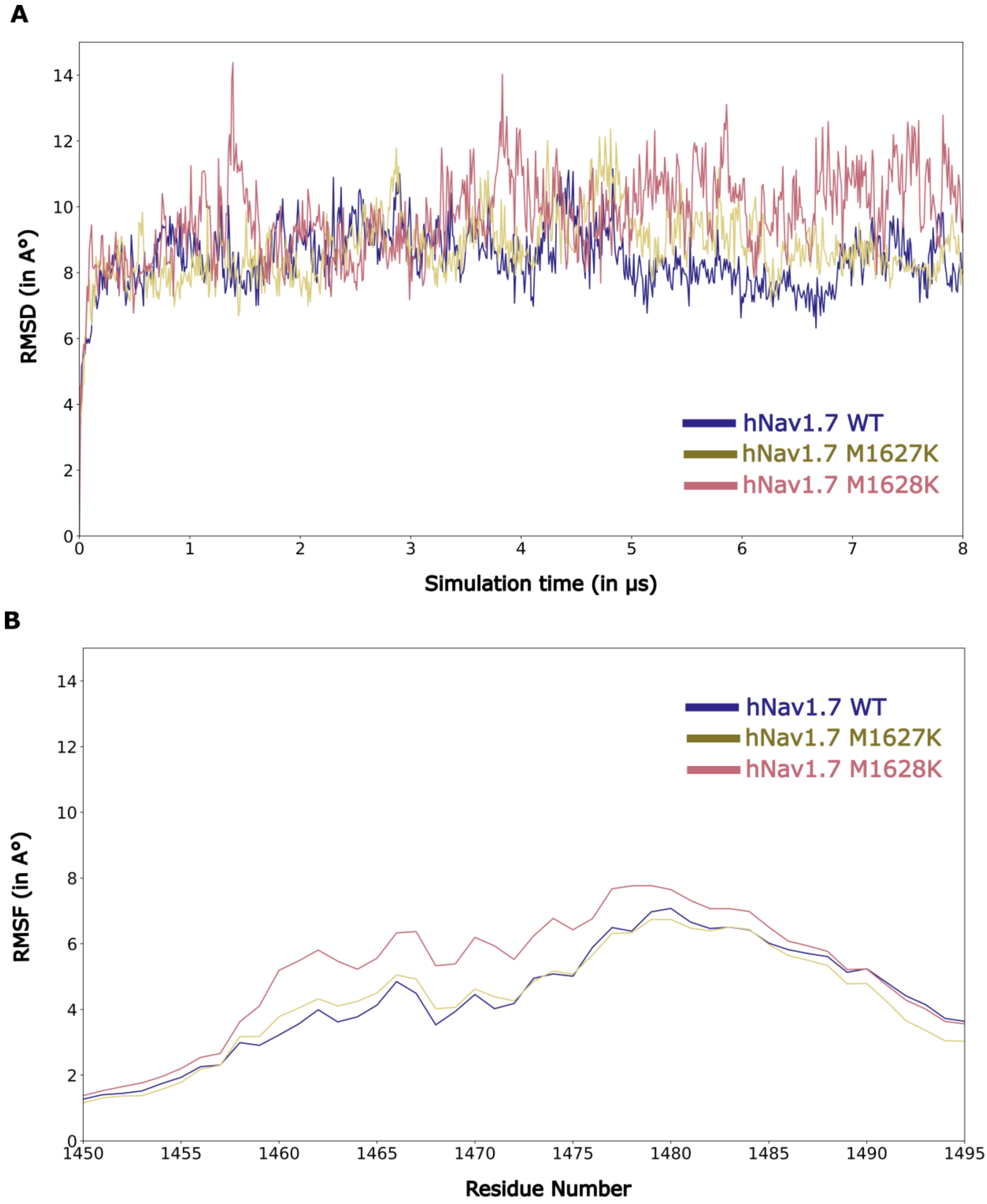

Figure S4 The average **(A)** RMSD and **(B)** RMSF of the backbone beads of the D3-D4 linker of the simulated frames of hNa$_v$1.7 WT, hNa$_v$1.7 M1627K and hNa$_v$1.7 M1628K. RMSD is plotted against the simulation time, while RMSF is plotted against the residue number. A clear increase in both RMSD and RMSF of these regions can be observed in hNa$_v$1.7 M1627K and hNa$_v$1.7 M1628K when compared to the hNa$_v$1.7 WT.

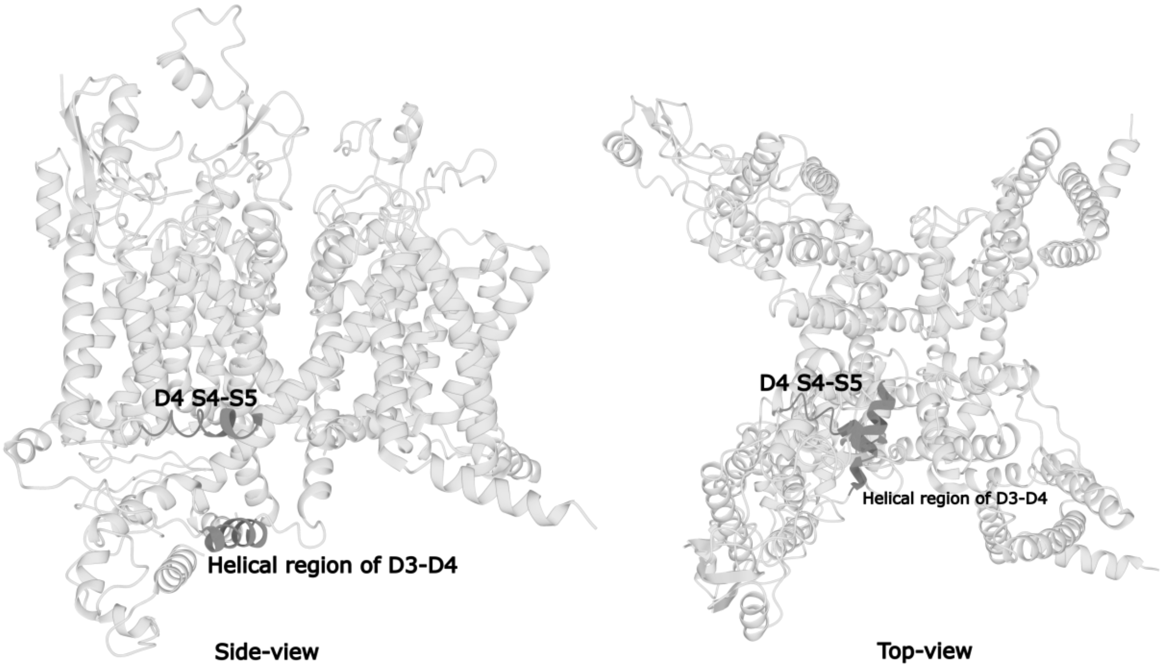

Figure S5 The perpendicular orientation of the D4 S4-S5 and the helical region of D3-D4 in the $Na_v1.7$ VSD4-NavPaS chimera bound to the scorpion toxin Aah2 published by (Clairfeuille et al., 2019) (PDB ID 6NT4). The toxin traps the VSD4 in a down state and likely represents a structural conformation where the IFM-like region is not bound. In both the side-view (left) and extracellular top view (right), we can see the almost perpendicular orientation of the two helices. This perpendicular orientation likely represents the conformational state of an IFM-unbound state.